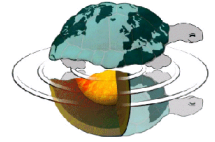




UNIVERSITÀ DEGLI STUDI DI MILANO

Dottorato di Ricerca in Scienze della Terra

Ciclo XXIX



**Advances in ordinary Portland cement clinker: reducing
the environmental impact of the production process**

Ph.D. Thesis

Matteo Galimberti

ID nr. R10541

Tutor

Prof.ssa Monica Dapiaggi

Academic Year

2015-2016

Coordinator

Prof.ssa Elisabetta Erba

Co-Tutor

Dott.ssa Nicoletta Marinoni

To my family and Sabrina

Contents

Research aim.....	5
Abbreviations.....	8
The ordinary Portland cement clinker.....	11
1.1 Binding materials.....	11
1.2 Historical milestones.....	12
1.3 World cement production and cements classification.....	13
1.4 OPC clinker production process.....	14
1.4.1 Raw materials selection, extraction and grinding.....	15
1.4.2 Raw meal preparation and pyro-processing.....	15
1.4.3 Clinker cooling and gypsum addition.....	16
1.4.4 Quality control parameters.....	16
1.5 Chemistry of OPC clinker pyro-processing.....	18
1.5.1 Solid-state reactions taking place below 1300 °C.....	18
1.5.2 Clinkering reactions at temperature between 1300 and 1450 °C.....	19
1.5.3 System cooling.....	19
1.6 High temperature thermochemistry of clinker.....	20
1.7 Clinker mineralogy.....	22
1.7.1 Tricalcium silicate.....	22
1.7.2 Dicalcium silicate.....	25
1.7.3 Tricalcium aluminate.....	26
1.7.4 Tetracalcium aluminium ferrite.....	28
1.7.5 Secondary clinker phases.....	28
1.8 Environmental impact.....	29
Analytical techniques.....	33
2.1 X-ray powder diffraction.....	33
2.1.1 The Rietveld method.....	33
2.1.2 Refinement strategy.....	34
2.2 X-ray fluorescence.....	35
2.3 Scanning electron microscopy.....	36
2.4 Electron microprobe.....	36
2.5 Optical microscopy.....	36
Effects of limestones petrography on OPC clinker raw meals burnability.....	39
3.1 Introduction.....	39
3.2 Materials.....	41
3.2.1 Geological overview.....	41
3.2.2 Experimental methods.....	43
3.2.3 Results.....	47

3.3	Burnability test.....	53
3.3.1	Raw meals formulation and firing cycle.....	53
3.3.2	Experimental methods	54
3.3.3	Results.....	55
3.4	Discussions	60
3.5	Conclusions.....	63
The effects of minor elements on the clinkerization process		65
4.1	Introduction.....	65
4.2	<i>Ex situ</i> experiments.....	67
4.2.1	Experimental procedure.....	67
4.2.2	Results and discussion	69
4.3	<i>In situ</i> temperature-resolved synchrotron XRPD experiments.....	89
4.3.1	The synchrotron radiation.....	89
4.3.2	Experimental procedure.....	89
4.3.3	Results and discussion	93
4.4	Conclusions.....	100
Heterogeneous raw meal systems		103
5.1	Introduction.....	103
5.2	Materials: characterization and preparation.....	105
5.3	Methods	107
5.3.1	Raw meals formulation.....	107
5.3.2	Thermal treatment.....	109
5.4	Results and discussion	110
5.4.1	Fluorine-free raw meals.....	111
5.4.2	Fluorine-doped raw meals	116
5.5	Conclusions.....	119
General conclusions		123
References.....		127
Appendix.....		137
	Appendix A1.....	137
	Appendix B1	143
	Appendix B2.....	161
	Appendix B3.....	167
	Appendix C1.....	171
	Appendix C2.....	175
Acknowledgements		179

Research aim

Hydraulic cement is an inorganic non-metallic substance, used as a bonding agent in the construction industry. It is a fine powder, made by a mixture of crystalline phases to which one or more forms of calcium sulphate have been added (Greer et al., 1992). When mixed with water, it forms a paste which sets and hardens by means of hydration reactions; once solidified, it retains its strength and stability even under water (UNI EN 197-1). Hence, cement is the essential glue bonding construction materials together.

Cement clinker is a hydraulic material which shall consist of two-thirds by mass of calcium silicates, whereas the remainder consisting of aluminium- and iron-containing phases and other compounds (UNI EN 197-1). It represents at least the 95% by mass of the so-called ordinary Portland cement. As a matter of fact, clinker and ordinary Portland cement production processes almost entirely superimpose (Figure I).

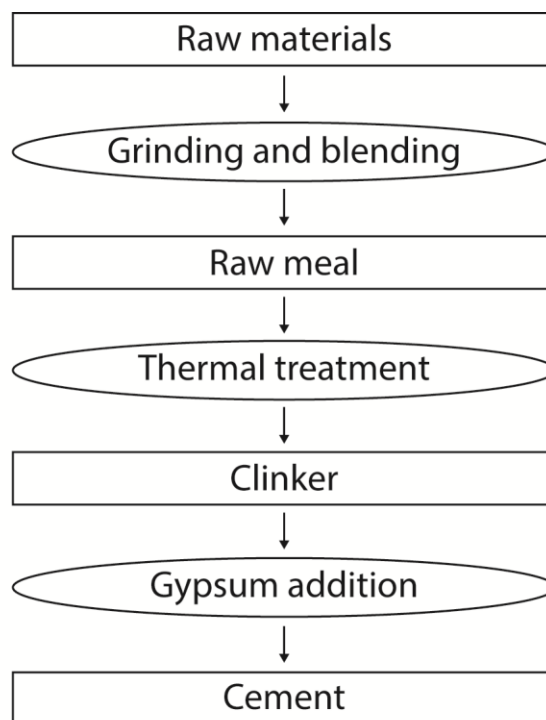


Figure I: Simplified flow diagram of ordinary Portland cement production process. Rectangles mark a material, whereas ellipses a procedure.

In the present thesis three different issues concerning the ordinary Portland cement clinker production process are investigated. The purpose is to better understand some key points of the clinkerization and to explore innovative raw meal configurations, in the global framework to reduce the environmental impact and the costs of cement manufacturing.

Chapter 1 gives first a general overview on the cements classification, defining the ordinary Portland cement. Then it illustrates the manufacturing process, from cradle to gate, of the ordinary Portland cement clinker, describing the mineralogy of the main crystalline phases and the chemical reaction occurring during the thermal treatment. Finally, the environmental impact of the production process in terms of greenhouse gases emissions, energy consumption, natural raw materials exploitation and pollutants is outlined.

Chapter 2 illustrates the main analytical techniques used in this work to gather raw data. Particular attention is paid to X-ray powder diffraction and spectroscopic chemical analyses. Instrumental setups and samples preparation procedures are also explained.

Chapter 3 aims to define an intrinsic parameter, closely linked to the raw materials, controlling the burnability of ordinary Portland cement clinker industrial raw meals. For this purpose eight different natural limestone samples were selected, to prepare just as many industrial raw meals; precisely limestones because they represent the overriding fraction within an industrial raw meal. These natural samples have been characterized by X-ray fluorescence, X-ray powder diffraction and optical microscopy; moreover, X-ray powder diffraction line profile analysis allowed to determine the calcite crystals average domains size and microstrain. Raw meals were thermally treated at different temperatures in an electrical furnace to evaluate the evolution of the phases assemblage by *ex situ* X-ray powder diffraction and to observe the final clinker morphology by scanning electron microscopy. Correlations between limestone petrography, calcite crystals microstructure and quantitative phase analyses results made possible to identify a parameter controlling the raw meals burnability.

Chapter 4 evaluates the effects of minor elements on the production process of ordinary Portland cement clinker. It deals with this already widely explored topic in cement chemistry from a different point of view: minor elements were indeed coupled together and natural raw materials were used instead of analytical reagents to prepare raw meals. This allowed to further validate or deny data from literature, when working with industrial natural raw materials. Sodium, magnesium and sulphur were considered as minor elements, whereas chlorine and fluorine as trace elements, these latter never coupled together. Raw meals were thermally treated at $T = 1450\text{ }^{\circ}\text{C}$ and the obtained clinker samples analysed by means of *ex situ* X-ray powder diffraction and electron microprobe. Moreover, a set of chlorine-doped raw meals was investigated by an *in situ* temperature-resolved synchrotron X-ray powder diffraction experiment, to evaluate chlorine effects on the clinkerization process and to identify, if possible, chlorine-bearing phases.

Chapter 5 is about an innovative approach concerning heterogeneous ordinary Portland cement clinker raw meals formulation, implying both the use of unconventional raw materials and non-standard setups. In particular, a magnesium-rich natural raw material has been used as a complete replacer of the clay fraction. Moreover, several combinations between fine- and coarse-grained limestone within raw meals were explored. Mixtures were thermally treated under standard laboratory firing conditions and clinker samples analysed by *ex situ* X-ray powder diffraction to carry out qualitative and quantitative crystalline phases analyses, in order to test the feasibility of these innovative arrangements concerning the raw meals formulation.

Abbreviations

In cement and concrete scientific literature, a shorthand notation that leaves the oxygen out is widely used to make chemical formulae shorter and more readable (Figure II). This notation can be combined with the standard one, for instance within a chemical equation, where the formulae of simple oxide phases are generally written in full.

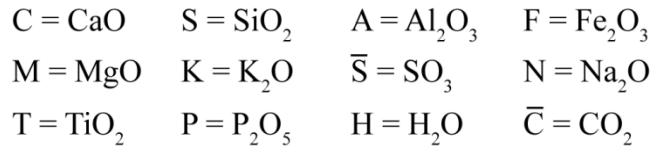


Figure II: Common oxides abbreviations according to the cement chemistry shorthand notation.

Other abbreviations commonly used in this thesis are as follows:

AR = alumina ratio (alumina modulus)

EMPA = electron microprobe analysis

L.o.I. = loss on ignition

LSF = lime saturation factor

OM = optical microscopy

OPC = ordinary Portland cement

SEM = scanning electron microscopy

SR = silica ratio (silica modulus)

XRPD = X-ray powder diffraction

XRF = X-ray fluorescence

WD-XRF = wavelength dispersive X-ray fluorescence

wt% = weight percentage fraction

Chapter 1

The ordinary Portland cement clinker

1.1 Binding materials

In the construction industry, binders are materials generally made up of a fine powder, obtained through the thermal treatment of fine-grained raw materials. Once mixed with water they give rise to a slurry suitable to be modelled; as the paste tends to lose water as a function of time, first it becomes hard to shape and then completely solidifies, developing mechanical properties through time (Taylor, 1990).

The transition from a plastic to a solid compound usually happens at room temperature, by chemical reactions between the binder and the surrounding environment.

Binders are usually classified in two broad categories, aerial and hydraulic respectively, relying on their ability to harden without or in presence of water.

Aerial binders or non-hydraulic cements such as gypsum and lime, need to react with atmospheric carbon dioxide to harden by means of a carbonation reaction once hydrated (Figure 1.1). Due to the limited carbon dioxide volume fraction in the atmosphere, this reaction requires a lot of time to complete and will only occur if the cement paste is exposed to air (Van Balen, 2003).

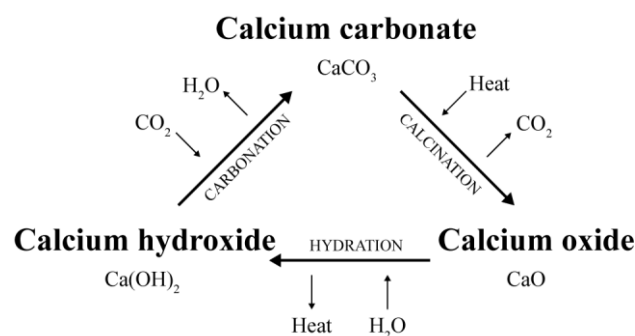


Figure 1.1: Reactions taking place during the hydration and hardening of lime, obtained from calcium carbonate calcination, through the so-called lime cycle.

Conversely, hydraulic binders such as hydraulic lime and cement, harden by an hydration process. For this reason they can be placed both in contact with air or with water, because of their capacity to harden underwater and to be water-resistant (Sabbioni et al., 2001, 2002).

For the sake of clarity an explanation concerning the difference between hydrated and hydraulic lime is necessary. Hydrated lime, $\text{Ca}(\text{OH})_2$, is obtained by adding water to burnt lime (CaO), whereas hydraulic lime is none other than a *poor* cement clinker. This shady nomenclature arose in the past when sometimes, by chance, a lime able to harden even in contact with water was obtained, ignoring that the actual reason of this behaviour lied in the carbonate fraction chemical composition: pure limestone for lime, argillaceous limestone for hydraulic lime.

1.2 Historical milestones

The accidental discovery of binders dates back to Ancient history or even Prehistory when man observed that the inner walls of furnaces made of limestone or gypsum used to change their aspect due to the continuous exposure to fire, leading to a new material. This new material, once in contact with water, formed a plastic paste that hardened once dried out. These early binders were probably originated by anhydrite rather than by lime, because of the lower temperature required to transform gypsum into anhydrite rather than limestone into lime.

The use of gypsum as a binder became widespread in the ancient Egypt, whereas a pioneering use of hydraulic lime dates to the 10th century BC in Israel.

The knowledge grew through centuries, since in Ancient Rome the limestone thermal decomposition into lime and its transformation into burnt lime by adding water were both well known. Moreover, as reported in the “De Architectura” by the Roman architect Vitruvius, the Romans also usually used to prepare cementitious materials able to set and harden in contact with water by blending natural pozzolan (an unconsolidated pyroclastic siliceous rock) or pottery with lime and water. The Pantheon, in particular its dome, built in the 2nd century AD by employing this kind of binder has survived until nowadays, perfectly witnessing the high performances achieved by Roman binders in terms of durability and mechanical properties.

In the timespan from the fall of the Western Roman Empire until the 18th century no significant innovations occurred in the building techniques. In 1756, the English civil engineer John Smeaton, entrusted with the construction of a lighthouse, took care to choose a binder able to harden underwater. He noted that the clay minerals content within a limestone was one of the key factors to determine the hydraulic properties of lime.

Between 1812 and 1818 the French engineer Louis Vicat scientifically studied hydraulic lime and confirmed Smeaton’s assumption: the best limestones to prepare hydraulic lime were the ones rich in clay minerals. This because during the thermal treatment the lime reacts with silica and alumina, from the clay minerals, to give a *poor* cement clinker. Poor because the weight proportions between lime, silica and alumina were not the proper ones, as well as the firing temperature was too low ($T \sim 900\text{-}1000\text{ }^\circ\text{C}$).

Again, across the 18th and the 19th century, various attempts to produce these binders at an industrial scale began, thanks mainly to James Parker that in 1796 patented a product able to harden underwater called “roman cement” because resembled to pozzolan from Lazio. Parker’s roman cement raw materials had a larger content of clay minerals and were fired at higher temperatures than Smeaton’s limestones, but the result was still far from modern cement clinker.

Wrongly, it is Joseph Aspdin credited to first invent the Portland cement, but his cement was approximately the same as Parker's roman cement, dating few years before. The working temperature was again too low, since no liquid phase used to form. It is thus possible to say that it was pretty far from what nowadays is called Portland cement, being rather again an hydraulic lime.

It is only in 1844 that a product very similar to a modern Portland cement was manufactured by the British cement manufacturer Isaac Charles Johnson. He proved that the appearance of a melt fraction during the production process was a key point.

Smeaton, Vicat and Johnson have to be credited as the pioneers of the modern cement industry. Smeaton and Vicat identified and scientifically described the concept of hydraulicity, whereas Johnson has to be actually ascribed as the owner of Portland cement invention.

Since the second half of the 19th century, the cement industry has spread from Great Britain to Europe. In Italy the manufacturing of hydraulic binders started in 1856 in Palazzolo sull'Oglio, employing argillaceous limestones from the Iseo Lake to produce hydraulic lime, whereas for Portland cement we had to wait until 1892, in Vittorio Veneto and again in Palazzolo.

1.3 World cement production and cements classification

Nowadays, cement industry is continuously increasing its output, making cement the most widespread construction material in the world (Kajaste and Hurme, 2016). Global cement annual production has increased by nearly the 200% in the last fifteen years, as reported in Figure 1.2.

In 2014, cement production exceeded 4.1 Gt, corresponding to 0.55 t of cement per person. China contributed to the 59% of the global production, followed by India (6%), United States (2%), Brazil (2%) and Turkey (2%). The remaining 29% was produced by the rest of the world, where the contribution of Italy was nearly 0.5% (U.S.G.S., 2016).

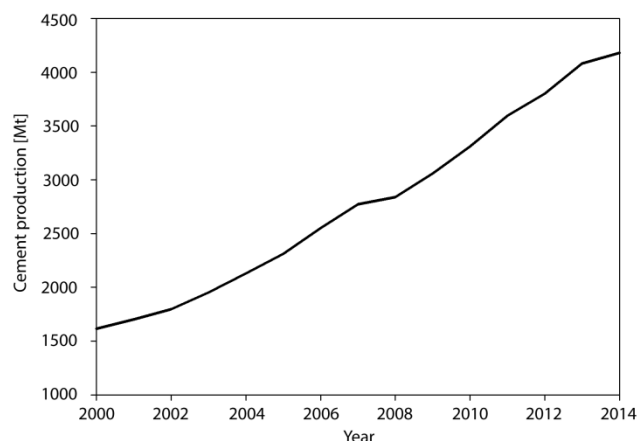


Figure 1.2: World cement production between the years 2000 and 2014 (U.S.G.S., 2002 – 2015).

UNI EN 197-1 normative classifies cements according to their composition and properties, in terms of components and mechanical resistance. Twenty-seven products and six strength classes are considered within the family of common cements; by combining them, over one-hundred and fifty different kinds of cement are theoretically possible. However, not all of these cements are actually manufactured due to technical difficulties or even impossibility to product or employ them.

The six strength classes are labelled as 32.5N, 32.5R, 42.5N, 42.5R, 52.5N and 52.5R respectively. The number indicates the minimum resistance value, expressed in MPa, carried out through a compressive test after 28 days, whereas letter N (normal) or R (rapid) indicates the minimum resistance to compressive strength, expressed in MPa, after 2 days (exceptionally after 7 days for 32.5N cement). In particular, R cements have a higher mechanical resistance in the short term than the N ones; however after 28 days the mechanical properties must be the same for both N and R cements. The twenty-seven cement types are classified into five main groups, from CEM I to CEM V, according to the weight proportion between clinker and *other materials*. *Other materials* can refer to blast furnace slag, silica fume, natural pozzolan, natural calcined pozzolan, siliceous fly ash, calcareous fly ash, burnt shale, limestone and calcium sulphates.

CEM I: ordinary Portland cement. Clinker content must be at least the 95 wt% and *other materials*, commonly calcium sulphates, ground granulated blast-furnace slags or fly ash, less than 5 wt%. This cement is usually employed for general construction works.

CEM II: Portland-composite cements, covering all kinds of hybrid Portland cements with *other materials*, where clinker weight content must be at least 65 wt%.

CEM III: Blastfurnace cements, where clinker is mixed to blast furnace slag in different proportions. The CEM III/C is the one with the lowest absolute clinker content and as a consequence also heat of hydration; the clinker to slags ratio is 5/95.

CEM IV: Pozzolanic cements, characterized by higher levels of pozzolanic material (up to 55 wt%) than type II cements.

CEM V: Composite cements containing a higher fraction of *other materials* than type II cements. They are also allowed to have more than one secondary material.

1.4 OPC clinker production process

As already stated, clinker is the main constituent of ordinary Portland cement; hence, the OPC manufacturing process superimposes to the one of clinker. The difference between OPC and clinker lies in the presence or absence of calcium sulphate, usually added to regulate the setting time.

Clinker production starts from a finely ground and homogeneous mixture of limestone and clay minerals, in a ratio ranging from 4:1 to 5:1, to ensure the proper weight proportions between CaO, SiO₂, Al₂O₃ and Fe₂O₃. However, small amounts of corrective materials such as bauxites, iron ore and quartz sand are usually added to the blend to raise the content of Al₂O₃, Fe₂O₃ and SiO₂, when too low. This blend, called raw meal or kiln feed, is thermally treated up to 1450 °C, when partial fusion occurs and nodules of clinker form.

The raw meal thermal treatment can be performed by a wet, a semi-wet or a dry process. In the wet process the raw meal enters the kiln in a form of a slurry with a water content about 24-48 wt%, in the semi-wet (or semi-dry) the water is reduced to 17-22 wt%, whereas in the dry process the raw meal is a powder with moisture lower than 1 wt%.

In the past the wet process was preferred because it was easier to both grind and mix the raw materials and to control the particle size distribution within a slurry. Technological advances in the grinding processes and in the pyro-processing systems reduced the need for the wet process, making it affordable only when the raw materials already have a significant water content. Hence, nowadays the

most common setup is represented by the dry process, because it requires ~40% less energy than the wet process (Ziegler, 1971; Mintus et al., 2006).

Henceforth, in the present thesis, only the dry process will be considered when referring to OPC clinker manufacturing.

Cradle-to-gate, the OPC manufacturing process consists of three steps:

- Raw materials selection, extraction and crushing;
- Raw meals preparation and pyro-processing to form clinker;
- Clinker cooling and gypsum addition to have cement.

1.4.1 Raw materials selection, extraction and grinding

Suitable limestones are essentially made of calcite, the ambient pressure polymorph of calcium carbonate. However they can contain minor elements, either as substituent ions in the calcite structure or due to secondary minerals occurrence. The threshold limits vary according to the element nature, stricter for alkalis and heavy metals than for silicon and magnesium.

As clays, rocks carrying minerals of the illite, kaolinite and to a less extent montmorillonite groups are taken into account. Their chemical composition should range among 55-60 wt% SiO₂, 15-25 wt% Al₂O₃, 5-10 wt% Fe₂O₃, with minor contents of MgO, Na₂O, K₂O and water. Clays are the product of meteoric alteration of aluminium silicates from the bedrock and can also contain relict minerals, such as quartz or iron oxides.

Relying on the local availability, limestones and clays can be replaced by schists or volcanic rocks of suitable composition.

Limestones and clays have low intrinsic economic value; therefore, they are often extracted close to the production plant, from open-face quarries (Figure 1.3a), because their transportation would not be cost-effective. These raw materials are roughly crushed at the quarry site into blocks of 5-10 cm of diameter and then delivered to the production plant (Figure 1.3b).

1.4.2 Raw meal preparation and pyro-processing

When raw materials arrive at the production plant, they are pre-homogenized to ensure a regular and defined chemical composition. Any correction, if needed, is made at this step.

Then, the raw mill refines this mixture in the form of a powder, to later ensure the best conditions during the thermal treatment. Raw materials, poured into the mill, undergo mechanical stresses such as collisions, compression and friction to reduce their grain size (Figure 1.3c). The obtained powder, called raw meal, is stacked into silos and further homogenized before entering the pyro-processing stage.

Raw meals are then prepared from a thermal and chemical point of view before entering the kiln, through a pre-heating and pre-calciner system, located in the cyclone tower (Figure 1.3d). Moisture and free water are completely evaporated, whereas clays and carbonates are fully destabilized into their constituent oxides, giving rise to a very reactive mixture suitable to enter the kiln. Short kiln with multistage preheater is the current most efficient technology (Sorrentino, 2011; Chatterjee, 2011).

The rotary kiln is a tube with a diameter ranging from 3 to 8 m, rotating 1 to 3 times per minute and installed at a 3-4° inclination. Rotation and inclination allow the material to slowly advance, from the top to the flame-end of the kiln, where the burner is installed. Hence, the raw meal moves down the kiln counter-current to hot air, experiencing a gradual heating and the completion of all the thermal reactions. As the raw meal advances through the kiln the temperature increases up to 1450 °C, when partial fusion occurs and clinker forms (Figure 1.3e).

1.4.3 Clinker cooling and gypsum addition

Cooling down clinker is a key point of the entire process, because it guarantees the proper mineralogical and textural composition, by achieving polymorphic transformation of tri- and di-calcium silicates and aluminates crystallization. Also backward reactions are partially hindered, in particular the dissociation of tricalcium silicate into dicalcium silicate and lime (Figure 1.3f). A common cooling method consists in running the material over a grid and blowing it by a room-temperature air flow; by-product hot air is routed back to the preheater unit.

Once cooled, clinker is stacked into silos (Figure 1.3g), finely ground in a rotating ball mill, added with gypsum (Figure 1.3h) and later homogenized, obtaining thus the cement (Figure 1.3i) ready to be dispatched (Figure 1.3j). The fineness of the cement powder has a key-role because the coarser the particles, the worse the cement reactivity. In a modern cement, at least the 90 wt% of the particles has a grain size between 2 and 90 μm, the 7-9 wt% is finer than 2 μm whereas the 0-4 wt% is coarser than 90 μm (Taylor, 1990).

1.4.4 Quality control parameters

Bulk chemical analyses of raw materials, cements and clinkers are usually expressed as oxides components mass percentage. Lime saturation factor, silica ratio and alumina ratio are widely used parameters, based on the oxide composition, to predict the expected clinker characteristics.

The lime saturation factor (Equation 1.1) is described as the mass ratio between CaO and SiO₂, Al₂O₃ and Fe₂O₃; common values in modern industrial clinker raw meals range from 0.92 to 0.98. Theoretically, a value equal to 1 indicates that no free lime will occur in the final product, being all combined to C₂S to give C₃S. Due to the impossibility to have a perfect raw meal homogenization, uncombined lime is present even if the LSF is below 1. Moreover, to convert all the belite into alite, a LSF value above 1 is needed.

$$LSF = \frac{CaO}{(2.8 SiO_2 + 1.2 Al_2O_3 + 0.65 Fe_2O_3)} \quad (1.1)$$

The silica ratio (Equation 1.2), or silica modulus, value ranges typically between 2.0 and 3.0. The higher the value, the more the calcium silicates weight fraction in the clinker, at the expense of the aluminates.

$$SR = \frac{SiO_2}{Al_2O_3 + Fe_2O_3} \quad (1.2)$$

The alumina ratio (Equation 1.3), or alumina modulus, determines the relative weight proportion between tricalcium aluminate and ferrite; high AR values lead to more tricalcium aluminate and less ferrite in the clinker. Common values span from 1 to 4.

$$AR = \frac{Al_2O_3}{Fe_2O_3} \quad (1.3)$$

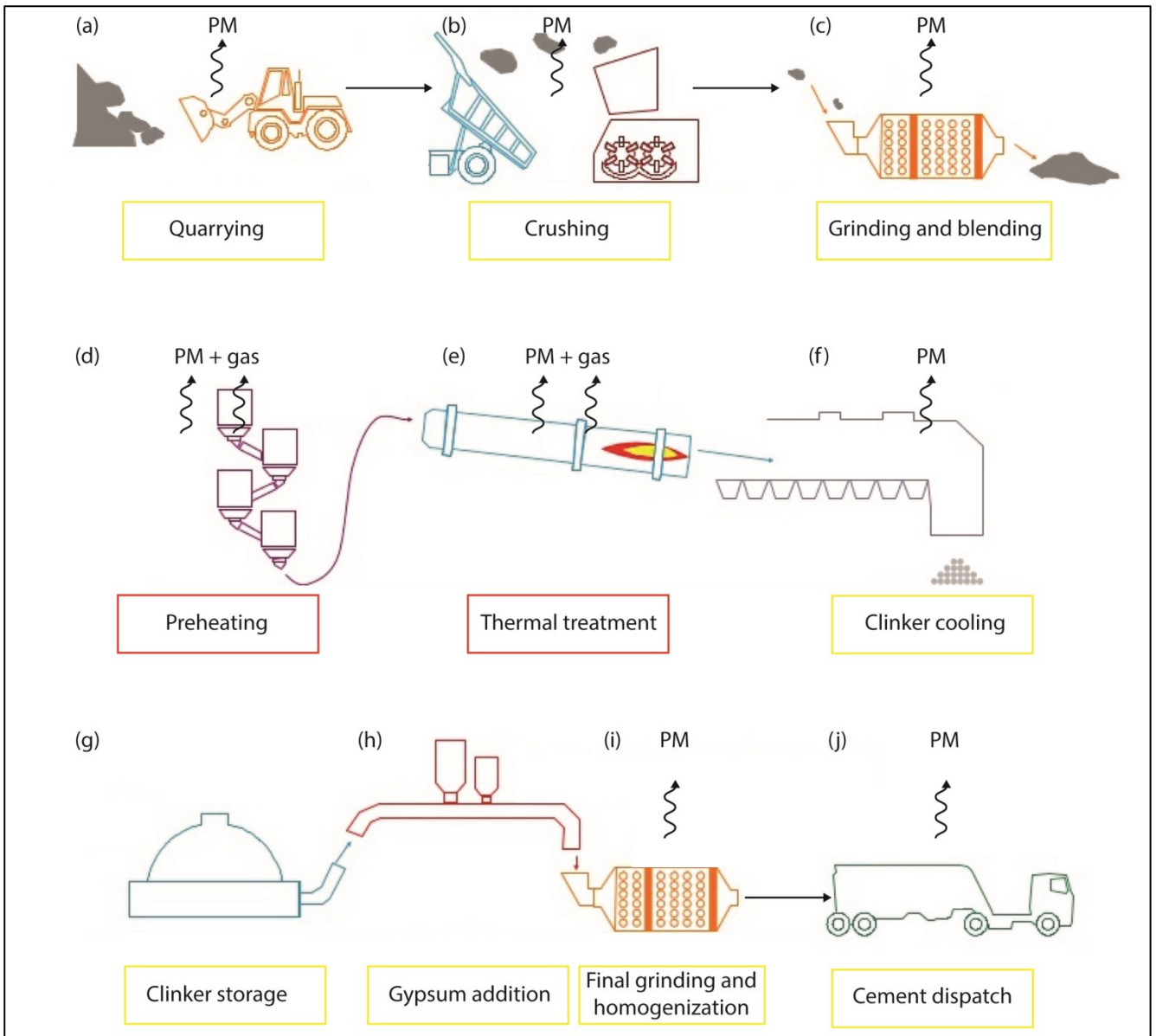


Figure 1.3: Schematic representation of the ordinary Portland cement manufacturing process. (a) raw materials quarrying; (b) on-site crushing; (c) blending and grinding at the production plant; (d) preheating and calcination inside the cyclone tower system; (e) rotary kiln thermal treatment; (f) clinker cooling; (g) clinker storage; (h) gypsum addition to obtain cement; (i) cement grinding and further homogenization; (j) final product dispatch. Yellow rectangles indicate a process requiring an energy input, red ones a heat input; PM = particulate matter emissions; gas = gaseous emissions.

1.5 Chemistry of OPC clinker pyro-processing

Figure 1.4 gives a more detailed overview of the chemical and physical processes taking place during the firing stage of the ordinary Portland cement clinker manufacturing process. They can be divided into three groups: (i) raw materials destabilization and solid-state reactions taking place at $T < 1300$ °C; (ii) clinkering reactions between $T = 1300$ and $T = 1450$ °C; (iii) clinker cooling down to room temperature.

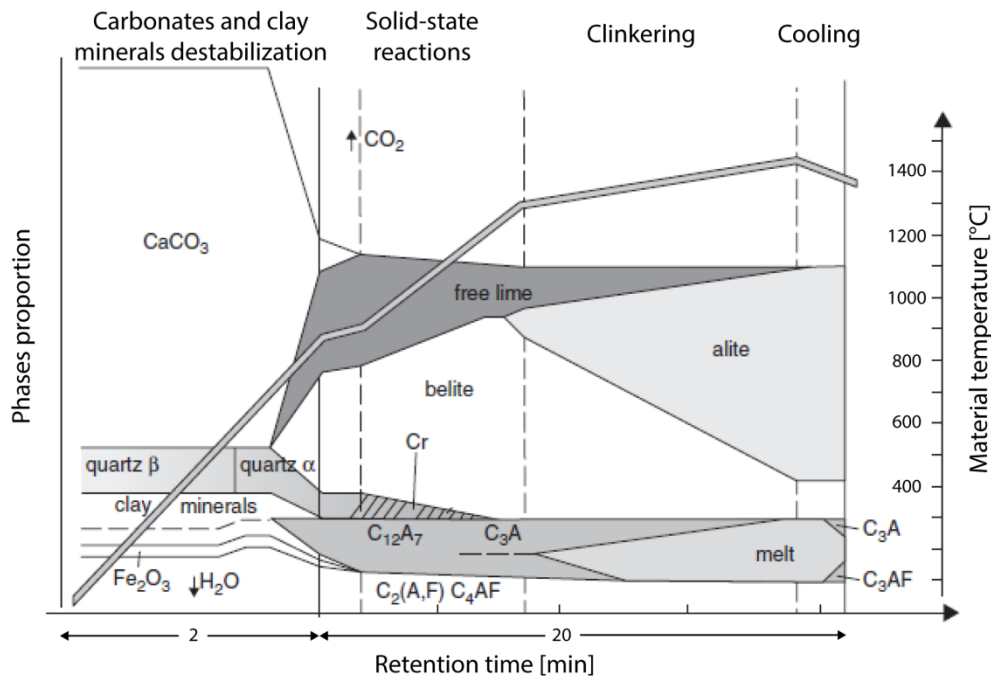


Figure 1.4: Phase transition of an OPC clinker raw meal, as a function of temperature and time. Redrafted after Kurdowski (2014).

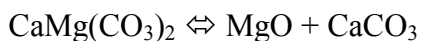
1.5.1 Solid-state reactions taking place below 1300 °C

Carbonates calcination and clay minerals decomposition are the main reactions taking place in the temperature range below 1300 °C.

Dealing with carbonates, the most common reactions are the calcite and to a lesser account the dolomite decomposition.



$$P = 1 \text{ atm} \quad T = 894 \text{ °C}$$



$$P = 1 \text{ atm} \quad T = 750 \text{ °C}$$

Experimental observations reported in Kurdowski (2014) highlight that these theoretical temperature are significantly lowered during the industrial manufacturing process, due to the interaction between the raw meal components. As an example, the calcite decomposition reaction could start at $T = 600 - 700$ °C, preceded by dolomite dissociation.

Physically, the calcite decomposition begins on the rim of the crystal and proceeds towards the core, increasing the porosity of the material until the complete transformation into calcium oxide is

achieved. The ever-growing porosity eases the escape of the released CO_2 , speeding up the entire decomposition process. As a consequence, the finer the calcite average grain size, the best the reactivity: this is one of the main reasons to finely grind raw materials below 80 μm .

The clay minerals decomposition is more heterogeneous, relying on the mineral species different structures, chemical compositions and average grain sizes. Main reactions taking place are the evaporation of adsorbed and interlayer water ($T < 300\text{ }^\circ\text{C}$), the complete dehydroxylation between 300 and 600 $^\circ\text{C}$ and the formation of new phases such as Al-Si spinel and cristobalite (600-1100 $^\circ\text{C}$) and mullite, this latter above 1100 $^\circ\text{C}$.

Silica polymorphic transitions also occurs, strongly affected by the intimate mixing with other compounds within the raw meal. That makes transition temperatures lower than the ones reported in literature: for example, Kurdowski (2014) observed that cristobalite already occurs at 1000 $^\circ\text{C}$, well below the theoretical 1470 $^\circ\text{C}$.

Carbonates and clay minerals decomposition reactions and silica polymorphic transitions are closely related to the appearance, already at $\sim 800\text{ }^\circ\text{C}$, of dicalcium silicate and aluminates. These latter will melt at higher temperatures and will recrystallize during the cooling stage, to be present as interstitial matrix between the silicate phases in the final product.

1.5.2 Clinkering reactions at temperature between 1300 and 1450 $^\circ\text{C}$

In the 1300 – 1400 $^\circ\text{C}$ temperature range the aluminates completely melt and about the 15-25 wt% of the system is thus made by a liquid phase. Then, increasing the temperature up to 1450 $^\circ\text{C}$, the reaction between dicalcium silicate and lime to give tricalcium silicate speeds up significantly, due to calcium and silicon ions diffusion through the melt fraction, characterized by an aluminate composition.

The combined effect of crystals acting as crystallization germs and melt lead to coalescence and to the following nodules formation, which dimensions span from 2 to 30 mm. Nodulization requires a significant melt fraction with low viscosity, high surface tension and dispersed fine-grained solid particles to happen.

1.5.3 System cooling

The cooling is a key issue of the entire process because it determines the final phase assemblage in clinker. When the equilibrium between the melt and the solid phases is maintained by a proper cooling rate, the silicates polymorphic transitions and the crystallization of aluminates happen, hindering the formation of an amorphous phase. On the contrary, a too fast cooling rate prevents the equilibrium between the melt and the solid phases, resulting in the occurrence of an amorphous phase in the room-temperature system; a too slow cooling rate guarantees no amorphous content but the final product quality is however poor due to the intense tricalcium silicate dissociation into dicalcium silicate and lime.

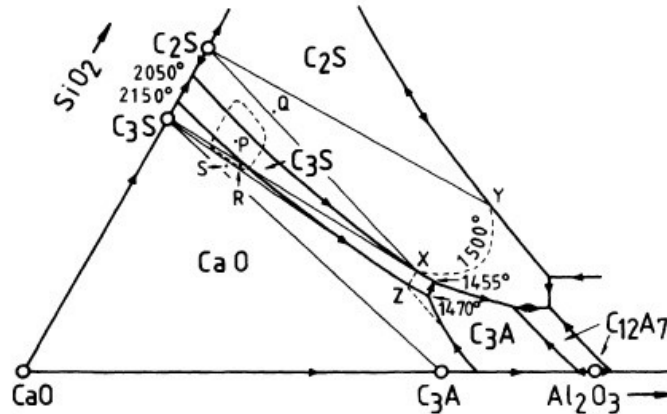


Figure 1.6: Close-up of the CaO-Al₂O₃-SiO₂ diagram, near the CaO corner (in Taylor, 1990).

When a melt of composition *P*, or close to it, is cooled, C₃S is the first phase to crystallize, moving the liquid composition away from the C₃S corner. When its composition meets the boundary line between C₃S and C₂S, also C₂S starts to form and the liquid composition will move along this boundary until the T = 1500 °C isotherm is reached. At these conditions, the two calcium-silicate phases are always in contact with a liquid, allowing them to grow up to relatively large dimensions; then, upon further cooling, also the interstitial matrix will form, in this case made only by C₃A because no iron is considered in the C-A-S system.

Bulk chemical compositions lying below the C₃S-Z line are not recommended in clinker manufacturing because they will cause calcium oxide occurrence as a proper phase, independently from the C₃S dissociation into C₂S and CaO at sub-solidus temperatures. The C₃S-Z line sets thus the maximum value of admissible CaO in the raw meal.

Lea and Parker (1935) studied the CaO-C₄AF-C₂S ternary system and the CaO-C₂S-C₁₂A₇-C₄AF tetrahedron (Figure 1.7) to get a complete analysis of the thermodynamic processes driving the clinker formation.

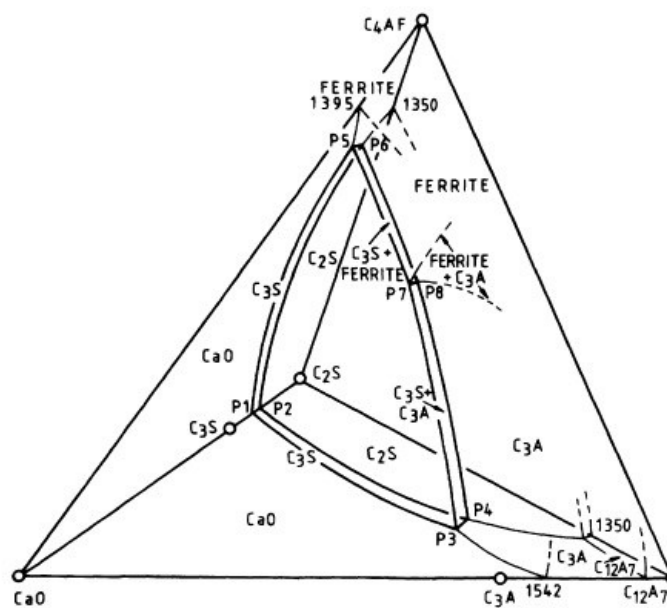


Figure 1.7: CaO-C₂S-C₁₂A₇-C₄AF pseudosystem (in Taylor, 1990).

Thanks to their results it was possible to fully control the maximum admissible CaO content, noticing that the lime saturation *plane* passes through the tetrahedron CaO-C₂S-C₁₂A₇-C₄AF with P3, C₃S and C₄AF as intersection points. The line joining P3 to C₃S was already identified as a lime saturation *line* in the C-A-S ternary diagram. It is thus possible to write a three-equation system for every intersection point between the lime saturation plane and the tetrahedron, imposing the saturation condition for each of them, defining thus the so-called lime saturation factor.

1.7 Clinker mineralogy

1.7.1 Tricalcium silicate

Crystal structure and polymorphism

Tricalcium silicate (alite, Ca₃SiO₅, C₃S) is the main component of an OPC clinker, representing at least half of the whole compound. Seven different polymorphs are known (Figure 1.8), stable as a function of temperature, at ambient pressure P = 0.1 MPa (1 atm).

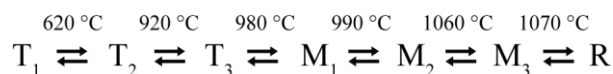


Figure 1.8: Pure C₃S polymorphic transitions as a function of temperature. T = triclinic, M = monoclinic, R = rhombohedral.

The polymorphs crystal structures are similar concerning the position of Ca²⁺ and O²⁻ ions and Si atoms. They differ regarding the degree of disorder determined by the SiO₄⁴⁻ tetrahedra spatial orientation and by the different coordination between the Ca²⁺ and the O²⁻ ions within the same tetrahedron (Jeffery, 1952).

Theoretically, for pure C₃S, the T1 polymorph is the only stable at ambient conditions. However, in industrial clinkers, the monoclinic forms M1 and M3 are found in the final product instead. The incorporation of foreign elements in the M1 and M3 structures at high temperatures, avoid their collapse on cooling, hindering the stabilization of the triclinic forms. Table 1.1 reports the main crystallographic information of the most common C₃S polymorphs.

Polymorph	Space group	Cell parameters (a, b, c in Å)						Reference
		a	b	c	α	β	γ	
T1	P-1	11.670	14.240	13.720	105.5°	94.3°	90.0°	Golovastikov et al., 1975
M3	Cm	33.083	7.027	18.499	90.0°	94.1°	90.0°	Nishi et al., 1985
M1	Pc	27.874	7.059	12.258	90.0°	116.03°	90.0°	Dunstetter et al., 2006
R	R3m	7.135	7.135	25.586	90.0°	90.0°	120.0°	Nishi and Takeuchi, 1984

Table 1.1: Crystallographic data for the most common C₃S polymorphs.

Chemically, pure C_3S contains 73.7 wt% of CaO and 26.3 wt% of SiO_2 , but 3–4 wt% of substituent oxides such as MgO, Al_2O_3 and Fe_2O_3 generally occurs in industrial clinker C_3S .

Mg^{2+} usually replaces Ca^{2+} , whereas both Al^{3+} and Fe^{3+} replace Ca^{2+} and Si^{4+} ; the maximum solubility limits are inversely proportional to temperature, decreasing from 2.0% at 1550 °C to 1.5% at 1420 °C in the case of MgO. Stand-alone Al_2O_3 and Fe_2O_3 exhibits 1.0% and 1.1% solubility limits respectively, but actually these values are lower because both chemical species compete for the same lattice site (Taylor, 1990).

Minor elements threshold limits are 1.4 wt% at 1500 °C for both Na_2O and K_2O (Woermann et al., 1979), whereas a 0.9 wt% value for SO_3 was found (Gartner and Tang, 1987; Regourd and Boikova, 1992).

Particular attention should be paid to MgO and SO_3 content in the clinker raw meal (Figure 1.9), because the MgO to SO_3 ratio controls the proportion between the forms M_1 and M_3 (Maki and Goto, 1982; Maki et al., 1992). Small and euhedral M_3 crystals will occur for high MgO/ SO_3 values, witnessing the predominance of nucleation over growth; vice-versa large M_1 crystals will form for low MgO/ SO_3 values, pointing out a rapid growth. To a lesser extent, the M_1 - M_3 polymorphism is also affected by the clinker cooling rate: a slow cooling promotes the transformation from M_3 to M_1 .

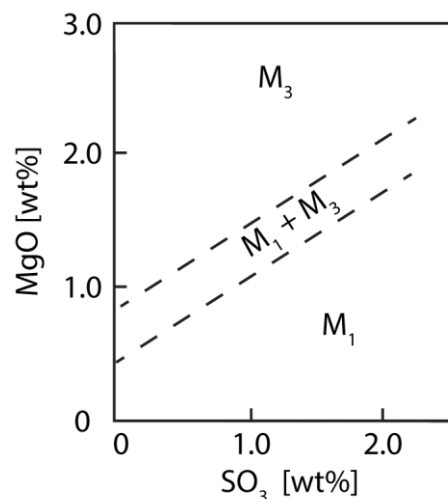


Figure 1.9: C_3S polymorphic modifications relying on the SO_3 and MgO wt% within the kiln feed.

XRPD identification

The XRPD patterns of alite polymorphs are visually quite similar and in commercial clinkers most of their peaks usually overlap the ones of other phases. Their profile relies both on the polymorph or mixture of polymorphs and on the type and amount of substituent ions within the crystal lattice. The fine structure of some peaks, in the 31.5–33° and 51–52° 2θ angular windows (with copper radiation), can be useful to distinguish between the different polymorphs. The peaks in the 31.5–33° window are the most intense ones, but using them to determine the polymorphs assemblage in a clinker is a hard task because they always overlap with the ones of other phases; they are useful only analysing pure C_3S compounds. On the contrary, the 51–52° 2θ window is the most meaningful one in commercial clinkers admixtures: here, the M_1 form gives a singlet (Figure 1.10a), with a poorly defined shoulder

towards high angles, whereas M3 defines a doublet (Figure 1.10b); a mixture of both M1 and M3 describes a scarcely defined doublet with the lower angle peak more intense than the higher angle one (Figure 1.10c). Still referring to the 51-52° 2θ window, triclinic forms do not exhibit a doublet but a well-defined triplet (Figure 1.10d). Figure 1.11 reports useful angular windows for M1 and M3 identification in commercial clinkers, taking into account regions where C_3S peaks are not overlapped to any other clinker phase.

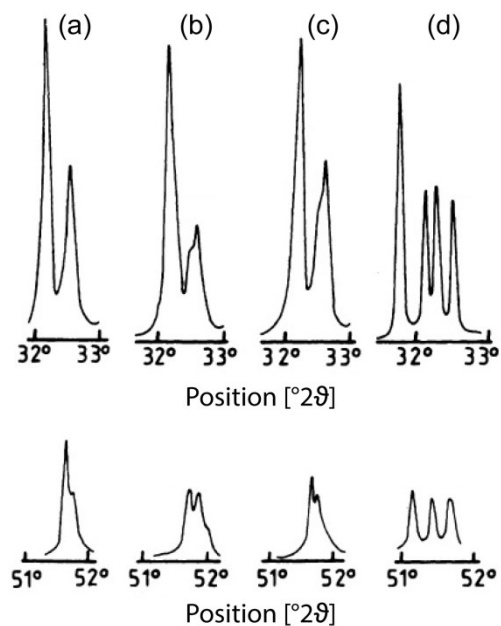


Figure 1.10: Pure C_3S compounds XRPD patterns angular windows for polymorphs identification, using copper radiation. (a) M1; (b) M3; (c) M1+M3; (d) T1. Redrafted after Taylor (1990).

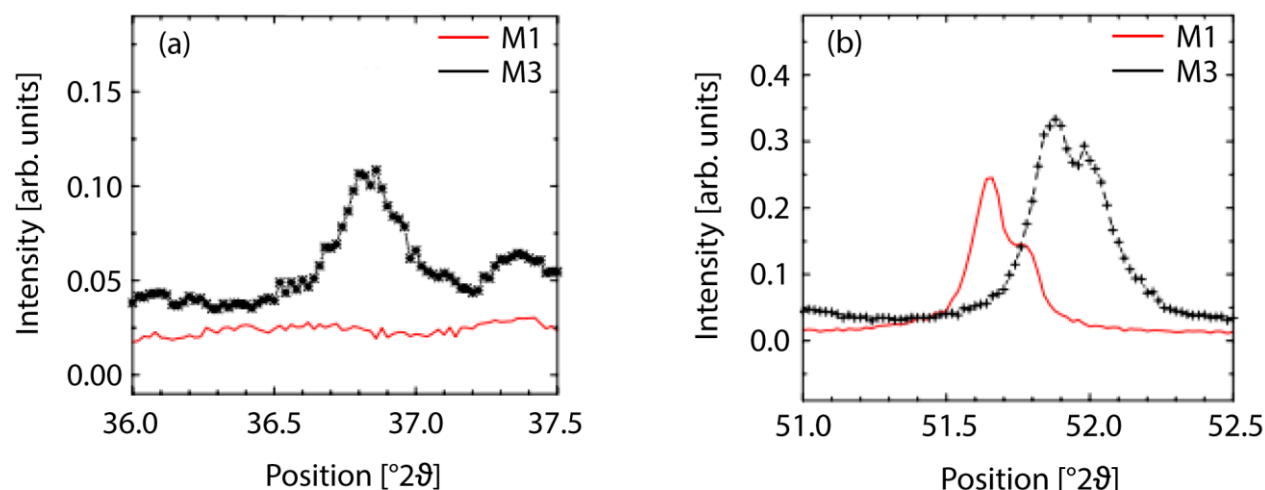


Figure 1.11: Useful angular windows for C_3S M1 and C_3S M3 identification in commercial clinkers, using copper radiation. Redrafted after Courtial et al., (2003).

Hydration

Alite reacts with water to form a poorly-crystalline calcium silicate hydrate (C-S-H) gel and calcium hydroxide (CH), through a fast-rate reaction. Usually, 70 wt% of the alite completely hydrates in 28 days (early hydration period) and theoretically 100 wt% within a year (long-term hydration) (Jennings et al., 1981).

1.7.2 Dicalcium silicate

Crystal structure and polymorphism

Dicalcium silicate (belite, Ca_2SiO_4 , C_2S) has five different known polymorphs as a function of temperature, at ambient pressure, as reported in Figure 1.12.

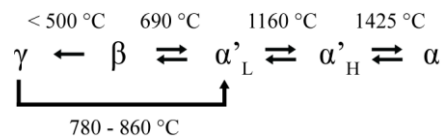


Figure 1.12: Pure C_2S polymorphic transitions as a function of temperature. L = low, H = high.

The α'_H , α'_L and β - C_2S structures derives from the α - C_2S one by a decrease of the symmetry. These structures, all glaserite-like, differ only by changes concerning the tetrahedrons orientations and slight Ca^{2+} ions movements (Moore, 1973). On the contrary, γ - C_2S , has a different structure, similar to that of olivine (Mumme et al., 1995; Udagawa et al., 1980).

As well as for alite, the high-temperature belite polymorphs survive the cooling down to room temperature. This because of the effect of some stabilizing ions and the fast cooling rate. Moreover, the lower the stability temperature of the polymorph, the less stabilizing ions are needed.

In industrial clinkers the β form is the most frequent one: β to γ transformation has to be avoided because γ has a lower density and its formation would cause the cracking of β crystals, compromising the clinker and cement properties. This transformation is usually hindered by the presence of the β form stabilizing ions in OPC raw meal; otherwise, if no stabilizers are present, small β crystals unable to convert into the γ form have to be obtained through a very fast cooling (Yannaquis and Guinier, 1959). Table 1.2 reports the C_2S polymorphs.

Polymorph	Space group	Cell parameters (a, b, c in Å)				Reference
		a	b	c	β	
γ	Pbnm	5.081	11.224	6.778	90.0°	Udagawa et al., 1980
β	P2 ₁ /n	5.512	6.758	9.314	94.6°	Mumme et al., 1995
α'_L	Pna2 ₁	20.527	9.496	5.590	90.0°	Mumme et al., 1996
α'_H	Pnma	6.870	5.601	9.556	90.0°	Mumme et al., 1996
α	P6 ₃ /mmc	5.420	5.420	7.027	90.0°	Mumme et al., 1996

Table 1.2: Crystallographic data for the C_2S polymorphs.

Pure C_2S contains 65.1 wt% of CaO and 34.9 wt% of SiO_2 , but a 4-6 wt% of substituent oxides, mainly Al_2O_3 and Fe_2O_3 , can occur. Furthermore, high- SO_3 clinker raw meals lead to a SO_3 -rich belite, by the $2Al^{3+} + S^{6+} = 3Si^{4+}$ substitution (Bonafous et al., 1995). The SO_3 content in clinker and belite are related by the $S_b = 1.23S_c + 0.24$ equation, with S_b the SO_3 content in belite (b) and S_c the one in clinker (c) (Hall and Scrivener, 1998).

XRPD identification

Characterizing the belite polymorphs, as for alite, by XRPD is difficult because of the similarities between the patterns of different polymorphs; moreover, the most intense peaks are completely overlapped by those of alite. However, β - C_2S can be identified by a weak, but clearly resolvable, peak at $31.0^\circ 2\theta$, α' by a peak at $33.3^\circ 2\theta$ and γ by a strong reflection at $29.6^\circ 2\theta$. All 2θ angles are expressed using copper radiation.

Hydration

Belite hydrates following the same process as C_3S , to give a poorly-crystalline C-S-H gel and calcium hydroxide. On the contrary, the hydration rate is slower: about 30 wt% of C_2S react with water by the first 28 days and 90 wt% within a year. Thus, C_2S accounts little to the early strength development, giving a significant contribution only throughout the long-term hydration.

1.7.3 Tricalcium aluminate

Crystal structure and polymorphism

Tricalcium aluminate (celite, $Ca_3Al_2O_6$, C_3A) usually occur in a concentration ranging from 5 to 15 wt% in OPC clinkers. Its structure is made by tetrahedron forming $(Al_6O_{18})^{-18}$ rings of six AlO_4 groups sharing their corners (Mondal and Jeffery, 1975).

Pure C_3A is cubic and has no polymorphs. However, solid solutions with general formula $Na_{2x}Ca_{3-x}Al_2O_6$ are possible, by Na^+ incorporation as a Ca^{2+} substituent (Takeuchi et al., 1975). A second Na^+ ion has to enter the structure to maintain the lattice electroneutrality, commonly in the middle of one ring. The crystalline structure remains unchanged up to ~ 1 wt% Na_2O incorporation; for a Na_2O wt% concentration from 1.0 to 2.4 a slight variation of the cubic form occurs. For higher Na_2O concentrations the structure switches to orthorhombic and monocline (Figure 1.13). Table 1.3 reports C_3A structural modification as a function of the Na_2O wt% content.

The incorporation of K^+ , again as a Ca^{2+} replacer, is difficult without other foreign stabilizing ions and does not cause the changing of the cubic structure. Silicon and iron occurrence facilitates the above-mentioned substitution (Regourd, 1978).

Aluminium can be replaced by other ions, in particular Fe^{3+} and Si^{4+} ; the maximum solubility limits are 3.0-4.0 wt% for Fe_2O_3 and 2.0 wt% for SiO_2 at equilibrium conditions (Lee et al., 1982).

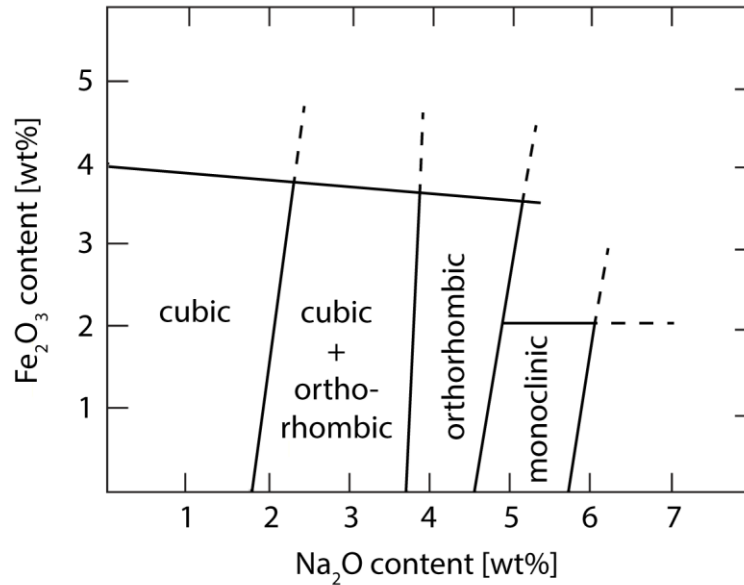


Figure 1.13: Na_2O and Fe_2O_3 threshold limit for C_3A polymorphs, at ambient temperature and pressure (Lee et al., 1982).

Na_2O [wt%]	Compositional range (x)	Polymorph designation	Crystal system	Space group
0 – 1.0	0 – 0.04	C_I	Cubic	Pa3
1.0 – 2.4	0.04 – 0.10	C_{II}	Cubic	P2_13
2.4 – 3.7	0.10 – 0.16	$\text{C}_{II} + \text{O}$	-	-
3.7 – 4.6	0.16 – 0.20	O	Orthorhombic	Pbca
4.6 – 5.7	0.20 – 0.25	M	Monoclinic	$\text{P2}_1/\text{a}$

Table 1.3: C_3A structural modifications as a function of Na_2O wt%, based on C_3A general formula $\text{Na}_{2x}\text{Ca}_{3-x}\text{Al}_2\text{O}_6$ (Takeuchi et al., 1980).

XRPD identification

C_3A , both cubic or orthorhombic, exhibits a strong diffraction signal around $33.3^\circ 2\theta$. The two forms are distinguishable by examining the profile and the intensity of two sets of diffraction peaks, within the $19\text{--}22^\circ$ and $33\text{--}34^\circ 2\theta$ angular windows. The cubic form shows three weak peaks in the $19\text{--}22^\circ 2\theta$ region and a strong singlet around $33.3^\circ 2\theta$; the orthorhombic form has only two peaks, of nearly the same intensity, in the $19\text{--}22^\circ 2\theta$ region and the strongest peak at 33.3° is split into a doublet. All 2θ angles are expressed using copper radiation.

Hydration

C_3A has a higher water reactivity than calcium silicates. Its hydration completes within a few hours after the contact with water, causing a fast stiffening, also known as flash setting. To bypass this problem a setting regulator, generally calcium sulphate, is added to clinker to slow down the C_3A hydration by the formation of primary ettringite (Pourchet et al., 2009).

1.7.4 Tetracalcium aluminium ferrite

Crystal structure and polymorphism

Tetracalcium aluminium ferrite (brownmillerite, $\text{Ca}_2(\text{Al}_x\text{Fe}_{1-x})_2\text{O}_5$, C_4AF) is present in clinker in a concentration ranging from 5 to 15% by mass. Theoretically, it is a solid solution between C_2A and C_2F ; at ordinary pressure and in absence of other components than CaO , Al_2O_3 and Fe_2O_3 , ferrite can be prepared in any composition for $0 < x < 0.7$ in the solid solution $\text{Ca}_2(\text{Al}_x\text{Fe}_{1-x})_2\text{O}_5$. Values of x greater than 0.7 are possible only at non-ambient pressure conditions; for instance, the end-member C_2A ($x = 1$) has been prepared under a 2500 MPa pressure (Aggarwal et al., 1972). C_4AF is the solid solution intermediate member, with $x = 0.5$.

C_4AF has orthorhombic symmetry; FeO_6 octahedrons and FeO_4 tetrahedrons are highly distorted and do not share oxygen atoms. Calcium ions are surrounded by nine oxygens and their coordination is very irregular. Layers of tetrahedrons are made by little-distorted and infinite chains parallel to a crystallographic direction (Taylor, 1990; Kurdowski, 2014).

Pure C_4AF has a 46.1 wt% CaO , 21.0 wt% Al_2O_3 and 32.9 wt% Fe_2O_3 oxide composition. Actually it can incorporate up to 10 wt% of impurities oxides, lowering the Fe_2O_3 content, with Mg^{2+} , Si^{4+} and Ti^{4+} replacing equal amounts of Fe^{3+} (Taylor, 1990; Kurdowski, 2014).

XRPD identification

Key diffraction peaks for C_4AF identification are those at 33.9° and $12.1^\circ 2\theta$, using copper radiation. In particular, the one at $12.1^\circ 2\theta$ is unequivocally the identifier of this phase. Moreover, C_4AF diffraction peaks shape is affected by the clinker cooling rate, because of different incorporation degree of magnesium, silicon and other elements.

Hydration

C_4AF hydrates rapidly after the contact with water but its contribution to cement strength is limited. The degree of reactivity with water is influenced by the Al/Fe ratio, decreasing when iron content increases (Collepari et al., 1979).

1.7.5 Secondary clinker phases

Calcium oxide

Primary and secondary calcium oxide can be found in clinker. The former usually appears in clusters and it represents the lime not reacted with other components of the raw meal during the thermal treatment; this could be due to coarse limestone grains, bad homogenization, high lime saturation factor, low kiln temperature and other issues relating both raw meal preparation and kiln setup. The latter, highly dispersed within the clinker matrix, derives from the alite decomposition into belite and lime upon cooling.

Uncombined (i.e. not incorporated in any clinker phase structure) lime represents a problem because of its expansion during the cement hydration. Nevertheless, its complete absence, although highly recommendable, is not cost and energy effective because too high kiln temperatures would be required to achieve it. Common CaO wt% values in commercial clinker attest around 1.0-2.0 wt%.

Magnesium oxide

Magnesium can be taken up in the structure of some main clinker phases. However, when it exceeds the 2.0 wt% in the calcined raw meal, magnesium will give periclase as a proper phase in the final product. Periclase usually appears in dense and compact crystals aggregates and represents a severe problem because it hydrates slowly and causes a delayed expansion in concrete, cracking it. Hence, it must not exceed the 5.0 wt% in a commercial cement clinker (UNI EN 197-1).

Minor phases

Alkali-sulphates phases and minor elements compounds can crystallize upon cooling when their building-elements exceed the concentration liable to enter the main clinker phases, as major elements replacers. Alkali-sulphates and minor elements can occur in the clinker raw meal due to the use unconventional raw materials and kiln fuels.

1.8 Environmental impact

Nowadays the environmental impact is mainly evaluated in terms of greenhouse gases release. The cement manufacturing process accounts to the 5-7% of the global anthropogenic carbon dioxide emissions, as seen in Figure 1.14. (Chen et al., 2010; Feiz et al., 2015).

Released carbon dioxide (900 kg every 1000 kg of manufactured cement) comes from four main sources: calcination of carbonates (50%), combustion of kiln fossils fuels in the pyro-processing stage (40%), raw materials transportation (5%) and generation of electricity (5%) consumed by the plant facilities (Benhelal et al., 2013).

Energy usage and raw materials exploitation are also intensive: to produce 1 tonne of cement, 3000 to 4300 MJ of fuel energy and 120 to 160 kWh of electrical energy are required, jointly to 1.5-1.6 tonnes of natural raw materials (Müller and Harnisch, 2008; Price et al., 2010).

Another issue related to cement clinker production is cement kiln dust (CKD), since manufacturing 1000 kg of clinker generates 80 kg of CKD (Van den Heede and De Belie, 2012). CKD mostly consists of silica, lime and calcium carbonate, followed by alkalis and chlorine compounds (Peethamparan et al., 2008) and usually concentrating contaminants from both raw materials and fuels (Huntzinger and Eatmon, 2009). It is carried out from the kiln system by exhausts gases and only partially (~60 wt%) recovered. The remaining (~40 wt%) is landfilled as an industrial waste or disperses in the atmosphere, accounting as the main local-scale impact contributor. Moreover, its average diameter size is smaller than 10 µm; hence is classified as PM10, within the size range of respirable particles (Van den Heede and De Belie, 2012).

All these considerations makes necessary to continuously improve the cement manufacturing process, to reduce the environmental impact without affecting the quality of the final product, stressing them as the main objectives of modern cement industry.

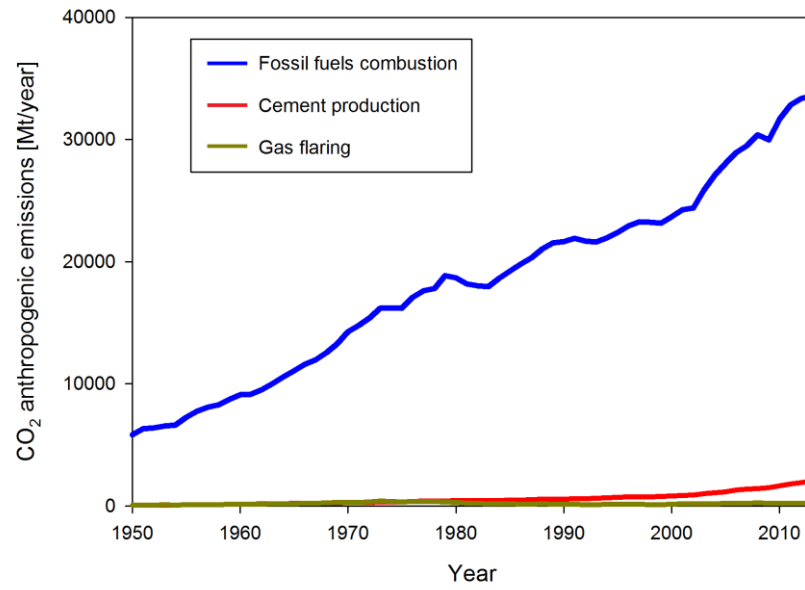


Figure 1.14: Global anthropogenic carbon dioxide emissions from 1950 to 2013 (Boden et al., 2016).

Chapter 2

Analytical techniques

This chapter provides information about the main instrumental techniques used to characterize natural raw materials and clinkers samples. First, the theoretical principles of each technique will be briefly outlined, then the samples preparation procedure and the measuring conditions will be described in details. Secondary analytical techniques will be instead explained throughout the text, when treated.

2.1 X-ray powder diffraction

X-ray powder diffraction is the most powerful technique to get a reliable phase analysis of an heterogeneous polycrystalline mixture (Dinnebier and Billinge, 2008). Hence, it was the most used instrumental technique to carry out raw data in this thesis, performed both *ex situ* and *in situ*. *Ex situ* means the data collection is run at ambient conditions, whereas during *in situ* experiments the patterns are directly measured at specific non-ambient conditions to follow the system evolution to changing environmental state. Temperature was the only ambient variable taken into account during the *in situ* experiments in this work.

XRPD patterns, after a qualitative phase identification, have often been processed by the full profile Rietveld refinement method, to gather information on the phases weight fraction (Bish and Howard, 1988; Bish and Post, 1993).

Hence, the key points concerning the Rietveld method and the adopted refinement strategy will be now illustrated. Instrumental setup and measurements conditions will be given from time to time through the text, because they were adjusted depending on the analysis type.

2.1.1 The Rietveld method

The aim of the Rietveld method is to minimize the differences between an observed (i.e. measured by the instrument) and a calculated (i.e. obtained by an algorithm implemented in dedicated software) XRPD pattern, by refining a set of user-selected parameters (Young, 1993). Refine means to optimize these parameters in order to minimize the differences, expressed by the value of the residual function R (Equation 2.1) between the observed and the calculated pattern. The minimization is achieved by a non-linear least square procedure extended to every measured step within the angular interval where the refinement is performed.

$$R = \sum_i w_i |y_i (obs) - y_i (calc)|^2 \quad (2.1)$$

It is possible to build the calculated pattern because the intensity of a diffraction signal relies on features completely describable by parameters. These are the instrumental characteristics, the phases intrinsic properties and the sample arrangement.

Equation 2.2 represents the intensity Y of a diffraction signal at every step i for a given phase a . S_a is the scale factor of the phase a ; $m_{(hkl)}$ the multiplicity of the hkl reflection; $F_{(hkl)a}$ the structure factor of the hkl reflection; $G(\Delta_{i,(hkl)a})$ the function describing the peak shape; $L_p(2\vartheta_i)$ the Lorentz-polarization factor; $P_{(hkl)a}$ the function describing the preferred orientation; Y_b the intensity of the background. The same for Equation 2.3, describing the intensity of a diffraction signal due to an heterogeneous mixture of n phases, at a given step i .

$$Y_i = S_a \sum_{(hkl)} m_{(hkl)} |F_{(hkl)a}|^2 G(\Delta_{i,(hkl)a}) L_p(2\vartheta_i) P_{(hkl)a} + Y_b \quad (2.2)$$

$$Y_i = \sum_n S_n \sum_{(hkl)} m_{(hkl)} |F_{(hkl)n}|^2 G(\Delta_{i,(hkl)n}) L_p(2\vartheta_i) P_{(hkl)n} + Y_b \quad (2.3)$$

It is thus clear that to perform a Rietveld refinement, the instrumental setup, the structural model of all the phases and the sample conditions must be previously known.

To get a quantitative phase analysis, particular attention should be paid to the value of the scale factor S , carrying the information on the phases weight percentage. Equation 2.4 represents the weight percentage fraction of phase a within n -phases sample; Z is the number of formula units for a single unit cell, M the molecular mass and V the cell volume.

$$Wt_a = \frac{S_a(ZMV)_a}{\sum_{i=1}^n S_i(ZMV)_i} \quad (2.4)$$

The agreement between the calculated and the observed pattern can be evaluated by a number of parameters, among which the most used is the weighted profile R-factor (R_{wp}), expressed in Equation 2.5. Rather than the R_{wp} absolute value at the end of the refinement, the efficiency of the strategy is witnessed by a continue R_{wp} decrease during the progression of the refinement.

$$R_{wp} = 100 \cdot \sqrt{\frac{\sum_{i=1}^n w_i (Y_i(obs) - Y_i(calc))^2}{\sum_{i=1}^n w_i Y_i^2(obs)}} \quad (2.5)$$

2.1.2 Refinement strategy

Full profile Rietveld refinements (Young, 1993) on *ex situ* XRPD patterns were performed by Topas Academic 5.1 software (Coelho, 2012). For each phase the cell parameters (a , b , c and α , β , γ), the scale factor and the peak profile shape, described by a pseudo-Voigt type function, were refined. Sample displacement was corrected and background was modelled by a six-terms Chebyshev polynomial function. Atomic coordinates and isotropic thermal parameters values from the structural model were instead kept fixed.

Table 2.1 reports the crystallographic structures of the main phases used for the *ex situ* refinements; further phases references will be reported when mentioned throughout the text.

Phase name	Reference	ICSD #
C ₃ S T3(M1)	De la Torre et al., 2008	162744
C ₃ S M3	Nishi et al., 1985	64759
C ₂ S β	Mumme et al., 1995	81096
C ₂ S α'	Mumme et al., 1995	81097
C ₃ A cubic	Mondal and Jeffery, 1975	1841
C ₃ A orthorhombic	Takeuchi et al., 1980	100220
C ₄ AF	Colville and Geller, 1971	9197
CaO	Natta and Passerini, 1929	61550
MgO	Sasaki et al., 1979	9863

Table 2.1: Crystallographic structures used for the *ex situ* Rietveld refinements; all the structures were the ones solved at room temperature. ICSD # refers to the collection code of the phase within the Inorganic Crystal Structure Database.

To determine the C₃S-M1 wt%, the C₃S-T3 structure was used: this because the published C₃S-M1 structure is an “average structure”, where some reflection peaks had not been indexed, eventually leading to a loose fit. This structures swap, valid only for low-magnesium clinker samples, is possible because C₃S-M1 and C₃S-T3 have the same diffraction pattern except for a secondary peak at d~2.44 Å (De la Torre et al, 2008).

2.2 X-ray fluorescence

Bulk chemical composition of both raw materials and raw meals was assessed by wavelength dispersive X-ray fluorescence. The wavelength dispersive spectrometer (WDS) system uses an analyser crystal to discriminate and then individually measure the intensity of every characteristic wavelength emitted by the sample, after the excitation by an incident X-ray beam. This allows a more accurate quantification of major elements and also a reliable trace elements determination, compared to the energy dispersive spectrometer (EDS) system where the entire energy spectrum is simultaneously measured leading to a lesser accuracy and to the impossibility to determine trace elements.

In this work, the measurements were carried out by Bruker S8 Tiger wavelength dispersive X-ray fluorescence (WD-XRF), operating at 50 kV and 80 mA. Samples have been prepared and analysed as glass beads to guarantee a quasi-perfect homogenization and eliminate matrix and mineralogical effects, dealing with an all-amorphous material. Glass beads were made by heating up to T = 1000 °C a mixture between the finely ground sample to be analysed (< 80 µm) and lithium tetraborate (Li₂B₄O₇) as flux, in a flux to sample ratio equal to 5.

The instrumental routine program allowed to carry out the concentration of SiO₂, Al₂O₃, Fe₂O₃, CaO, MgO, SO₃, K₂O, Na₂O, TiO₂, P₂O₅ and Mn₂O₃ as oxide weight fraction and the one of chromium as mg/kg. Moreover, SrO wt% and Zn, Ni, Cu concentration were assessed by a semi-quantitative analysis. The instrumental threshold detection limit is 0.01 wt% and the data resolution gradually deteriorates towards the limit.

Loss on ignition was determined gravimetrically by weighting the samples before and after a thermal treatment at T = 1000 °C for 20 mins. Limestones were previously pulverized below 80 µm and dried at T = 105 °C in an electrical laboratory oven, to remove non-stoichiometric carbon dioxide and water and attain a constant weight.

2.3 Scanning electron microscopy

Scanning electron microscope allowed to obtain morphological and textural information on the clinker samples, several orders of magnification greater than optical microscopy. In this thesis only backscattered images were acquired, by Carl Zeiss EVO MA 15 electron microscope. The instrument operated at nearly-vacuum conditions, under an acceleration voltage of 15 kV, an highly focused electron beam emitted by a lanthanum hexaboride (LaB_6) filament and a 11 mm working distance. Samples have been prepared by embedding them in epoxy resin, polishing the surface to be analysed and applying a micrometric graphite layer to this surface to ensure the sample conductivity.

2.4 Electron microprobe

Electron microprobe was the non-destructive technique employed to carry out spot chemical analyses on the samples surface. In order to individuate spots where analyses are actually performed, an electron microscope is always coupled within the same instrument. Hence, the main difference between WD-XRF and WD-microprobe analyses lies in the fact that the former returns bulk analyses whereas the latter spot analyses of selected regions of the sample. Elemental species identification and quantification is performed following the same principles valid for WD-XRF.

Analyses were carried out by JEOL JXA-8200 electron microprobe, operating at 15kV accelerating voltage, 15 nA beam current intensity and at nearly-vacuum condition in the sample chamber ($P = 6 \times 10^{-4}$). Electrons are emitted by a tungsten filament and accurate spot chemical analyses are possible due to the high focalization of the electron beam ($\sim 1 \mu\text{m}$ diameter), obtained by electromagnetic lenses. Samples were analysed for F, Na, Mg, Al, Si, S, Cl, K, Ca, Ti, Mn, Fe and Sr using silicate and oxide certified calibration standards. Results were corrected by ZAF routines, where Z is the atomic number correction, A the absorption correction and F the secondary fluorescence correction. The sample preparation procedure was the same as for scanning electron microscopy analyses (cf. subsection 2.1.4).

2.5 Optical microscopy

Transmitted light optical microscopy permitted to evaluate the natural samples texture and morphology and to perform a semi-quantitative analysis of their components. Clinker samples were not characterized by optical microscopy because of crystalline phases too small average dimensions. Optical microscopy observations were performed by Laboval-3 microscope, both in transmitted plane-(PPL) and cross-polarized light (XPL), on $30 \mu\text{m}$ thick sections. Colour micrographs, at 1.2 megapixels, were simultaneously acquired by Nikon Coolpix 990 digital camera, installed on the microscope eyepiece.

Chapter 3

Effects of limestones petrography on OPC clinker raw meals burnability

3.1 Introduction

Limestones represent up to the 80-85% by mass of a common OPC clinker raw meal (Taylor, 1990). They almost entirely consist of calcite, the room temperature and pressure calcium carbonate polymorph; quartz and dolomite can occur as secondary phases. According to a review published by Van Oss and Padovani (2002), limestones decomposition (calcination) during OPC clinker raw meals thermal treatment releases in the atmosphere the 5% by mass of the global anthropogenic greenhouse gases emissions, significantly raising their volume in the atmosphere.

As a consequence, understanding limestones thermal behaviour is a primary task for modern cement industry in order to reduce the environmental impact. Calcination itself has been widely investigated in the past, independently from the field of application: some authors clarified the kinetic mechanisms controlling it (Lech, 2006c; Rodriguez-Navarro et al., 2009; Beruto et al., 2010), other focused on the way the limestone petrographic features influence the thermal decomposition of carbonates used for lime and clinker production (Moropoulou et al., 2001; Lech 2006a, b; Lech et al., 2009; Soltan et al., 2011, 2012; Alaabed et al., 2014; Marinoni et al., 2015). They found that a limestone should not be considered as a mere sum of carbonate minerals, taking only into account the bulk chemical composition as an evaluation criterion. Attention has to be paid to the mineralogical assemblage and to the microfabric too, because they affect the overall thermal behaviour of the whole rock. As an example it was proved that the presence of dolomite speeds up also the calcite decomposition (Lech, 2006c; Marinoni et al., 2012), because dolomite destabilizes through a single-step and faster reaction, without the growth of a calcite intermediate phase. Moreover, dolomite decomposes at a lower temperature than calcite, cracking the crystals of this latter and easing thus the heat diffusion through the sample and the carbon dioxide escape. Generally, impurities play a major role on the carbonate decomposition kinetics and as a consequence on the lime formation, whose microstructure will be influenced by the calcite decomposition process (Beruto et al., 2010; Soltan et al., 2012).

Dealing with the rock texture, it affects the lime thermal behaviour because the calcite microstructure tends to transpose into the one of lime, determining differences in the overall reactivity, even in an all-powdered material. Different kinds of lime will later influence both the stability field of the clinker phases and the free lime content in the final product (Marinoni et al., 2015).

Starting from these assumptions, it will be investigated, for the first time, how the limestone microfabric and the calcite crystals microstructure affect the clinkerization process, in terms of OPC clinker raw meals burnability. The aim is to identify an objective quantifiable parameter controlling the burnability. All the past works on a similar topic, as the ones previously reported, always use to correlate the reactivity with some features not unequivocally definable by a number. Moreover, none of them performed a complete characterization of the clinkering manufacturing process, from the raw materials to the final product. That purpose will be here achieved by first performing a detailed characterization of eight different limestones natural samples, then used for OPC clinker raw meals preparation, by X-ray fluorescence, X-ray powder diffraction, optical microscopy and digital image analysis techniques and by later describing the obtained clinkers by XRPD and scanning electron microscopy.

To explain the nomenclature hereafter used, *microfabric* encloses the overall rock texture, such as the grain size of its components and the micrite to sparite ratio; *microstructure*, referred to calcite, summarizes the average domain size of crystallites and the root mean square microstrain value of calcite crystals. A more detailed explanation of these latter will be given in the following.

Finally, the term *burnability*, with regard to an OPC clinker raw meal, indicates the way the calcite decomposes upon heating and how the resulting CaO reacts with other oxides (mainly SiO₂, Al₂O₃ and Fe₂O₃) to form the clinker crystalline phases. The burnability will be optimal if the carbonates destabilize at low temperature and through a fast-rate reaction, giving a clinker high in calcium silicates and low in free lime, the latter not exceeding the 5% by mass (Gosh and Kurdowski, 1991).

For the sake of clarity, this chapter is divided in two main parts. The first one deals with a geological overview of the studied limestones, followed by a detailed chemical and mineralogical characterization and petrographic description. The second one concerns the burnability test performed to evaluate the thermal behaviour of eight different OPC clinker raw meals prepared employing the previously characterized limestones; quantitative phase analysis results will be shown.

Finally a general discussion is developed, combining and analysing simultaneously the results from both the limestones characterization and the raw meals burnability test.

Petrographic descriptions of limestone samples were carried out in cooperation with Prof. G. Della Porta from the Earth Sciences department of the University of Milan.

3.2 Materials

3.2.1 Geological overview

The eight natural limestone rock samples, selected as starting materials, are from the Mediterranean region (Table 3.1). It was necessary to space widely in terms of outcrop location, depositional environment and age to strictly fulfil the following requirements:

Calcite content must be higher than 98% by mass within the whole rock, to avoid significant effects due to impurities and minor elements occurrence during the thermal treatment;

Limestones must show a wide array of carbonate microfacies, to have a variety of microfabrics;

Each category of the classification of the depositional texture of carbonate rocks proposed by Dunham (1962) has to be covered, to increase textural differences.

Limestone sample	Age	Outcrop location	Depositional environment
<i>SA</i>	Quaternary	NE Sardinia (Italy)	Karstic cave within marine limestone
<i>SL</i>	Eocene (Ypresian)	Kras Region (SW Slovenia)	Protected inner ramp
<i>UM</i>	Late Cretaceous (Cenomanian)	Umbria-Marche Apennines	Pelagic marine basin
<i>MO1</i>	Early Jurassic (Pliensbachian)	Djebel Bou Dahar, High Atlas Mts. (central-eastern Morocco)	Reef at platform margin/upper slope
<i>MO2</i>	Early Jurassic (Pliensbachian)	Djebel Bou Dahar, High Atlas Mts. (central-eastern Morocco)	Platform interior (subtidal lagoon/intertidal zone)
<i>MO3</i>	Early Jurassic (Pliensbachian)	Djebel Bou Dahar, High Atlas Mts. (central-eastern Morocco)	Platform interior (intertidal zone)
<i>MO4</i>	Early Jurassic (Pliensbachian)	Djebel Bou Dahar, High Atlas Mts. (central-eastern Morocco)	Platform interior (supratidal zone)
<i>AS</i>	Pennsylvanian (Moscowian)	Sierra del Cuera (Asturias, N Spain)	Upper slope of high-relief carbonate platform

Table 3.1: Age, outcrop location and depositional environment of the selected limestones, listed in reverse chronological order from younger to older. The names of the limestone samples derive from their geographical provenience (*SA*=Sardinia, *SL*=Slovenia, *UM*=Umbria-Marche, *MO*=Morocco, *AS*=Asturias).

The *SA* calcite cement crust is a karstic cave filling grown within the Upper Jurassic limestone of north-eastern Sardinia (Italy), due to the hosting limestone subaerial exposure and the consequent meteoric vadose and phreatic diagenesis. Its age, likely Quaternary, cannot be unequivocally defined.

Sample *SL* derives from the Lower Eocene (Ypresian) *Alveolina-Nummulites* Limestone cropping out in the Kras Plateau, near Divača (SW Slovenia). It belongs to the Komen Thrust Unit of the NW External Dinarides fold-and-thrust belt. During the Late Cretaceous and Paleogene, shallow-water carbonate accumulations developed on the marginal areas of the Adriatic Carbonate Platform, an extended Mesozoic carbonate depositional system. The *Alveolina-Nummulites* Limestone represents a

succession typical of a protected inner ramp, characterized by muddy to grainy carbonate substrates close to seagrass beds (Zamagni et al., 2008).

UM is an Upper Cretaceous (Cenomanian) pelagic limestone from the Scaglia Bianca Formation, within the Umbria-Marche Basin (Umbria-Marche Apennines, Italy). It settled on the passive southern margin of the Tethys Ocean, in a pelagic environment at a paleo-depth of approximately 1000-1500 m (Arthur and Fischer, 1977; Premoli Silva and Sliter, 1995).

MO1, *MO2*, *MO3* and *MO4* samples are all from the Djbel Bou Dahar carbonate platform in the High Atlas range in central-eastern Morocco. This platform developed during the Early Jurassic on the footwall high of an active marine rift (Merino-Tomé et al., 2012); the depositional system evolved from a low-angle ramp into a high-relief platform, with a shallow subtidal to supratidal top, delimited by steep slopes with coral-microbial reefs growing during the Pliensbachian at the margin of the upper slope (Verwer et al., 2009; Della Porta et al., 2013).

Finally, the *AS* limestone was sampled on the Sierra del Cuera (Cantabrian Mountains, Asturias, Spain), representing the marine foreland of the Variscan Orogen during the Pennsylvanian (Moscovian) (Bahamonde et al., 2015). In the distal part of this Cantabrian foreland basin, high-relief progradational carbonate platforms with steep slopes, such as the Sierra del Cuera, dominated by microbialites developed (Della Porta et al., 2003).

Figure 3.1 gives a simplified overview on the limestones depositional environments.

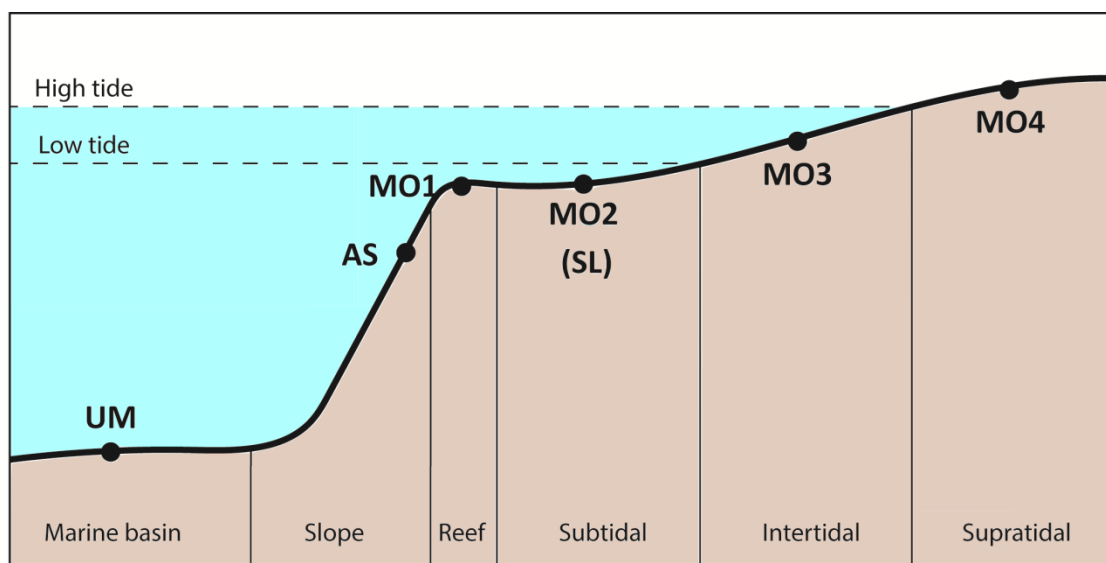


Figure 3.1: Schematic representation of the depositional environments of the studied limestones; sample *SA*, from a karstic cave, is not reported; sample *SL* is marked out in brackets because it should not be represented in this scheme, being from a different depositional environment, but similar to the *MO2* one. Horizontal and vertical dimensions are not to scale.

3.2.2 Experimental methods

X-ray fluorescence

WD-XRF allowed to obtain an accurate chemical characterization of the limestone samples, in order to evaluate their suitability for OPC clinker production. Measurement conditions and samples preparation procedure are reported in Section 2.2.

X-ray powder diffraction and calcite microstructural analysis

Qualitative phase analyses on limestones were provided by *ex situ* X-ray powder diffraction experiments, carried out by PANalytical X'Pert Pro diffractometer arranged in a θ - 2θ Bragg-Brentano geometry, operating at 40 kV and 40 mA, using copper $K\alpha$ radiation ($\lambda = 1.5418 \text{ \AA}$) and equipped with multi-channel X'Celerator detector. Measurements were collected over the 5 - 80° 2θ angular range, with a step size of 0.02° 2θ and a counting time of 30 s/step.

Quantitative phase analysis was performed processing the collected patterns by the full profile Rietveld method (Young, 1993), implemented in the TOPAS-Academic 5.1 software (Coelho, 2012).

By XRPD measurements the calcite crystals microstructural features were also assessed, working under the same instrumental conditions just reported, except for the step size, now equal to 0.008° 2θ . The collected patterns were processed by Materials Analysis Using Diffraction (MAUD) software (Ferrari and Lutterotti, 1994). This open-source software enables the full profile Rietveld structure refinement as well as the assessment of the crystals microstructure such as the average crystallites, or domains, size and the root mean square microstrain. For simplicity, in this chapter they will be addressed simply as domains size and microstrain.

Domains are coherently diffracting regions within each single crystal, whereas microstrain is a dimensionless parameter indicating the magnitude of dislocations, vacancies, defects and chemical impurities affecting the crystal structure.

Their contribution to the diffraction peak broadening is modelled by first deconvolving the instrumental component $g(x)$ from the experimental pattern $f(x)$ and then by separating the domains and the microstrain contributions. For this purpose, it was necessary to previously collect, under exactly the same instrumental conditions, an XRPD pattern of a defect-free external standard, to evaluate the instrumental contribution to Bragg's peaks broadening. The lanthanum hexaboride (NIST SRM 660a LaB₆) was chosen as external standard due to the high degree of crystallinity.

Data were then processed following the principles outlined by Stokes and Wilson (1942) and Warren and Averbach (1952), refining the instrumental parameters by adopting an iterative least square minimization procedure.

Optical Microscopy

Optical microscopy observations allowed to characterize limestones according to Dunham's classification of the depositional texture of carbonate rocks (Dunham, 1962), taking also in account the integrations made by Embry and Klovan (1971). In addition a semi-quantitative description of the microfacies components, such as the texture, the matrix composition and the grains type was performed.

Dunham’s classification is based on the grain and matrix components of a limestone, both features defining the texture (Figure 3.2). The main distinction is between mud-supported (the grains are dispersed within a matrix) and grain-supported carbonates (the grains are mutually in contact).

Mud-supported carbonates are sub-divided into mudstones and wackestones. In a mudstone, the grain components represent less than the 10% of the total volume; in a wackestone they represent more than the 10% of the total volume. Mudstones and wackestones can only be mud-supported because it is impossible to remove the mud matrix and precipitate a cement, keeping the grains not in contact each other. The grains will come into contact after the mud removal and the rock will be no longer mud-supported but grain-supported.

Grain-supported limestones are divided into packstones and grainstones. In a packstone, the grain components are in contact each other and the intraparticle porosity is filled by a clay- and silt-size sediment (mud); on the contrary, in a grainstone the interparticle porosity is filled by a carbonate cement precipitated after the rock deposition.

Boundstones and crystalline carbonates represent two separate categories. In a boundstone the rock components were bound together at the deposition time (e.g. a coral reef), whereas in a crystalline carbonate the depositional texture is not recognizable (e.g. a speleothem).

Embry and Klovan expanded Dunham’s classification to emphasize the importance of the grain size in packstones and grainstones and the types of binding organisms in boundstones, as reported in Figure 3.3.




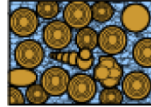
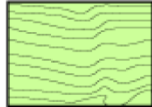
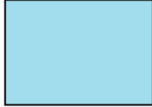
Recognisable depositional texture					Depositional texture not recognisable
Components not bound together at deposition			Bound at deposition		
Contains mud			Lacks mud		
Mud-supported		Grain-supported			
Less than 10 % grains	More than 10 % grains				
Mudstone	Wackestone	Packstone	Grainstone	Boundstone	Crystalline carbonate
					

Figure 3.2: Dunham’s classification of limestones depositional textures. Redrafted after Dunham (1962).

Allochthonous		Autochthonous		
Components not bound organically at deposition		Components bound organically at deposition		
> 10% of grains > 2 mm				
Matrix supported	Supported by > 2 mm components	Organisms that act as baffles	Organisms that encrust and bind	Organisms that build a rigid framework
Floatstone	Rudstone	Bafflestone	Bindstone	Framestone

Figure 3.3: Embry and Klovan classification of reef limestones. Redrafted after Embry and Klovan (1971) and James (1984).

Digital Image Analysis

Thin sections were digitalized at high resolution (4800 dpi) by Epson V7 perfection scanner, to be processed by Image-Pro Plus 4.5 software to define the micrite to sparite ratio (M/S) within the thin section area and considering it representative for the whole rock.

An iterative strategy was followed to obtain numerical values of the M/S ratio (Marinoni et al., 2005; Voltolini et al., 2011), as outlined in Figure 3.4.

Each digitalized red-green-blue image was converted into a grey scale (8 bit) one. This conversion is advised to better split, later, the image into dark and light areas, corresponding to micrite and sparite respectively.

A 3x3 pixels median filter was applied to reduce the background noise, again to ease the image splitting into dark and light areas.

A segmentation of the image was performed, selecting a pixel value (from 0 to 255) as a separator between dark and light areas.

A mask was applied and the image converted into a black and white one.

The extent, in pixels, of black and white areas was calculated obtaining thus the values for micrite and sparite distribution.

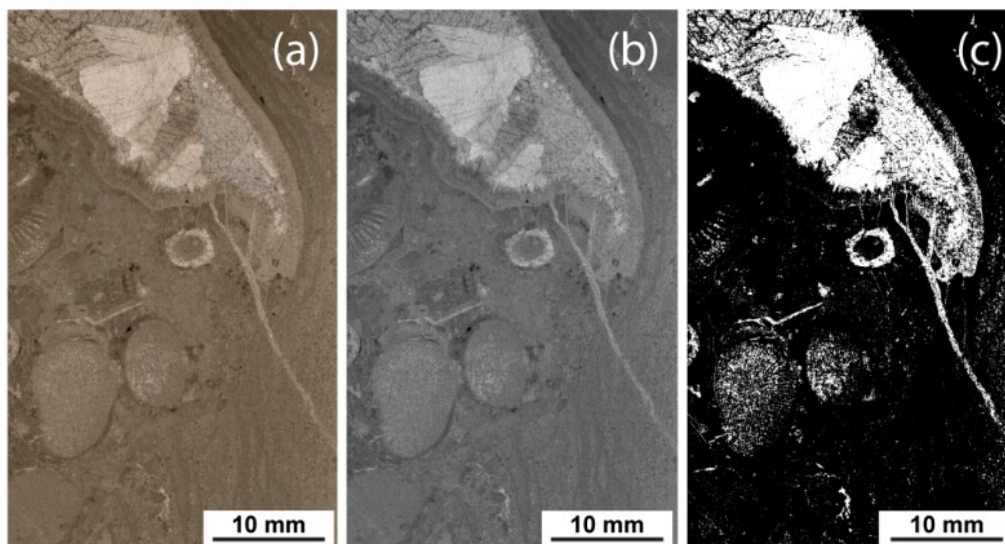


Figure 3.4: Main steps of the strategy followed to evaluate the micrite to sparite ratio (limestone *MOI*). (a) thin section high-resolution RGB scan; (b) grey scale converted image; (c) black and white image assuming black = micrite and white = sparite.

This iterative process was applied three times per image to reduce the error due to the subjectivity of the analysis, because it was not possible to set a fixed pixel value to unequivocally split dark and light objects, despite the same scanning conditions. The final M/S ratio value is the geometric mean between each of the three measurements.

Definition of micrite and sparite

Micrite is a term identifying microcrystalline calcite with a grain size below 4 μm , appearing dense, dull-looking through petrographic observation under a polarized light microscope (Folk, 1959; Tucker, 1988). Micrite commonly derives from abrasion, disintegration and endolithic boring of skeletal fragments, representing thus the finest, mud-grade, portion of a carbonate sediment; however, it can precipitate in association with organic substrates and microbial mediation (Flügel, 2004). In this work, the category *micrite* includes the carbonate matrix below 4 μm , the clotted peloidal micrite forming the microbialites and all the skeletal and non-skeletal grains appearing dark in transmitted polarized light observations due to their microcrystalline structure, such as peloids, fecal pellets, micritic intraclasts, coating of grains and miliolids and textularid foraminifers.

Sparite and microsparite, hereafter both considered as sparite, are translucent calcite crystals with a grain size between 4 and 62 μm and larger than 62 μm respectively, making the rhombohedral cleavage clearly visible. The former includes all kinds of cement precipitated in a carbonate rock, from the early marine to the late burial or phreatic meteoric diagenesis; the latter can be a primary cement or the result of primary micrite recrystallization and grain size increase during the diagenesis, through a process called aggrading neomorphism (Tucker, 1991). In this work, the category *sparite* includes calcite crystals larger than 4 μm making up the cements filling the intergranular porosity, the primary and secondary cavities, the fractures and the intragranular spaces between fossils. Regarding the skeletal fragments it includes all the fossils with a crystalline and hyaline appearance and all the originally aragonitic fossil shells replaced by calcite during the diagenesis.

3.2.3 Results

Mineralogical and chemical composition

From a mineralogical point of view (Table 3.2), calcite and very few quartz are the only mineralogical species of the investigated limestones; dolomite occurs, as an accessory phase, only in sample *AS* (Figure 3.5). The mineralogical similarity agrees well with the XRF results, where CaO is the main constituent, followed by minor amounts of silicon, magnesium and alkalis oxides (Table 3.3).

Sample	Calcite	Quartz	Dolomite
<i>SA</i>	99.8(1)	0.2(1)	b.d.l.
<i>SL</i>	99.7(1)	0.3(1)	b.d.l.
<i>UM</i>	99.3(2)	0.7(2)	b.d.l.
<i>MO1</i>	99.9(1)	0.1(1)	b.d.l.
<i>MO2</i>	99.5(2)	0.5(2)	b.d.l.
<i>MO3</i>	99.6(1)	0.4(1)	b.d.l.
<i>MO4</i>	99.7(1)	0.3(1)	b.d.l.
<i>AS</i>	98.3(2)	0.4(1)	1.3(2)

Table 3.2: Mineralogical composition of limestones (wt%, b.d.l. = below detection limit), carried out by XRPD data. Samples are listed in reverse chronological order, from younger to older.

Oxide	<i>SA</i>	<i>SL</i>	<i>UM</i>	<i>MO1</i>	<i>MO2</i>	<i>MO3</i>	<i>MO4</i>	<i>AS</i>
SiO ₂	0.32	0.01	0.58	0.09	0.70	0.31	0.50	1.54
Al ₂ O ₃	0.17	< 0.01	0.17	0.02	0.21	0.09	0.25	0.87
Fe ₂ O ₃	0.07	0.01	0.05	0.03	0.10	0.05	0.10	0.30
CaO	54.56	54.66	54.24	55.27	53.68	55.26	53.73	53.37
MgO	0.06	0.46	0.26	0.22	0.51	0.33	0.68	1.03
SO ₃	< 0.01	0.04	0.08	0.03	0.06	0.05	0.08	0.13
K ₂ O	0.02	< 0.01	0.05	< 0.01	0.05	< 0.01	0.06	0.16
Na ₂ O	< 0.01	< 0.01	0.07	< 0.01	< 0.01	< 0.01	< 0.01	0.02
TiO ₂	0.01	0.01	0.02	0.01	0.02	0.01	0.02	0.03
P ₂ O ₅	0.11	0.01	0.08	0.02	0.05	0.01	0.05	0.02
Mn ₂ O ₃	< 0.01	< 0.01	0.02	0.01	0.01	0.01	0.01	0.03
L.o.I.*	44.00	44.15	43.81	44.03	43.91	43.96	43.94	42.94
Total	99.32	99.35	99.43	99.73	99.30	100.08	99.42	100.44

Table 3.3: Bulk chemical composition (wt%) of limestones, as determined by WD-XRF. *L.o.I. = loss on ignition. Declared average uncertainty of about 0.05 wt%.

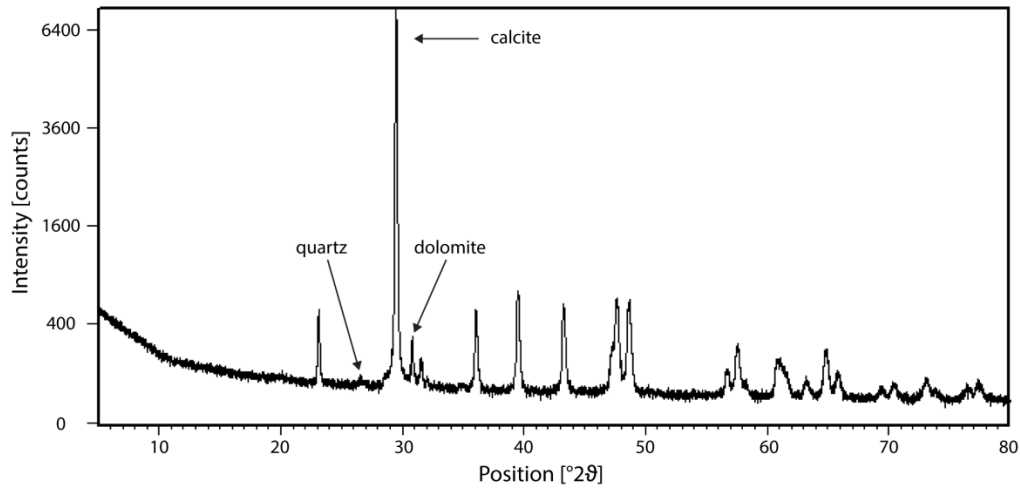


Figure 3.5: XRPD pattern of limestone *AS*. The most intense peak of every crystalline phase is marked out; square root y (intensity) axis was used to better highlight the weak peaks of dolomite and especially quartz.

Calcite microstructural analysis

The XRPD profile of calcite varies among the samples, keeping fixed the instrumental setup, sign of different distancing from the ideal crystal structure. As an example, Figure 3.6 shows the 28.5-30.5° 2θ window for samples *UM*, *MO2* and *MO1*, displaying the calcite (104) reflection. For samples *UM* and *MO1* its shape is well defined and it has a full width at half maximum (FWHM) of $\sim 0.06^\circ$ 2θ, making visible also the copper $K_{\alpha 2}$ shoulder. On the contrary, for sample *MO2* the same peak is broader (FWHM $\sim 0.12^\circ$ 2θ) and the Cu- $K_{\alpha 2}$ is not anymore recognizable. This difference reflects a smaller domains size and a higher microstrain for sample *MO2* compared to *UM* and *MO1*. Furthermore, this peak exhibits the same intensity and shape for *MO1* and *UM* samples, both relying on very similar microstructural features of calcite.

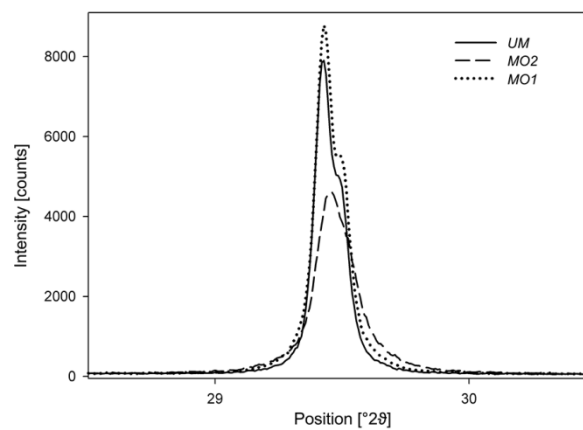


Figure 3.6: Visual comparison between the calcite (104) XRPD peak profile, concerning limestone samples *UM*, *MO2* and *MO1*.

Table 3.4 shows the detailed results of the calcite crystals, belonging to the selected limestones, microanalysis. The highest domains size is observed for sample *UM*, whereas the lowest for *MO2*; concerning the microstrain, *SA* and *AS* represent the two end-members. It is noteworthy to observe that the two values are independent from each other.

Sample	Domains size [Å]	Microstrain [10^{-4}]
<i>SA</i>	794(1)	0.07(1)
<i>SL</i>	864(1)	8.48(3)
<i>UM</i>	1380(2)	5.55(2)
<i>MO1</i>	1198(2)	5.91(2)
<i>MO2</i>	737(1)	11.15(4)
<i>MO3</i>	1188(2)	11.93(3)
<i>MO4</i>	805(1)	12.09(4)
<i>AS</i>	1323(2)	18.54(5)

Table 3.4: Domains size and microstrain values of calcite crystals belonging to the selected limestones, assessed from XRPD data. Samples are listed in reverse chronological order, from younger to older.

Petrographic description

Petrographic analyses confirmed the expected textural variability of the limestones, even at the millimetre to centimetre scale.

Sample *SA* is a framework of sparite crystals with few inclusions and complete absence of bioclasts (Figure 3.7a-b); according to these features it is classified as a crystalline carbonate or sparstone.

SL limestone is a grain-supported rock, with both micrite and microsparite as matrix, classified as a skeletal peloidal packstone (Figure 3.7c-d). Grains are mainly foraminifers (*Alveolina* and *Nummulites*), peloids and fragments of echinoderms, suggesting a protected inner ramp environment (Zamagni et al., 2008).

UM is a mudstone to wackestone, accumulated in a deep-water pelagic depositional environment (Premoli Silva and Sliter, 1995). It entirely consists of micrite matrix with sparse bioclasts, especially planktonic foraminifers (Figure 3.7e).

The *AS* sample is characterized by a red-stained micrite matrix rich in skeletal grains, with stylolites due to compaction and pressure solution during the burial diagenesis, filled by iron and manganese oxides (Figure 3.7f). Areas of skeletal grainstone and biocementstone also occur: the former are made by skeletal fragments and equant sparite crystals, due to the removal of the micrite matrix through dissolution processes, between the grains (Figure 3.7g); the latter by radial fibrous calcite embedding bryozoans and brachiopods (Figure 3.7h). The depositional environment is represented by the upper zone of a steep carbonate slope, dipping more than 30°, bordering a shallow-water flat-topped platform, at approximately 200 m paleo-depth (Della Porta et al., 2003). The rock can be classified as a wackestone to floatstone.

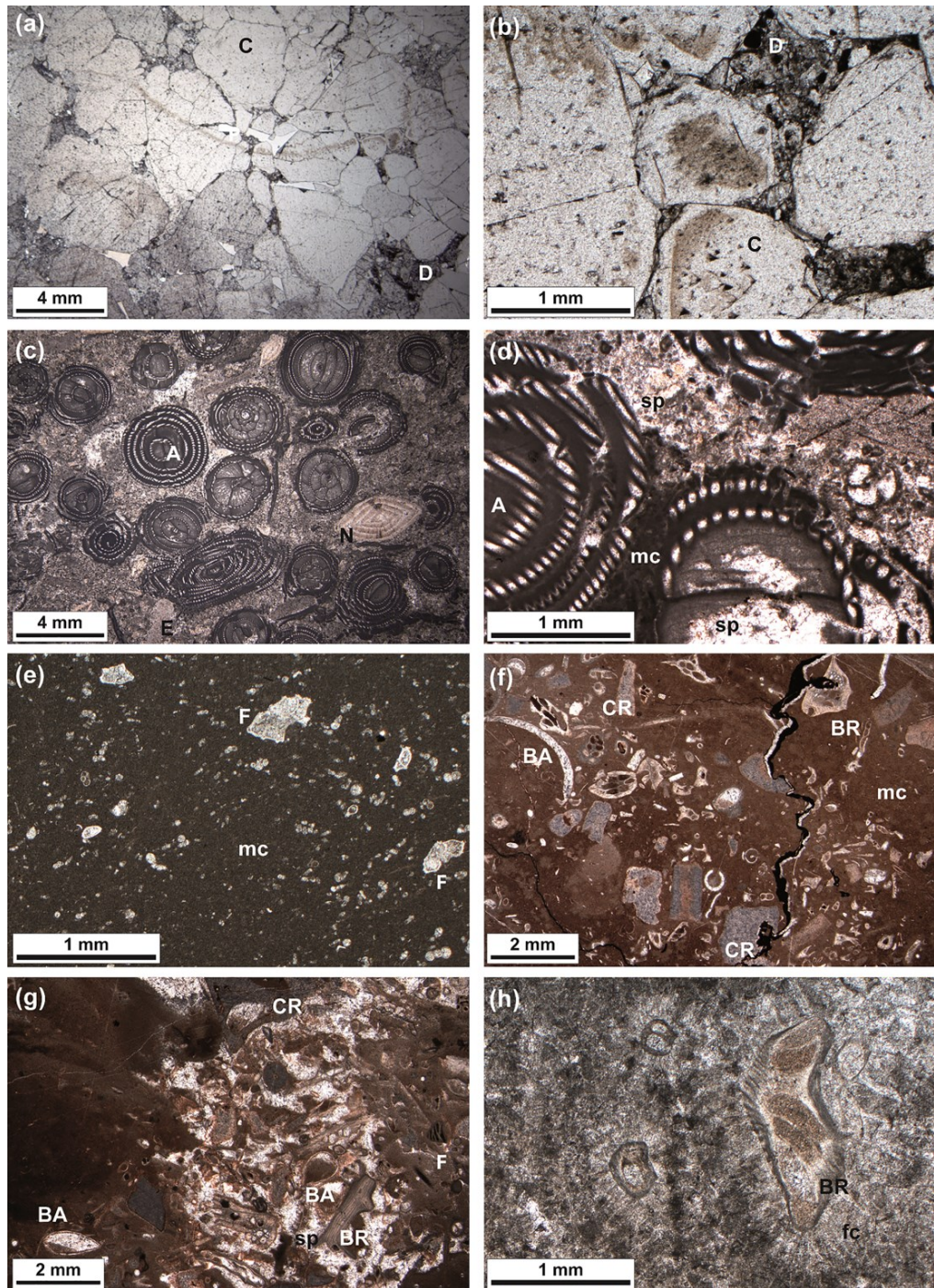


Figure 3.7: Optical micrographs of the investigated limestones-1. **a** *SA* limestone framework of sparite crystals (C) and detrital silt-size sediment (D) filling the intercrystalline porosity. **b** *SA* limestone close-up of the detrital sediment (D) between calcite crystals (C). **c** *SL* limestone skeletal peloidal packstone with *Alveolina* (A), *Nummulites* (N) foraminifers and fragments of echinoderms (E). **d** *SL* limestone micrite (mc) and sparite (sp) as matrix and as filling of the chambers of an *Alveolina* (A). **e** *UM* limestone skeletal wackestone to mudstone with micrite (mc) matrix and scattered planktonic foraminifers (F). **f** *AS* limestone – *microfacies A* skeletal wackestone/floatstone with a red micrite matrix (mc) rich in iron and manganese oxides. Fragments of crinoids (CR), fenestellid bryozoans (BR) and brachiopods (BA). **g** *AS* limestone – *microfacies B* skeletal grainstone where micrite was removed by dissolution and sparite (sp) precipitated in the interparticle space. Bioclasts are crinoids (CR), benthic foraminifers as *Tetrataxis* (F), bryozoans (BR) and brachiopods (BA) with geopetal sediment filling indicative of the stratigraphic way-up. **h** *AS* limestone – *microfacies C* biocementstone with radiaxial fibrous calcite (fc) embedding fenestellid bryozoans (BR).

The four *MO* samples are time-equivalent carbonate facies accumulated side by side along across a Lower Jurassic carbonate platform (Della Porta et al., 2013).

MO1 is a coral-microbial boundstone with microbial encrustations, associated with peloidal skeletal packstone and grainstone areas between the corals, pointing out the extreme textural variability, even at the centimetre scale, in a reef environment. Two different generations of calcite cement occur within the cavities (Figure 3.8a): early marine radial fibrous calcite crystals cover the inner walls of the cavities, then occluded by equant calcite crystals precipitated during burial diagenesis. Blocky sparite also fills the main fractures. Skeletal reef components are mainly phaceloid corals (Figure 3.8b), originally aragonitic and then replaced by calcite during the diagenesis, associated with benthonic foraminifers and echinoderms fragments.

Samples *MO2* (Figure 3.8c-d) and *MO3* (Figure 3.8e-f) are mainly packstones and locally grainstones, characterized by peloids, skeletal fragments and fenestrae, these latter primary cavities due to degassing, desiccation and degradation of the organic matter in the intertidal zone, later filled by calcite cement.

According to these features, the depositional environment of samples *MO1*, *MO2* and *MO3* is a low-energy platform interior, spacing from a protected subtidal lagoon to the intertidal zone.

Finally, limestone *MO4* shows a grain-supported cemented texture, associated with few millimetre-wide packstone areas. The widespread distribution of pisoids and the marine vadose diagenetic features such as pendant and meniscus cements (Figure 3.8g-h) indicate a supratidal depositional environment. Three generations of calcite surround peloids and intraclasts: on the grain surface a pendant yellowish layer of fibrous cement, mostly on the lower part of the grains because of gravity and associated with a thin clotted peloidal microbial crust, occur, followed by isopachous rims of fibrous calcite and finally by blocky sparite at the core of the cavities.

Detailed petrographic description taking into account textural features and grains composition is reported in Appendix A1 (Table A1).

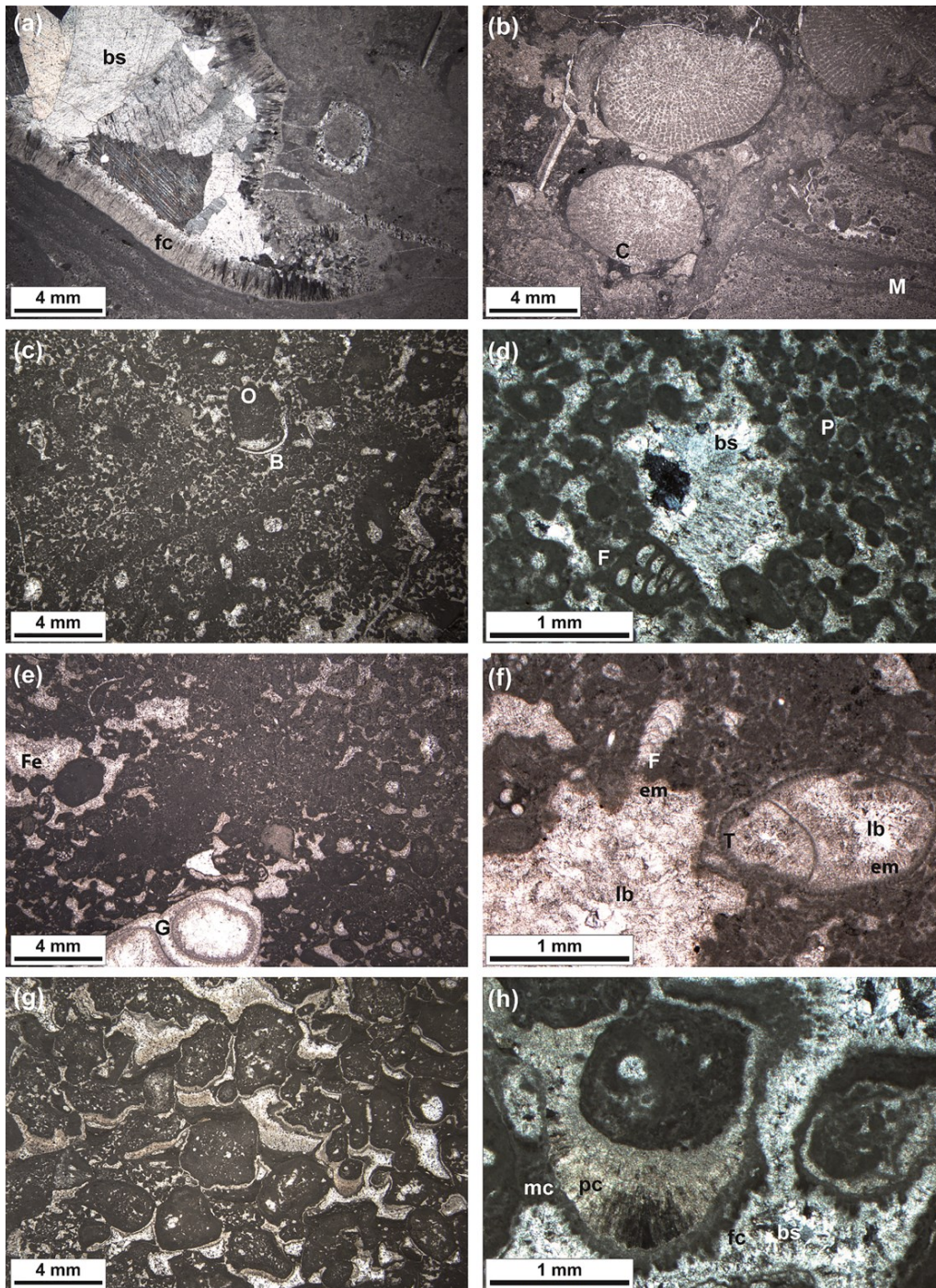


Figure 3.8: Optical micrographs of the investigated limestones-2. **a** *MO1* limestone primary reef cavity filled by isopachous rims of radiaxial fibrous calcite (fc) and equant blocky sparite (bs), due to early marine and late burial diagenesis, respectively. Image in XPL. **b** *MO1* limestone coral (C) boundstone and peloidal packstone with laminated microbialites (M). **c** *MO2* limestone peloidal skeletal packstone to grainstone with oncoids (O) and fragments of bivalves (B). **d** *MO2* limestone cavity filled by equant blocky sparite (bs) surrounded by peloids (P) and textularid foraminifer (F). Image in XPL. **e** *MO3* limestone peloidal packstone with gastropod (G) and fenestral voids (Fe) filled by sparite cement. **f** *MO3* limestone with the alga *Thaumaporella parvovesiculifera* (T), foraminifer (F) and cavity filled by an early marine (em) and a late burial (lb) cement. **g** *MO4* limestone coated grain peloidal packstone and grainstone with interparticle pore space filled by several generations of calcite cement and micrite crusts. **h** *MO4* limestone close-up view of pendant cement (pc) and laminated micritic crusts (mc) due to vadose diagenesis. Isopachous rims of fibrous calcite (fc) and equant blocky sparite (bs) at filling the pores, due to early marine and late burial diagenesis, respectively. Image in XPL.

Digital image analysis

Table 3.5 reports the micrite to sparite ratio within the investigated limestone samples.

<i>SA</i>	<i>SL</i>	<i>UM</i>	<i>MO1</i>	<i>MO2</i>	<i>MO3</i>	<i>MO4</i>	<i>AS</i>
0.0(0)	7.9(3)	73.6(7)	4.7(3)	3.3(2)	6.5(2)	4.3(3)	2.0(1)

Table 3.5: Micrite to sparite ratio, as determined by digital image analysis on thin sections scans. Samples are listed in reverse chronological order from younger to older.

3.3 Burnability test

3.3.1 Raw meals formulation and firing cycle

After the deep limestone characterization, eight industrial raw meals for ordinary Portland cement clinker production have been prepared, one for each limestone.

In addition to limestones, the other employed raw materials were clay, silicon oxide and iron oxide. Clay is a natural Quaternary sample from Sabbio Chiese (northern Italy, Brescia Alpine foothills), commonly used for industrial OPC clinker raw meals preparation. Its chemical composition, determined by WD-XRF analysis, is reported in Table 3.6.

On the contrary, silicon oxide and iron oxide are certified analytic reagents: SiO₂ (99.90 wt% - Merck Millipore) and Fe₂O₃ (99.95 wt% - Carlo Erba Reagents).

<i>Sample</i>	SiO ₂	Al ₂ O ₃	Fe ₂ O ₃	CaO	MgO	SO ₃	K ₂ O	Na ₂ O	TiO ₂	P ₂ O ₅	Mn ₂ O ₃	L.o.I.	Total
<i>Clay</i>	45.06	24.53	9.97	0.27	1.10	<0.01	1.77	0.13	1.19	0.15	0.09	14.74	99.00

Table 3.6: Bulk chemical composition (wt%) of the clay fraction, as determined by WD-XRF.

Before blending the raw materials together, limestones and clay were finely ground below 80 µm in a jaw crusher, to reach the correct fineness for raw meal preparation. On the other hand, silicon and iron oxides were already at the right grain size and no grinding was necessary.

In order to guarantee the same chemical composition, concerning the major oxides, during the raw meals preparation, lime saturation factor (LSF=97.00), silica ratio (SR=2.50) and alumina ratio (AR=1.50) values were kept fixed.

Once blended, the raw meals were mechanically homogenized for 90 min, by means of a “Turbula” automatic shaker-mixer.

Then, before undergoing the thermal treatment, loose powders were pressed for a few seconds under a 400 bar pressure, using an hydraulic press (Enerpac VLP-106P142) obtaining thus 5-grams pellets. Pelletizing the powders is necessary to optimize the contact between grains and ease the reactions upon heating; this problem is however bypassed in the industrial process because, dealing with tons of material, the raw materials are self-compacting under their own weight.

The burnability test aims to simulate, in a laboratory furnace, the temperature conditions usually occurring inside the rotary kiln at the production plants. Each raw meal was thermally treated in an electrical horizontal tube furnace (Nabertherm RHTC 80) at seven different temperatures with a soaking time of 20 min per temperature, as reported in Figure 3.9. The soaking time is advised to ensure the thermal equilibration of the pellet: this because the material is not poured into a kiln already

at its operating temperature, but in a laboratory furnace heated starting from room temperature. At each of these temperatures, a pellet was drawn from the furnace and quenched by a room-temperature air flow.

Clinker samples will be hereafter addressed as *clinker_x* where *x* refers to the limestone used in the raw meal; e.g. *clinker_{AS}* will concern clinker obtained after the thermal treatment of a raw meal where the limestone *AS* represents the carbonate fraction.

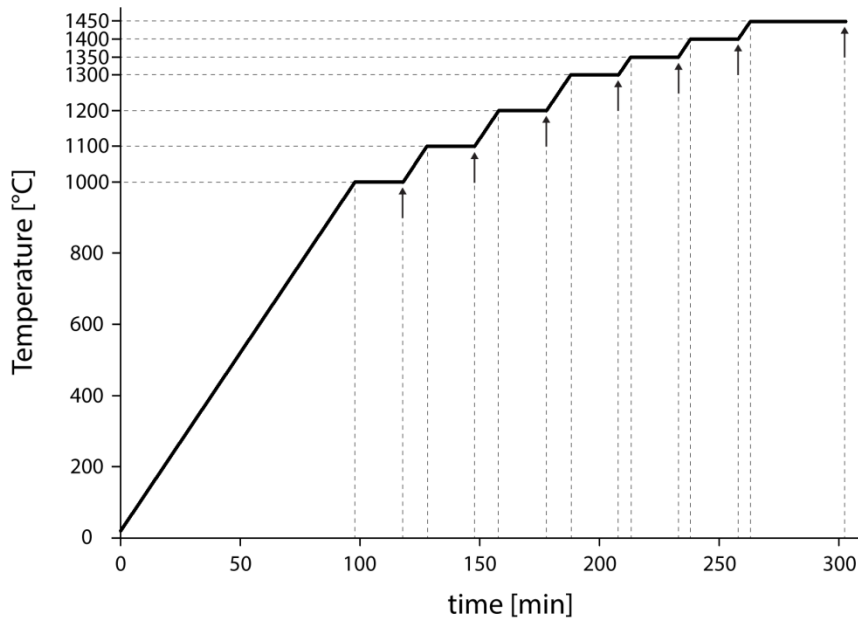


Figure 3.9: Visual representation of the firing cycle heating ramp. Arrows indicate when samples were drawn from the furnace.

3.3.2 Experimental methods

X-ray powder diffraction

Qualitative phase analyses on clinkers were provided by *ex situ* X-ray powder diffraction experiments, carried out under the same conditions reported in Section 3.2.2.

In the same way, quantitative phase analysis was performed processing the collected patterns by the full profile Rietveld method (Young, 1993), implemented in the TOPAS-Academic 5.1 software (Coelho, 2012).

Scanning electron microscopy (SEM)

Polished sections of clinkers sintered at $T = 1450$ °C during the burnability test were investigated by scanning electron microscopy, to understand the spatial distribution of the clinker phases and their morphology. Instrumental setup is reported in Section 2.3.

3.3.3 Results

Quantitative phase analysis

Figure 3.10 reports an example of Rietveld refinement on clinker from raw meal made by employing limestone *SL*, whereas Table 3.7 the Rietveld quantitative phase analysis results on three selected samples obtained through the burnability test. Complete results reported in Appendix A1 (Table A2).

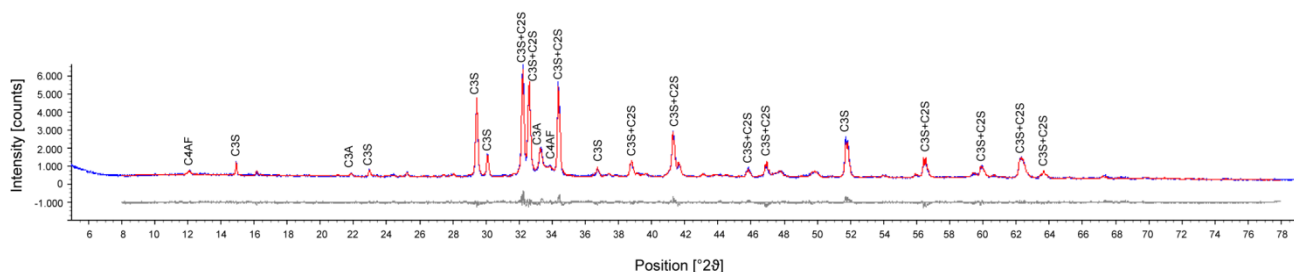


Figure 3.10: Observed (blue) and calculate (red) patterns and difference curve (grey) for clinker sample *SL* obtained at $T = 1450$ °C during the burnability test. XRPD peaks are labelled according to the cement chemistry shorthand notation.

	Temperature [°C]						
<i>Clinker_SA</i>	1000	1100	1200	1300	1350	1400	1450
C ₃ S	-	-	-	6.3	64.1	71.2	77.7
C ₂ S	10.3	25.0	34.3	58.8	13.2	8.4	5.3
C ₃ A	1.3	1.0	2.7	8.1	11.8	10.5	8.7
C ₄ AF	4.4	7.3	10.4	10.1	4.3	4.8	5.9
CaO	53.6	45.8	38.4	15.5	5.5	4.3	1.7
Others*	30.4	20.9	14.2	1.2	1.1	0.8	0.7
<i>Clinker_MO2</i>	1000	1100	1200	1300	1350	1400	1450
C ₃ S	-	-	-	32.2	59.5	69.3	69.8
C ₂ S	18.4	29.2	34.4	39.7	15.9	11.7	10.1
C ₃ A	1.7	0.3	2.8	5.8	11.9	9.2	9.2
C ₄ AF	3.3	7.3	8.8	11.1	6.7	6.0	8.1
CaO	51.6	44.0	37.0	10.8	5.3	3.1	1.9
Others*	25.0	19.2	17.0	0.4	0.7	0.7	0.9
<i>Clinker_AS</i>	1000	1100	1200	1300	1350	1400	1450
C ₃ S	-	-	-	46.5	66.4	72.5	72.2
C ₂ S	22.0	32.0	39.4	27.4	15.6	10.6	13.1
C ₃ A	1.6	1.0	3.0	8.1	3.5	3.2	3.7
C ₄ AF	5.3	8.8	11.4	10.6	12.2	12.7	10.7
CaO	47.7	40.9	36.3	7.2	2.0	0.9	0.3
Others*	23.4	17.3	9.9	0.2	0.3	0.1	-

Table 3.7: Phase composition (wt%) of clinkers samples from three selected raw meals, at all the temperatures of the burnability test, as determined processing XRPD data by Rietveld refinements. The category “others” refers to C₂AS, C₁₂A₇, S, M and CH. Samples are listed in reverse chronological order from younger to older. Uncertainty not reported because the aim was to evaluate trends and not absolute values.

Independently from the limestone features, the destabilization of calcite and clays aluminosilicates leads to the formation of lime, followed by the crystallization of belite and aluminates in all the OPC clinker raw meals. Then, between $T = 1300$ and 1350 °C, a melt appears and also alite starts to grow significantly; the appearance of the melt is not directly measured but it is inferred by the decrease of both the aluminates.

On the contrary, significant differences among the samples appear taking into account the mass percentage of the crystalline phases as a function of the temperature. Belite and lime weight fraction are directly correlated at the lowest temperatures: in particular the more the belite content, the less the free lime. For instance the CaO content at 1000 °C spans from the 54 wt% to the 48 wt%, for *clinker_SA* and *AS* respectively, the two end-members considering calcite microstrain. Conversely, the C_2S content is symmetrical with respect to CaO wt%, varying from 10 wt% to 22 wt% in the same two samples. Differences concerning the crystalline phases content between clinkers are even clearer at 1300 °C, being also the C_3S wt% directly linked to the microstrain value of the calcite employed as carbonate fraction.

Figure 3.11 visualizes this behaviour, by plotting the weight content of C_2S and C_3S as a function of the microstrain and the domains size of the calcite crystals in the limestone rock. The direct correlation between the calcite microstrain and the OPC clinkers crystalline phases can be observed only at the lowest temperatures, whereas no correlation occurs by plotting the same results as a function of the calcite domains size, at all the temperatures.

Figure 3.12 visualizes the CaO decrease as a function of temperature in the raw meals prepared using the two end members concerning calcite crystals microstrain.

Then, raising the temperature up to 1350 - 1400 °C, the correlation between crystalline phases weight content and calcite microstrain fades out (Figure 3.13), in correspondence to the aluminates decrease due to their destabilization and consequent melt formation. From now on, neither the microstrain nor the domain size have relevant effects on the mixtures reactivity, because the melt appears indeed and the reactions take place no more at the solid state.

Despite this homogenization of the thermal behaviour at the highest temperatures, some differences in terms of crystalline phases weight fraction can be still observed in clinkers sintered at 1450 °C, as plotted in Figure 3.14.

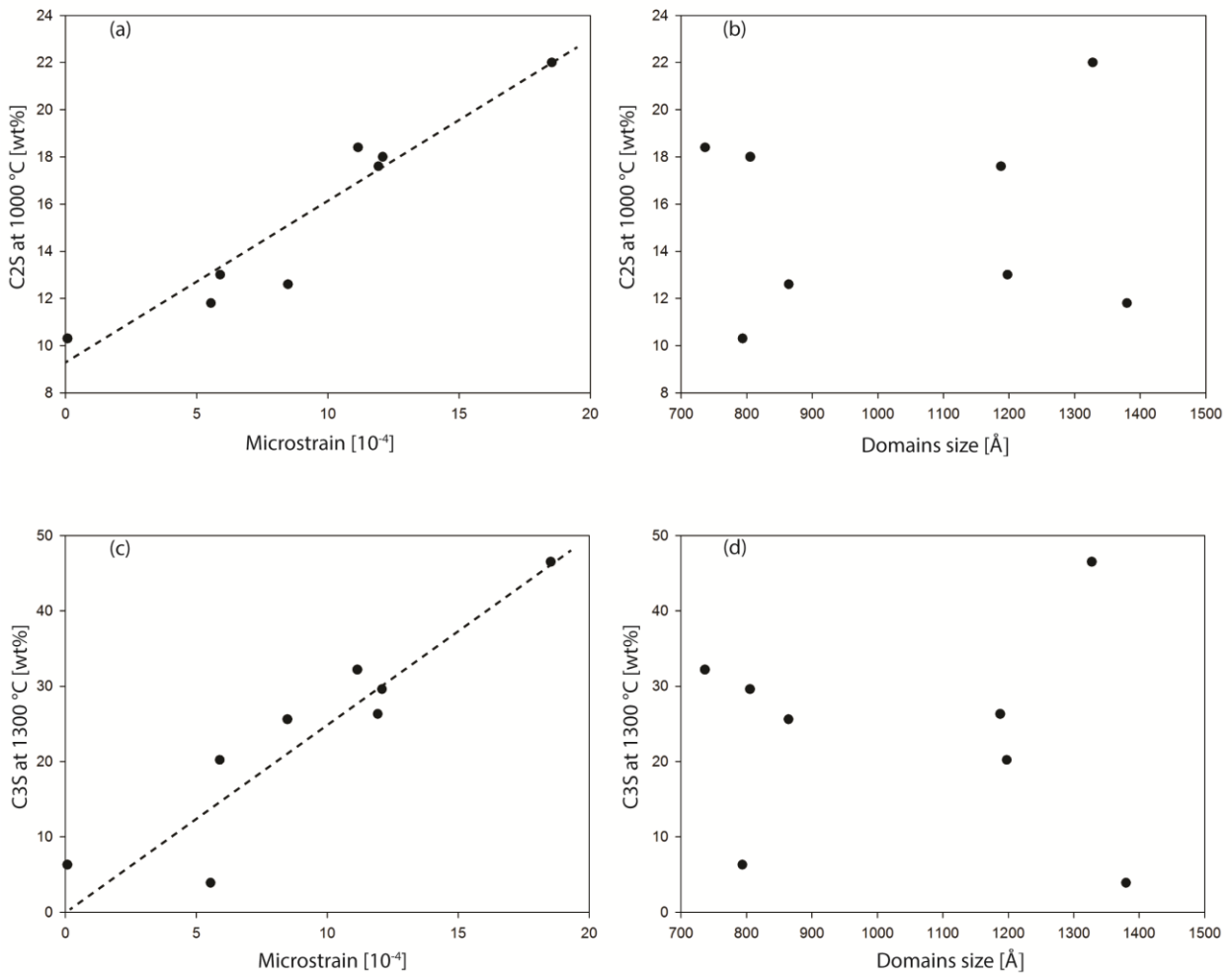


Figure 3.11: C₂S wt% at T = 1000 °C as a function of microstrain (a) and domains size (b); C₃S wt% at T = 1300 °C as a function of microstrain (c) and domains size (d). Trend-lines are drawn to highlight the correlation between calcite microstrain and crystalline phases content.

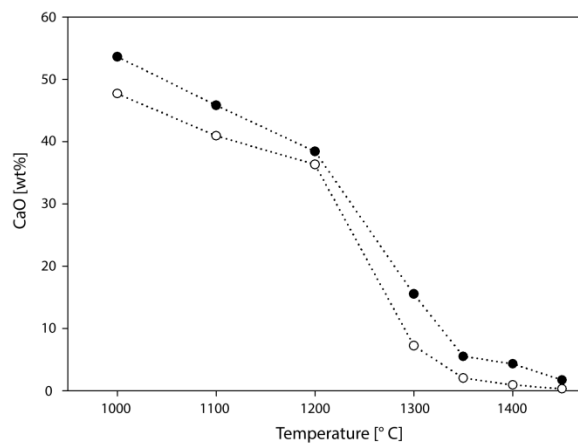


Figure 3.12: CaO wt% as a function of temperature during the burnability test of raw meals SA (black circles) and AS (white circles).

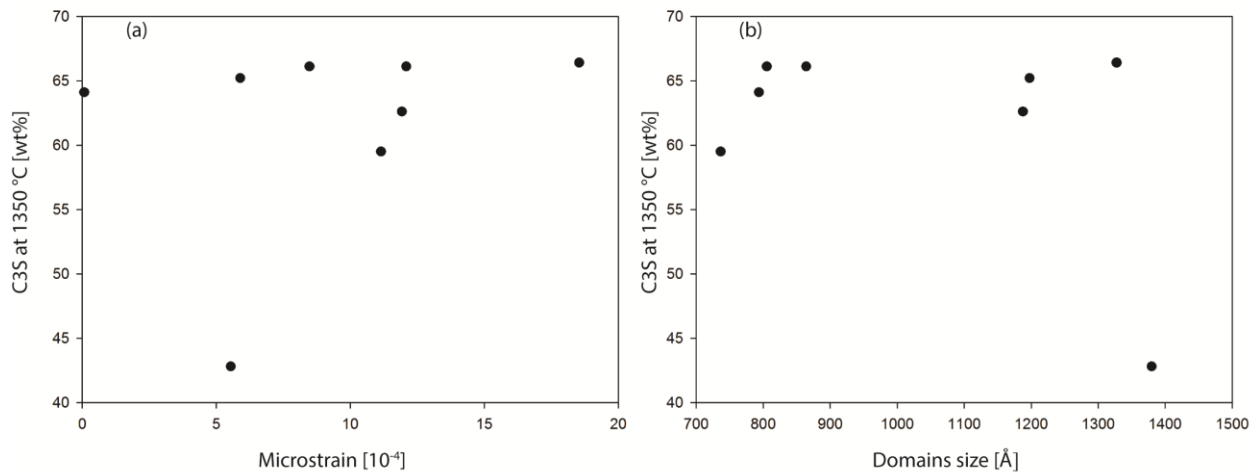


Figure 3.13: C₃S wt% at T = 1350 °C, as a function of calcite microstrain (a) and domains size (b). No significant trend-lines can be drawn.

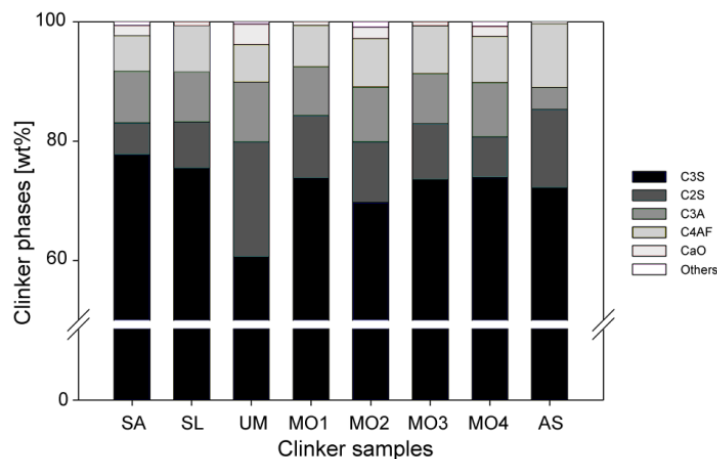


Figure 3.14: Bar chart of quantitative phase analysis results on clinker samples obtained at T = 1450 °C during the burnability test. Results are normalized to 100 wt% of crystalline phases.

Scanning electron microscopy

Scanning electron microscopy was performed only on clinker samples sintered at 1450 °C, to evaluate if processes with different reactivity would also affect the final product morphology. All the samples exhibit the expected phase assemblage, as also previously confirmed by quantitative XRPD analyses.

Figure 3.15a shows predominant C₃S and clusters of well-rounded and poorly fractured C₂S crystals, surrounded by an interstitial matrix made by the aluminates; in addition, traces of unreacted lime and C₂S inclusions within the C₃S are detected, as an indicator of a good overall burnability.

Differences among clinker samples arise in terms of crystalline phases spatial distribution, morphology and size. *Clinker_SA* displays (Figure 3.15b) large tabular crystals of C₃S, ranging from 10 to 100 μm, pointing out the predominance of the growth process over the nucleation; conversely, *clinker_AS*

exhibits (Figure 3.15c) small tabular C_3S crystals, suggesting a predominance of the nucleation over the growth.

Focusing on the interstitial phases, quantitative XRPD results underline that their overall mass percentage ranges from 14 to 17 wt%. Despite the similar abundance, SEM micrographs highlight a different distribution, as in *clinker_AS* ferrite dominates on the tricalcium aluminate (Figure 3.15c), vice-versa in *clinker_SA* (Figure 3.15d). Also their morphology is different: as an example C_3A morphology varies significantly from *clinker_MO4* to *clinker_MO1*, becoming more tabular and increasing its average size.

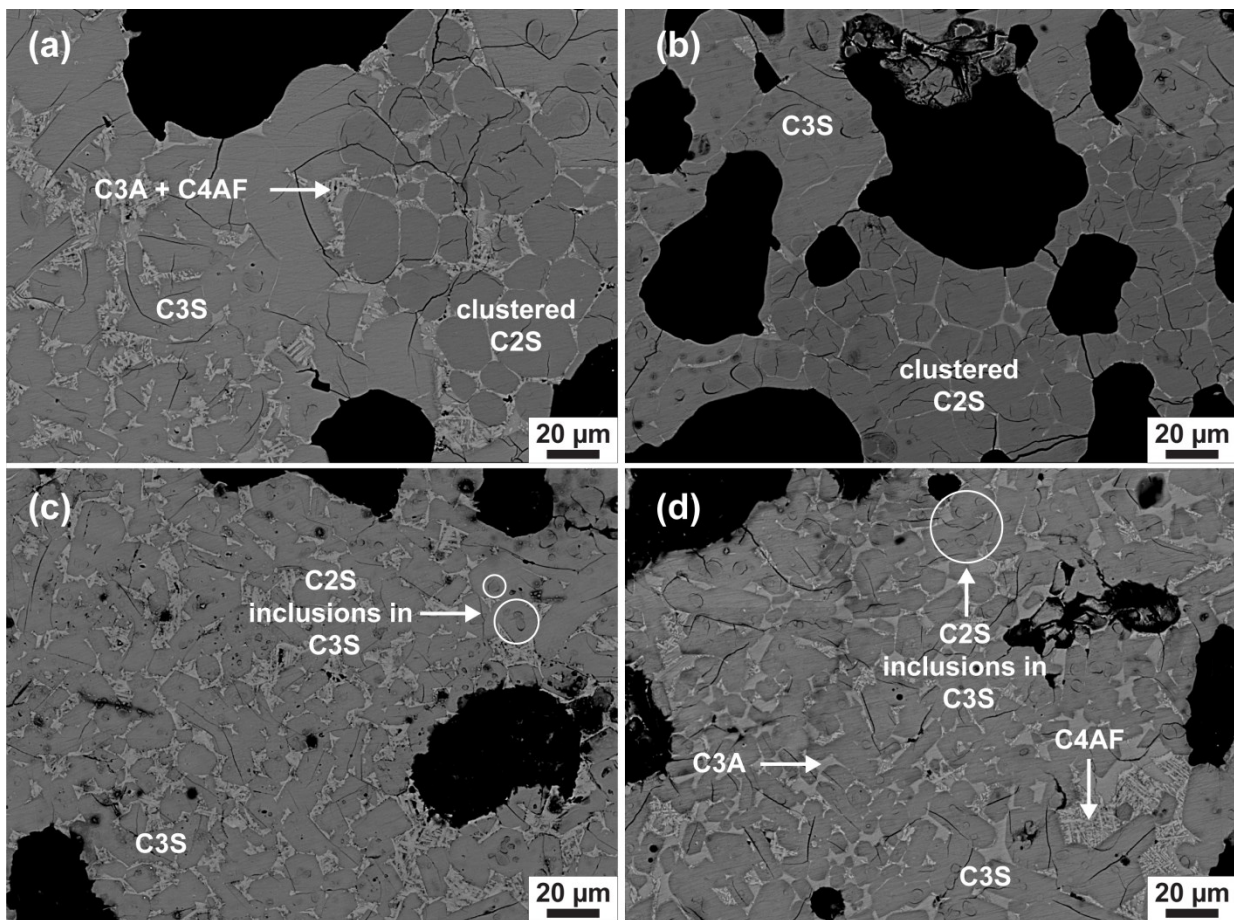


Figure 3.15: Backscattered electrons (BSE) SEM micrographs of clinkers sintered at $T = 1450$ °C. (a) *clinker_MO4* uniform phase distribution. Tabular C_3S and well-rounded C_2S crystals; aluminates occur as interstitial phases. (b) *clinker_SA* alite crystals up to 80-100 μm and clustered belite near the holes due to the specimen preparation. (c) small and tabular C_3S crystals with very few C_2S inclusions in *clinker_AS*. (d) *Clinker_MO1* large tricalcium aluminate crystals and interstitial ferrite crystals between tabular alite with few belite inclusions.

3.4 Discussions

Chemical and mineralogical analyses on the selected limestones proved their similarity and their suitability for OPC clinker production. However, optical microscopy and image analysis stressed a high variability both at the macro and micro scale. Macro-scale refers to the different micrite to sparite ratio, to the fossil content, grains type and diagenetic features; micro-scale pertains the calcite crystals microstrain value and domains size, determined by line profile analysis XRPD. These dissimilarities reflect limestones different depositional environments, geological ages and diagenetic histories; up to three microfacies can be observed even at the thin-section scale, as in limestone *AS*, witnessing a strong textural variability even at the millimetre scale. Moreover, the microstrain value spans as a function of depositional environment, diagenetic history and sample age, whereas the domains size seems to be influenced by none of these factors.

In existing literature, some papers report the influence of limestones microstructural features on the thermal decomposition of carbonates or on the reactivity of the resulting oxides. For instance it was studied how the fossils content in grainstones rocks reflects on the reactivity of the quicklime derived from their destabilization (Soltan et al., 2011); the mineralogical assemblage, jointly to the bulk chemical composition, has been proved to be the controlling variable of mud-supported limestones reactivity, even after their complete calcination (Soltan et al., 2012), as also described by Marinoni et al. (2012) evaluating the influence of dolomite on the clinker manufacturing process.

Results presented here confirm that predicting the OPC clinker raw meal burnability only taking into account the whole limestone texture is an almost prohibitive task, since no univocal relationships between limestones petrographic features and the way their burnability proceeds can be defined. This is due to the fact that the effects induced by each single feature do not merely sum each other, but interact between them making thus impossible to ascertain each single contribution. For example, limestones *UM* and *SA* lead to a final clinker with a very similar mineralogy, crystals morphology and texture, despite they are the two end-members of the Dunham's classification of sedimentary rocks textures, a mudstone and a crystalline carbonate respectively. In the same way, limestones similar from a textural point of view, such as *UM* and *AS*, behave differently during the clinkerization.

Starting from these assumptions, the present work aimed to find a univocal predictive proxy of the OPC clinker raw meal burnability; the calcite crystals microstrain and domains size were identified as promising tools, also because describable by numerical parameters.

Quantitative phase analyses results on obtained clinkers point out the calcite crystals microstrain as the driving factor on the way the clinkerization proceeds, even when the calcite is fully decomposed. Generalizing, the higher the calcite microstrain, the better the burnability of the raw meal. On the contrary, the domains size has no relevant effects on the process. Moreover, also the micrite to sparite ratio has no influence on the raw meal burnability in terms of calcium silicate formation and lime consumption, despite it was demonstrated that the higher the micrite to sparite ratio, the lower the time to completely destabilize the carbonates (Marinoni et al., 2015). The reasons for this conflicting behaviour can be the followings: (i) the rate of carbonate decomposition has no consequences on the reactivity of the produced lime, rather unconvincing, based on the present work results; (ii) the occurrence of micrite or sparite does not implicitly mean to have high-defective and low-defective

calcite crystals respectively, despite their sizes. A smaller crystal can be less defective than a larger one, or vice versa.

A raw meal prepared starting from a high-strained calcite limestone, brings at the same time to a clinker higher in calcium silicates phases and lower in free lime than the ones obtained using a low-strained calcite limestone. Comparing the two calcite microstrain end-members at $T = 1300\text{ }^{\circ}\text{C}$, the higher the microstrain the higher the C_3S weight fraction and at $T = 1450\text{ }^{\circ}\text{C}$ the lower free lime weight fraction. As an example, free lime content in *clinker_SA* and *clinker_AS* attests on 2 wt% and <1 wt% respectively.

Hence, it is proved that during solid-state reaction processes, the early burnability and calcium silicates formation are affected by the calcite microstrain. *Early burnability* in this case means *before the melt formation* because when the liquid phase appears this correlation is completely cancelled, being the burnability driven by the amount of the liquid phase, its viscosity and its surface tension.

Noteworthy, despite this homogenization of the raw meal burnability at the highest temperatures due to the melt appearance, differences during the early burnability affect the final clinker mineralogy and morphology.

High-strained calcite raw meals lead, in addition to small and well-faceted alite crystals, to an interstitial matrix dominated by ferrite. According to a study published by Uda et al. in 1998, this behaviour can be ascribed to the reduction of primary phase volume of tricalcium aluminate because in these raw meals alite starts to crystallize earlier, trapping Al^{3+} in its structure as a Ca^{2+} - Si^{4+} substituent or as interstitial ion. This decreases the aluminium available for the tricalcium aluminate formation, inducing a shift of its volume to a smaller one than the expected.

Figure 3.16 plots a correlation between the calcite microstrain in the raw meal and the aluminates weight fraction in clinkers sintered at $T = 1450\text{ }^{\circ}\text{C}$ during the burnability test. The values of the coefficient of determination of the linear regressions, especially the one for the C_4AF , are a proof of the correlation validity.

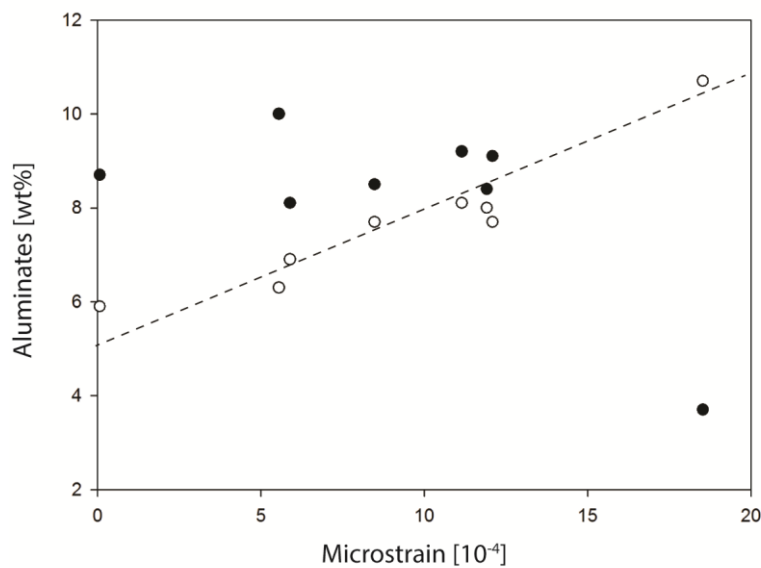


Figure 3.16: C_3A (black circles) and C_4AF (white circles) weight fraction in clinkers sintered at $T = 1450\text{ }^{\circ}\text{C}$, plotted as a function of the microstrain of calcite crystals belonging to the limestone used to prepare the raw meals. Trend-line for C_4AF is also drawn.

Finally, it was made a successful attempt to correlate the calcite microstrain value to a geological feature of the rock, to ease the limestones selection procedure at the quarry-site. It was found that the older the limestone, the higher the average value of the calcite crystals microstrain (Figure 3.17). This because the oldest limestones samples likely experienced several diagenetic processes, whose effects usually superimpose each other. This is witnessed by sets of fractures and multiple cement generations, occurred during geological-time geodynamic processes, usually in non-equilibrium conditions, inducing thus stresses and deformations even at the microscale of calcite crystals lattice. However, discrepancies from the linearity of the correlation *sample age-microstrain* value can happen, as in case of limestone *MO1*. The reason lies in the fact that domains size and microstrain evaluation by XRPD line profile analysis gives an average value. Sample *MO1* is a mostly micritic limestone, but crossed by fractures later filled by sparite. Hence its lower microstrain value than contemporary *MO2*, *MO3* and *MO4* limestones, because sparite underwent a shorter diagenetic history and thus it is less defective. A similar conflict between age and microstrain is also detected taking into account samples *UM* and *SL*, where *SL* is younger than *UM* but has a higher microstrain value. The discrepancy is again due to different diagenetic histories; sample *UM* settled in a marine basin that underwent less complex diagenetic processes, compared to the fold-and-thrusts belt from which sample *SL* is from.

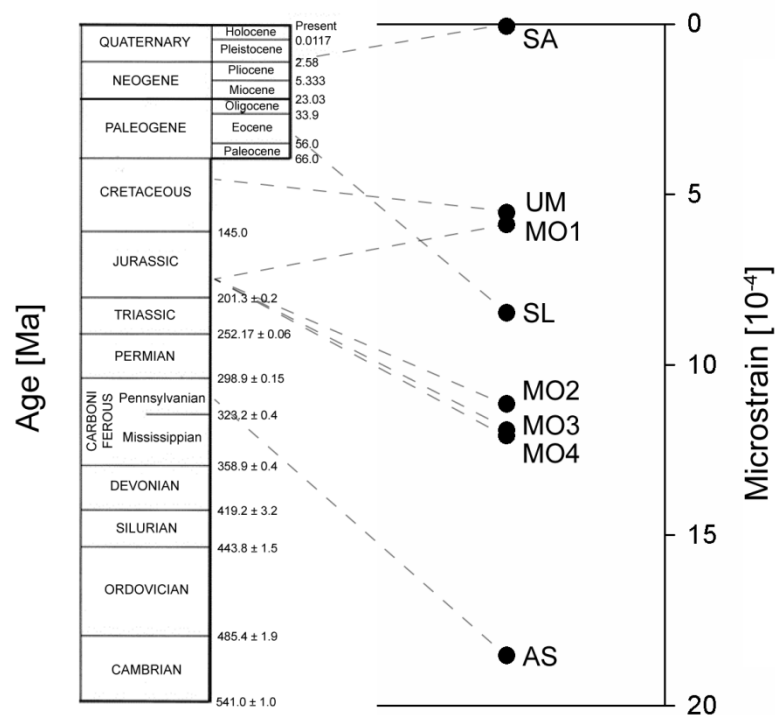


Figure 3.17: Correlation between calcite crystals microstrain values and limestones age.

3.5 Conclusions

The investigated OPC clinker raw meals were similar from a chemical and mineralogical point of view, making thus possible comparisons between them and to ascribe the differences concerning the thermal behaviour to the limestones intrinsic features.

Results confirmed that predicting the OPC clinker raw meals burnability taking into account only the overall limestone petrography is a prohibitive task, because single effects are not additive. Moreover, limestone petrography is not describable by a number, making correlations between petrography and burnability weak.

Line profile analysis on limestones XRPD patterns allowed to estimate the calcite crystals microstrain and average domains size, reasonably assuming these limestones entirely made by calcite on the basis of the chemical and mineralogical analyses. It was found that the calcite crystals microstrain value, relying on the age of the rock, is a reliable tool to predict the OPC clinker raw meals burnability, moreover quantifiable by an objective parameter. In particular, the higher the microstrain of calcite crystals, the better the burnability during the early stage of the thermal treatment. On the contrary, both the average domains size of the calcite crystals and the micrite to sparite ratio within the whole carbonate rock show no explicit correlation with the burnability of the OPC clinker raw meals, at least for $T \geq 1000$ °C. Finally, these differences concerning the burnability have also implications on the final clinker mineralogy and texture, however different burnabilities start to homogenize after the melt appearance. Especially, high-strained calcite leads to clinker with small C_3S crystals and an interstitial matrix dominated by ferrite, vice-versa for low-strained calcite.

Chapter 4

The effects of minor elements on the clinkerization process

4.1 Introduction

Calcium, silicon, aluminium and iron are the major elements occurring in a raw meal for OPC clinker production, because they will build up the structure of the main crystalline phases after the thermal treatment.

Minor and trace elements distribution within an OPC clinker raw meal is due to the employment of natural raw materials, generally limestones and clay minerals, which can virtually carry all the elements. Additional minor and trace elements sources are represented by the kiln fuels and by the use of alternative raw materials, such as industrial wastes or by-products, to partially or totally replace the natural ones (Schreiber et al., 2007). In this chapter, the wording *minor elements* refers to elements usually occurring in a concentration between 1 and 5 wt% in a commercial clinker raw meal, whereas *trace elements* to the remaining ones below 1 wt%.

In this study, sodium, magnesium and sulphur were selected as minor elements to couple together because they often occur in an OPC clinker raw meal, mainly from raw materials or alternative kiln fuels (Taylor, 1990). On the contrary, fluorine and chlorine were chosen as trace elements, never combined together in the experimental raw meals, to evaluate their possible effects both on the clinkerization and on the behaviour of the abovementioned minor elements.

Sodium mainly derives from the raw materials, in particular the clay fraction; sometimes, also the limestone fraction can carry sodium, in the form of soluble salts (Bhatty, 1995). It acts as a fluxes during the burning process but its occurrence is highly undesirable than other minor elements, because it can lead to the alkali-silica reaction in the hardened cement paste, causing serious cracking (Bucchi, 1980).

Magnesium is commonly from dolomite occurrence within limestones and secondly from clay (Lea, 1971). Limited quantities improve the raw meal burnability, otherwise it leads to the deleterious periclase occurrence.

Sulphur enters the raw meal usually from coal, petroleum coke and scrap tyres used as fuels and from pyrite used as iron content corrective. Sulphates and sulphides can also occur both in limestones and clay as secondary minerals (Bhatty, 1995). During the thermal treatment sulphur combines with alkalis

to give alkali-sulphates, partially volatilising at the highest temperatures or leading to the occurrence of apthitalite and arcanite in the final product.

Dealing with trace elements, fluorine and chlorine were treated separately, within the same raw meals doped by combinations of the above-mentioned minor elements.

Fluorine occurs both in the limestone fraction and in the kiln fuels (Sprung, 1988), whereas fluorite (CaF_2) is widely used both as a mineraliser and as a flux to lower the burning temperature and increase the alite formation and weight fraction within the clinker (Klemm et al., 1979). Fluorine forms fluoroaluminates at the early stages of the thermal treatment, which later destabilise releasing fluorine that is thus incorporated into tricalcium silicate.

Chlorine generally enters an OPC clinker raw meal mainly through both primary and secondary kiln fuels and natural raw materials (Akstinat et al., 1988). Chlorine reacts with alkalis during the thermal treatment, reducing thus their concentration in the raw meal by alkali chlorides formation and subsequent volatilization; due to that volatilization process, the chlorine amount retained within clinker phases is commonly less than 0.03 wt% operating in standard conditions, due to their high volatility indeed (Mishulovich, 1994). On the contrary, when CaCl_2 content in the raw meal is increased up to 20 wt%, alinite clinkers are produced; their manufacturing process is less energy-intensive than a standard OPC clinker, requiring a burning temperature between 1000 and 1100 °C (Patel, 1989). Their standard composition is 60-80 wt% of the so-called alinite phase ($21\text{CaO}\cdot 6\text{SiO}_2\cdot \text{Al}_2\text{O}_3\cdot \text{CaCl}_2$), followed by 10-30 wt% of C_2S and 2-10 wt% of calcium aluminoferrite (Bikbaou, 1980; Kim et al., 2003). Alinite clinkers properties are close to those of a standard OPC clinker, making them an attractive material, whose investigation falls however outside the purpose of this study.

The aim of this chapter is to collect, for the first time, information concerning the behaviour of the abovementioned minor elements – sodium, magnesium and sulphur respectively – when coupled together within an industrial OPC clinker raw meal. Fluorine and chlorine are also added separately to the raw meals, in order to evaluate possible effects of these two trace elements on the behaviour of the chosen minor elements. The innovative nature of this work lies in the fact that the starting raw mixture – limestone and clay – is from an actual OPC clinker manufacturing plant, whereas past investigations usually dealt with raw meals prepared employing only analytical chemical reagents. Hence, in the here-investigated raw meals, all the major elements derive from natural raw materials and not from chemical analytical reagents, allowing thus to test the behaviour of the selected minor and trace elements when all the chemical elements could theoretically occur.

The chapter is divided in two parts: the first one deals with raw meals laboratory furnace thermal treatments and with the mineralogical and chemical characterization of the obtained clinkers by *ex situ* XRPD and electron microprobe analyses; the second one concerns a temperature-resolved *in situ* synchrotron XRPD experiment, taking into account three different chlorine concentrations within the same minor-elements doped raw meals.

4.2 *Ex situ* experiments

4.2.1 Experimental procedure

Samples preparation

Raw meals were prepared starting from an industrial raw mixture matching the chemical requirements for OPC clinker production, as confirmed by its bulk chemical analysis, reported in Table 4.1.

Sample	SiO ₂	Al ₂ O ₃	Fe ₂ O ₃	CaO	MgO	SO ₃	K ₂ O	Na ₂ O	TiO ₂	P ₂ O ₅	Mn ₂ O ₃	L.o.I.	Total
Industrial raw mixture < 75 μm	13.75	3.28	1.95	42.20	0.64	0.20	0.59	0.09	0.19	0.09	0.09	35.80	98.87

Table 4.1: Chemical composition (wt%) of the industrial raw mixture, as determined by WD-XRF analysis.

Four different doped raw meals were prepared by adding minor elements compounds, once characteristics moduli have been fixed to LSF = 97, SR = 2.5 and AR = 1.5. Certified chemical reagents were used as minor elements carriers, in particular: Na₂CO₃ (> 99.5 wt%, Merck Millipore), MgCO₃ (> 99.0 wt%, BDH) and CaSO₄*2H₂O (> 99.0 wt%, Fluka). Reagents were previously dried out, except for gypsum, in an electrical laboratory oven for 20 hours at 60 °C to remove moisture and attain a constant weight. Analytical reagents rather than natural raw materials were employed to be in full control on the actual concentration of each minor element, without adding further variables to the studied systems.

Table 4.2 reports the composition of each doped raw meal, expressed as components weight percentage; all the components were previously powdered below 80 μm. Calcium carbonate (> 99.0 wt%, Merck Millipore) has to be also added in *raw meals 1* and *2* to balance the calcium excess in *raw meals 3* and *4* due to calcium sulphate addition as sulphur carrier, in order to keep the same characteristic moduli in all the raw meals.

Raw meal	Raw mixture*	CaSO ₄ *2H ₂ O	MgCO ₃	Na ₂ CO ₃	CaCO ₃
1	99.16	0.00	0.02	0.00	0.82
2	95.70	0.00	2.96	0.55	0.79
3	98.05	1.36	0.04	0.55	0.00
4	95.66	1.35	2.98	0.01	0.00

Table 4.2: Composition of the doped raw meals (wt%). *Raw mixture = limestone + clay.

Raw meal 1 is the reference without any addition of doping elements, *raw meal 2* is enriched in magnesium and sodium, *raw meal 3* in sulphur and sodium and *raw meal 4* in sulphur and magnesium. These raw meals were separately added with the 1.0 wt% of CaF₂ (99.5 wt%, Fluka) or CaCl₂*2H₂O (> 99.5 wt%, Fluka) or respectively, obtaining additional eight raw meals.

Raw meal were finally homogenised in an automatic shaker for 2 hours and pelletized to ease the contact between particles and guarantee the optimal reactivity during the thermal treatment.

Table 4.3 recaps the twelve investigated raw meals.

Raw meal 1	Raw meal 2	Raw meal 3	Raw meal 4
Raw meal 1F	Raw meal 2F	Raw meal 3F	Raw meal 4F
Raw meal 1C	Raw meal 2C	Raw meal 3C	Raw meal 4C

Table 4.3: Labelling of the thermally treated raw meals. F = fluorine, C = chlorine.

Firing cycle

Pellets were initially calcined in a muffle furnace at 950 °C for 45 minutes to fully destabilize carbonates and avoid carbon dioxide release during the firing cycle. Photometric titrations to assess the fluorine and chlorine content on the calcined material confirmed that both elements have not yet volatilized at $T = 950$ °C.

Pre-calcination was necessary because the pellets underwent the thermal treatment sealed into platinum crucibles, to suppress elements evaporation. An eventual late carbon dioxide release within the sealed crucibles will lead to inner pressure increase, lid opening and light elements escape from the system. Moreover, crucibles were completely filled by raw meals pellets to reduce as much as possible the air volume and the sealing material consisted of the same powders inside the crucible. Crucibles configuration during the thermal treatment is pictured in Figure 4.1, whereas Figure 4.2 reports the thermal treatment heating ramp, achieved by Carbolite RHF 16/35 electrical furnace. At the end of the firing cycle, after a 45 min soaking time at 1450 °C, crucibles were drawn from the furnace and quenched with a room temperature air flow.



Figure 4.1: Platinum crucible configuration during the laboratory furnace thermal treatments.

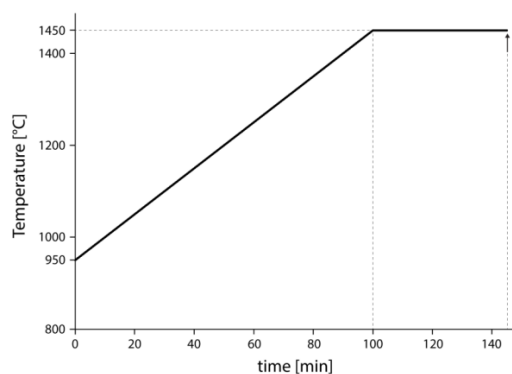


Figure 4.2: Visual representation of the firing cycle heating ramp. The arrow indicates when samples were drawn from the furnace.

Data collection and instrumental setups

Ex situ XRPD patterns on clinkers samples were collected by Bruker D8 Advance diffractometer, using Cu-K_{α1} radiation. The angular window between 5 and 80° 2 θ was explored, with a step-size of 0.02° 2 θ and a 0.04 seconds counting time. The qualitative analysis was performed by PANalytical X'Pert Highscore, whereas quantitative phase analysis results were carried out by the full profile Rietveld method implemented in the Topas Academic 5.1 software.

Clinkers obtained from chlorine or fluorine doped raw meals were also investigated by electron microprobe. Spot analyses results on silicate phases are accurate due to sufficient crystal dimensions; on the contrary, the ones on the interstitial phases are unreliable due to these crystals too low mean dimensions, around 1 μm , leading to contamination from the neighbours crystals. Complete electron microprobe analysis results are reported in Appendix B1.

4.2.2 Results and discussion*Reference clinkers*

Table 4.4 reports the quantitative phase composition of reference clinkers obtained by thermally treating the four raw meals without chlorine or fluorine. For clarity, clinker samples are addressed as *clinker_x*, where *x* indicates the starting raw meal; as an example, *clinker_1* is the clinker produced by the thermal treatment of raw meal 1.

Phase	<i>clinker_1</i> (reference)	<i>clinker_2</i> (Mg-Na)*	<i>clinker_3</i> (S-Na)*	<i>clinker_4</i> (S-Mg)*
C ₃ S-M1	26.4(6)	15.7(6)	22.4(5)	23.1(6)
C ₃ S-M3	32.2(9)	44.6(8)	32.2(7)	36.4(8)
β -C ₂ S	9.7(4)	8.2(3)	17.6(5)	18.4(7)
α' -C ₂ S	14.3(4)	10.7(6)	9.9(5)	4.4(3)
C ₃ A cubic	5.1(3)	0.2(1)	6.9(4)	2.6(3)
C ₃ A orthorhombic	0.8(2)	7.3(2)	0.0(0)	0.0(0)
C ₄ AF	9.3(4)	9.2(3)	7.4(3)	11.9(4)
CaO	1.8(2)	1.5(2)	3.4(2)	1.5(1)
Ca(OH) ₂	0.3(1)	0.5(2)	0.1(1)	0.0(0)
MgO	0.1(0)	2.1(1)	0.1(0)	1.7(1)

Table 4.4: Quantitative phase analysis results (wt%) on clinkers sintered starting from reference raw meals, obtained by processing *ex situ* XRPD data by the Rietveld method. * combination of doping elements within the raw meal.

From a preliminary data analysis, it can be stated that the clinkering conditions were appropriate, since all the samples exhibit the standard crystalline phases assemblage, independently from the minor elements combination. In particular, alite is the predominant phase, followed by belite and aluminates. As secondary phases, free lime occurs in all the clinkers regardless the minor elements combination, whereas periclase only in clinkers obtained from magnesium-doped raw meals. However, both these secondary phases are within their admissible limit in a commercial OPC clinker (UNI EN 197-1).

Finally, sulphate and alkaline phases cannot be detected in any clinker because sulphur and alkalis, at these concentrations, are completely incorporated by the main clinker phases. Nevertheless, some sulphur likely escaped the system despite employing sealed crucibles.

On the contrary, minor elements affect the weight fraction of clinker phases and their polymorphism.

Tricalcium silicate weight fraction does not experience strong variations between the different clinkers (Figure 4.3), exhibiting the highest values in *clinker_2* and *clinker_4*, both from magnesium-doped raw meals. C₃S incorporates magnesium in its structure by the Mg²⁺ - Ca²⁺ substitution, allowing more calcium to be available in the liquid phase to form further C₃S. Moreover, magnesium also partially hinders the C₃S dissociation into C₂S and CaO down on cooling (Taylor, 1990).

The highest C₃S wt% value is detected in *clinker_2* obtained from the raw meal where magnesium is coupled to sodium. Magnesium increases the C₃S formation by lowering its appearance temperature and speeding up the clinkering reactions, whereas sodium acts as flux, lowering the appearance temperature and the viscosity of the melt (Ludwig and Zhang, 2015).

Sulphur, despite being a flux too, does not raise the C₃S wt% because it is a C₂S mineraliser and also eases the C₃S dissociation into C₂S and CaO during the cooling stage (Bonafous et al., 1995). That justifies the overall similarity between the C₃S wt% in *clinker_1* and *clinker_4*, because in this latter the effects of magnesium and sulphur reciprocally balance.

Conversely, the lowest C₃S wt% is detected in *clinker_3*, where sodium and sulphur are coupled in the raw meal. They both are C₂S mineralisers and do not enter significantly the C₃S structure (Kurdowski, 2014).

Concerning the phase polymorphism (Figure 4.3), it is mainly driven by the value of the MgO to SO₃ ratio within the raw meal: high values favour the M3 form, low values the M1 (Maki and Goto, 1982). *Clinker_2* has the lowest M1/M3 ratio, because it was obtained from a raw meal high in magnesium and low in sulphur. *Clinker_4*, from the sulphur- and magnesium-doped raw meal, has a less pronounced M3 wt% than *clinker_2* when compared with *clinker_1*. Finally, low values of MgO/SO₃ in the *raw meal 3* determine a M1 increase in *clinker_3* compared with *clinker_2*, without however inverting the M1/M3 ratio, likely due to the occurrence of other minor elements in the raw mixture (limestone + clay minerals).

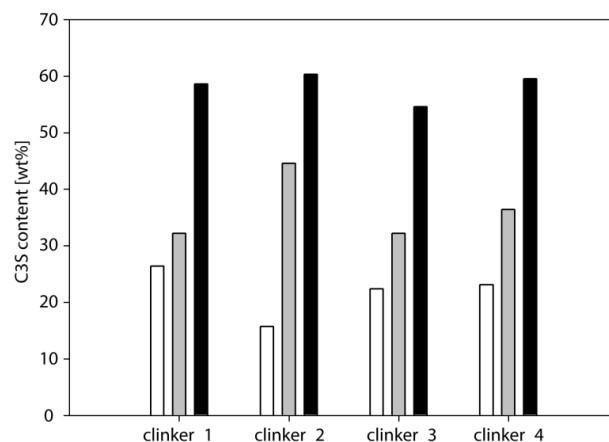


Figure 4.3: M1 (white bars) and the M3 (grey bars) C₃S polymorphs weight fraction and their sum (black bars) in clinkers obtained from the four reference raw meals, as determined processing XRPD data by the Rietveld method.

Dicalcium silicate absolute weight fraction does not move excessively between all clinkers, except dealing with *clinker_2*. Here, the C_2S wt% remarkably decreases because magnesium and partially sodium are both fluxes and the former also a C_3S mineraliser; they both increase the C_3S wt% and also hinder its dissociation during the cooling stage (Ludwig and Zhang, 2015). Conversely, C_2S formation is promoted in *clinker_3*, from a raw meal doped with sulphur and without added magnesium, as found by Li et al. (2014).

Sulphur appears as the minor element mostly affecting the C_2S polymorphism, favouring the β form, confirming the findings by Staněk and Sulovský (2012). *Clinker_3* and *clinker_4*, from sulphur-doped raw meals, exhibit the β form as the most occurring one; this effect is weakened by sodium occurrence in the raw meal, as for *clinker_3*, because sodium partially replaces calcium in the α' form structure, stabilizing it.

On the contrary, in *clinker_1* and *clinker_2* where no sodium occurs, the prevalent polymorph is the α' . Figure 4.4. summarises results concerning C_2S weight fraction and polymorphism in the four reference (without any fluorine or chlorine) clinkers.

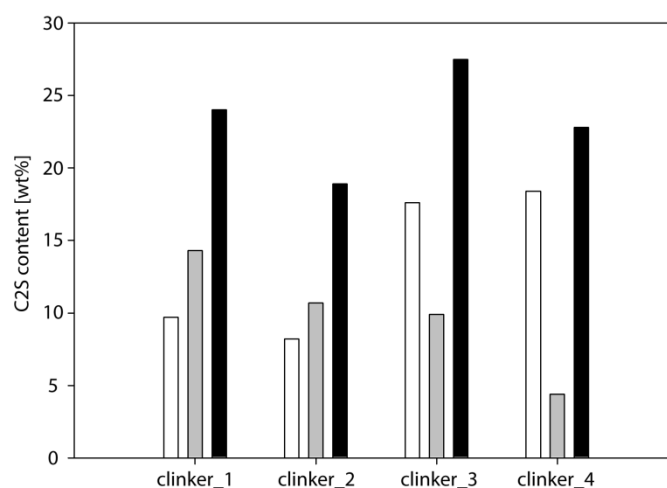


Figure 4.4: β (white bars) and α' (grey bars) C_2S polymorphs weight fractions and their sum (black bars) in clinkers obtained from the four reference raw meals, as determined processing XRPD data by the Rietveld method.

Dealing with interstitial aluminate phases, C_3A weight fraction attests on similar values in *clinker_1*, 2 and 3, whereas a significant decrease is detected only in *clinker_4*. This confirms the findings by Horkoss et al. (2011), affirming that high values of the sulphates to alkalis ratio, such as in *raw meal 4*, promote a C_3A decrease. Magnesium and sulphur are indeed ferrite stabilizers, because they can replace Fe^{3+} and Ca^{2+} in the C_4AF structure, easing thus its crystallization to C_3A detriment (Ludwig and Zhang, 2015). In particular sulphur, by stabilizing C_2S also reduce the available aluminium fraction, leading to an aluminium-depleted melt fraction causing the consequent C_3A wt% decrease; available aluminium concentration is lowered because of the $2Al^{3+} + S^{6+} = 3Si^{4+}$ substitution.

From literature (Takeuchi et al., 1980), sodium stabilises orthorhombic C_3A , as confirmed by *clinker_2*. On the contrary, in *clinker_3* the stabilizing effect of sodium on the orthorhombic form is completely hindered by sulphur, as highlighted by the occurrence of only the cubic form (Figure 4.5). This because sulphur, stabilizing the α' - C_2S , allows sodium to also enter its structure, reducing the amount available to stabilize the orthorhombic C_3A . Moreover, C_3A usually crystallizes on cooling,

when C_2S is already formed. This hypothesis was confirmed by microprobe analysis on clinkers from fluorine- and chlorine-doped raw meals.

On the contrary, sodium has an opposite behaviour concerning C_4AF compared with sulphur, since in *clinker_3* there is a decrease of the C_4AF wt% (Figure 4.6). Sodium replaces calcium in C_3A indeed, easing its stability and allowing thus C_4AF to increase only in clinkers from sodium-free raw meal, such as in *clinker_4*.

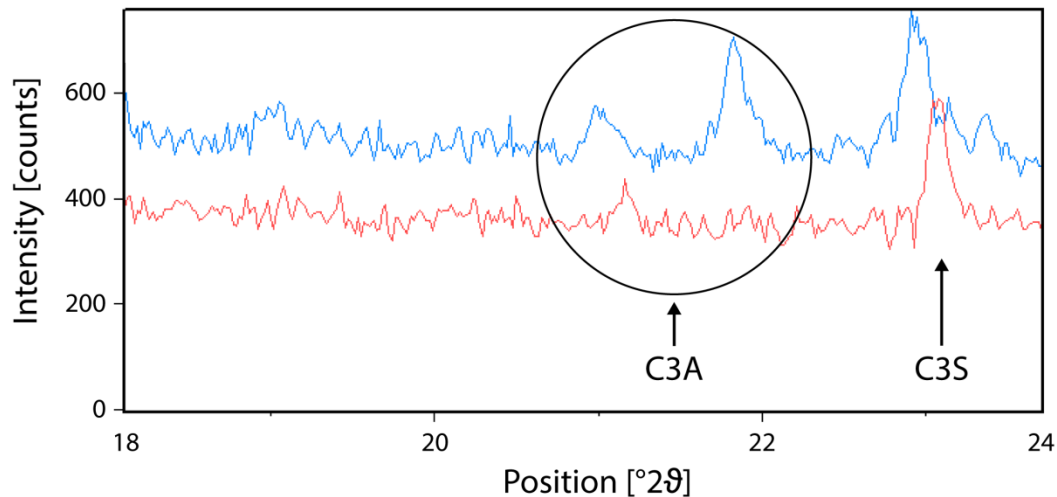


Figure 4.5: Visual comparison between *clinker_2* (red) and *clinker_3* (blue) XRPD patterns in the 18-24° 2 θ diagnostic window to identify C_3A polymorphs. Cubic C_3A has a diffraction peak at ~22° 2 θ and a less intense one at ~21° 2 θ , whereas orthorhombic C_3A does not exhibit the peak at ~22° 2 θ . Positions using copper radiation.

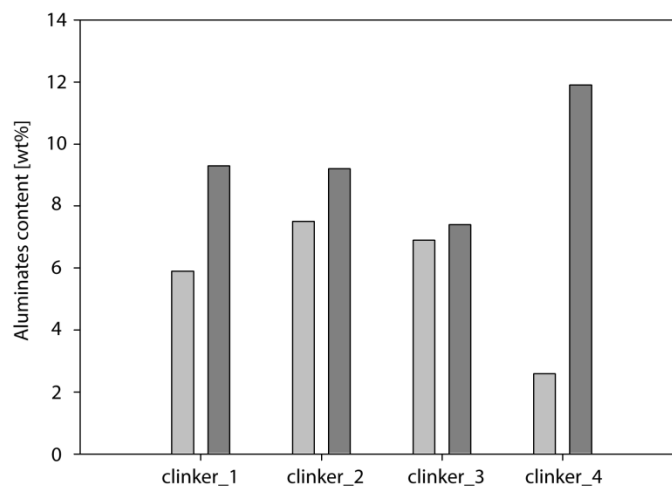


Figure 4.6: C_3A (light grey bars) and C_4AF (dark grey bars) weight fraction in clinkers obtained from the four reference raw meals (without fluorine or chlorine), as determined processing XRPD data by the Rietveld method.

Finally focusing on minor and secondary phases, free lime weight content attests on nearly the same values in *clinker_1*, *clinker_2* and *clinker_4*, whereas a slightly higher value is pointed out by *clinker_3*, however below the admissible limits (UNI EN 197-1).

Periclase occurs in a significant amount only in *clinker_2* and *clinker_4*, the ones obtained starting from magnesium-doped raw meals. Further secondary phases are not detected, as previously stated.

Fluorine-doped raw meals

Table 4.5 reports the quantitative phase composition of clinkers obtained by the thermal treatment of the four fluorine-doped raw meals.

For the sake of clarity, similarly as clinkers from reference raw meals, samples will be addressed as *clinker_xF*, where *x* indicates the starting reference raw meal and *F* the fluorine addition; as an example, *clinker_1F* is the clinker obtained by the thermal treatment of reference raw meal 1 doped with 1.0 wt% of calcium fluoride.

Phase	<i>clinker_1F</i>	<i>clinker_2F</i>	<i>clinker_3F</i>	<i>clinker_4F</i>
C ₃ S-M1	32.2(7)	19.6(8)	24.4(6)	25.0(7)
C ₃ S-M3	37.2(7)	51.7(9)	44.3(7)	42.9(9)
β-C ₂ S	15.2(5)	11.2(4)	15.6(6)	13.1(5)
α'-C ₂ S	0.1(0)	0.9(2)	0.0(0)	2.3(3)
C ₃ A cubic	1.3(2)	1.0(2)	1.6(2)	0.9(2)
C ₃ A orthorhombic	0.0(0)	0.0(0)	0.0(0)	0.0(0)
C ₄ AF	12.1(5)	13.2(4)	12.5(4)	13.1(3)
CaO	1.2(2)	1.4(1)	1.3(2)	1.3(2)
Ca(OH) ₂	0.3(1)	0.2(1)	0.3(1)	0.0(0)
MgO	0.4(1)	0.8(1)	0.0(0)	1.4(2)

Table 4.5: Quantitative phase analysis results (wt%) on clinkers sintered starting from reference raw meals added with 1.0 wt% of calcium fluoride, obtained processing *ex situ* XRPD data by the Rietveld method.

These results, compared to the ones obtained on clinkers from reference raw meals, immediately point out a significant increase of the C₃S wt%, as expected (Figure 4.7). This increase is independent from the minor elements combination in the raw meal, being exclusively due to fluorine acting both as a flux and as a C₃S mineraliser (Klemm et al., 1979). Moreover, *clinker_2F*, obtained starting from the magnesium and sodium doped raw meal, exhibits the highest C₃S wt% because also magnesium enhances the C₃S formation (Ludwig and Zhang, 2015). However, this absolute variation is slight, suggesting that the mineralizing effect of fluorine is order of magnitude stronger than the one of magnesium.

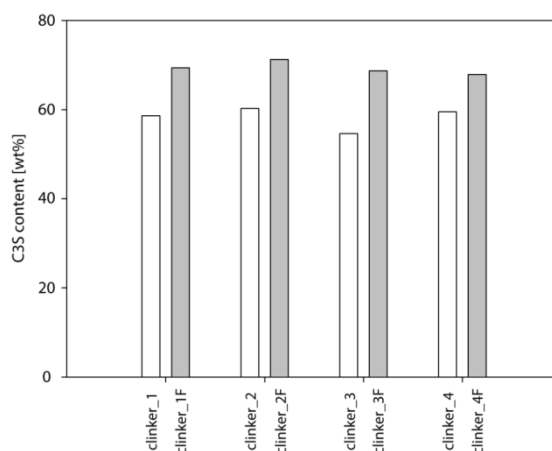


Figure 4.7: C₃S content (wt%) comparison between clinkers obtained from reference raw meals (white bars) and from fluorine-doped raw meals (light grey bars), as determined processing XRPD data by the Rietveld method.

Concerning C_3S polymorphism, fluorine alone stabilizes the M1 form, as evinced from the increase of the M1 to M3 ratio in *clinker_1F* compared with *clinker_1* (Figure 4.8). In clinkers from raw meals where fluorine occurs together with sulphur, a further increase of the M1 to M3 ratio would be reasonably expected because of the stabilizing effect on M1 of sulphur (Maki and Goto, 1982). On the contrary, this M1 to M3 increase actually happens only when comparing *clinker_2F* with *clinker_2*, where sulphur does not occur. This is a prove that minor elements effects are not simply additive, but often interact between them, suggesting that each minor elements combination should be investigated separately.

In *clinker_2F* the M1 form decreases compared to *clinker_1F*, but increases compared to *clinker_2*, supporting a stabilizing effect of fluorine on the M1 polymorph.

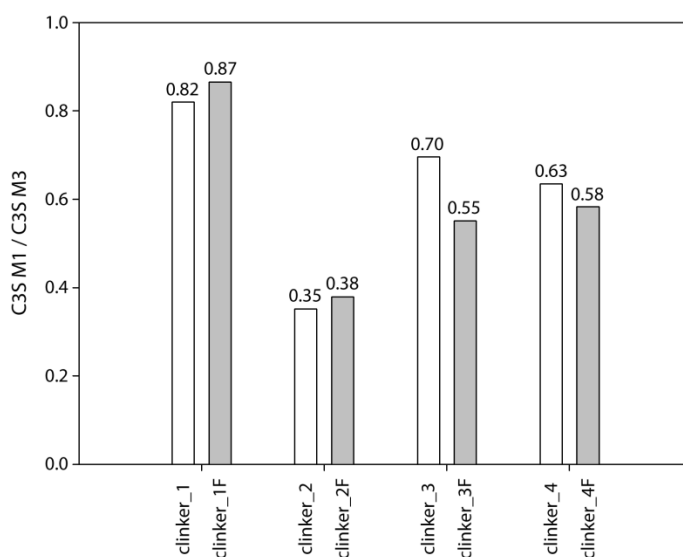


Figure 4.8: Ratio between C_3S M1 and C_3S M3 in clinkers obtained from reference raw meals (white bars) and from fluorine-doped raw meals (grey bars).

Microprobe analyses confirmed the fluorine mineralizing effect on C_3S due to the $F^- + Al^{3+} = O^{2-} + Si^{4+}$ substitution (Tran, 2011). Figure 4.9 reports the partitioning of fluorine between C_3S and C_2S carried out from electron microprobe spot analyses, highlighting that fluorine is strictly incorporated only in the C_3S structure, independently from the minor elements combination. As a consequence, the mean chemical composition of C_3S from *clinker_1F* is fluorine- and aluminium-enriched and silicon-depleted, when compared to the benchmark C_3S composition reported in Taylor (1990). This justifies the general decrease of the tricalcium aluminate: in particular C_3A attests nearly on ~ 1 wt%, because less aluminium is available for its structure.

The preference of a given oxide between two phases is determined by plotting the oxide wt% in both phases on an xy Cartesian plane, where x-axis corresponds to phase a and y-axis to phase b . Then an $y = x$ straight line is plotted on the graph; if the point determined by the intersection of the oxide wt% in phase a and b falls below this line, the oxide has a preference for phase a , vice versa for phase b . Obviously, a point lying on the straight line has no preferential partitioning between the two phases.

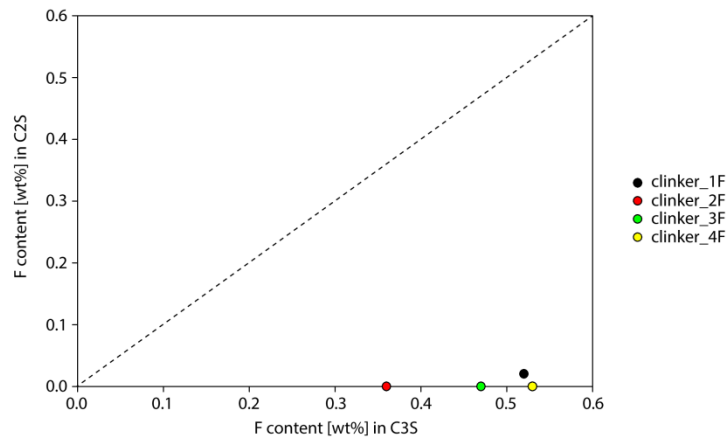


Figure 4.9: Partitioning of fluorine between C_3S and C_2S , as determined by electron microprobe analyses (wt%). Each single marker represents the mean value carried out from a series of sixteen spot analyses per phase.

Magnesium is the only other minor element occurring in the investigated raw meals having a significant preference for C_3S (Figure 4.10a), whereas the aluminium preference for C_3S is weak, being significant only in *clinker_4F* (Figure 4.10b). Aluminium slightly enters the C_3S structure because it takes part with fluorine to the $F^- + Al^{3+} = O^{2-} + Si^{4+}$ substitution to guarantee the electroneutrality. These correlations are valid despite the standard deviation values because these standard deviation values are similar between different clinkers.

Figure 4.11 shows the Ca and Mg atomic ratio in C_3S ; it can be noted that in *clinker_2F* and *clinker_4F*, both from Mg-doped raw meals, a calcium decrease is observed in correspondence to a magnesium increase, as a consequence of the $Mg^{2+} - Ca^{2+}$ substitution. This proves that magnesium effectively replace calcium in the C_3S structure.

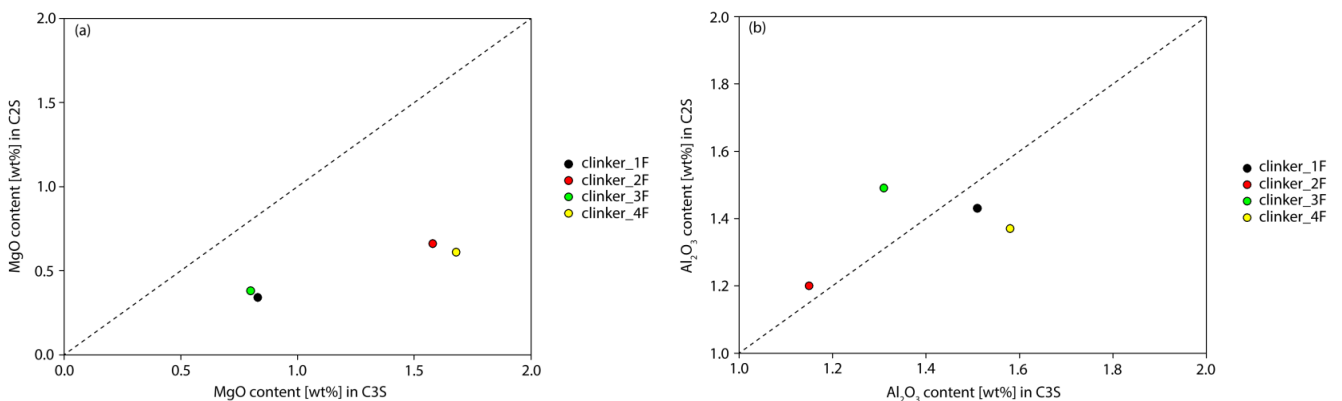


Figure 4.10: MgO (a) and Al_2O_3 (b) distribution (wt%) between C_3S and C_2S , as determined by electron microprobe analyses. Each single marker represents the mean value carried out from a series of sixteen spot analyses per phase.

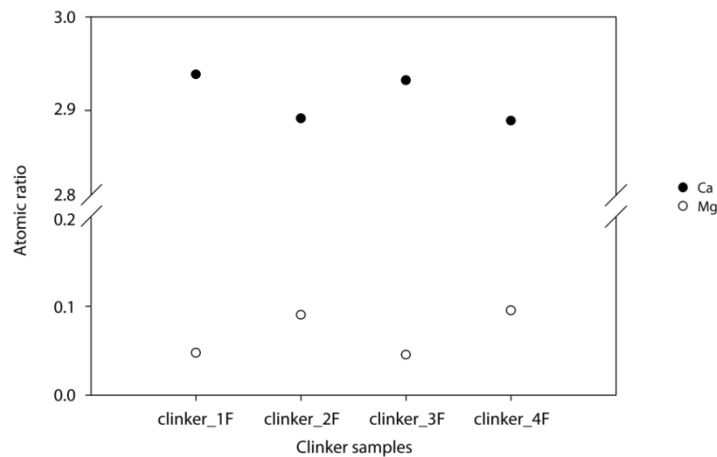


Figure 4.11: Calcium (black circles) and magnesium (white circles) atomic ratio in C_3S crystals within clinkers obtained from fluorine-doped raw meals.

Taking into account the elements mainly partitioning in the C_3S structure (fluorine, magnesium and aluminium), it was also investigated if they have a preferential distribution between different types of C_3S crystals. In details, C_3S crystals with or without C_2S inclusions and clustered or single C_3S crystals surrounded by the aluminates matrix were considered. The selection between the different kinds of crystals was visually made on backscattered scanning electron microscopy images. Figure 4.12 illustrates the different C_3S crystals. Obviously, a crystal may belong to different categories; as an example a clustered crystal can or cannot have C_2S inclusions.

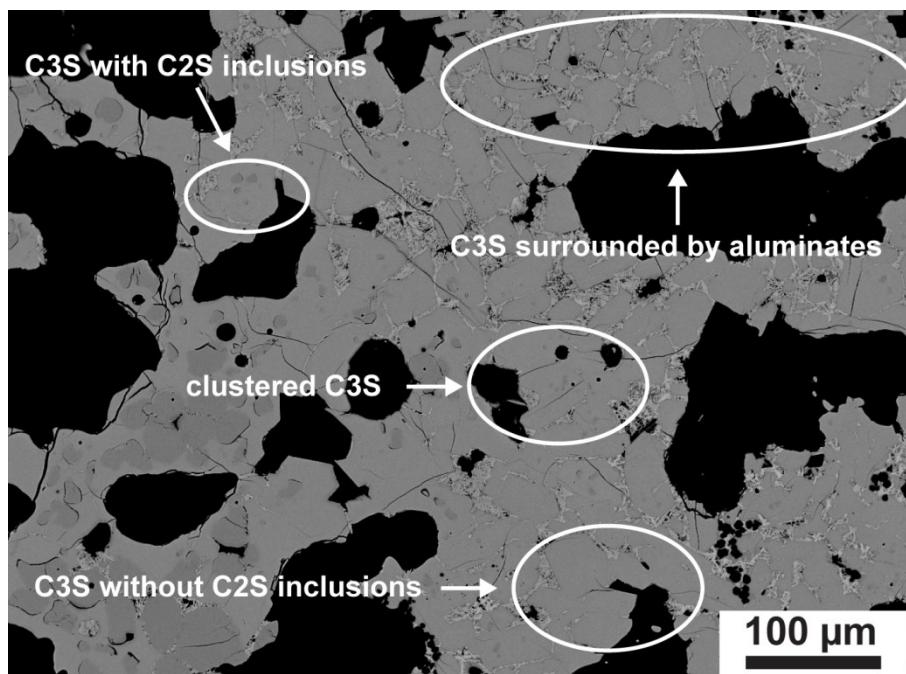


Figure 4.12: *Clinker_2F* SEM image pointing out the different considered types of C_3S crystals.

Magnesium (Figure 4.13a-b) shows no preferred distribution between different types of C_3S crystals. On the contrary, aluminium (Figure 4.13c-d) has a slight preference for crystals without C_2S inclusions and crystals surrounded by aluminates; these crystals are likely the ones which better reacted during the thermal treatment, in particular the ones without the C_2S inclusions. The same even more marked for fluorine, indicating these crystals as the better mineralised (Figure 4.13e-f) and again confirming the aluminium affinity for fluorine.

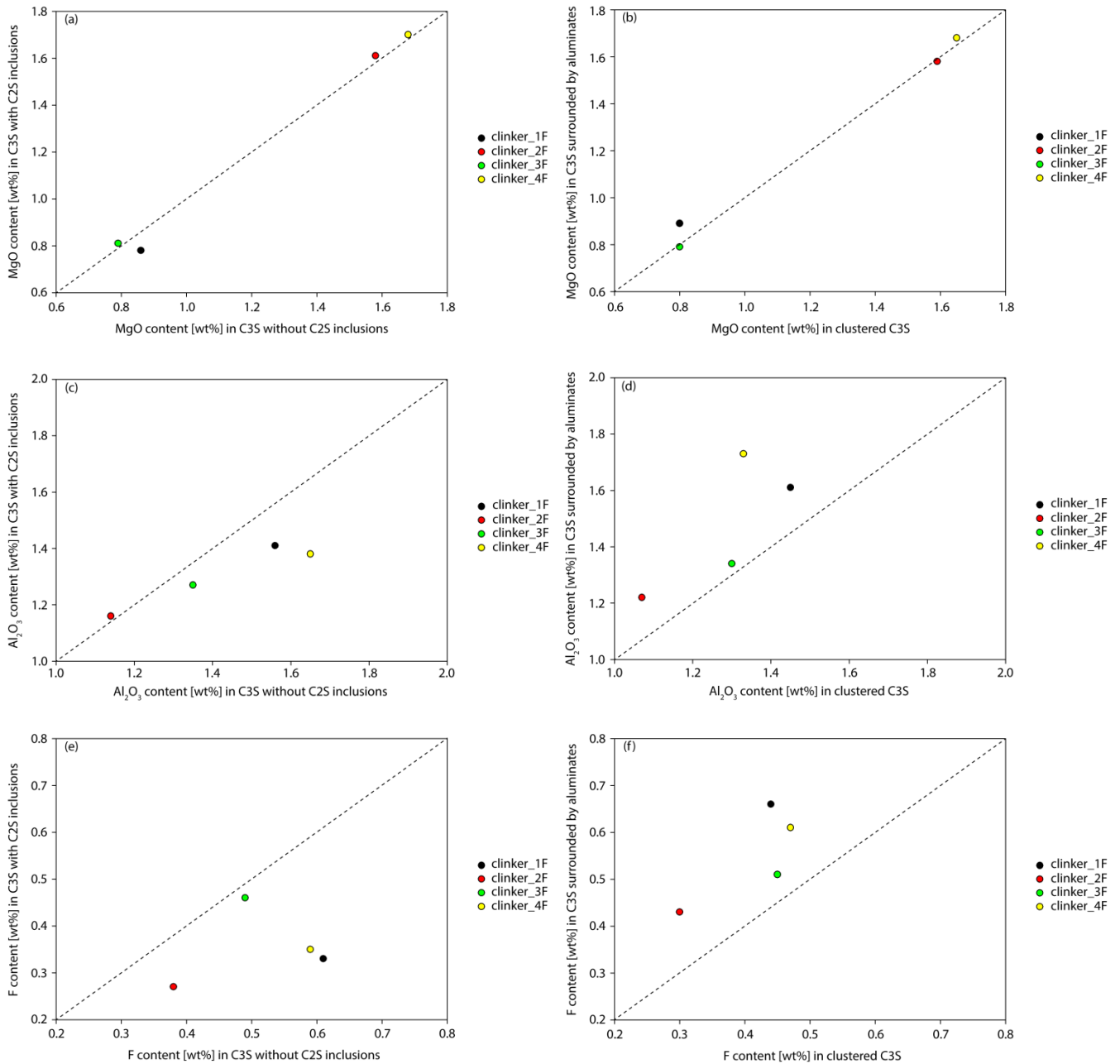


Figure 4.13: Partitioning of magnesium (a, b), aluminium (c, d) and fluorine (e, f) between different types of C_3S crystals, as determined by electron microprobe analyses (wt%).

Drawing the attention to C_2S , it can be observed that its overall weight fraction decreases in all clinkers (Figure 4.14), as a consequence of the C_3S increase by the mineralising effect of fluorine. The lowest values is found in *clinker_2F* obtained thermally treating the raw meal doped with magnesium and without sulphur, whereas the strongest decrease happens switching from *clinker_3* to *clinker_3F*, both from the raw meal high in C_2S mineralisers (sulphur and secondary sodium). Concerning the polymorphism, fluorine occurrence in the raw meals stabilizes mainly the β form, conversely with respect to clinkers from reference raw meals.

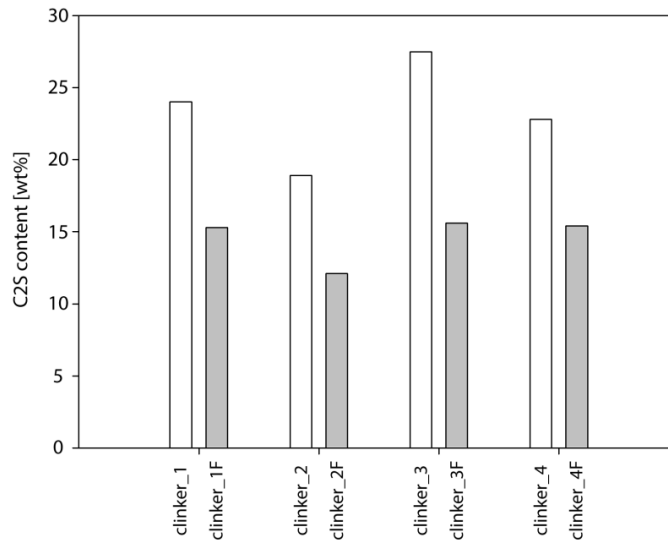


Figure 4.14: C_2S (wt%) content comparison between clinkers obtained from reference raw meals (white bars) and from fluorine-doped raw meals (light grey bars).

Microprobe analyses proved the marked preference of sulphur for the C_2S structure (Figure 4.15a); also alkalis (Figure 4.15b-c) and to a lesser extent iron (Figure 4.15d) have the same behaviour. Atomic ratios between sulphur, aluminium and silicon confirm the validity, even in fluorine-doped raw meals, of the $2Al^{3+} + S^{6+} \Leftrightarrow 3Si^{4+}$ substitution within the C_2S structure (Figure 4.16).

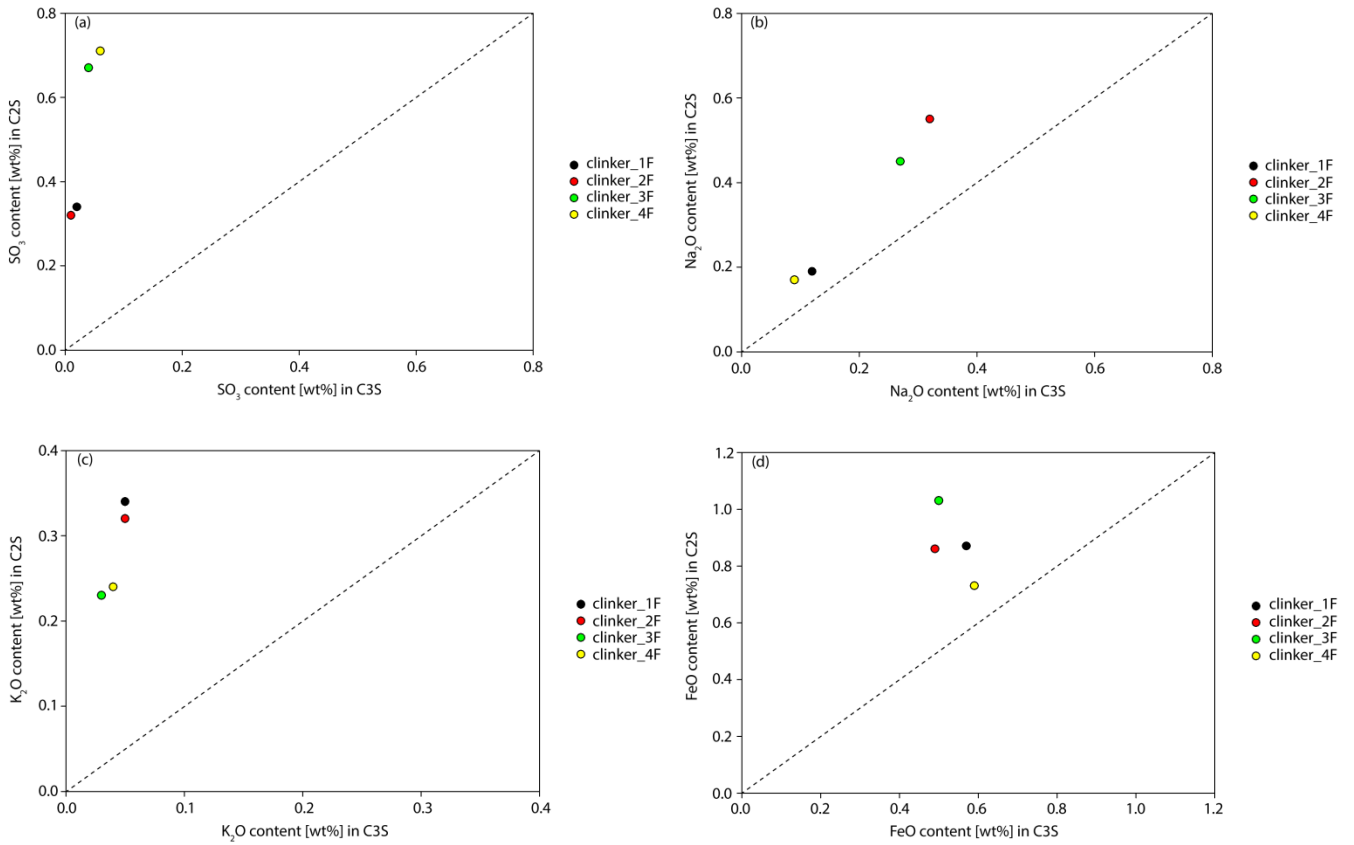


Figure 4.15: Partitioning of SO_3 (a), Na_2O (b), K_2O (c) and FeO (d) between C_3S and C_2S , as determined by electron microprobe analyses (wt%). Each single marker represents the mean value carried out from a series of sixteen spot analyses per phase.

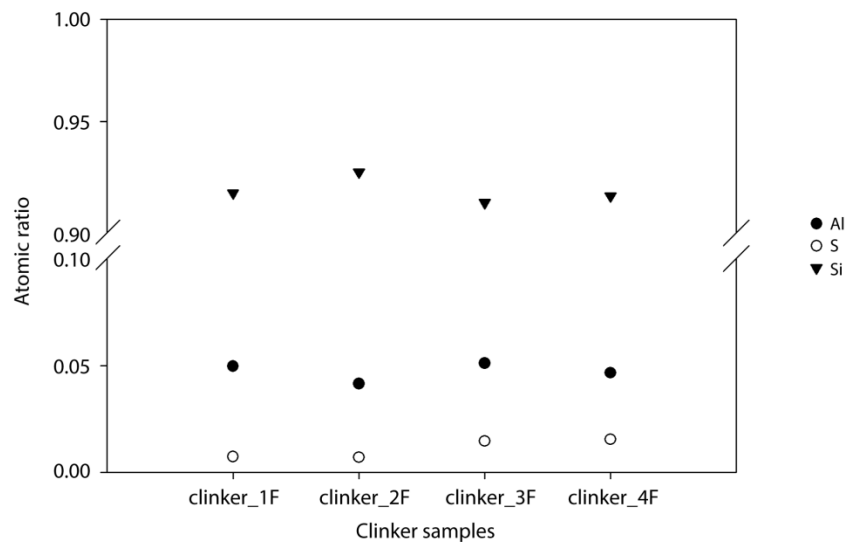


Figure 4.16: Al (black circles), S (white circles) and Si (black triangles) atomic ratios in C_2S crystals within clinkers obtained from fluorine-doped raw meals.

In the same way as C_3S , it was also evaluated if dealing with minor elements mostly entering the C_2S structure (sulphur, alkalis and iron), a partitioning between the different types of crystals can be found. Clustered and well-rounded C_2S crystals and C_2S inclusions within C_3S were considered (Figure 4.17).

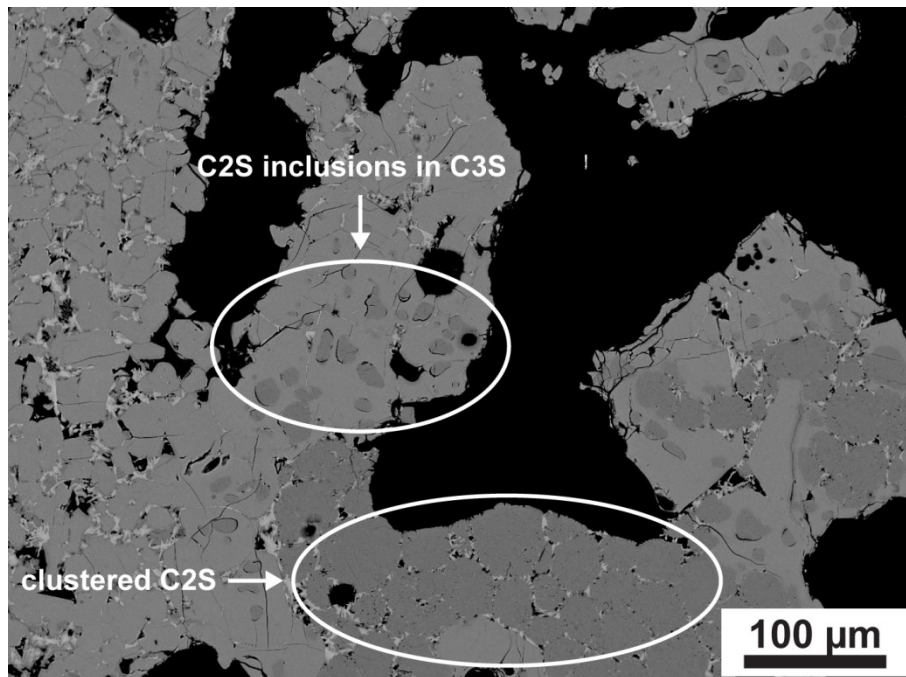


Figure 4.17: *Clinker_4F* SEM image pointing out clustered C_2S and C_2S inclusions in C_3S .

Sulphur (Figure 4.18) and to a lesser extent alkalis exhibit a weak preference for clustered C_2S instead of inclusions, in particular in *clinker_3F*, where only C_2S stabilisers are present jointly to the magnesium absence. Conversely, iron has no preferred distribution between the two types of crystals, except again *clinker_3F*.

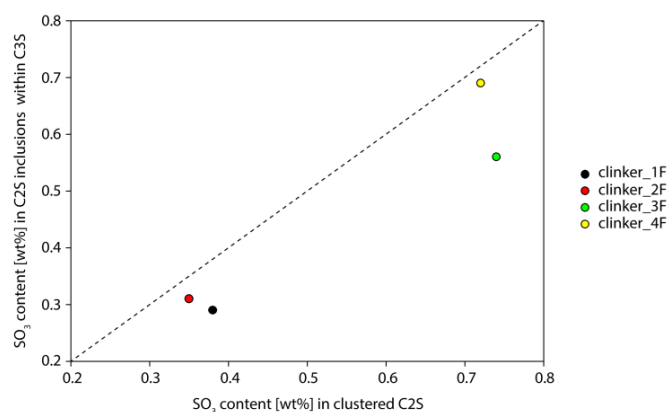


Figure 4.18: Partitioning of SO_3 between different types of C_2S crystals, as determined by electron microprobe spot analyses (wt%).

Finally, aluminates weight fraction attests on similar values in all clinkers. C_3A overall content is around 1 wt% and the effect of sodium in stabilizing the orthorhombic form is totally hindered; C_4AF attests between 12 and 13 wt% and its general increase compared to reference clinkers is a

consequence of the C_3A decrease and mainly to a marked mineralising effect of magnesium and sulphur (Ludwig and Zhang, 2015). Microprobe analyses on these interstitial phases are not reliable because of their small mean crystal sizes compared to the diameter of the analyser beam.

The mineralizing effect of fluorine has an impact on the free lime content, generally decreasing in all the clinkers obtained from fluorine-doped raw meals, as an indicator of a better reactivity of the mixtures (Figure 4.19a). Similarly, also periclase content decreases in *clinker_2F* and *clinker_4F*, the ones from magnesium-rich raw meals (Figure 4.19b).

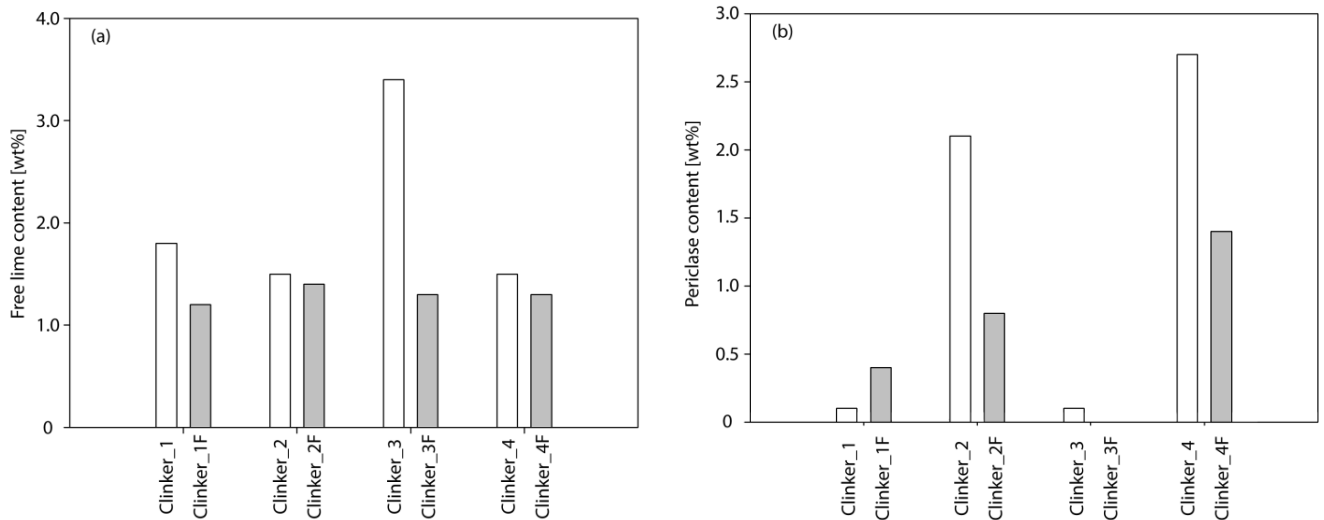


Figure 4.19: Free lime (a) and periclase (b) weight content comparison between clinkers obtained from reference raw meals (white bars) and from fluorine-doped raw meals (light grey bars), as determined processing XRPD data by the Rietveld method.

Chlorine-doped raw meals

Table 4.6 reports the quantitative phase composition of clinkers obtained by the thermal treatment of the four chlorine-doped raw meals.

Likewise for reference and fluorine-doped raw meals, clinkers will be addressed as *clinker_xC*, where *x* indicates the starting reference raw meal and *C* the chlorine addition; as an example, *clinker₁C* is the clinker obtained by the thermal treatment of reference raw meal 1 doped with 1.0 wt% of calcium chloride.

Phase	<i>clinker₁C</i>	<i>clinker₂C</i>	<i>clinker₃C</i>	<i>clinker₄C</i>
C ₃ S-M1	35.7(8)	21.5(5)	34.0(9)	28.7(7)
C ₃ S-M3	22.1(6)	32.3(7)	15.1(5)	21.7(7)
β-C ₂ S	24.3(5)	17.3(7)	24.3(5)	26.2(8)
α'-C ₂ S	2.4(2)	8.5(5)	10.7(6)	5.9(4)
C ₃ A cubic	2.2(2)	3.8(3)	2.8(4)	0.7(2)
C ₃ A orthorhombic	0.0(0)	0.8(2)	0.3(1)	0.0(0)
C ₄ AF	11.1(3)	11.2(3)	10.3(2)	12.7(4)
CaO	2.0(1)	2.9(2)	2.4(1)	2.3(2)
Ca(OH) ₂	0.2(1)	0.2(1)	0.0(0)	0.2(1)
MgO	0.0(0)	1.5(1)	0.1(1)	1.6(2)

Table 4.6: Quantitative phase analysis results (wt%) on clinkers obtained starting from reference raw meals added with 1.0 wt% of calcium chloride, as determined processing *ex situ* XRPD data by the Rietveld method.

Comparing *clinker₁* and *clinker₁C*, it can be observed that chlorine does not have a mineralizing effect on C₃S, since the absolute difference between the two clinker samples is below ~1 wt%. Similarly, even in clinker samples from the raw meals where chlorine is coupled with minor elements, no mineralizing effects on C₃S occurs; actually, a general C₃S wt% decrease can be observed, more marked when chlorine is associated with sulphur.

Taking into account the C₃S polymorphism, chlorine on its own stabilizes the M1 polymorph, as observed by the inversion of the M1/M3 ratio between *clinker₁* and *clinker₁C*. C₃S-M1 is also the prevailing polymorph in *clinker₃C* and *clinker₄C* where chlorine is coupled with sulphur, because they are both M1 stabilizers. Considering *clinker₂C*, the M1/M3 ratio decreases compared to *clinker₁*, but a further confirmation of the M1 stabilization by chlorine is given by comparing *clinker₂* and *clinker₂C*. In the former the M1/M3 ratio is 0.35, whereas in the latter increases up to 0.67; hence, chlorine balances the effect of sodium and magnesium, both C₃S-M3 stabilizers.

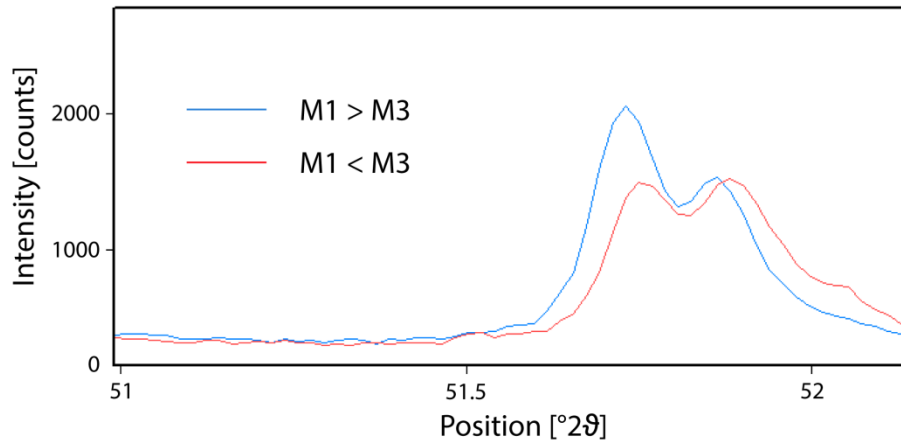


Figure 4.20: Visual comparison between *clinker_1* (red) and *clinker_1C* (blue) XRPD patterns in the 51-52° 2 θ diagnostic window to identify M1 and M3 C₃S polymorphs. Positions using copper radiation. For M1 > M3 the low-angle peak of the doublet is more intense than the high-angle one; for M3 > M1 both the peaks tend to the same intensity.

Figure 4.21 shows the C₃S polymorphism in clinkers from chlorine-doped raw meals, their sum and the comparison with the reference clinkers.

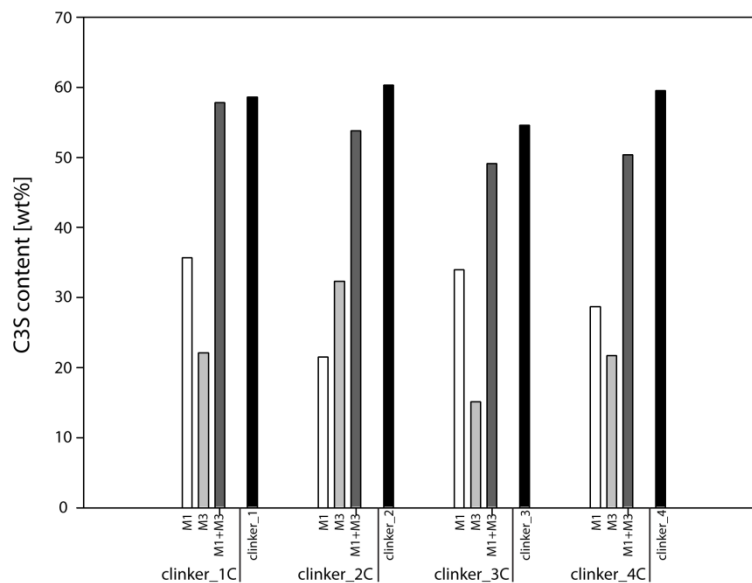


Figure 4.21: C₃S M1 (white bars) and M3 (light grey bars) in clinkers obtained from chlorine-doped raw meals, their sum (dark grey bar) and the sum comparison with the clinkers from reference raw meals (black bar).

Chlorine slightly increases the C₂S wt%, as evinced by comparing *clinker_1* and *clinker_1C*, where no additional minor elements occur. This mineralizing effect on C₂S is more evident when chlorine is coupled with other C₂S mineralizers such as sulphur and to a lesser extent sodium: *clinker_3C* is the one with the highest C₂S wt% indeed. Dealing with C₂S polymorphism, the beta form is the prevailing

one in all clinkers; however also the α' polymorph always occurs, especially in *clinker_2C* and *clinker_3C* where chlorine is coupled with sodium in the raw meals.

The overall C_3A weight fraction decreases in all the clinkers, in particular in *clinker_3C* due to the minor elements (sodium and sulphur) combination. The cubic form is the prevailing polymorph, whereas the orthorhombic form is below 1 wt% in all clinkers, regardless the sodium occurrence in the raw meals. This behaviour is a result of the alkalis volatilization, as confirmed by electron microprobe spot analyses.

C_4AF wt% increases weakly in all the clinkers, attesting on an overall ~11 wt%, presumably as a consequence of the general C_3A wt% decrease.

Minor phases, such as free lime and periclase, are not significantly affected by chlorine. Lime weight fractions in clinkers from chlorine-doped raw meals are similar to reference clinkers. This confirms the fact that even if chlorine enhances CaO reactivity and dissolution during the clinkering process (Mishulovich, 1994), a low free lime content in the final product would not be guaranteed. Periclase is detected only in *clinker_2C* and *clinker_4C*, the ones obtained from magnesium-doped raw meals independently from the chlorine addition.

Finally, no chlorine compounds occurs in any clinker, independently from the minor elements combination within the raw meals. Calcium chloride from the raw meals destabilize during the clinkering process releasing chlorine into the system; however the retained chlorine content within clinker phases is very low, as supported by microprobe analyses detailed below.

In fact, microprobe analyses proved a strong chlorine volatilization in all the four mixtures during the thermal treatment, independently from the minor elements combination. This upholds and extends the validity of the findings summarised in Taylor (1990) and Kurdowski (2014) according to which most of chlorine and its compounds do not leave the kiln system within the clinker, but volatilize earlier during the high-temperature stage. Chlorine weight concentration values within clinker phases carried out by spot chemical analyses are comparable to the chlorine general retained amount in clinkers reported by Bhatti (1995), below the 0.03 wt%. Little chlorine is detected only in the interstitial matrix of clinkers from alkalis-free raw meals (*clinker_1C* and *clinker_4C*); however it cannot be precisely determined which phase it enters, due to the too low mean size of interstitial phases to get a reliable spot chemical analysis. However, XRPD analyses did not detect any chlorine phase, so this limited chlorine amount has to be likely incorporated within the aluminates.

As already stated, the chlorine content after the calcination was assessed by photometric titrations, confirming that it had not already left the system. Hence, chlorine leaves the system during the high-temperature stage of the clinkerization process ($T = 950-1450$ °C).

Taylor (1990) and Mishulovich (1994) report that chlorine does not volatilize in the elemental form from the raw meal system, but it usually combines with alkalis to give alkali-chlorides. Therefore, alkalis content is now assessed to confirm these assumptions even in raw meals doped with minor elements.

Sodium content in silicate phases is lower in most of the clinker samples when compared with the ones from fluorine-doped raw meals. On the contrary, its average content in the interstitial aluminate phases slightly raises; however, this increase is not enough to balance the fraction not incorporated within the silicates, pointing out that some sodium has to be escaped from the system (Figure 4.22).

Potassium behaves in a very similar way, decreasing in both the silicate phases in clinkers from the chlorine-doped raw meals, compared with clinkers from fluorine-doped raw meals. Concerning the interstitial phases, potassium content remains nearly stationary. As in the case of sodium, some potassium has to leave the system during the high-temperature stage (Figure 4.23).

These results stress that the alkalis volatilization takes place in all the mixtures, independently from the minor elements combination. The absolute decrease is naturally more marked in *clinker_2C* and *clinker_3C*, obtained from sodium-doped raw meals.

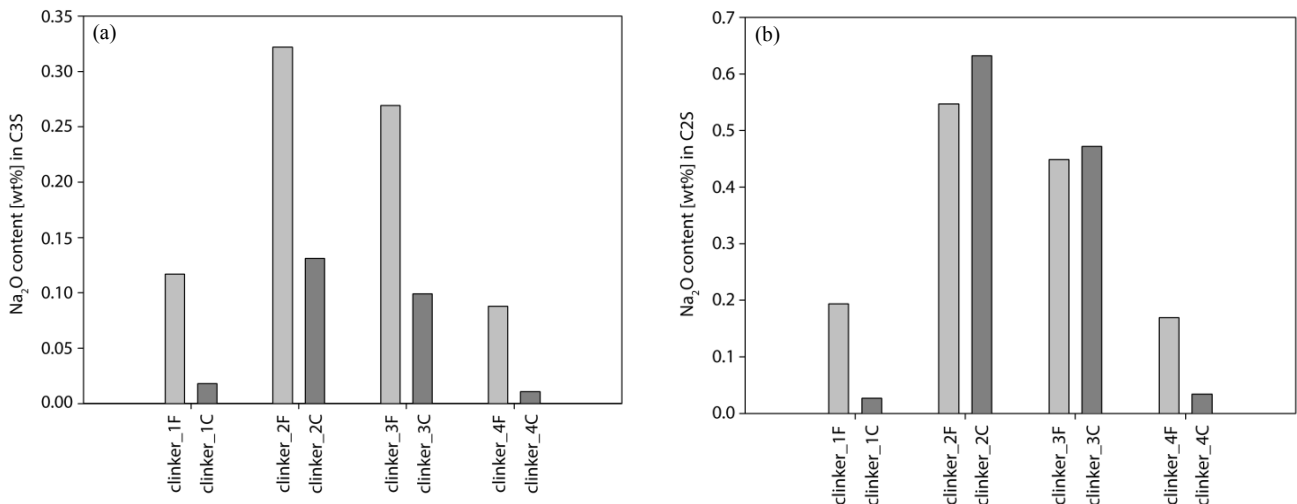


Figure 4.22: Na₂O content (wt%), as determined by microprobe spot chemical analyses, in C₃S (a) and C₂S (b) from fluorine- (light grey bars) and chlorine-doped (dark grey bars) raw meals.

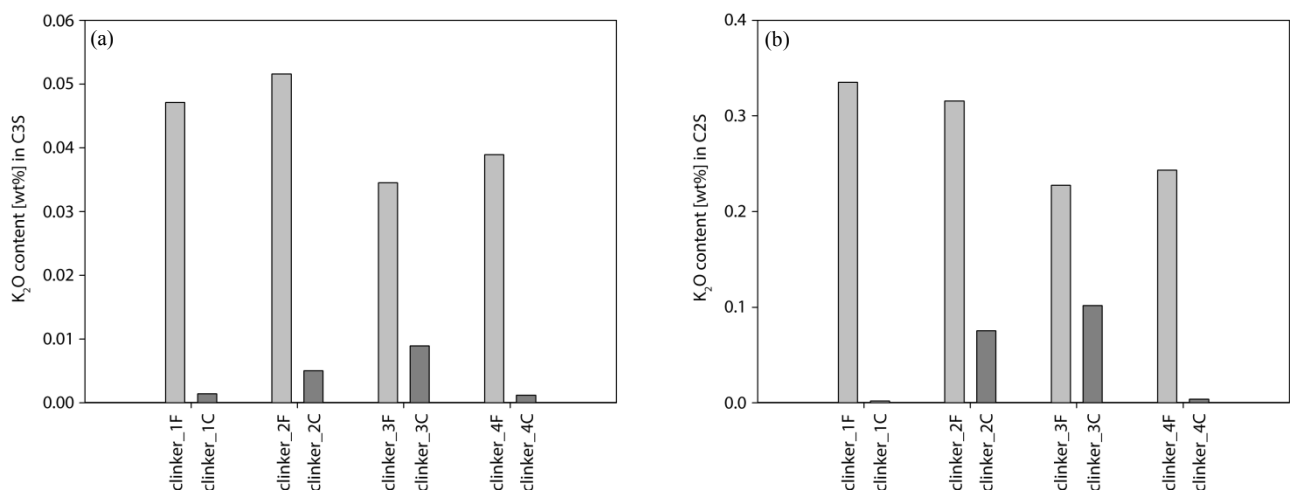


Figure 4.23: K₂O content (wt%), as determined by microprobe spot chemical analyses, in C₃S (a) and C₂S (b) from fluorine- (light grey bars) and chlorine-doped (dark grey bars) raw meals.

Taking into account the sulphur content, it increases in both silicate and aluminate phases comparing them with clinkers from fluorine-doped raw meals (Figure 4.24). Actually, chlorine addition indirectly reduces the volatilization of sulphur during the thermal treatment. This because sulphur usually combines with alkalis to form volatile alkalis sulphates that evaporate at the highest temperatures, removing thus from the system both sulphur and alkalis (Arceo and Glasser, 1990). However, in these investigated raw meals, alkalis already escaped from the system by combining with chlorine at lower temperatures. As a direct consequence, sulphur cannot combine with alkalis to give volatile phases and it is thus retained by the clinker system, mainly entering the C_2S structure and enhancing its weight fraction.

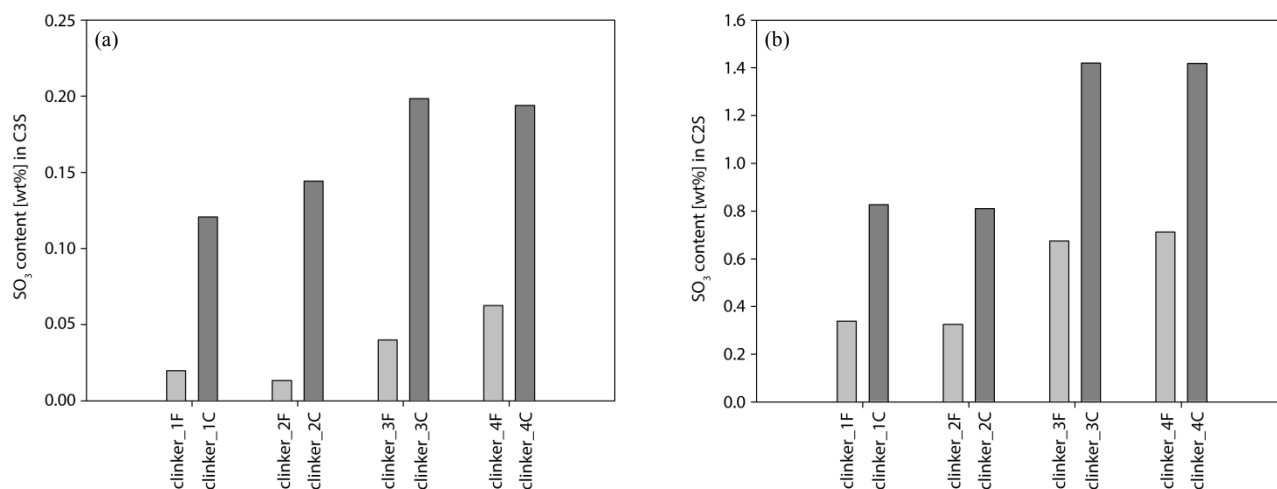


Figure 4.24: SO_3 content (wt%), as determined by microprobe spot chemical analyses, in C_3S (a) and C_2S (b) from fluorine- (light grey bars) and chlorine-doped (dark grey bars) raw meals.

The relatively large amounts of sulphur in the system allow to explain also the significant partitioning of aluminium within the C_2S structure, when compared with clinkers from chlorine-free raw meals where it does not show any noticeable preference between the two calcium-silicate phases. The reason lies in the fact that aluminium follows sulphur into the C_2S structure due to the $2Al^{3+} + S^{6+} = 3Si^{4+}$ replacement; this substitution is confirmed by an overall decrease of the silicon content in C_2S , partially replaced by aluminium and sulphur in fact (Figure 4.25).

Finally, magnesium is not affected by chlorine, since it still mainly enters the C_3S structure, as in clinkers from fluorine-doped raw meals. Moreover, the overall amount retained in silicate phases is slightly smaller, leading to a little increase concerning the periclase weigh fraction.

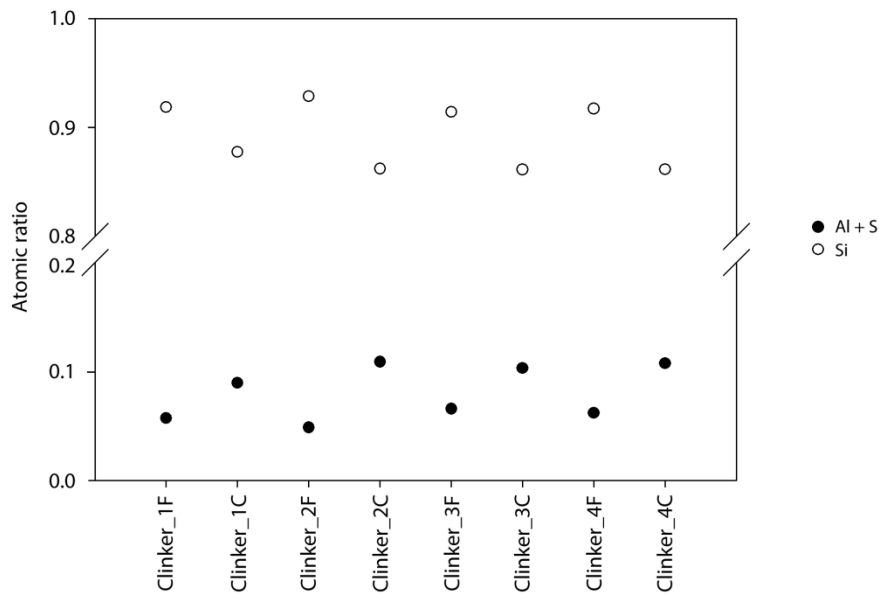


Figure 4.25: Al+S (black circles) and Si (white circles) atomic ratios in C₂S from clinkers obtained by thermally treating fluorine- and chlorine-doped raw meals.

As in the case of fluorine, it will be now investigated if minor elements significantly partitioning in a specific crystalline phase have a preference between different types of crystals. In particular, magnesium and sulphur will be considered, for C₃S and C₂S respectively.

C₃S crystals with or without C₂S inclusions and clustered or single crystals surrounded by the aluminates matrix were considered, as in the case of fluorine (Figure 4.12). Data highlight that magnesium has no preferential distribution between different types of alite crystals as pointed out by Figure 4.26. Dealing with also the sulphur content within the same types of belite crystals as in the case of fluorine-doped clinkers (Figure 4.17), no preferential distribution can be again observed (Figure 4.27). The absence of a significant partitioning between different types of crystals of the same phase has probably to be ascribed to the absence of a strong mineraliser able also to influence minor elements distribution, opposite to the case of fluorine-doped raw meals.

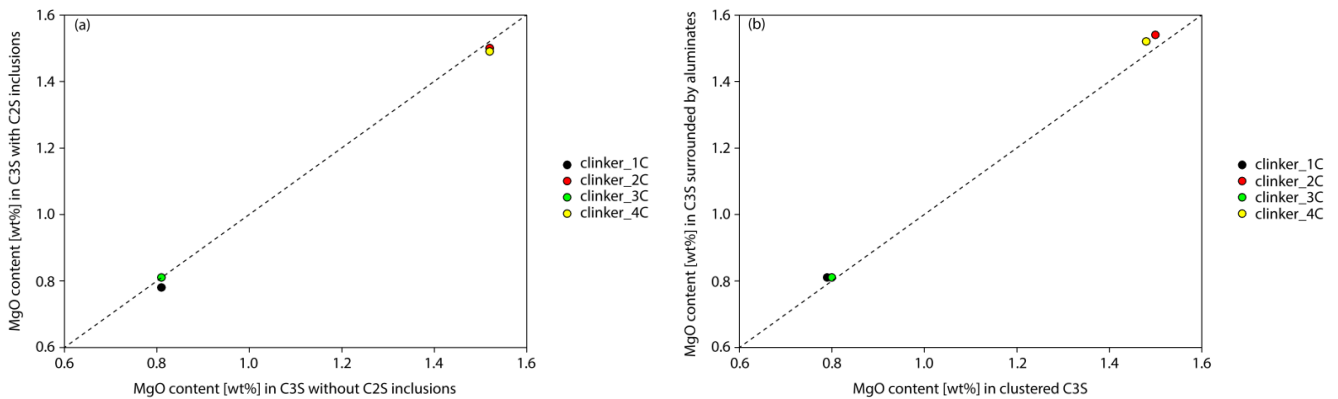


Figure 4.26: MgO distribution (wt%) among the different types of C₃S crystals (a) and (b).

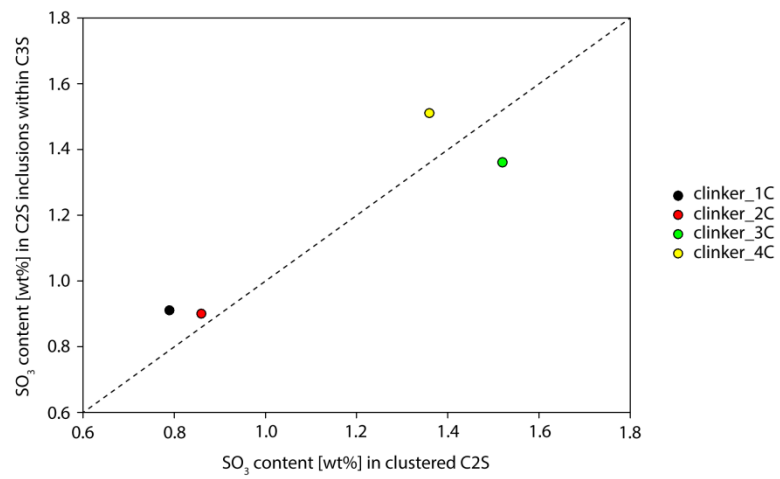


Figure 4.27: SO₃ distribution (wt%) among clustered C₂S and C₂S inclusions within C₃S.

4.3 *In situ* temperature-resolved synchrotron XRPD experiments

4.3.1 The synchrotron radiation

In situ experiments allow to probe information on samples in real time, without reporting them to room temperature through a quenching process; moreover, also the time variable can be added to evaluate the system evolution to changing temperature.

To perform the *in situ* study of the chlorine-doped raw meals it was necessary to use a synchrotron radiation because these raw meals, as for laboratory furnace firings, have to be thermally treated in a closed environment to avoid light elements evaporation. For this purpose, powders were sealed into platinum capillaries and synchrotron radiation was used because it is able to penetrate the wall of the capillaries. Platinum capillaries are required because of their refractory at the clinkering temperatures, melting well above $T = 1450\text{ }^{\circ}\text{C}$.

Synchrotron light is the electromagnetic radiation emitted by charged particles, usually electrons, when travelling at relativistic speeds under an accelerating field. This radiation is in the X-ray range, highly collimated and has a high brightness jointly to a strong polarization within the orbital plane of the circulating particles. In modern synchrotron radiation sources, electrons circulate following a close trajectory imposed by a magnetic field inside the storage ring. The ring is a pseudo-toroidal cavity, made by a succession of straight and curve sections; the whole system is kept under ultra-high vacuum conditions to avoid collisions between the electron and other particles and the consequent loss of energy, maximizing thus the efficiency. Particles energy loss due to synchrotron light emission and still possible collisions is continuously restored by the radio-frequency equipment. Synchrotron radiation is primarily emitted in correspondence to the curve sections of the storage ring, where the bending magnets are situated; insertion devices, set up along the straight sections, generate a magnetic field too, forcing the electrons to wiggle and undulate and allowing thus further radiation emission (Cockcroft and Fitch, in Dinnebier and Billinge, 2008).

Beamlines and experimental hutches are installed over the bending magnets (BM) or the insertion devices (ID) to fully exploit the radiation emission.

4.3.2 Experimental procedure

Samples preparation

In situ experiments were performed thermally treating only the chlorine-doped raw meals. In addition to the raw meals investigated during *ex situ* experiments (reference mixtures and the ones with the 1.0 wt% CaCl_2 addition, cf. Table 4.3), two further sets of raw meals have been prepared by adding the 0.5 wt% and the 1.5 wt% of CaCl_2 to the same reference raw meals. Table 4.7 shows the investigated raw meals during the *in situ* experiment. The aim is to evaluate the effects of multiple chlorine concentrations when coupled with minor elements during the firing process and to identify possible chlorine-bearing phases. Both the reference raw meals and the calcium chloride source were the same used for *ex situ* experiments, as well as the homogenization procedure.

Raw meal 1_0.0% CaCl ₂	Raw meal 2_0.0% CaCl ₂	Raw meal 3_0.0% CaCl ₂	Raw meal 4_0.0% CaCl ₂
Raw meal 1_0.5% CaCl ₂	Raw meal 2_0.5% CaCl ₂	Raw meal 3_0.5% CaCl ₂	Raw meal 4_0.5% CaCl ₂
Raw meal 1_1.0% CaCl ₂	Raw meal 2_1.0% CaCl ₂	Raw meal 3_1.0% CaCl ₂	Raw meal 4_1.0% CaCl ₂
Raw meal 1_1.5% CaCl ₂	Raw meal 2_1.5% CaCl ₂	Raw meal 3_1.5% CaCl ₂	Raw meal 4_1.5% CaCl ₂

Table 4.7: Labelling of the investigated raw meals during the *in situ* temperature-resolved synchrotron experiment. CaCl₂ concentration expressed as wt%.

Before the experiment, raw meals were calcined in a laboratory muffle furnace at 950 °C for 45 minutes. After the calcination process, the chlorine content was assessed by photometric titrations, to check it had not escaped the system yet. Homogenised raw meals powders were then sealed by an arc-sealer in platinum (99.95%) capillaries of 0.52 mm inner diameter and 0.04 mm wall thickness. Hence, the previous muffle calcination is necessary to avoid the capillary explosion due to carbon dioxide released by the calcite decomposition upon heating; on the contrary, air thermal expansion represents a negligible problem to capillaries mechanical resistance and vacuum-sealing is not required. Figure 4.28 shows the employed configuration of the capillary system during the *in situ* synchrotron experiments.

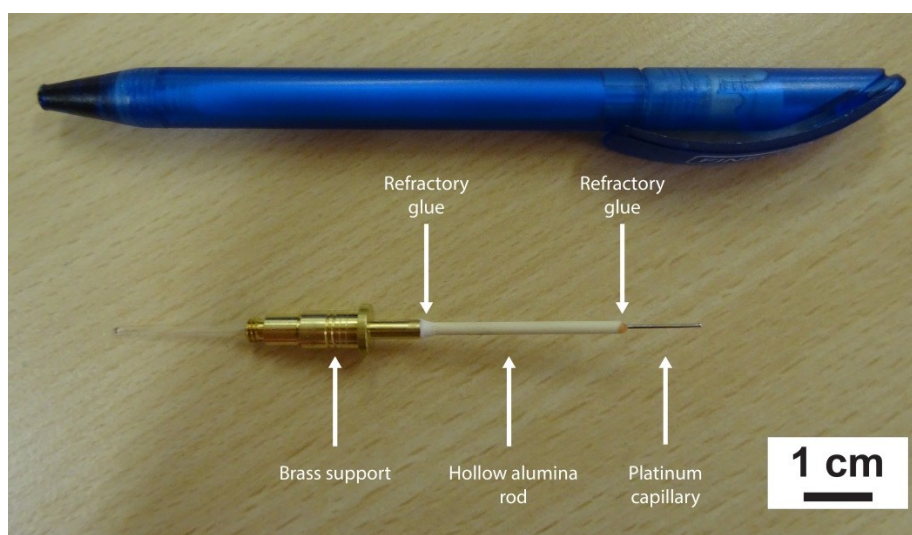


Figure 4.28: Platinum capillary setup during the high-temperature *in situ* synchrotron experiments.

Experimental setup

In situ high temperature XRPD experiments were performed at ID22 (former ID31) beamline at the European Synchrotron Radiation Facility (ESRF) in Grenoble, France (Fitch, 2004). The diffractometer works in Debye-Scherrer geometry, with a spinning capillary system. The incident beam is monochromated by a Si 111 double-crystal, cooled by liquid nitrogen, whereas nine scintillation detectors, two degree apart each and preceded by a Ge 111 analyser crystal, measure the diffracted beam.

During the experiments the wavelength was 0.32635 Å, to minimize the absorption effects due to the platinum capillary. The samples were heated up to clinkering temperature (~1450 °C) by means of a parabolic optical furnace (Figure 4.29), by varying the voltage of three 150-W halogen lamps (Moussa et al., 2003). To ensure the maximum efficiency of the furnace, the lamps filaments must lie in the

same plane of the sample rotation axis, focusing thus a 4 mm section along this axis. The achievement of every set temperature is almost instantaneous because of the lamp power and the capillary dimensions; however a two-minute waiting time before starting each measurement was fulfilled, to let the system completely balance to changing temperature.

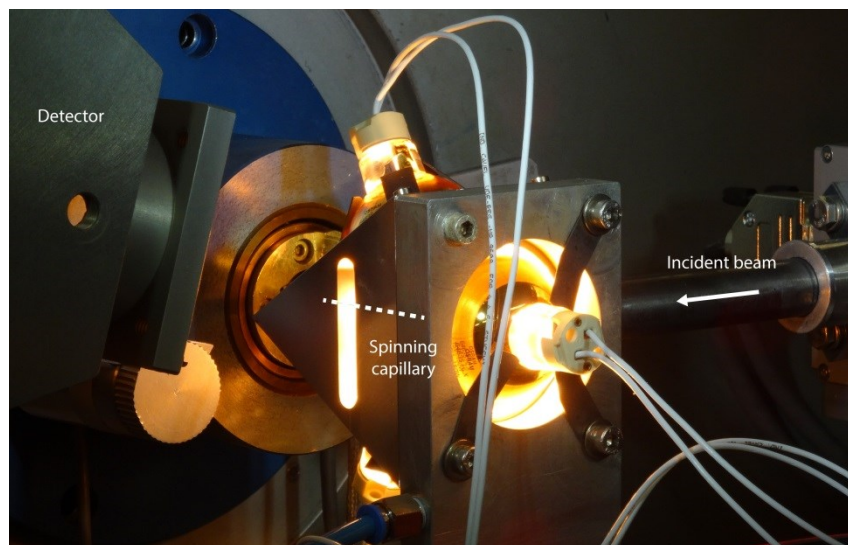


Figure 4.29: Parabolic furnace setup during the *in situ* temperature-resolved synchrotron experiments. Platinum capillary spins inside the furnace, perpendicular to the incident beam.

The furnace technical configuration allows no direct temperature measurement on the sample during the experiment; hence, platinum from the capillary has been used as an internal standard, reasonably assuming the inner and the outer temperature as identical, due to the capillary extremely small size and the platinum optimal heat conductivity. The actual temperature was thus calculated at each applied voltage during all the experiments, obtained by determining the value of the lattice constant a from the position of the platinum 111 diffraction peak and then using thermal expansion coefficients known from literature (Edwards et al., 1951).

$$\frac{\Delta a_0}{a_0} = 7.543 * 10^{-6}(T - 291) + 2.362 * 10^{-9}(T - 291)^2 \quad (4.1)$$

Equation 4.1 is applicable over the temperature range between 1140 and 2005 K (867 and 1732 °C respectively), perfectly fitting the investigated temperatures during our *in situ* experiment; a_0 is the platinum lattice constant at 291 K (18 °C) and Δa_0 the change in the lattice constant between 291 K and some higher temperature T .

Data analysis procedure

Table 4.8 reports the crystallographic structures used to perform Rietveld refinements on *in situ* XRPD patterns. The high temperature structures were used for C_3S , C_2S , and SiO_2 , whereas for the other phases the room temperature structures have to be employed due to the lack of the high temperature ones. In these latter the unit cell parameters were thus first manually adjusted and then refined without

any constraint. For all the atoms of every phase at every temperature a value of the atomic displacement parameter $B_{(iso)} = 2.37$ was set and kept fixed.

Phase	Reference	ICSD #
C ₃ S rhombohedral	Nishi and Takeuchi, 1984	30889
C ₂ S α _L	Mumme et al., 1996	82996
C ₂ S α _H	Mumme et al., 1996	82997
C ₂ S α	Mumme et al., 1996	82998
C ₃ A cubic	Mondal & Jeffery, 1975	1841
C ₃ A orthorhombic	Takeuchi et al., 1980	100220
C ₄ AF	Colville & Geller, 1971	9197
CaO	Natta & Passerini, 1929	61550
SiO ₂	Wright et al., 1981	26430
Mayenite	Boysen et al., 2007	241000
Chlormayenite	Ma et al., 2011	182076

Table 4.8: Crystallographic structures used for the *in situ* Rietveld refinements. ICSD # refers to the collection code of the phase within the Inorganic Crystal Structure Database.

Full profile Rietveld refinements on the *in situ* XRPD patterns were performed by Topas Academic 5.1 software (Coelho, 2012). For each phase the cell parameters (a, b, c and α, β, γ), the scale factor and the peak profile shape, described by a pseudo-Voigt type function, were refined; background was modelled by a six-terms Chebyshev polynomial function. To follow the lattice parameters evolution as a function of temperature, the sample displacement was refined only in the first pattern of every measure series and the obtained value kept fixed for all temperatures.

Moreover, the melt fraction has been indirectly calculated from the aluminates weight fractions just before their melting (de la Torre et al., 2007), following two different approaches. If the aluminates reach a maximum weight fraction value at a measured temperature (T) and at the next one (T + 1) are completely destabilized, the melt fraction will be equal to their sum at temperature (T), prior to the melting. If they start to destabilize at temperature (T) and at temperature (T + 1) they will be decreased but they will not be completely destabilised, the melt fraction at temperature (T + 1) is calculated by solving the equation (4.2)

$$(1 - L) * \frac{C_3A_{(T+1)} + C_4AF_{(T+1)}}{100} + L = \frac{C_3A_{(T)} + C_4AF_{(T)}}{100} \quad (4.2)$$

and then multiplying the result by 100, where L is the melt (liquid) fraction to be found at the given temperature (T + 1) and T is the temperature at which the aluminates weight fraction is at its maximum. When at temperature (T + n) they however completely destabilize, the melt fraction will simply corresponds to their maximum weight fraction at temperature (T). As a consequence the weight fractions of the crystalline phases at the highest temperatures were normalised taking also into account the melt content, not handled directly by the Rietveld method.

Finally, after the *in situ* experiments, cross-sections of the capillaries from *raw meals 1, 2, 3* and *4_1.5% CaCl₂* were analysed by electron microprobe, aiming to identify possible chlorine-hosting phases in the quenched material. The preparation of these polished sections required an appropriate procedure because capillaries cannot be cut before be included in epoxy resin, otherwise the material

loss would be certain. Capillaries were thus included as they were in the epoxy resin and the cross-section was simply obtained by scraping the resin until arriving at the capillary; when clinker powder contained in the capillary became visible, additional glue was applied under vacuum conditions to impregnate the powder and better fix them to the capillaries. Then, further polishing was performed and a micrometric graphite layer was applied under vacuum conditions. However, despite these arrangements, powders of *raw meal 3_1.5% CaCl₂* and *raw meal 4_1.5% CaCl₂* were lost during sample preparation.

4.3.3 Results and discussion

In situ XRPD experiments

The crystalline phases detected in all the mixtures are alite, belite, aluminates, lime and silica, independently from both the minor elements combination and the calcium chloride concentration. No minor phases are observed because both main and minor elements likely completely enter the crystalline structure of the above-mentioned phases or are released into the liquid phase at the highest temperatures. Moreover, calcium chloride is not present at any temperature because at ambient pressure it melts at ~ 775 °C (Patnaik, 2003), well below the starting temperature of these *in situ* experiments. Figure 4.30 shows the *in situ* XRPD patterns collected during the heating of *raw meal 3_1.0% CaCl₂*, highlighting the phases evolution as a function of temperature.

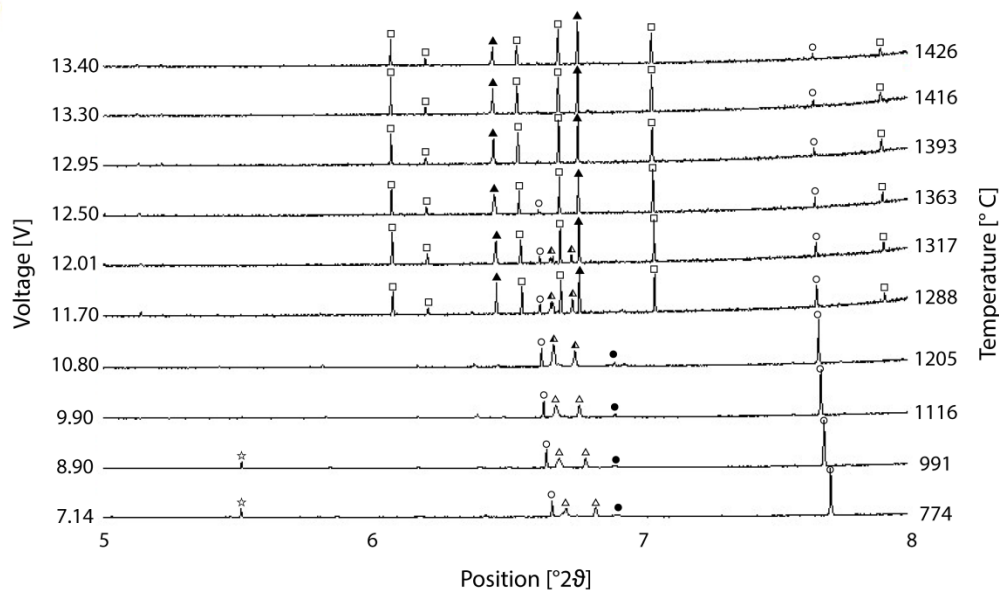


Figure 4.30: *In situ* XRPD patterns collected during the thermal treatment of *raw meal 3_1.0% CaCl₂*. Main crystalline phases are labelled as follows: SiO₂ (star), CaO (white circle), aluminates (black circle), C₂S α'_L (white triangle), C₂S α'_H (half-black triangle), C₂S α (black triangle), C₃S rhombohedral (white square).

Despite the similar voltages applied during all the measurements taking into account the expected ageing of the lamps, the actual temperatures carried out by evaluating the platinum thermal expansion however varied from one experiment to another, making thus raw data from different raw meals not directly comparable each other. This behaviour is mainly due to the different ageing rate of the halogen lamps, despite the corrections applied to set voltages from one measurement series to another. To make the data comparable, nine different temperatures were chosen (900, 1000, 1100, 1200, 1250, 1300, 1350, 1400 and 1450 °C respectively) and the weight fraction of every phase at these temperatures has been obtained by an interpolation procedure. Calculated data are highly reliable because *in situ* XRPD patterns were actually collected at several temperature points during the experiment, allowing to obtain an accurate interpolation. Figure 4.31 plots the variation of the phases content as a function of temperature for *raw meal 3_1.0% CaCl₂*.

During the earliest stage of the heating process ($T = 900$ °C) only lime, ranging from 26.4 wt% to 50.3 wt%, $C_2S \alpha'_L$ low temperature polymorph, SiO_2 and $C_{12}A_7$ are the crystalline phases occurring in all the raw meals, independently from the minor elements combination. Clay minerals already destabilized well-before the calcination temperature whereas carbonates at $T = 700 - 900$ °C, both releasing highly-reactive constituent oxides, mainly CaO, Al_2O_3 , SiO_2 , into the raw meals.

Increasing the temperature up to 1200 °C, just before or in correspondence of the first melt appearance, $C_2S \alpha'_H$ high temperature polymorph becomes the prevalent crystalline phase varying on average from ~60 to ~70 wt%. Low- and high-temperature α'_L and α'_H C_2S form mainly at the expenses of CaO and residual SiO_2 , these latter continuously decreasing due to the reaction between CaO and SiO_2 to give C_2S .

Then, between 1200 and 1250 °C, also rhombohedral C_3S starts to form by the $C_2S + CaO \rightleftharpoons C_3S$ reaction. As a direct consequence, C_2S and CaO wt% undergoes a strong decrease. Moreover, at this temperatures a melt starts to form due to the aluminates destabilization. The liquid fraction, increases as a function of temperature and reaches its maximum between 1250 and 1350 °C, in correspondence to the complete melting of the aluminates. As a consequence, the melt eases and speeds up the raw meals reactivity and C_3S experiences a dramatic increase and becomes the prevailing phase in all the mixtures. Rhombohedral C_3S , α - C_2S and sometimes free uncombined lime are the only crystalline phases occurring at $T = 1450$ °C, jointly to a melt fraction averaging on 15 wt%. During the cooling process, not investigated during these *in situ* experiments due to machine time reasons, C_3A and C_4AF will crystallize from the melt and part of the C_3S will dissociate into C_2S and CaO, leading to the standard proportions between crystalline phases in a commercial clinker.

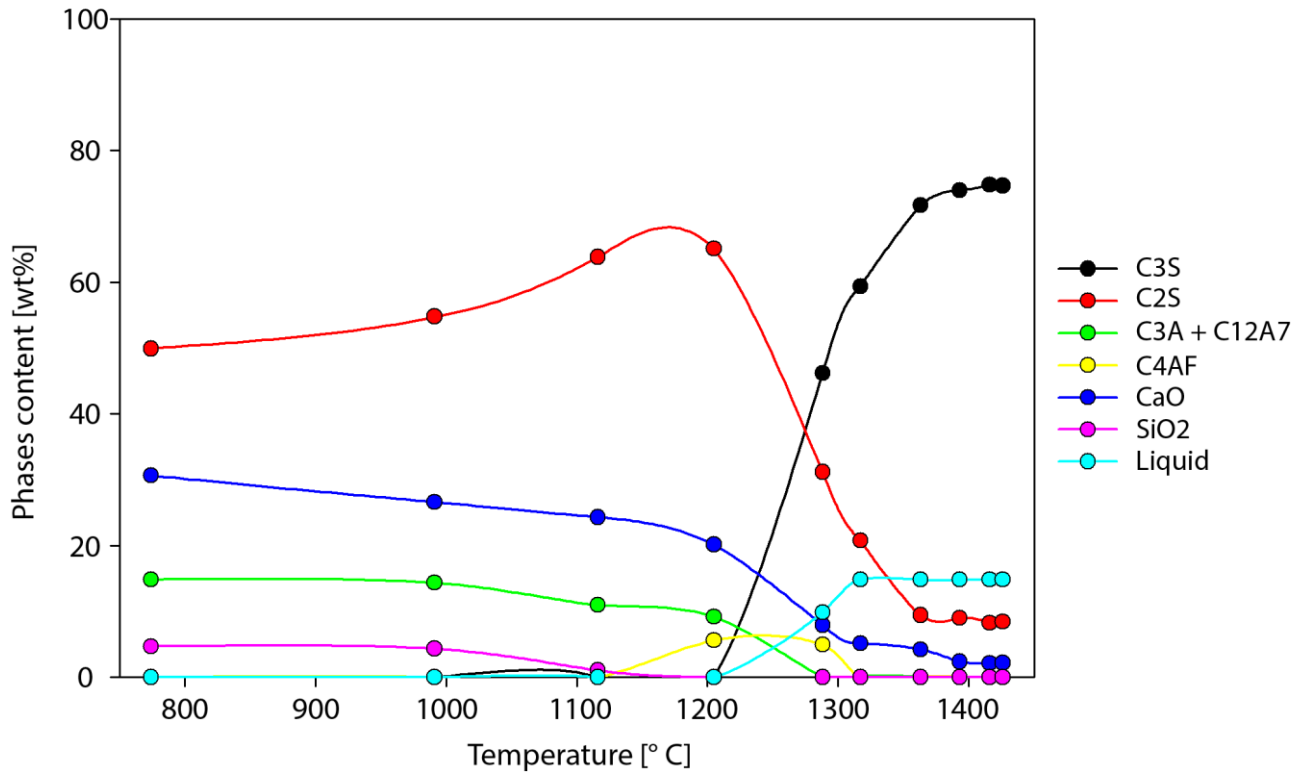


Figure 4.31: Phases content variation during the *raw meal 3_1.0% CaCl₂* thermal treatment, as determined processing *in situ* XRPD data by Rietveld refinements.

The possible effects of chlorine will be now investigated by comparing the quantitative phase analysis results among both the same raw meal (at varying CaCl_2 concentrations) and the raw meals doped with different combinations of minor elements. During the discussion, C_3A , mayenite and chlormayenite are considered together as *aluminates*.

Chlorine seems to increase the aluminates weight fraction in all the raw meals, independently from the minor elements combinations; the aluminates content in *raw meal 2* and *raw meal 4* for every calcium chloride concentration is reported in Figure 4.32.

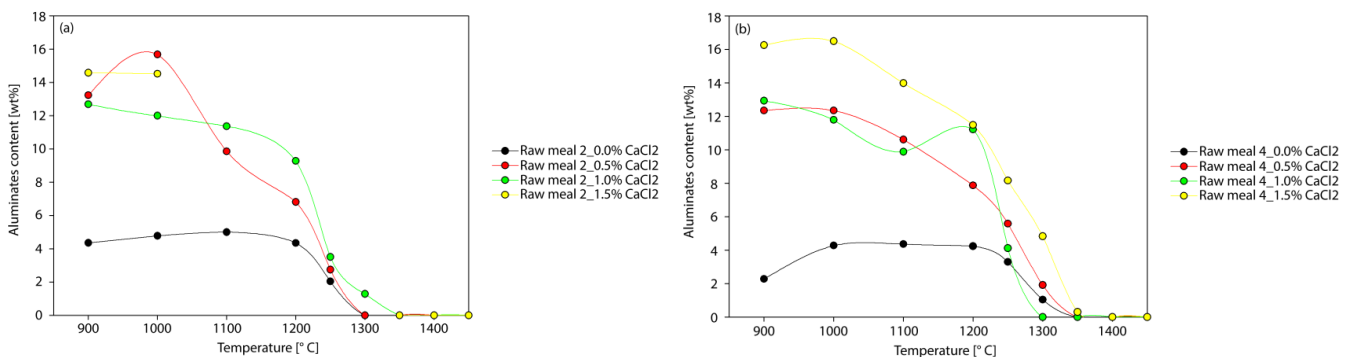


Figure 4.32: Aluminates content (wt%) variation as a function of temperature during the *raw meal 2* (a) and the *raw meal 4* (b) series thermal treatment, as determined processing *in situ* XRPD data by Rietveld refinements.

At $T = 900\text{ }^{\circ}\text{C}$ a significant aluminates fraction is already occurring, ranging from ~ 12 to ~ 16 wt% in the raw meals with the chlorine addition, whereas its value spans from ~ 1 to ~ 4 wt% in chlorine-free raw meals. The aluminates weight fraction reaches its maximum in chlorine-doped raw meals at $\sim 1000\text{ }^{\circ}\text{C}$, starting then a slow decrease. This slow decrease is not due to a melting process but probably to solid state reactions to form other crystalline phases, such as C_4AF that appears later in all the mixtures indeed. A strong decrease of the aluminates starts between 1200 and $1250\text{ }^{\circ}\text{C}$, where the melt likely appears; as a direct consequence of a melt fraction becoming more and more widespread, also rhombohedral C_3S starts to grow significantly turning into the prevailing crystalline phase. By $1350\text{ }^{\circ}\text{C}$ the aluminates are completely destabilized in all the mixtures; from literature data (Taylor, 1990; Kurdowski, 2014), pure mayenite melts at nearly $T \sim 1400\text{ }^{\circ}\text{C}$, more than $\sim 50\text{ }^{\circ}\text{C}$ higher than temperature values found in these experiments. This discrepancy can be ascribed to minor elements acting as a flux and to the fact that chlorine can be incorporated into the mayenite structure to give chlormayenite (Ma et al., 2011), lowering thus its melting temperature. Moreover, it is noteworthy the fact that raw meal 1_0.0% CaCl_2 is the only one where the aluminates content continues to increase up to $1350\text{ }^{\circ}\text{C}$ and then completely melt as expected in the thermal treatment of a standard raw meal, without any minor element addition.

Chlorine, likely as an indirect consequence of promoting the aluminates formation, also increases the melt fraction available in all the raw meals, independently again from the minor elements combination, as pointed out by Figure 4.33; this increase concerning the melt fraction, from chlorine-free to chlorine-doped raw meals, is more marked in mixtures where also sulphur is present. Minor elements affect the temperature at which the melt appears: at $T = 1250\text{ }^{\circ}\text{C}$ a little melt fraction already happens in raw meals doped with minor elements, in particular the ones high in sodium, a well-known flux; this effects is not related to chlorine occurrence. In fact, in *raw meal 1* series, whatever the chlorine concentration, the melt appears on average $\sim 50\text{ }^{\circ}\text{C}$ higher than in minor-elements doped raw meals.

Finally, chlorine also increases the reactivity of CaO in the raw meals doped with sulphur especially during the early stages of the thermal treatment (Figure 4.34); in particular, at same temperatures, chlorine-doped raw meals exhibit a lower CaO wt% than the chlorine-free raw meal. On the contrary, this behaviour is not observed in the *raw meal 1* and *raw meal 2* series, whatever the calcium chloride concentration is, independently from the minor elements combination.

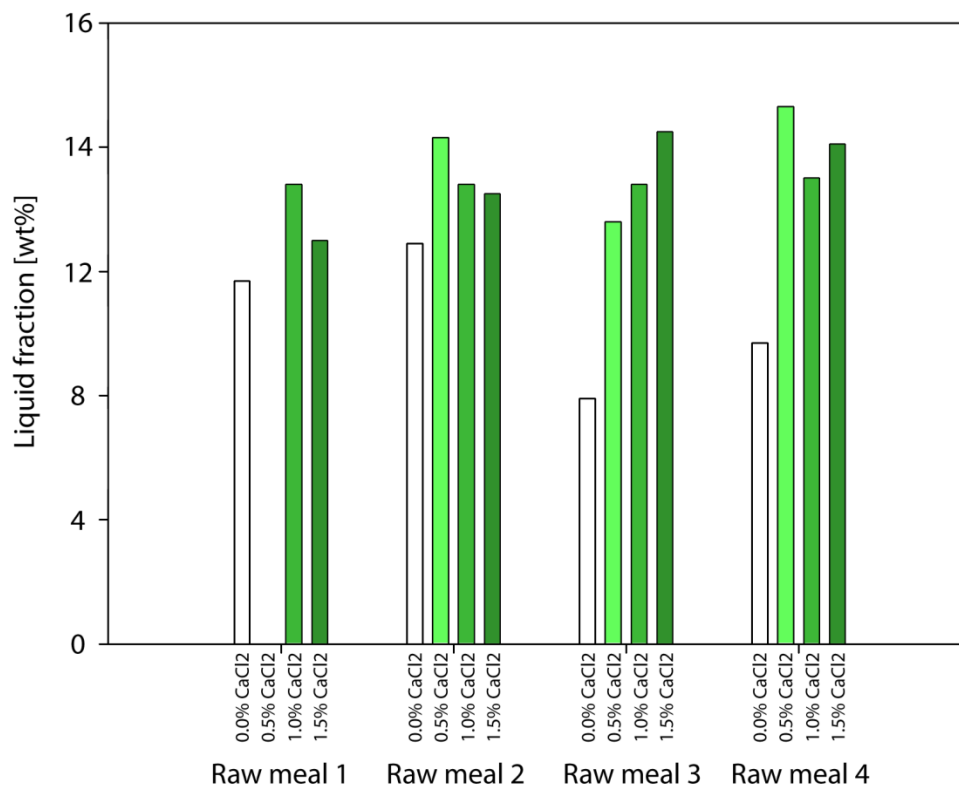


Figure 4.33: Variation of the maximum content (wt%) of the liquid phase among the four raw meals series as a function of calcium chloride concentration, carried out indirectly processing *in situ* XRPD data by Rietveld refinements. The shade of green is directly proportional to the raw meal chlorine content.

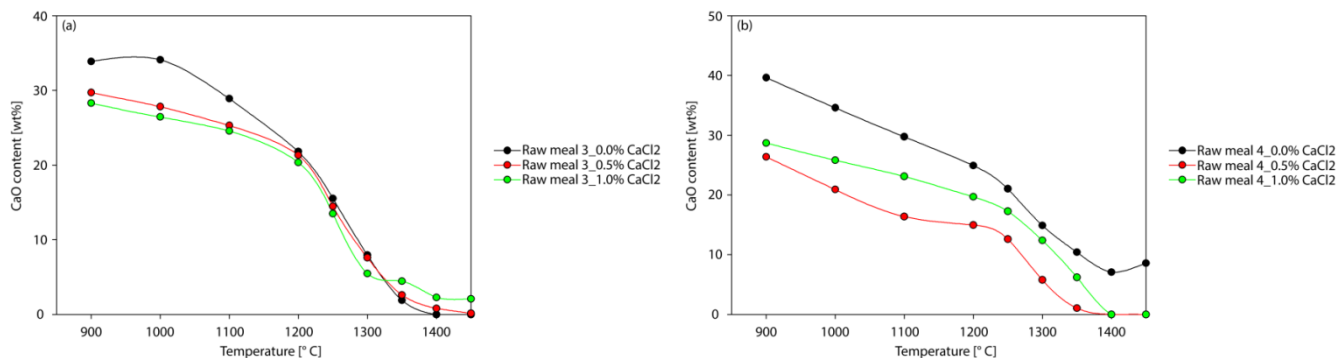


Figure 4.34: CaO content (wt%) variation as a function of temperature in *raw meal 3* (a) and *raw meal 4* (b) series, as determined processing *in situ* XRPD data by Rietveld refinements.

Electron microprobe spot analyses

Cross-section of capillaries containing the clinkers obtained from thermally treating the raw meals doped with a 1.5% CaCl_2 addition were analysed by EMPA aiming to identify possible chlorine-bearing phases. Figure 4.35 shows SEM backscattered images of capillaries containing clinkers from *raw meal 1_1.5% CaCl₂* and *raw meal 2_1.5% CaCl₂*.

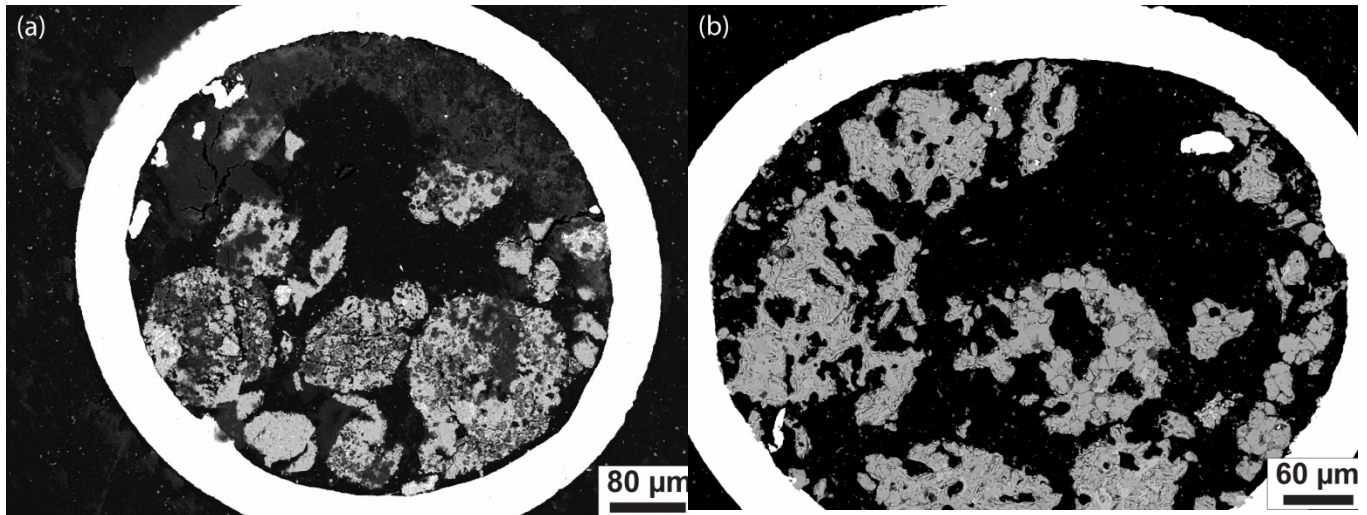


Figure 4.35: SEM backscattered images of a cross-section of capillaries containing clinkers from *raw meal 1_1.5% CaCl₂* (a) and *raw meal 2_1.5% CaCl₂* (b).

SEM investigations revealed a significant volumetric shrinkage, larger than expected, occurred during the quenching process as highlighted by the widespread porosity in both the samples. However, part of the material has been likely lost during the sample preparation due to its extremely powdered nature, despite having followed the procedure previously outlined. Moreover, the average size of crystals is well-below 40 μm in both samples and issues of an incipient hydration are also visible.

Spot chemical analyses reports chlorine only in one phase (Figure 4.36), which oxide average composition is given in Table 4.9, in clinker from *raw meal 1_1.5% CaCl₂*; on the contrary no chlorine is detected in any phase in clinker from *raw meal 2_1.5% CaCl₂*. Chlorine content has been also checked within the walls of the platinum capillaries, confirming its complete absence due to values equal to zero. Complete microprobe analyses results on capillary cross-sections, taking also into account microcrystalline phases, are reported in Appendix B3. Missing chlorine has possibly been incorporated in some crystalline phases that were removed during the sample preparation or more likely escaped from the system, even if the platinum capillaries were sealed.

Phase	SiO ₂	TiO ₂	Al ₂ O ₃	FeO	MgO	CaO	MnO	SrO	Na ₂ O	K ₂ O	SO ₃	Cl	-O=Cl	Total
Cl-bearing phase	4(2)	0.1(0)	36(3)	4.4(3)	0.6(5)	48(2)	0.0	0.1(1)	0.0	0.0	0.1(1)	3.8(4)	0.9(1)	96(1)

Table 4.9: Average chemical composition of the chlorine-bearing phase, as determined by electron microprobe analyses.

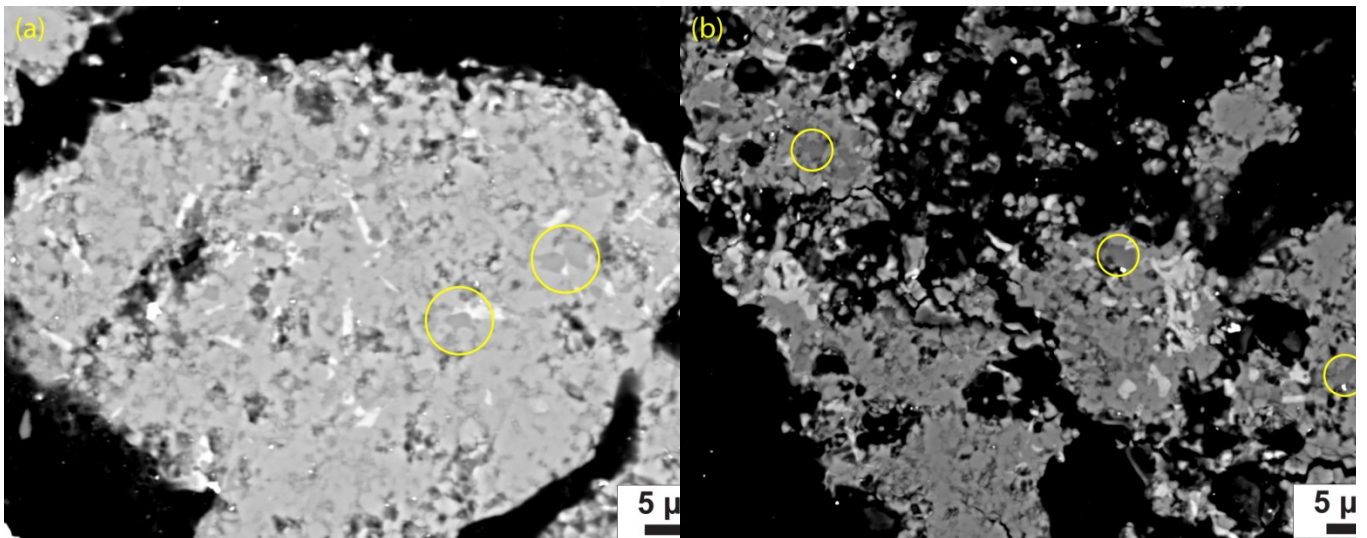


Figure 4.36: SEM backscattered images of clinker from *raw meal 1_1.5% CaCl₂* (a) and (b). Yellow circles indicates the dark-grey chlorine-bearing phase on which electron microprobe spot chemical analyses were performed.

4.4 Conclusions

The effects of minor (sodium, magnesium and sulphur) and trace (fluorine and chlorine) elements within industrial raw meals were studied by means of both *ex situ* XRPD and electron microprobe analyses on clinkers obtained from laboratory furnace thermal treatments. Moreover the influence of chlorine during the firing process was further investigated by an *in situ* synchrotron XRPD experiment. Dealing with the laboratory thermal treatments of both fluorine- and chlorine-doped raw meals, qualitative and quantitative phase analyses on *ex situ* XRPD data confirmed, as expected, that the effects of minor elements are not simply additive but every combination should be taken into account and investigated separately. As an example, the mineralizing effect of fluorine on tricalcium silicate is remarkable in every raw meal whatever the combination of minor elements is, whereas sodium does not always stabilize the orthorhombic form of the tricalcium aluminate, depending on minor elements combination within the raw meal indeed.

Microprobe spot analyses on clinkers obtained from fluorine-doped raw meals confirmed that fluorine enters the alite structure by the $F^- + Al^{3+} = O^{2-} + Si^{4+}$ substitution, whereas its content within belite is zero. As a consequence of that substitution, also aluminium exhibits a slight preference for the alite structure. Taking into account the other minor elements occurring in a significant amount within the same raw meals, magnesium preferentially enters the structure of alite, whereas sulphur and alkalis prefer belite. Hence, their general behaviour is not affected by the occurrence of fluorine.

On the contrary, chlorine does not considerably enter any of the clinker silicate phases, whereas a little amount is detected in the interstitial matrix; identify exactly the phase was not possible due to the too low average size of these crystals. However, most of chlorine volatilize from the system during the thermal treatment, even working with sealed crucibles. Alkalis partial removal from the system is a side effect of chlorine volatilization, because chlorine does not leave the raw meal in the elemental form but mainly forming alkali-chlorides. Again, as well as in the case of fluorine, the distribution of minor elements between alite and belite is not significantly driven by the chlorine occurrence.

Finally, *in situ* experiments allowed to identify a possible chlorine-bearing phase, only in the clinker obtained from the minor elements-free raw meal, jointly to evaluate the chlorine effects during the raw meals thermal treatment. In particular, chlorine enhances the aluminates formation and as a consequence it increases the available melt fraction at the highest temperatures of the clinkerization process. However, this increase in the melt fraction is not a guarantee of a better clinker, in terms of tricalcium silicate and free lime content, because the relation the more the melt fraction the more the tricalcium silicate in the final clinker is not always verified in the investigated raw meals.

Chapter 5

Heterogeneous raw meal systems

5.1 Introduction

The ordinary Portland cement clinker production process, as already stated in the introduction of this thesis work (Section 1.8), has a remarkable impact in terms of energy consumption, costs, greenhouse gases emissions and dusts generation.

This chapter deals, for the first time, with both the development and the testing of an OPC clinker unconventional raw meal setup, in terms of employed raw materials and components grain size. The expected benefits of this unexplored raw meal configuration would mainly concern the energy consumption and the consequent reduction of costs.

The innovative OPC clinker raw meal setup was achieved by following two main steps during their formulation:

- the use of basalt as a complete replacer of clay, as acid fraction
- the use of a mixture of fine- and coarse-grained limestone, as basic fraction

Use of basalt as a complete clay replacer

Past works dealing with the use of basalt as a *partial* replacer of the acid fraction in an OPC clinker raw meal were carried out successfully and have been the basis and the starting point of this whole work (Khadilkar et al., 1990; Hassaan, 2000; Darweesh, 2001; El-Sayed, 2002; El-Hafiz et al., 2015). Moreover the use of basalt has several advantages, now briefly outlined.

Basalt rock is the most widespread volcanic rock on the Earth surface, where large volumes above the sea level mainly occur as continental flood basalt (Ronov, 1985). Furthermore, most of these vast basalt outcrops are located in top-ranked countries as regard the cement and clinker production, such as India, Russia, United States and Brazil (U.S.G.S., 2016).

Moreover, basalt is commonly employed as an aggregate in concrete manufacturing, in particular where quartz-feldspathic rocks lack (Kozul and Darwin, 1997). This application generates tons of vesicular basalt and basalt fines, both not appropriate to be used as a reinforcing material and generally landfilled in large-scale dumps. Vesicular basalt is not suitable because its porosity adversely affects the resistance to compression of concrete, whereas basalt fines have a too low average grain size (Andrade et al., 2010). Hence, they represent cost-effective alternative materials, very attractive for cement clinker industry; in particular, basalt quarry-fines are almost already ground down to an adequate fineness for their use in OPC clinker raw meals preparation.

Dealing with mineralogical and chemical composition, basalt-forming minerals are silicates, mostly feldspars and pyroxenes, followed by olivine and secondary minerals, these latter due to alteration processes. Hence, the bulk chemical composition is higher in calcium, iron, magnesium and alkalis compared to a standard clay used to prepare OPC clinker raw meals. The occurrence of these oxides during the thermal treatment has some advantages: for example iron oxide is an active mineraliser accelerating the dissociation of calcium carbonate; magnesium oxide allows the formation of a low-viscosity liquid phase at lower temperatures than the standard ones; alkalis provide the increase of aluminates formation and act as fluxes (El-Didamony et al., 2010). These thermochemical advantages also enable to reduce the use of fluorine compounds as mineralisers, this latter contributing to the decay of the refractory kiln coating (Blanco-Varela et al., 1984). Moreover, at ambient pressure basalt rock melts completely between 1240 and 1280 °C: the presence of a wide melt fraction at these temperatures during the OPC clinker production eases the reactivity of the whole mixture.

Finally, basalt has a heavier specific weight than clay, $2.9\text{-}3.3 \times 10^3$ and 2.2×10^3 kg/m³ respectively, permitting to reduce transportation costs, for a fixed volume (El-Ashkar, 2002). Moreover, pulverizing basalt generates a heavier powder, easier to be recollected or to be re-precipitated, reducing thus powder-related environmental issues.

Based on these considerations, this work takes consistently into account the use of basalt as a *complete* replacer of the clay fraction.

Use of a mixture of fine- and coarse-grained limestone

Dealing with the basic fraction, the use of a coarse-grained limestone is only partially due to comminution costs, because refining limestone below 80 µm has not a considerable impact on the production costs, due to the calcite easy grindability (Sinha et al., 1980). The actual reason has petrologic implications, in the C-A-S ternary diagram (Lörke et al., 2001; Lörke, 2011).

The use of two different grain sizes, below 80 µm and between 80 and 500 µm respectively, allows to obtain a significant weight fraction of the easy-to-melt silicates CS (CaSiO₃ – wollastonite) and C₃S₂ (Ca₃Si₂O₇ – rankinite), rather than the difficult-to-melt C₂S, before the appearance of a melt. This will increase the melt fraction and ease the clinkerization, at the same temperatures: as a consequence energy saving and kiln output increase are possible.

Following this procedure, the best eutectics in the C-A-S diagram to form clinker lie in the CS-CAS₂-S and C₃S₂-C₂AS-CS compositional triangles, both at a lower temperature than the standard one within the C₂S-C₃A-C₁₂A₇ triangle. The formation of the CS and C₃S₂ silicates is a prerequisite to the existence of these low melting eutectics.

However, in the CaO-SiO₂ binary system, C₂S is always the first silicate phase to form, whatever the CaO/SiO₂ ratio value is. Easy-melting CS or C₃S₂, once fixed the CaO/SiO₂ equal to 1 or 1.5 respectively, form only when all the CaO capable of solid-state reactivity will be completely combined. Since C₂S is the first silicate to form, the eutectics in the CS-CAS₂-S and C₃S₂-C₂AS-CS systems are hindered until C₂S would start to convert into CS. To allow this conversion, the CaO weight fraction able to react at solid-state must correspond to the one at the eutectic. Employing a common all-powdered raw meal, it is impossible to obtain these eutectics during the thermal treatment because the total CaO weight fraction never corresponds to that of the eutectics, but it is shifted towards the C apex of the C-A-S diagram.

This issue is bypassed by using a mixture of fine- and coarse-grained limestone as the basic fraction, source of CaO. The finely-ground limestone represents the only fraction able of solid-state reactivity and it has to be enough to form only the easy-to-melt CS silicate and the aluminates (C_3A and C_4AF); in this way no C_2S will thus form. It is implied the raw meal acid component has to meet an adequate fineness too in order to react with CaO at the solid-state.

Producing this widespread and low-temperature melt fraction, the clinker phases will then form directly from a silicate melt due to the destabilization of the easy-to-melt silicates. In this way the mechanism of formation of C_3S changes drastically: it will form no longer from the $C_2S + C$ solid-state reaction, but directly from the silicate melt.

Coarse-grained limestone is finally needed only to move the overall chemical composition from the low-temperature eutectic to the OPC clinker raw meal standard bulk chemical composition.

5.2 Materials: characterization and preparation

Limestone

Limestone is from the Rezzato quarry, representing one of the most important exploitation site of limestone for OPC clinker production in Northern Italy. It is located in the Brescia Prealps in the Lombardy region and geologically belongs to the “Formazione della Corna” of Jurassic age (Boni and Cassinis, 1973).

Optical thin-section observations (Figure 5.1) highlighted variable textural features even at the millimetre to centimetre scale, from mudstone to grainstone according to Dunham’s classification (Dunham, 1962). Microcrystalline calcite, partially recrystallizing into microsparite due to diagenetic processes, occurs within the mudstone and wackestone areas; on the contrary, two different generations of calcite cement, primary marine and late burial, can be identified in the grainstone areas. Fractures and skeletal fragments are widespread across the whole rock.

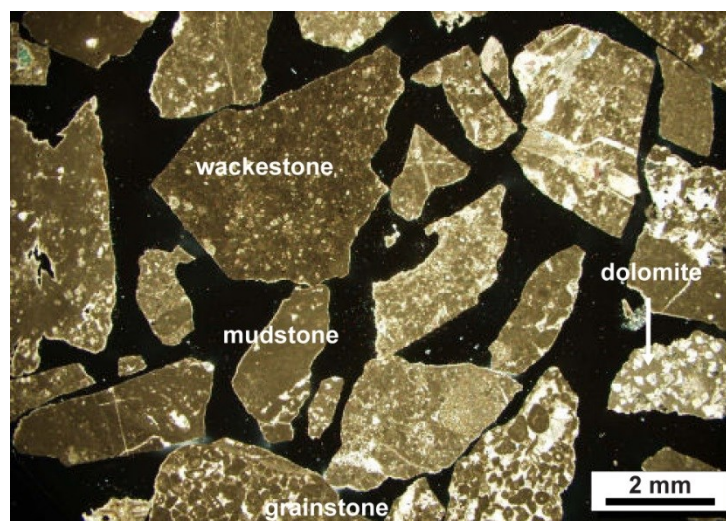


Figure 5.1: Thin section optical micrograph of the limestone sample, under cross polarised light. Textural variability at the millimetre scale and rhombic dolomite crystals are highlighted.

Basalt

Basalt rock sample as it is was not available: this made impossible to describe its textural features. However, optical microscopy observations on the ground material, both in transmitted plane (PPL) and cross (XPL) polarized light, allowed to obtain a qualitative mineralogical analysis and to confirm the basaltic nature of the rock (Figure 5.2).

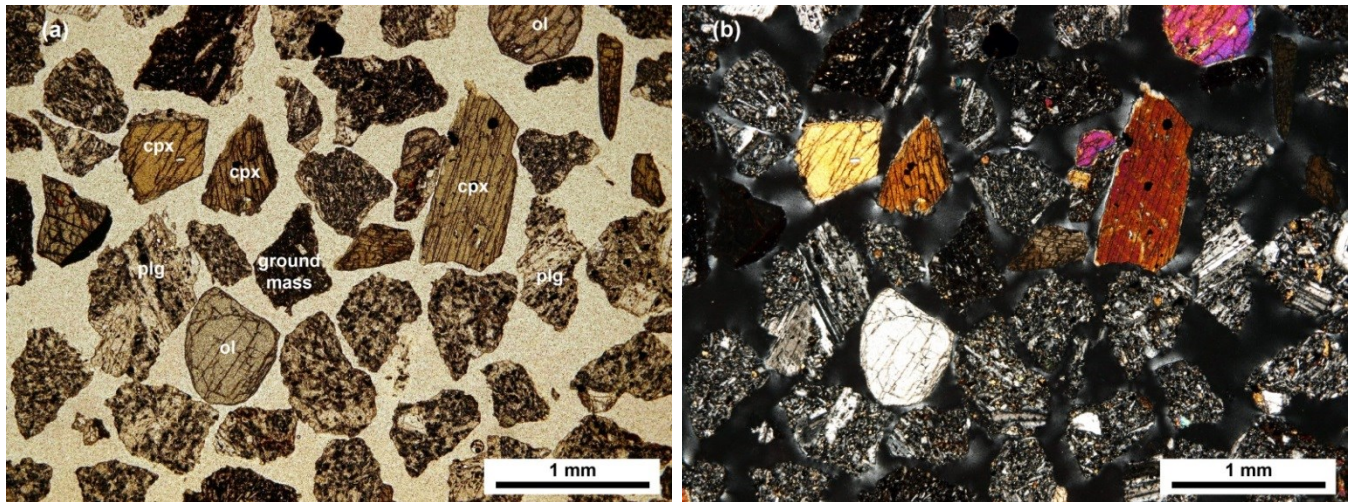


Figure 5.2: Thin section optical micrographs of basalt, under plane polarized light (a) and cross polarized light (b). Phenocrysts are clinopyroxene (cpx), olivine (ol) and plagioclase (plg); groundmass refers to microcrystalline phases, mainly feldspars and glass, between the phenocrysts.

Sieving procedure and chemical characterization

Natural raw materials were preliminary crumbled by a jaw crusher down to an adequate fineness to be then sorted into five different particle size distribution classes below 1 mm by mechanical sieving (Table 5.1). Standard sieves with certified mesh size were employed.

Raw material	Particle size distribution classes [μm]				
Limestone	< 75	75 - 150	150 - 500	500 - 1000	> 1000
Basalt	< 75	75 - 150	150 - 500	500 - 1000	> 1000

Table 5.1: Particle size fractions of limestone and basalt, expressed in μm , obtained by mechanical sieving.

Raw materials grain size classes selected for raw meals preparation were analysed by WD-XRF to evaluate their chemical suitability for OPC clinker production. Results are reported in Table 5.2.

Raw material	SiO ₂	Al ₂ O ₃	Fe ₂ O ₃	CaO	MgO	SO ₃	K ₂ O	Na ₂ O	TiO ₂	P ₂ O ₅	Mn ₂ O ₃	L.o.I.*	Total
Limestone < 75 μm	1.58	0.46	0.21	50.83	2.96	0.06	0.06	0.01	0.04	0.02	0.01	43.67	99.91
Limestone 150-500 μm	0.46	0.12	0.14	51.59	3.07	0.08	0.01	0.02	0.01	0.01	0.00	44.39	99.90
Basalt < 75 μm	48.48	17.57	10.41	10.15	5.03	0.01	1.67	4.01	1.56	0.44	0.20	0.00	99.53

Table 5.2: Chemical composition (wt%) of the selected raw materials grain size classes, as determined by WD-XRF. Detection limit is 0.01 wt% and data resolution gradually deteriorates towards the limit. * loss on ignition.

5.3 Methods

5.3.1 Raw meals formulation

To prepare raw meals a two-step procedure was followed. First, six eutectic mixtures were prepared by blending in different proportions only fine-grained basalt and fine-grained limestone. Then, coarse-grained limestone was added to achieve the proper chemical composition for OPC clinker production. For the sake of clarity, mixtures were labelled as follow. Lower case *c* and *b* indicate respectively fine-grained ($< 75 \mu\text{m}$) limestone and fine-grained ($< 75 \mu\text{m}$) basalt, whereas upper case *C* indicates coarse-grained limestone ($150\text{-}500 \mu\text{m}$); *x* varying from 1 to 6 identifies the eutectic mixture taken into account, as reported in the C-A-S diagram (Figure 5.3) and in Table 5.3. For instance, *bc*₁ indicates the eutectic mixture made by blending fine-grained basalt and limestone, which chemical composition is defined by the red dot labelled *bc*₁ in the C-A-S diagram (Figure 5.3).

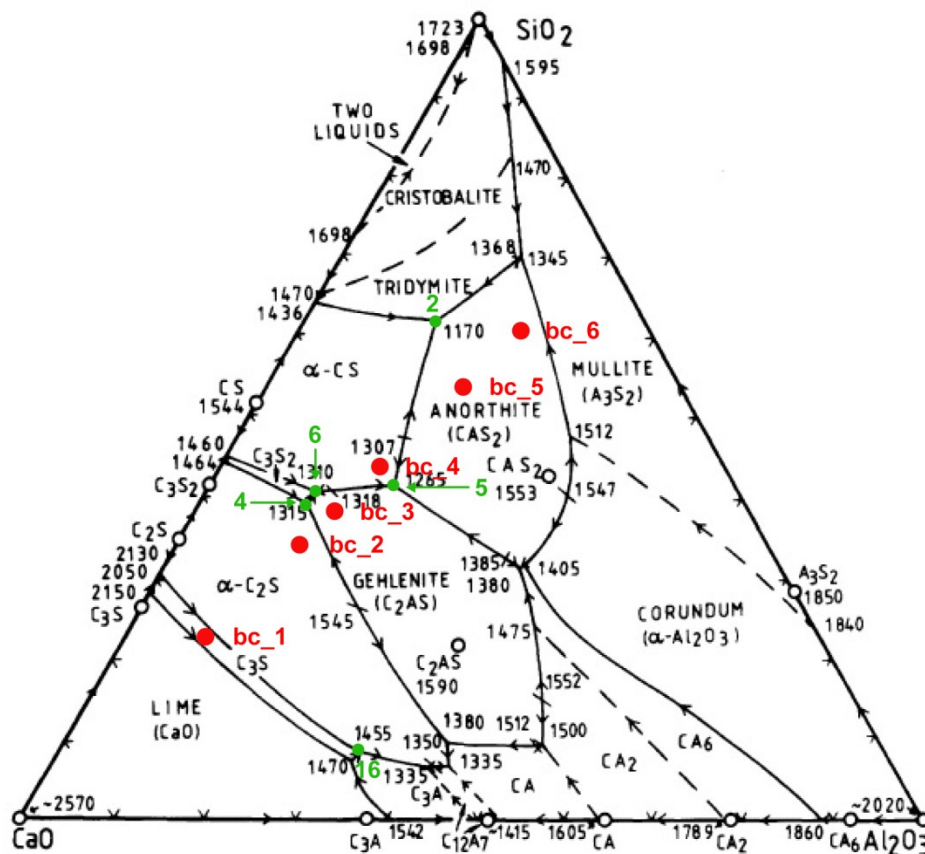


Figure 5.3: Bulk chemical composition (red dots) of the six eutectic mixtures made by fine-grained basalt and fine-grained limestone, plotted in the C-A-S ternary diagram. Green dots indicate the eutectics corresponding with each mixture; eutectic numbering after Greig (1927).

Eutectic mixture	Sub-system	T _e [°C]	Melt composition at the eutectic		
			CaO	Al ₂ O ₃	SiO ₂
<i>bc_1</i>	C ₃ S-C ₂ S-C ₃ A	1455	58	33	9
<i>bc_2</i>	C ₂ S-C ₃ AS-C ₃ S ₂	1315	49	10	39
<i>bc_3</i>	CS-C ₃ S ₂ -C ₂ AS	1310	48	11	41
<i>bc_4</i>	CS-C ₂ AS-CAS ₂	1265	38	20	42
<i>bc_5</i>	S-CS-CAS ₂	1170	23	15	62
<i>bc_6</i>	S-CS-CAS ₂	1170	23	15	62

Table 5.3: Selected eutectic mixtures in the C-A-S ternary phase diagram. Sub-system, eutectic temperature (T_e) and melt chemical composition are also given for every eutectic mixture.

As said before, different weight proportions of coarse-grained limestone had to be then added to the eutectic mixtures to attain the standard chemical composition for OPC clinker production. Qualitative information on the grain size composition of raw meals are obtained in the same way as for the eutectic ones, by combining *C*, *c* and *b* labels. For example, *C&bc_3* indicates the raw meal made by adding coarse-grained limestone (*C*) to the eutectic mixture *bc_3*. Table 5.4 reports the detailed raw meals formulation design, once set the moduli target to LSF = 96.0, SR = 2.5 and AR = 1.5.

The chemical composition of the eutectic mixture *bc_1* already coincides to the one of a standard OPC clinker raw meal and no coarse-grained limestone was later added indeed. On the contrary, shifting from eutectic mixtures *bc_2* to *bc_6*, more and more coarse-grained limestone has to be added to attain the proper bulk chemical composition, moving towards the CaO apex of the C-A-S diagram. Figure 5.4 reports a schematic representation of the considered raw meals.

OPC clinker raw meal	Fine-grained limestone + fine-grained basalt (wt%)	Coarse-grained limestone (wt%)
<i>C&bc_1</i> *	100.00	0.00
<i>C&bc_2</i>	59.92	40.08
<i>C&bc_3</i>	47.18	52.82
<i>C&bc_4</i>	39.95	60.05
<i>C&bc_5</i>	29.12	70.88
<i>C&bc_6</i>	23.98	76.02

Table 5.4: Combination between fine-grained limestone + fine-grained basalt and coarse-grained limestone, to achieve the proper chemical composition for OPC clinker production. *Raw meal *C&bc_1* will be from now on addressed simply as *bc_1*, because no coarse-grained limestone was added.

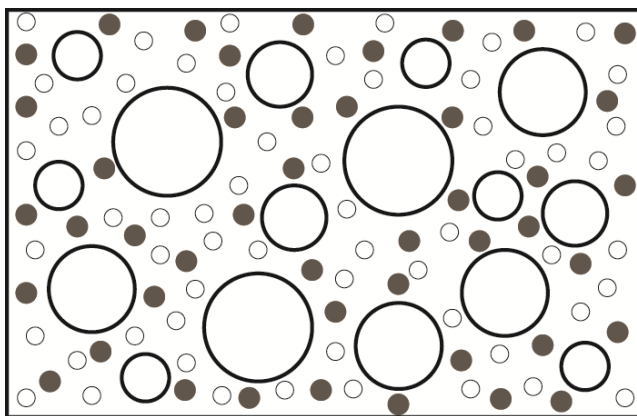


Figure 5.4: Schematic representation of the investigated raw meals heterogeneous particle size distribution (except for raw meal *bc_1*). White circles represent both fine- and coarse-grained limestone, whereas dark grey circles represent fine-grained basalt. Volume proportions are just indicative and not representative of any particular raw meal.

Before the thermal treatment, the raw meals were homogenized by an automatic shaker for 90 minutes and moulded into pellets to ease the contact between grains and guarantee the best reactivity. The raw meals shaping into pellets is required dealing with limited amounts of material; on the contrary inside the industrial kiln where tons of material are processed the whole mass is self-compacting under its own weight.

Simultaneously, a second set of the same raw meals was also prepared by adding the 0.5 wt% of CaF_2 (99.99 % Sigma-Aldrich) as a mineraliser, aiming to reduce the expected high free lime and periclase contents and to increase the alite formation.

5.3.2 Thermal treatment

Pellets were thermally treated in an electrical laboratory furnace (Carbolite 16/35), following the cycle reported in Figure 5.5; at the end of the thermal treatment, clinkers were drawn from the furnace and quenched with a room-temperature air flow.

Despite the raw meals were automatically homogenized, heterogeneity within a pellet is still possible due to the extremely different particle size distribution. To minimize this issue, two pellets from every raw meal was fired simultaneously during the thermal treatment, to later average the quantitative phase analysis results.

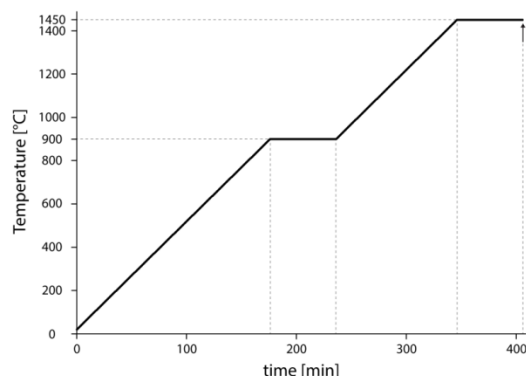


Figure 5.5: Representation of the firing cycle ramp. A one-hour soaking time is required both at 900 and 1450 °C; the former to achieve the full dissociation of carbonates and the latter to complete the clinkerization. The arrow indicates the moment when samples were drawn from the furnace.

5.4 Results and discussion

Ex situ XRPD patterns on the obtained clinkers were collected under the same instrumental conditions reported in Section 3.2.2. Data were first analysed by X'Pert Highscore to get a qualitative phase analysis and then processed by the full-profile Rietveld method implemented in the Topas-Academic 5.1 software to get a quantitative phase analysis. The amorphous content was not taken into account due to absorption problems related to the available external standard, alumina. However, it can be reasonably assumed that its content is close to zero, because of the absence of its characteristic bulge in the background of the XRPD patterns within the 20-30° 2 θ angular window, jointly to a proper quenching method.

Qualitative phase analysis performed on the entire set of samples highlighted that the clinkers are made by the usual crystalline phases assemblage (Figure 5.6). In details: alite (M1 and M3 polymorphs), belite (β and α' polymorphs), tricalcium aluminate (cubic and orthorhombic polymorphs), ferrite and free lime. Periclase and very few portlandite also occur, the former due to the high magnesium content in the raw meals whereas the latter due to free lime incipient hydration (Figure 5.7).

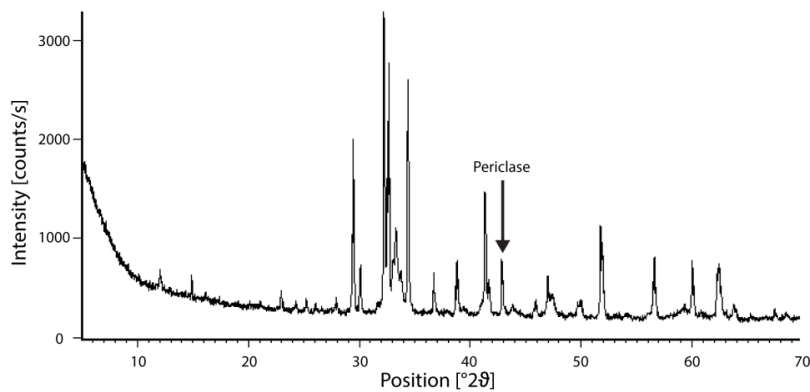


Figure 5.6: XRPD pattern of clinker obtained by thermally treating raw meal *bc_1* at $T = 1450$ °C. The arrow indicates the characteristic peak of periclase (MgO) at $\sim 43^\circ 2\theta$.

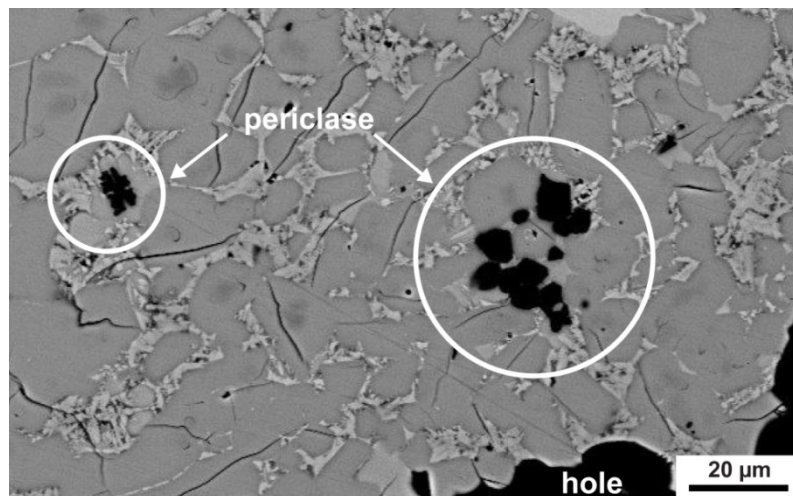


Figure 5.7: SEM backscattered image of clinker sample *bc_1*. Periclase occurrence due to the high magnesium content in the raw meal is marked out.

5.4.1 Fluorine-free raw meals

Table 5.5 reports the quantitative phase composition of clinkers obtained from the six different raw meals, without taking into account the polymorphism, whereas Figure 5.8 an example of a Rietveld refinement on clinker *C&bc_4*. Detailed results are given in Appendix C1, including the phases polymorphism.

Phase	<i>bc_1</i>	<i>C&bc_2</i>	<i>C&bc_3</i>	<i>C&bc_4</i>	<i>C&bc_5</i>	<i>C&bc_6</i>
C ₃ S	61.8	41.5	37.0	47.7	42.5	31.2
C ₂ S	9.1	25.6	31.7	21.1	28.1	35.9
C ₃ A	13.7	14.7	14.5	14.4	14.0	12.9
C ₄ AF	10.0	9.0	9.9	9.3	8.0	11.0
CaO	0.4	4.6	2.5	2.9	4.0	5.0
Ca(OH) ₂	0.7	0.8	0.9	0.8	0.5	0.4
MgO	4.2	3.8	3.6	3.8	3.0	3.6

Table 5.5: Quantitative phase composition (wt%) of clinkers obtained from fluorine-free raw meals, as determined processing XRPD data by the Rietveld method. Uncertainty not reported because the results shown here are average values between the two firing series.

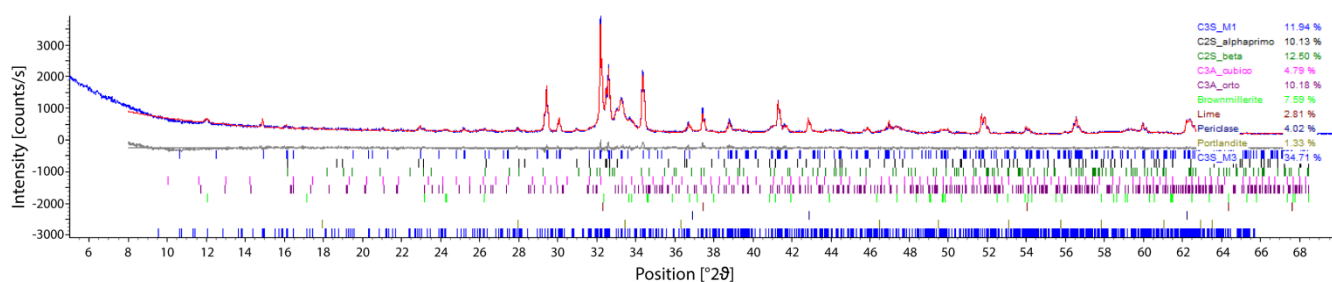


Figure 5.8: Rietveld refinement of clinker *C&bc_4* from the first firing series. Observed pattern (blue line), calculated pattern (red line) and the difference between them (grey line) are reported. Vertical bars indicate the position of the Bragg's reflections for every phase considered during the refinement.

The burnability of each raw meal was evaluated by observing the overall C₃S and CaO content (Figure 5.9a). As expected, clinker obtained starting from the raw meal *bc_1* exhibits the best C₃S/CaO ratio (Figure 5.9b) due to a high C₃S content (~62 wt%) coupled with limited free lime (~0.4 wt%). This because raw meal *bc_1* is the only one without the coarse-grained carbonate fraction, corresponding thus to a standard raw meal in terms of the components particle size distribution. However, the extremely high value of the C₃S/CaO ratio in clinker from raw meal *bc_1* has to be properly interpreted: the burnability of raw meal *bc_1* compared with the one of the other raw meals is not ten times greater. The extremely high value is due to the very low CaO wt% that make the C₃S/CaO ratio remarkably increase; as an example, the differences between clinker *bc_1* and *C&bc_4* concerning C₃S and CaO weight fraction are around 15 wt% and 2.5 wt% respectively.

Shifting the attention from raw meal *bc_1* towards the raw meals from *C&bc_2* to *C&bc_6* it would be reasonable to assume that the burnability will get linearly worse, because the coarse-grained limestone

fraction gradually increases up to the 76 wt% of the total. Quantitative phase analysis results deny this assumption: the expected negative trend of the raw meals burnability happens from raw meal *bc_1* to raw meal *C&bc_3* and again from raw meal *C&bc_4* to raw meal *C&bc_6*. On the contrary, raw meal *C&bc_4* points out the best burnability, second only to the standard *bc_1*. Clinker obtained from raw meal *C&bc_6* has the worst burnability: low C_3S (31.2 wt%) jointly to high CaO (5.0 wt%). However, data concerning clinker *C&bc_6* have to be handled with care due to the parent raw meal extreme configuration, almost entirely made by basalt and coarse-grained limestone.

This general behaviour of the six studied raw meals can be ascribed to a combination between the raw mixture (fine-grained limestone plus fine-grained basalt) eutectic temperature and the coarse-grained limestone wt% within the OPC clinker raw meal. In particular, raw meals *C&bc_3* and *C&bc_4* exhibits a good burnability because they have the best ratio between the eutectic temperature of the corresponding raw mixture (1310 and 1265 °C respectively) and the coarse-grained limestone weight fraction in the raw meal (~53 and ~60 wt% respectively). On the contrary, raw mixtures *bc_5* and *bc_6* do have a lower eutectic temperature (1170 °C), but the coarse-grained limestone fraction within the raw meal is too abundant, greater than 70 wt%, to react properly during the thermal treatment. Hence, the appearance of the melt at a lower temperature is not enough to ensure the proper reactivity of the raw meal.

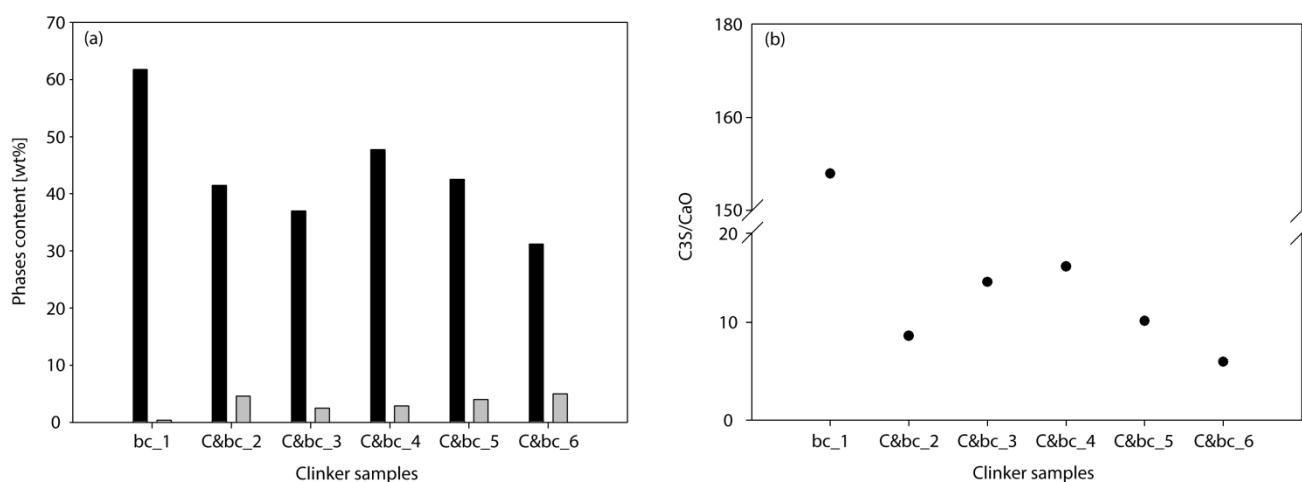


Figure 5.9: (a) C_3S (black bars) and CaO (grey bars) weight content in clinker samples, as determined processing XRPD data by Rietveld refinements. (b) C_3S to CaO weight fraction ratios, pointing out a positive bulge corresponding to clinker sample *C&bc_4*. Samples are listed in both graphs according to increasing coarse-grained limestone fraction.

The positive burnability peak involving raw meal *C&bc_4* can be stressed considering the C_3S/C_2S wt% ratio too, as outlined by Figure 5.10 where the overall trend is similar to the one reported in Figure 5.9b. First, the C_3S/C_2S ratio decreases from clinker *bc_1* to clinker *C&bc_3*, then exhibits the expected positive peak for clinker *C&bc_4* and finally decreases again from clinkers *C&bc_4* to *C&bc_6*.

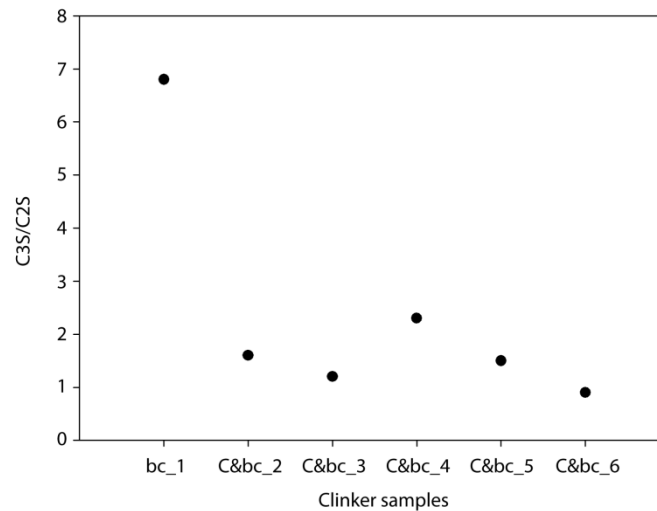


Figure 5.10: C₃S to C₂S weight fractions ratios, pointing out a positive bulge corresponding to clinker sample *C&bc_4*. Samples are listed according to increasing coarse-grained limestone fraction.

Dealing with the aluminates, the weight fractions of C₃A, C₄AF and their sum are not significantly affected by the proportions between fine- and coarse-grained limestone in the raw meal (Figure 5.11). This can seem in contrast to the different composition of the eutectic melts. But, shifting from an eutectic to another except for *bc_1*, the overall aluminium content in the eutectic melt remains nearly the same, ranging from 10 to 20 wt%. Aluminium wt% is likely be the driving factor on the aluminates weight fraction during the cooling stage, whereas silicon and calcium content do not affect the aluminates crystallization, probably because these elements are incorporated within the clinker silicate phases.

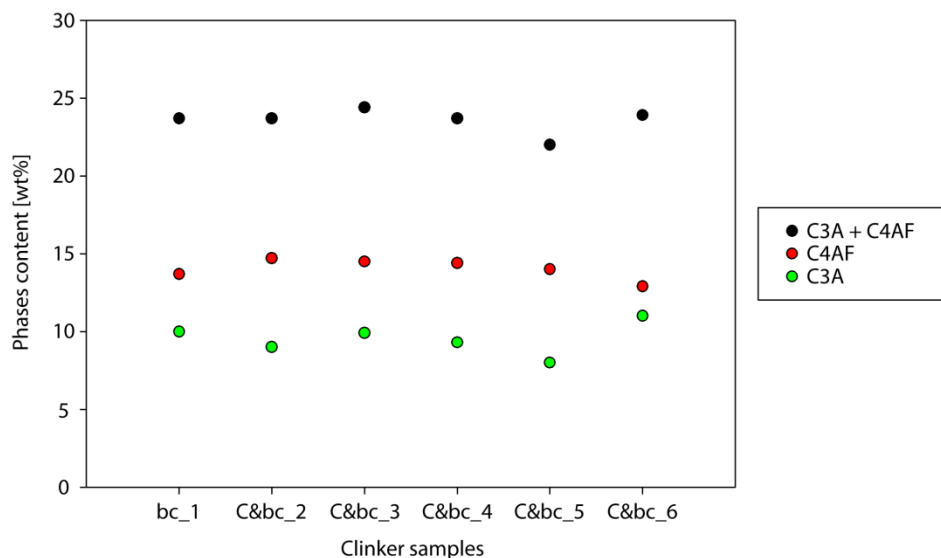


Figure 5.11: C₃A (green circles), C₄AF (red circles) and their sum (black circles) weight fraction, as determined processing XRPD data by Rietveld refinements. Samples are listed according to increasing coarse-grained limestone fraction.

Concerning minor and secondary phases, free lime content is significant in all the clinkers except *bc_1*, the only one obtained from an homogeneous raw meal without the coarse-grained limestone fraction. Conversely, it attests above the 4.0 wt% in clinkers *C&bc_2*, *C&bc_5*, *C&bc_6* and between

2.5 and 3.0 wt% in clinkers *C&bc_3* and *C&bc_4* pointing out again the good burnability of these latter.

Periclase content is significant in the whole set of clinker samples, ranging from 3.0 to 4.2 wt%, because of the high magnesium content in the raw meals due to the use of basalt. Noteworthy the fact that the clinker obtained from raw meal *bc_1* is the one with more periclase. Despite this, the content is always below the maximum admissible limit in commercial clinkers (Figure 5.12), equal to 5.0 wt% as reported by the European normative UNI EN 197-1.

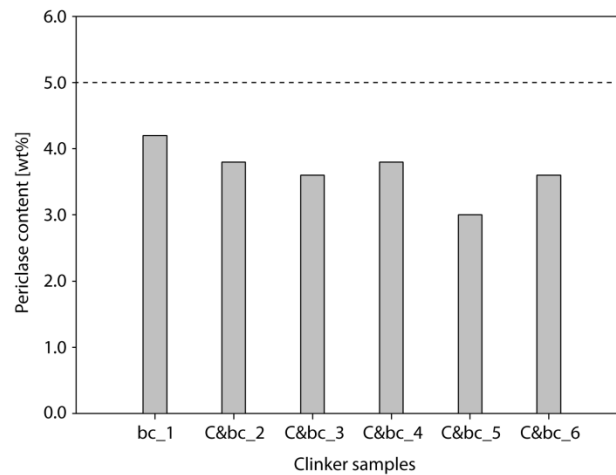


Figure 5.12: Periclase weight content in clinker samples obtained at $T = 1450\text{ }^{\circ}\text{C}$, as determined processing XRPD data by Rietveld refinements. Dashed line indicates the maximum admissible limit for MgO (5.0 wt%) in an ordinary Portland cement clinker.

The polymorphism of the main crystalline phases is mostly affected by the raw meals bulk chemical composition rather than by the different proportions between fine- and coarse-grained limestone. High MgO and low SO_3 contents in the raw meals and a consequently high MgO/ SO_3 ratio drive the C_3S polymorphism (Maki and Goto, 1982; Maki et al., 1992): the M3 form always prevails over the M1 in all the clinkers (Figure 5.13) as the M3/M1 ratio is well above one in all the samples. Moreover, C_3S polymorphism proves the correctness of the quenching method because a slow cooling rate would have promoted the crystallization of the M1 form (Kurdowski, 2014). Similarly, the relatively high Na_2O wt% in the raw meals drives the C_3A polymorphism (Takeuchi et al., 1980), stabilizing mainly the orthorhombic form rather the cubic one as reported in Figure 5.14. This behaviour further extends the findings outlined in Chapter 4 concerning the effects of minor elements, even dealing with heterogeneous industrial raw meals. Magnesium and sodium effects on the C_3S and C_3A polymorphism are still valid indeed, even treating unconventional raw meals configuration in terms of components particles size distribution.

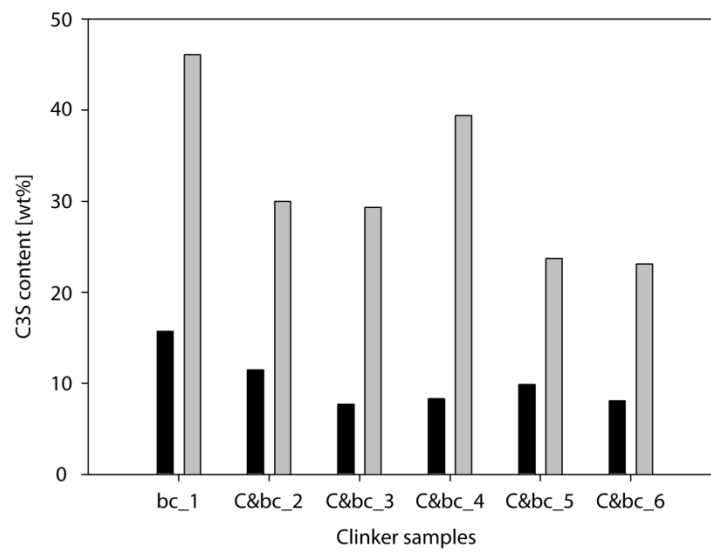


Figure 5.13: C_3S M1 (black bars) and M3 (grey bars) polymorphs weight fraction in sintered clinkers, as determined processing XRPD data by Rietveld refinements.

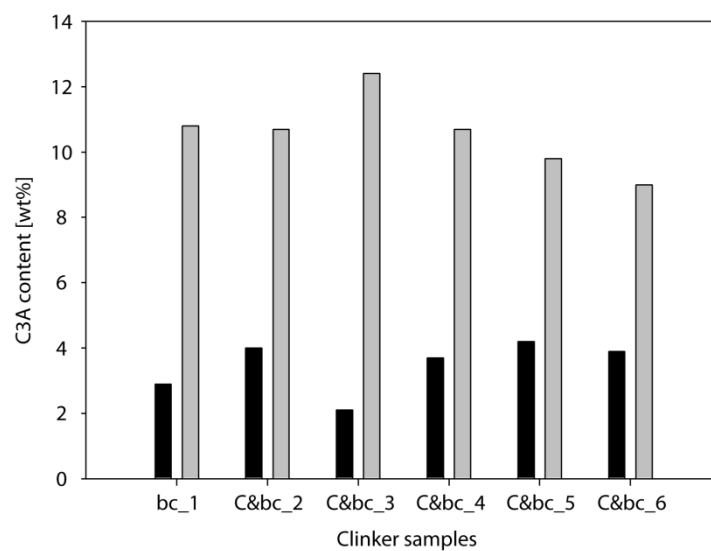


Figure 5.14: Cubic (black bars) and orthorhombic (grey bars) C_3A polymorphs weight fraction, as determined processing XRPD data by Rietveld refinements.

5.4.2 Fluorine-doped raw meals

The same raw meals previously investigated (now addressed as *bc_1F*, *C&bc_2F*, *C&bc_3F*, *C&bc_4F*, *C&bc_5F* and *C&bc_6F*) were also doped by a 0.5 wt% CaF₂ addition to enhance the C₃S content in the clinkers. Crystalline phases and polymorphic assemblage are the same encountered in fluorine-free clinkers; fluorine concentration within the raw meals is too low to give proper fluorine phases in the final product. Table 5.6 reports the quantitative phase analysis results without taking into account the polymorphism; detailed results, including phases polymorphism, are given in Appendix C2.

Phase	<i>bc_1F</i>	<i>C&bc_2F</i>	<i>C&bc_3F</i>	<i>C&bc_4F</i>	<i>C&bc_5F</i>	<i>C&bc_6F</i>
C ₃ S	63.6	48.4	46.7	55.9	45.6	47.3
C ₂ S	8.3	21.2	24.5	15.7	24.2	16.2
C ₃ A	8.5	11.1	9.9	9.5	8.5	6.1
C ₄ AF	15.5	13.2	11.3	11.8	14.1	13.9
CaO	0.3	2.2	3.6	3.3	4.2	13.2
Ca(OH) ₂	0.1	0.3	0.4	0.3	0.4	0.4
MgO	3.7	3.6	3.6	3.6	3.1	2.9

Table 5.6: Quantitative phase composition (wt%) of clinkers obtained from CaF₂-doped raw meals, as determined processing XRPD data by the Rietveld method. Uncertainty not reported because the results shown here are average values between the two firing series.

The mineralizing effect of fluorine is significant, concerning the C₃S weight fraction. All clinkers effectively exhibit high C₃S wt% with respect to the ones obtained from fluorine-free raw meals. Figure 5.15 compares the C₃S wt% from the two sets of raw meals. The average percentage increase of C₃S wt% is ~ 20 %, more marked in clinkers obtained starting from heterogeneous raw meals with both fine- and coarse-grained limestone fractions. As a consequence of the C₃S wt% increase, the C₂S wt% decreases (Figure 5.16).

As in fluorine-free clinkers, raw meal *bc_1* exhibits the best burnability in terms of C₃S/CaO wt% ratio. Again, the burnability does not decrease linearly from raw meal *bc_1* to raw meal *C&bc_6*, but a positive outlier is represented by *C&bc_4* raw meal (Figure 5.17).

Taking into account the C₃S polymorphism, it is not affected by the fluorine addition, relying again on the MgO and SO₃ wt% within the raw meals and as a consequence on the MgO/SO₃ ratio. M3 is again the most occurring polymorph in all clinkers. As regards the C₂S polymorphism, β-C₂S is the most occurring form, in agreement with results reported in Chapter 4 concerning the fluorine effect on standard OPC raw meals.

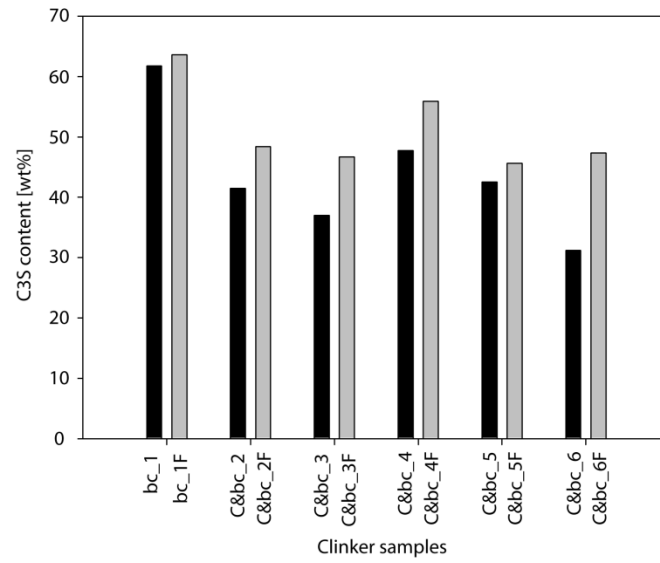


Figure 5.15: Comparison between C₃S wt% in clinkers obtained from fluorine-free raw meals (black bars) and fluorine-doped raw meals (grey bars).

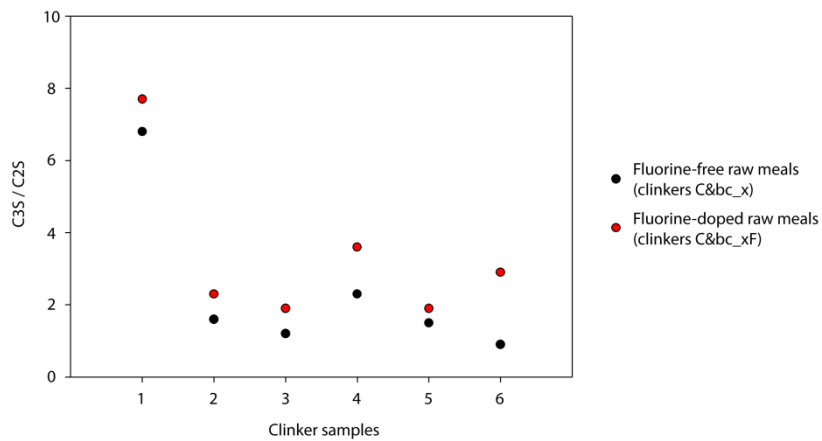


Figure 5.16: Comparison of the C₃S/C₂S ratio in clinkers obtained from fluorine-free (black circles) and fluorine-doped (red circles) raw meals. Letter *x* reported in the plot legend allows to identify the clinker samples, as reported on the x-axis.

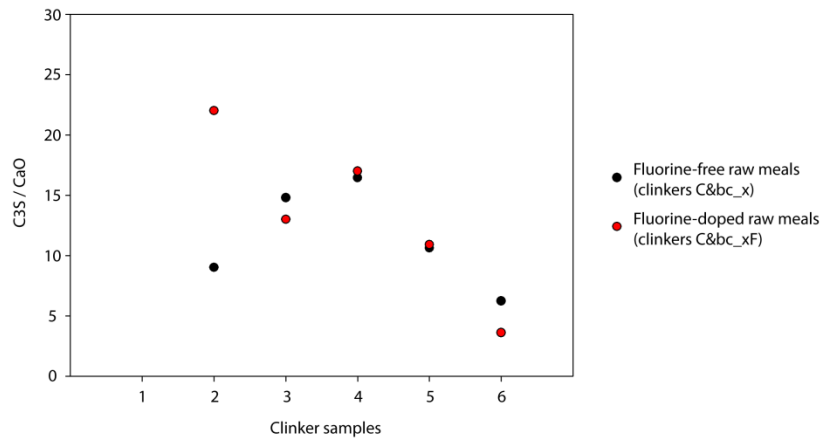


Figure 5.17: Comparison of the C_3S/CaO ratio in clinkers obtained from fluorine-free (black circles) and fluorine-doped (red circles) raw meals. Letter x reported in the plot legend allows to identify the clinker samples, as reported on the x-axis. Values corresponding to clinker samples bc_I and bc_IF are not shown (out of scale) to better highlight the differences between other samples.

Dealing with the aluminates, the weight fractions of C_3A , C_4AF and their sum are not significantly different compared with results obtained on clinkers from fluorine-free raw meals. However an inversion of the C_3A/C_4AF ratio is observed, switching from values greater than one to values lower than one (Figure 5.18); this effect can be ascribed to the fluorine occurrence because the bulk chemical composition between fluorine-free and fluorine-doped raw meals is identical, except for fluorine (Odler, in Ghosh and Kurdowski, 1991). Moreover, concerning the C_3A polymorphism, the cubic form is not anymore the prevailing one, despite the high sodium content in the raw meals (Figure 5.19). This is in agreement with the results found in Chapter 4, where the fluorine addition hinders the orthorhombic form stabilization even in clinkers from sodium-doped raw meals.

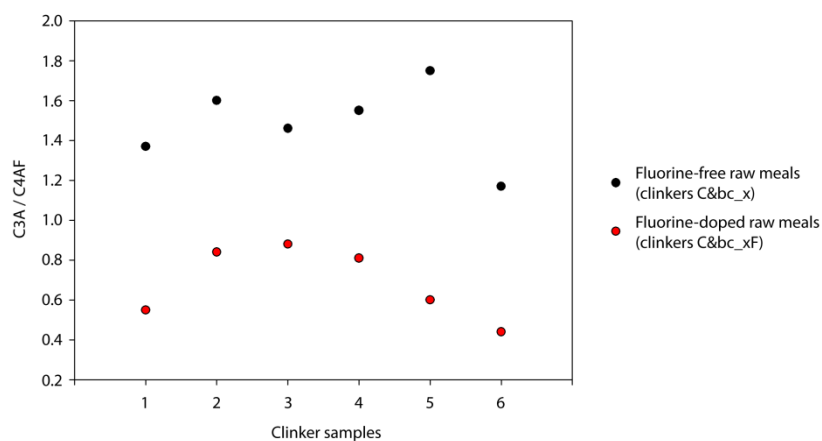


Figure 5.18: Comparison of the C_3A/C_4AF ratio in clinkers obtained from fluorine-free (black circles) and fluorine-doped (red circles) raw meals. Letter x reported in the plot legend allows to identify the clinker samples, as reported on the x-axis.

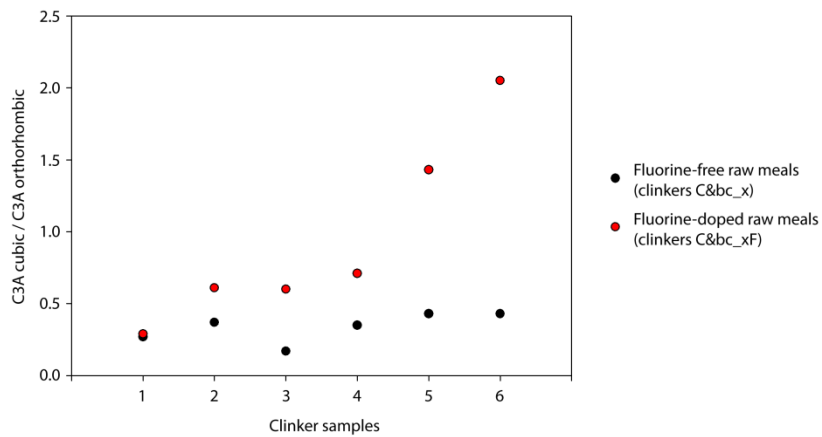


Figure 5.19: Comparison of the cubic C_3A to orthorhombic C_3A ratio in clinkers obtained from fluorine-free (black circles) and fluorine-doped (red circles) raw meals. Letter x reported in the plot legend allows to identify the clinker samples, as reported on the x-axis.

Again, free lime is detected in all the clinkers except bc_1 , the only one obtained from an homogeneous raw meal without the coarse-grained limestone fraction. It significantly decreases only in clinker $C\&bc_2F$, whereas in clinkers from $C\&bc_3F$ to $C\&bc_5F$ on values ranging from ~ 3 to ~ 4 wt% keeping close to values reported in fluorine-free clinkers. The value found in clinker $C\&bc_6$ represents an outlier, again due to the extreme setup of its raw meal.

Finally, periclase weight fraction slightly decrease, switching from an average 3.7 wt% in fluorine-free clinkers to a 3.4 wt% in fluorine-doped clinkers. This because more magnesium is likely incorporated in the C_3S structure as calcium replacer.

5.5 Conclusions

The behaviour of heterogeneous raw meals was tested in this chapter, taking jointly into account different limestone grains size and unconventional raw materials for OPC clinker raw meals formulation. This issue could play a key role in reducing the environmental impact of the OPC clinker production process; however very little research had been done on it yet.

Under standard conditions, a decrease in both the burnability of a raw meal and as a consequence in the final clinker quality would be expected when increasing the heterogeneity of raw materials in terms of components grain size and mineralogical composition. Results carried out from this study demonstrated that the raw meals burnability does not point out a negative trend when increasing the coarse-grained limestone weight fraction. In particular, the second best burnability after the reference raw meal (where only fine-grained components were employed) is outlined by an intermediate raw meal, made by ~ 60 wt% of coarse-grained limestone. Despite this raw meal has not the lowest eutectic temperature dealing with its fine-grained limestone and basalt composition, it is the right proportion between the limestone coarse-grained fraction wt% and the corresponding raw mixture eutectic temperature that eases the burnability and lead to high silicate content jointly to low free lime.

Finally, the addition of fluorine within the second series of thermal treatments proved that the mineralizing effect of fluorine on the tricalcium silicate remains substantial even in very heterogeneous raw meal systems. Higher tricalcium silicate and low free lime content were found when compared with fluorine-free raw meals. Both in fluorine-free and fluorine-doped raw meals the crystalline phases polymorphism is driven by the bulk chemical composition rather than by the system heterogeneity.

Chapter 6

General conclusions

The present thesis dealt with advances in the characterization and formulation of ordinary Portland cement clinker raw meals. In particular, the influence of limestones petrography and calcite microstructure, minor elements and raw meals heterogeneity were investigated respectively, employing several complementary analytical techniques. The three aforementioned topics were studied separately but they clearly interact each other at the industrial scale. They were chosen because held to be the most relevant concerning ordinary Portland cement clinker production, within the global framework to reduce the environmental and economic impact of the whole manufacturing process. Moreover, the extreme variability pertaining to the production process was highlighted: an almost infinite numbers of mutually-affecting parameters can influence both the raw meals thermal behaviour and the clinker quality.

First, an alternative approach to limestones selection was introduced, taking also into account the geological features of the raw carbonate rock, jointly to its bulk chemical composition. Precisely limestones because they are the main constituent by mass of a standard OPC clinker raw meal and because they are usually considered taking into account only their bulk chemical composition, merely looking at them as calcium carbonate. Here it was proved, by comparing a detailed petrographic description with data from X-ray powder diffraction, that the diagenetic history underwent by the rock can have a significant impact on the OPC clinker raw meals burnability, especially at low temperatures. A positive trend linking the age of the sample to the calcite crystals microstrain was found. Differences in burnability reflects both on the crystalline phases weight fraction during the thermal treatment and even on the final product mineralogy and morphology. Despite the overall chemical composition remains a condition to be strictly fulfilled to have a marketable product, these findings allow to both exploit families of limestones usually not considered for OPC clinker production and to improve the efficiency of the thermal treatment.

Then, an equally important topic dealing with the OPC clinker production was investigated, despite it has already been widely explored throughout years: the influence of minor elements on the clinkerization process. The innovation lies in the fact that this part of the thesis glanced at the minor elements issue from a different point of view. Tests were indeed performed employing a natural raw mixture from a production plant as a starting material, instead of a mixture made by analytical chemical reagents as usually reported in literature. The aim was to transpose and verify results from

past studies obtained from fully chemically controlled raw meals into an actual industrial situation, where all the elements can simultaneously occur. Magnesium, sodium and sulphur were chosen as minor elements because they are usually present in natural raw materials; fluorine and chlorine because the former is a well-known alite mineraliser whereas the latter occurs in attractive industrial by-products suitable for clinker production. It was found that the investigated chemical elements when coupled together does not always affect the clinker crystalline phases assemblage of the final product, in terms of weight fraction and polymorphism, as reported by literature data. The *in situ* experiment revealed instead how chlorine, despite not being significantly incorporated in main clinker crystalline phases, could influence some major factors during the thermal treatment such as the lime reactivity or the overall melt fraction.

Finally, an unconventional and still unexplored topic, again concerning the formulation of OPC clinker raw meals, was investigated: the burnability of raw meals prepared starting from both an heterogeneous particle size distribution of limestone and an unconventional mineralogical composition. Despite the uncommon raw meal setup in terms of heterogeneity, promising and unexpected results were found. In particular, the burnability of the investigated raw meals, mainly evaluated by both tricalcium silicate and free lime content in the final clinker, does not experience a negative trend to the increase of the weight fraction of the coarse-grained limestone within the raw meal. The advantages arising from this unconventional configuration are potentially attractive. They will allow to significantly lower the economic and environmental impact of the entire production process, because of the reduction of the kiln energy consumption, of the raw materials grinding costs and of the environmental exploitation.

Chapter 7

References

- Aggarwal P.S., Gard J.A., Glasser F.P., Biggar G.M. (1972) “*Synthesis and properties of dicalcium aluminate, $2CaO \cdot Al_2O_3$* ” *Cement and Concrete Research* (2) 291-297.
- Akstinat M.H., Rott C. (1988) “*Coulometric determination of low halide concentration in inorganic binders and minerals raw materials*” *Zement Kalk Gips International* (3) 138-143.
- Alabeed S., Soltan A.M., Abdelghany O., Amin B.E.M., El Tokhi M., Khaleel A., Musalim A. (2014) “*United Arab Emirates limestones: impact of petrography on thermal behaviour*” *Mineralogy and Petrology* (108) 837-852.
- Andrade F.R.D., Pecchio M., Bendoraitis D.P., Montanheiro T.J., Kihara Y. (2010) “*Basalt mine-tailings as raw-materials for Portland clinker*” *Cerâmica* (56) 39-43.
- Arceo H.B., Glasser F.P. (1990) “*Fluxing reactions of sulphate and carbonates in cement clinkering. I. Systems $CaSO_4$ - K_2SO_4 and K_2SO_4 - $CaCO_3$* ” *Cement and Concrete Research* (20) 862-868.
- Arthur M.A., Fischer A.G. (1977) “*Upper Cretaceous-Paleocene magnetic stratigraphy at Gubbio, Italy*” *Geological Society of America Bulletin* (88) 367-371.
- Bahamonde J.R., Merino-Tomé O., Della Porta G., Villa E. (2015) “*Pennsylvanian carbonate platforms adjacent to deltaic systems in an active marine foreland basin (Escalada Fm., Cantabrian Zone, NW Spain)*” *Basin Research* (27) 208-229.
- Benhelal E., Zahedi G., Shamsaei E., Bahadori A. (2013) “*Global strategies and potentials to curb CO_2 emissions in cement industry*” *Journal of Cleaner Production* (51) 142-161.
- Beruto D.T., Botter R., Cabella R., Lagazzo A. (2010) “*A consecutive decomposition-sintering dilatometer method to study the effect of limestone impurities on lime microstructure and its water reactivity*” *Journal of the European Ceramic Society* (30) 1277-1286.
- Bhatty J.I. (1995) “*Role of minor elements in cement manufacture and use*” RD109T, Portland Cement Association, Skokie, Illinois, USA.
- Bikbaou M. (1980) “*Mineral formation processes and phase composition of alinite clinker*” *Proceedings of the 7th International Congress on Chemistry of Cement, Paris, France*, 371-376.
- Bish D.L., Howard S.A. (1988) “*Quantitative phase analysis using the Rietveld method*” *Journal of Applied Crystallography* (21) 86-91.
- Bish D.L., Post J.E. (1993) “*Quantitative mineralogical analysis using the Rietveld full-pattern fitting method*” *American Mineralogist* (78) 932-940.
- Blanco-Varela M.T., Palomo A., Vázquez T. (1984) “*Effect of fluorspar on the formation of clinker phases*” *Cement and Concrete Research* (14) 397-406.

- Boden T.A., Andres R.J., Marland G. (2016) “*Global, regional and national fossil-fuel CO₂ emissions*” Carbon Dioxide Information Analysis Center, Oak Ridge National Laboratory, U.S. Department of Energy, Oak Ridge TN, U.S.A. doi 10.3334/CDIAC/00001_V2016.
- Bonafous L., Bessada C., Massiot D., Coutures J.P., Le Holland B., Colombet P. (1995) “*²⁹Si MAS NMR study of dicalcium silicate: the structural influence of sulfate and alumina stabilizers*” Journal of the American Ceramic Society (78) 2603-2608.
- Boni A., Cassinis G. (1973) “*Carta geologica delle Prealpi Bresciane a sud dell’Adamello*” Atti dell’Istituto Geologico dell’Università di Pavia (23) 119-159.
- Boysen H., Lerch M., Stys A., Senyshyn A. (2007) “*Structure and oxygen mobility in mayenite (Ca₁₂Al₁₄O₃₃): a high-temperature neutron powder diffraction study*” Acta Crystallographica B (63) 675-682.
- Bucchi R. (1980) “*Influence of the nature and preparation of raw materials on the reactivity of raw mix*” Proceedings of the 7th International Congress on Chemistry of Cement, Paris, France, 3-43.
- Chatterjee A.K. (2011) “*Chemistry and engineering of the clinkerization process – Incremental advances and lack of breakthroughs*” Cement and Concrete Research (41) 624-641.
- Chen C., Habert G., Bouzidi Y., Jullien A. (2010) “*Environmental impact of cement production: detail of the different processes and cement plant variability evaluation*” Journal of Cleaner Production (18) 478-485.
- Cockcroft J.K., Fitch A.N. (2008) “*Experimental setups*”. In: Dinnebier R.E., Billinge S.J.L. (ed) “*Powder diffraction: Theory and practice*” Royal Society of Chemistry Publishing, Cambridge, UK.
- Coelho A. (2012) “*TOPAS-Academic, Version 5.1*” Computer Software, Bruker AXS, Karlsruhe.
- Collepari M., Monosi S., Moriconi G., Corradi M. (1979) “*Tetracalcium aluminoferrite hydration in the presence of lime and gypsum*” Cement and Concrete Research (9) 431-437.
- Colville A.A., Geller S. (1971) “*The crystal structure of brownmillerite, Ca₂FeAlO₅*” Acta Crystallographica B (27) 2311-2315.
- Courtial M., de Noirfontaine M.-N., Dunstetter F., Gasecki G., Signes-Frehel M. (2003) “*Polymorphism of tricalcium silicate in Portland cement: a fast visual identification of structure and superstructure*” Powder Diffraction (18) 7-15.
- Darweesh H.H.M. (2001) “*Low temperature Portland cement clinker based on alkaline basaltoid and composite mineralizers*” Industrial Ceramics (21) 5-8.
- De la Torre M.A.G., Morsli K., Zahir M., Aranda M.A.G. (2007) “*In situ synchrotron powder diffraction study of active belite clinkers*” Journal of Applied Crystallography (40) 999-1007.
- De la Torre M.A.G., De Vera R.N., Cuberos A.J.M., Aranda M.A.G. (2008) “*Crystal structure of low magnesium-content alite: Application to Rietveld quantitative phase analysis*” Cement and Concrete Research (38) 1261-1269.
- Della Porta G., Kenter J.A.M., Bahamonde J.R., Immenhauser A., Villa E. (2003) “*Microbial boundstone dominated carbonate slope (Upper Carboniferous, N Spain): microfacies, lithofacies distribution and stratal geometry*” Facies (49) 175-207.
- Della Porta G., Merino-Tomé O., Kenter J.A.M., Verwer K. (2013) “*Lower Jurassic microbial and skeletal carbonate factories and platform geometry (Djebel Bou Dahar, High Atlas, Morocco)*”. In:

- Verwer K., Playton T.E., Harris P.M. (ed) *“Deposits, architecture and controls of carbonate margin, slope and basinal settings”* SEPM Special Publication 105.
- Dinnebier R.E., Billinge S.J.L. (2008) *“Powder diffraction: Theory and practice”* Royal Society of Chemistry Publishing, Cambridge, UK.
- Dunham R.J. (1962) *“Classification of carbonate rocks according to depositional texture”* American Association of Petroleum Geologists Memories (1) 108-121.
- Dunstetter F., De Noirfontaine M.N., Courtial M. (2006) *“Polymorphism of tricalcium silicate, the major compound of Portland cement clinker: 1. Structural data: review and unified analysis”* Cement and Concrete Research (36) 39-53.
- Edwards J.W., Speiser R., Johnston H.L. (1951) *“High temperature structure and thermal expansion of some metals as determined by X-ray diffraction data. I. Platinum, tantalum, niobium and molybdenum”* Journal of Applied Physics (22) 424.
- El-Ashkar A.A.A. (2002) *“Studies on mineralogical, geochemical and physical characteristics on basalts of Cairo-Suez road for evaluation for using in cement industry”* Thesis, El-Azhar University.
- El-Didamony H., Rahman A.A., Nassar F., Saraya M. (2010) *“Effect of basalt on the burnability of raw meal of Portland cement clinker”* Indian Journal of Engineering & Materials Sciences (17) 282-288.
- El-Hafiz N.A.A., El-Moghny M.W.A., El-Desoky H.M., Afifi A.A. (2015) *“Characterization and technological behaviour of basalt raw materials for Portland cement clinker production”* International Journal of Innovative Science, Engineering & Technology (2).
- El-Sayed A.E.A. (2002) *“Influence of altered basalt on the burnability of Portland cement clinker”* Indian Journal of Engineering & Materials Sciences (9) 147-152.
- Embry A.F., Klovan J.E. (1971) *“A Late Devonian reef tract on the Northeastern Banks Island, NWT”* Canadian Petroleum Geologists Bulletin (19) 730-781.
- Feiz R., Ammenberg J., Baas L., Eklund M., Helgstrand A., Marshall R. (2015) *“Improving the CO₂ performance of cement, part I: utilizing life-cycle assessment and key performance indicators to assess development within the cement industry”* Journal of Cleaner Production (98) 272-281.
- Ferrari M., Lutterotti L. (1994) *“Method for the simultaneous determination of anisotropic residual stresses and texture by X-ray diffraction”* Journal of Applied Physics (76) 7246-7255.
- Fitch A.N. (2004) *“The high resolution powder diffraction beam line at ESRF”* Journal of Research of the National Institute of Standards and Technology (109) 133-142.
- Flügel E. (2004) *“Microfacies of carbonate rocks. Analysis, interpretation and application”* Springer-Verlag, Berlin.
- Folk R.L. (1959) *“Practical petrographic classification of limestones”* American Association of Petroleum Geologists Bulletin (43) 1-38.
- Gartner E.M., Tang F.J. (1987) *“Formation and properties of high sulfate Portland cement clinkers”* Cemento (84) 141-164.
- Golovastikov N.I., Matveeva R.G., Belov N.V. (1975) *“Crystal structure of the tricalcium silicate 3CaO.SiO₂ = C₃S”* Soviet Physics Crystallography (20) 441.
- Gosh S.N., Kurdowski W. (1991) *“Cement and concrete science technology”* ABI Books Private Ltd., New Delhi.

- Greer W.L., Johnson M.D., Morton E.L., Raught E.C., Steuch H.E., Trusty Jr C.B. (1992) “Portland cement” in “Air pollution engineering manual” Buonicore A.J., Davis W.T. (eds), Van Nostrand Reinhold, New York.
- Greig J.W. (1927) “Immiscibility in silicate melts: Part I” American Journal of Science (13) 1-44.
- Hall C., Scrivener K.L. (1998) “Oilwell cement clinkers: X-ray microanalysis and phase composition” Advanced Cement Based Materials (7) 28-38.
- Hassaan M.Y. (2001) “Basalt rock as an alternative raw material in Portland cement manufacture” Materials Letters (50) 172-178.
- Horkoss S., Lteif R., Rizk T. (2011) “Influence of the clinker SO_3 on the cement characteristics” Cement and Concrete Research (41) 913-919.
- Huntzinger D.N., Eatmon T.D. (2009) “A life-cycle assessment of Portland cement manufacturing: comparing the traditional process with alternative technologies” Journal of Cleaner Production (17) 668-675.
- James N.P. (1984) “Shallowing-upward sequences in carbonates”. In: Walker, R.G. (ed) “Facies Models” Geological Association of Canada, Geoscience Canada Reprint Series (1) 213–228.
- Jeffery J.W. (1952) “The crystal structure of tricalcium silicate” Acta Crystallographica (5) 26.
- Jennings H.M., Dalgleish B.J., Pratt P.L. (1981) “Morphological development of hydrating tricalcium silicate as examined by Electron Microscopy techniques” Journal of the American Ceramic Society (64) 567-572.
- Kajaste R., Hurme M. (2016) “Cement industry greenhouse gas emissions – management options and abatement cost” Journal of Cleaner Production (112) 4041-4052.
- Khadilkar S.A., Gosh D., Page C.H. (1990) “Investigations on the use of basalt as a corrective in Portland cement manufacture – a case study” 2nd International Seminar on Cement and Building Materials, New Delhi, India.
- Kim Y.M., Lee J.H., Hong S.H. (2003) “Study of alinite cement hydration by impedance spectroscopy” Cement and Concrete Research (33) 299-304.
- Klemm W.A., Bhatti J.I., Holub K.J. (1979) “Effects of calcium fluoride mineralization on silicates and melt formation on Portland cement clinker” Cement and Concrete Research (9) 489-496.
- Kozul R., Darwin D. (1997) “Effects of aggregate type, size and content on concrete strength and fracture energy” SM Report 43, University of Kansas centre for research, Lawrence.
- Kurdowski W. (2014) “Cement and concrete chemistry” Springer Science + Business Media B.V.
- Lea F.M., Parker T.W. (1935) “The Quaternary System $CaO-Al_2O_3-SiO_2-Fe_2O_3$ in relation to cement technology” Building Research Technical Paper (16), London.
- Lea F.M. (1971) “Chemistry of cement and concrete, 3rd Edition” Arnold Chemical Publishing, New York, USA.
- Lech R. (2006a) “Thermal decomposition of limestone: Part 1 – Influence of properties on calcination time” Silicates Industriels (71) 103-109.
- Lech R. (2006b) “Thermal decomposition of limestone: Part 2 – Influence of contraction, phase composition, phase concentrations and heating on calcination time” Silicates Industriels (71) 110-114.
- Lech R. (2006c) “Thermal decomposition of limestone: Part 3 – Kinetic curves” Silicates Industriels (71) 143-148.

- Lech R., Wodnicka K., Pedzich Z. (2009) “*Effect of the limestone fabric on the fabric development in burnt lime*” Zement Kalk Gips International (62) 63-72.
- Lee F.C., Banda H.M., Glasser F.P. (1982) “*Substitution of Na, Fe and Si in tricalcium aluminate and the polymorphism of solid solutions*” Cement and Concrete Research (12) 237-246.
- Li X., Xu W., Wang S., Tang M., Shen X. (2014) “*Effect of SO₃ and MgO on Portland cement clinker: formation of clinker phases and polymorphism*” Construction and Building Materials (58) 182-192.
- Lörke P., Lörke A., inventors; Lörke P., Lörke A., assignees. “*Method of producing cement clinker and associated device*” United States patent US 6264738 B1, July 24th 2001.
- Lörke P. (2011) “*Innovative, energy-efficient manufacture of cement by means of controlled mineral formation – Part I*” Zement Kalk Gips International (1) 48-58.
- Ludwig H.-M., Zhang W. (2015) “*Research review of cement clinker chemistry*” Cement and Concrete Research (78) 24-37.
- Ma C., Connolly H.C., Beckett J.R., Tschauner O., Rossman G.R., Kampf A.R., Zega T.J., Sweeney-Smith S.A., Schrader D.L. (2011) “*Brearleyite, Ca₁₂Al₁₄O₃₂Cl₂, a new alteration mineral from the NWA 1934 meteorite*” American Mineralogist (96) 1199-1206.
- Maki I., Goto K. (1982) “*Factors influencing the phase constitution of alite in Portland cement clinker*” Cement and Concrete Research (12) 301-308.
- Maki I., Fukuda K., Yoshida H., Kumaki J. (1992) “*Effect of MgO and SO₃ on the impurity concentration in alite in Portland cement clinker*” Journal of the American Ceramic Society (75) 3163-3165.
- Marinoni N., Pavese A., Foi M., Trombino L. (2005) “*Characterization of mortar morphology in thin sections by digital image processing*” Cement and Concrete Research (35) 1613-1619.
- Marinoni N., Allevi S., Marchi M., Dapiaggi M. (2012) “*A kinetic study of the thermal decomposition of limestone using in situ high temperature X-ray powder diffraction*” Journal of the American Ceramic Society (95) 2491-2498.
- Marinoni N., Bernasconi A., Della Porta G., Marchi M., Pavese A. (2015) “*The role of petrography on the thermal decomposition and burnability of limestones used in industrial cement clinker*” Mineralogy and Petrology (109) 719-731.
- Merino-Tomé O., Della Porta G., Kenter J.A.M., Verwer K., Harris P.M., Adams E., Playton T.E., Corrochano D. (2012) “*Sequence development in an isolated carbonate platform (Lower Jurassic, Djebel Bou Dahar, High Atlas, Morocco): Influence of tectonics, eustasy and carbonate production*” Sedimentology (59) 118-155.
- Mintus F., Hamel S., Krumm W. (2006) “*Wet process rotary cement kilns: modelling and simulations*” Clean Technologies and Environmental Policy (8) 112-122.
- Mishulovich A. (1994) “*Halides as catalysts for calcination*” RD1991, Portland Cement Association, Skokie, Illinois, USA.
- Mondal P., Jeffery J.W. (1975) “*The crystal structure of tricalcium aluminate, Ca₃Al₂O₆*” Acta Crystallographica B (31) 689-697.
- Moore P.B. (1973) “*Bracelets and pinwheels: a topological-geometrical approach to the calcium orthosilicate and alkali sulfate structures*” American Mineralogist (58) 32-42.

- Moropoulou A., Bakolas A., Aggelakopoulou E. (2001) “*The effects of limestone characteristics and calcination temperature to the reactivity of quicklime*” Cement and Concrete Research (31) 633-639.
- Moussa S.M., Ibberson R.M., Bieringer M., Fitch A.N., Rosseinsky M.J. (2003) “*In situ measurements of cation order and domain growth in an electroceramic*” Chemistry of Materials (15) 2527-2533.
- Muan A., Osborn E.F. (1965) “*Phase equilibria among oxides in steel-making*” Addison-Wesley, Reading, MA, USA.
- Müller N., Harnisch J. (2008) “*A blueprint for a climate friendly cement industry*” WWF International, Switzerland.
- Mumme W.G., Hill R.J., Bushnellwye G., Segnit E.R. (1995) “*Rietveld crystal-structure refinements, crystal-chemistry and calculated powder diffraction data for the polymorphs of dicalcium silicate and related phases*” Neues Jahrbuch für Mineralogie. Abhandlungen (169) 35-68.
- Mumme W.G., Cranswick L., Chakoumakos B. (1996) “*Rietveld crystal structure refinements from high temperature neutron powder diffraction data for the polymorphs of dicalcium silicate*” Neues Jahrbuch für Mineralogie. Abhandlungen (170) 171-188.
- Natta G., Passerini L. (1929) “*Soluzioni solide, isomorfismo e sinmorfismo tra gli ossidi dei metalli bivalenti. I. Sistemi: CaO-CdO, CaO-MnO, CaO-CoO, CaO-NiO, CaO-MgO*” Gazzetta Chimica Italiana (59) 129-154.
- Nishi F., Takeuchi Y. (1984) “*The rhombohedral structure of tricalcium silicate at 1200 degrees °C*” Zeitschrift für Kristallographie (168) 197-212.
- Nishi F., Takeuchi Y., Maki I. (1985) “*The Tricalcium silicate Ca₃O[SiO₄]: the Monoclinic Superstructure*” Zeitschrift für Kristallographie (172) 297-314.
- Odler I. “*Improving energy efficiency in Portland clinker manufacturing*” in Ghosh S.N. and Kurdowski W. (1991) “*Cement and concrete science and technology: Volume 1, Part I*” ABI books private limited, New Delhi, India.
- Patel M. (1989) “*Cement from chloride containing wastes*” Silicates Industriels (3) 55-60.
- Patnaik P. (2003) “*Handbook of Inorganic Chemicals*”. The McGraw-Hill Companies, Inc., 162.
- Peethamparan S., Olek J., Lovell J. (2008) “*Influence of chemical and physical characteristics of cement kiln dusts (CKDs) on their hydration behaviour and potential suitability for soil stabilization*” Cement and Concrete Research (38) 803-815.
- Pourchet S., Regnaud L., Perez J.P., Nonat A. (2009) “*Early C₃A hydration in the presence of different kinds of calcium sulfate*” Cement and Concrete Research (39) 989-996.
- Premoli-Silva I., Sliter W.V. (1995) “*Cretaceous planktonic foraminiferal biostratigraphy and evolutionary trends from the Bottaccione section, Gubbio, Italy*” Palaeontographia Italica (82) 1-89.
- Price L., Hasanbeigi A., Lu H. (2010) “*Analysis of energy-efficiency opportunities for the cement industry in Shandong Province, China: a case study of 16 cement plants*” Energy (35) 3461-3473.
- Rankine G.A., Wright F.E. (1915) “*The ternary system CaO-Al₂O₃-SiO₂*” American Journal of Science, 4th Series (39) 1-79.
- Regourd M. (1978) “*Cristallisation et réactivité de l'aluminate tricalcique dans les ciments Portland*” Il Cemento (3) 323-335.
- Regourd M., Boikova A.I. (1992) “*Polymorphism and structure of Portland phases*” Proceedings of the 9th International Congress on the Chemistry of Cement, New Delhi, India.

- Rodriguez-Navarro C., Ruiz-Agudo E., Luque A., Rodriguez-Navarro A.B., Ortega-Huertas M. (2009) "Thermal decomposition of calcite: mechanism of formation and textural evolution of CaO nanocrystals" *American Mineralogist* (94) 578-593.
- Ronov A.B. (1985) "The distribution of basalts, andesites and rhyolites on the continents and continental margins and in the oceans" *International Geology Review* (27) 1276-1284.
- Sabbioni C., Zappia G., Riontino C., Blanco-Varela M.T., Aguilera J., Puertas F., Van Balen K., Toumbakari E.E. (2001) "Atmospheric deterioration of ancient and modern hydraulic mortars" *Atmospheric Environment* (35) 539-548.
- Sabbioni C., Bonazza A., Zappia G. (2002) "Damage on hydraulic mortars: the Venice Arsenal" *Journal of Cultural Heritage* (3) 83-88.
- Sasaki S., Fujino K., Takeuchi Y. (1979) "X-ray determination of electron-density distribution in oxides, MgO, MnO, CoO and NiO and atomic scattering factors of their constituent atoms" *Proceedings of the Japan Academy B* (55) 43-48.
- Schreiber, Yonley and Associates (2007) "Beneficial reuse of materials in the cement manufacturing process" SN2868, Portland Cement Association, Skokie, Illinois, USA.
- Sinha S.K., Handoo S.K., Chatterjee A.K. (1980) "Comminution and dissociation characteristics of Indian Limestones" *Proceedings of the 7th International Congress on the Chemistry of Cement, Paris*, 108-113.
- Soltan A.M., Kahl W.A., Hazem M., Wendschuh M., Fischer R.X. (2011) "Thermal microstructural changes of grain-supported limestones" *Mineralogy and Petrology* (103) 9-17.
- Soltan A.M., Kahl W.A., Wendschuh M., Hazem M. (2012) "Microstructure and reactivity of calcined mud supported limestones" *Mineral Processing and Extractive Metallurgy* (121) 5-11.
- Sorrentino F. (2011) "Chemistry and engineering of the production process: State of the art" *Cement and Concrete Research* (41) 616-623.
- Sprung S. (1988) "Trace elements concentration build-up and measures for reduction" *Zement Kalk Gips International* (5) 251-257.
- Staněk T., Sulovský P. (2012) "Dicalcium silicate doped with sulfur" *Advances in Cement Research* (24) 233-238.
- Stokes A.R., Wilson A.J.C. (1942) "A method of calculating the integral breadths of Debye-Scherrer lines" *Mathematical Proceeding of the Cambridge Philosophical Society* (38) 313-322.
- Takeuchi Y., Nishi F., Maki J. (1975) "Crystal structure of $Ca_{9-x}/2Na_x(Al_6O_{18})$ as a function of x" *Acta Crystallographica A* S72-S72.
- Takeuchi Y., Nishi F., Maki I. (1980) "Crystal-chemical characterization of the $3CaO \cdot Al_2O_3 \cdot Na_2O$ solid-solution series" *Zeitschrift für Kristallographie* (152) 259-307.
- Taylor H.F.W. (1990) "Cement chemistry" Academic Press, London.
- Tran T.T. (2011) "Fluoride mineralization of Portland cement: applications of double-resonance NMR spectroscopy in structural investigations of guest ions in cement phases" PhD Thesis, Faculty of Sciences, Aarhus University, Aarhus, Denmark.
- Tucker M.E. (1988) "Techniques in sedimentology" Blackwell Scientific Publications, London.
- Tucker M.E. (1991) "Sequence stratigraphy of carbonate-evaporitic basins: models and application to the Upper Permian (Zechstein) of Northeast England and adjoining North Sea" *Journal of the Geological Society of London* (148) 1019-1036.

- Uda S., Asakura E., Nagashima M. (1998) “*Influence of SO₃ on the phase relationship in the system CaO-SiO₂-Al₂O₃-Fe₂O₃*” *Journal of the American Ceramic Society* (81) 725-729.
- Udagawa S., Urabe K., Natsume M., Yano T. (1980) “*Refinement of the crystal structure of γ -Ca₂SiO₄*” *Cement and Concrete Research* (10) 139-144.
- UNI EN 197-1 (2001) “*Cement – Composition, specifications and conformity criteria for common cements*”.
- United States Geological Survey (USGS) “*Mineral Commodity Summaries, 2002-2015*” <http://minerals.usgs.gov/minerals/pubs/commodity/cement/> Last verified on September 1st, 2016.
- Van Balen K. (2003) “*Understanding the lime cycle and its influence on historical construction practice*” *Proceedings of the first international congress on construction history, Madrid 20-24th January 2003*.
- Van den Heede P., De Belie N. (2012) “*Environmental impact and life cycle assessment (LCA) of traditional and green concretes: Literature review and theoretical calculations*” *Cement and Concrete Composites* (34) 431-442.
- Van Oss H.G., Padovani A.C. (2002) “*Cement manufacture and the environment: Part I – Chemistry and technology*” *Journal of Industrial Ecology* (6) 89-105.
- Verwer K., Della Porta G., Merino-Tomé O., Kenter J.A.M. (2009) “*Controls and predictability of carbonate facies architecture in a Lower Jurassic three-dimensional barrier-shoal complex (Djebel Bou Dahar, High Atlas, Morocco)*” *Sedimentology* (56) 1801-1831.
- Voltolini M., Marinoni N., Mancini L. (2011) “*Synchrotron X-ray computed microtomography investigation of a mortar affected by alkali-silica reaction: a quantitative characterization of its microstructural features*” *Journal of Materials Science* (46) 6633-6641.
- Warren B.E., Averbach B.L. (1952) “*The separation of cold-work distortion and particle-size broadening in X-ray patterns*” *Journal of Applied Physics* (23) 497.
- Woermann E., Hahn T., Eysel W. (1979) “*The substitution of alkalis in tricalcium silicate*” *Cement and Concrete Research* (9) 701-711.
- Wright A.F., Lehmann M.S. (1981) “*The structure of quartz at 25 and 590 °C determined by neutron diffraction*” *Journal of Solid State Chemistry* (36) 371-380.
- Yannaquis N., Guinier A., (1959) “*La transition polymorphique β - γ de l'orthosilicate de calcium*” *Bulletin de la Société française de minéralogie* (82) 126.
- Young R.A. (1993) “*The Rietveld method*” *International Union of Crystallography, Oxford University Press, Oxford*.
- Zamagni J., Mutti M., Košir A. (2008) “*Evolution of shallow benthic communities during the Late Paleocene-Earliest Eocene transition in the Northern Tethys (SW Slovenia)*” *Facies* (54) 25-43.
- Ziegler E. (1971) “*Burning process – kilns, preheaters, coolers and firing equipment*” *Zement Kalk Gips International* (12) 543.

Chapter 8

Appendix

Appendix A1

Sample	Microfacies (if more than one present)	Rock texture	Components	Diagenetic features
SA		Crystalline carbonate/sparstone	Porosity between calcite crystals partially filled by silt-grade fragments of sparite crystals, Fe oxides and clay minerals	Prismatic calcite crystals (1-5 mm in cross section, 5-12 cm in length) Dissolution processes and erosion of calcite crystals forming a detrital silt partially filling the intercrystalline porosity
SL		Skeletal peloidal packstone with large benthic foraminifers with micrite matrix, microsparite and sparse sparite cement filling irregular dissolution vugs	Foraminifers (dominant <i>Alveolina</i> , sparse <i>Nummulites</i> , <i>Assilina</i> , miliolids, rotalids), fragments of echinoderms Peloids (size from 20 to 400 μm)	Shell breakage and sutured grain contact (mechanical and chemical compaction with pressure solution during burial diagenesis) Microsparite precipitation within the Alveolinid intraparticle pores Millimetre-size irregular dissolution vugs in the interparticle space and within Alveolinid foraminifers filled by equant sparite (100-400 μm) Partial neomorphic recrystallization of micrite into microsparite
UM		Skeletal wackestone/mudstone with bioclasts in micrite matrix	Planktonic foraminifers (size from 10 to 500 μm), thin shelled bivalves, ostracodes	Sparite precipitation within the foraminifer test chambers. Bioclasts recrystallization into microsparite
MO1	microfacies A	Coral-microbial boundstone with centimetre-size (1-2 cm) cement-filled primary reef cavities	Phaceloid corals (4-8 mm diameter corallites) encrusted by clotted peloidal micrite, intraparticle space filled by micrite Intercoralline space: peloidal-skeletal packstone/grainstone with peloids (20-400 μm), benthic foraminifers, echinoderms	Replacement of originally aragonite coral skeleton by calcite microsparite; micrite and microsparite filling intersepta space; partial neomorphic recrystallization of micrite into microsparite. Primary reef cm-size cavities filled by isopachous rims (1-1.7 mm thick) of radial fibrous calcite (early marine diagenesis) followed by a drusy mosaic of blocky sparite (0.5-5 mm equant crystal size; late burial diagenesis). Fractures filled by equant blocky sparite
	microfacies B	Laminated clotted peloidal micrite microbial boundstone (stromatolites)	Clotted peloidal micrite made of peloids (10-100 μm in diameter) embedded in micrite and microsparite forming millimetre-thick undulose laminae Area of peloidal skeletal grainstone with brachiopods and peloids up to 1 mm in size	Partial neomorphic recrystallization of micrite into microsparite
MO2		Peloidal skeletal packstone to grainstone with millimetre-size irregular voids (fenestrae)	Peloids (50-600 μm), micrite coated intraclasts (0.5-3 mm), oncoids (0.5-5 mm), dasycladacean algae (<i>Palaeodasycladus mediterraneus</i>), benthic foraminifera (textularids, miliolids), gastropods, bivalves and rare fragments of echinoderms	Bioerosion and micrite envelopes around molluscs; replacement of mollusc original aragonite shell by calcite equant sparite; equant sparite cement (100-800 μm) in interparticle pore space and primary voids
MO3		Peloidal packstone to rarely grainstone with millimetre-size irregular voids (fenestrae)	Peloids (50-600 μm), micrite coated intraclasts (0.5-3.5 mm), benthic foraminifera (textularids, miliolids), gastropods, bivalves, algae <i>Thaumatoporella parvovesiculifera</i>	Bioerosion and micrite envelopes around molluscs; replacement of mollusc original aragonite shell by calcite equant sparite; equant sparite cement (100-600 μm) in interparticle pore space and primary voids Fenestrae, originated by degassing, shrinking and organic matter degradation in intertidal environment later filled by both early marine (radial fibrous calcite isopachous rims) and burial equant sparite cement
MO4		Micrite coated grain and peloidal packstone and grainstone Areas of peloidal skeletal wackestone	Micrite coated intraclasts (1-7 mm) from the intertidal zone, pisoids, peloids (50-500 μm), gastropods, bivalves, benthic foraminifers, algae <i>Thaumatoporella parvovesiculifera</i> and <i>Cayeuxia</i>	Pendant and meniscus cement and meniscus laminated micritic crusts (vadose diagenesis); isopachous rims of fibrous calcite 100-200 μm thick (marine diagenesis); equant blocky sparite mosaic (meteoric phreatic to burial diagenesis) replacement of mollusc original aragonite shell by calcite equant sparite

Table A1.1 (part I): Textural features and grains composition of the selected limestones, as determined by optical microscopy observations.

AS	microfacies A	Skeletal wackestone/floatstone	Fragments of echinoderms, mostly crinoids (1-4 mm), fenestellid bryozoans, brachiopods, bivalves, gastropods, benthic foraminifera (<i>Tetrataxis</i> , <i>Climacammina</i> , <i>Ozawainella</i>), ostracodes, sponge spicules in red-stained micrite matrix rich in Fe and Mn oxides	Replacement of mollusc original aragonite shell by calcite equant sparite Stylolites (burial compaction and pressure solution) rich in Fe and Mn oxides and a late sparite following the reopening of the stylolite Intraparticle space, dissolution vugs and fractures filled by equant sparite cement
	microfacies B	Skeletal grainstone (removal of micrite by dissolution)	Brachiopods, fenestellid bryozoans, fragments of echinoderms (crinoids), benthic foraminifers	Diagenetic grainstone texture due to micrite dissolution and precipitation of equant sparite cement (nearly 100 µm crystal size) fills interparticle and intraparticle space
	microfacies C	Biocementstone with bryozoans and brachiopods in radiaxial fibrous calcite cement	Radiaxial fibrous calcite embedding fenestellid bryozoans and brachiopods	Radiaxial fibrous calcite cement (early marine diagenesis) Cavities with late saddle dolomite cement (hydrothermal late diagenesis)

Table A1.1 (part II): Textural features and grains composition of the selected limestones, as determined by optical microscopy observations.

Sample	Temperature [°C]						
	1000	1100	1200	1300	1350	1400	1450
<i>Clinker_SA</i>	1000	1100	1200	1300	1350	1400	1450
C ₃ S	-	-	-	6.3	64.1	71.2	77.7
C ₂ S	10.3	25.0	34.3	58.8	13.2	8.4	5.3
C ₃ A	1.3	1.0	2.7	8.1	11.8	10.5	8.7
C ₄ AF	4.4	7.3	10.4	10.1	4.3	4.8	5.9
CaO	53.6	45.8	38.4	15.5	5.5	4.3	1.7
Others*	30.4	20.9	14.2	1.2	1.1	0.8	0.7
<i>Clinker_SL</i>	1000	1100	1200	1300	1350	1400	1450
C ₃ S	-	-	-	25.6	66.1	74.2	75.4
C ₂ S	12.6	27.6	36.7	52.5	13.4	7.6	7.7
C ₃ A	0.9	0.7	2.1	6.0	9.9	9.9	8.5
C ₄ AF	3.2	7.9	10.1	8.7	6.6	6.0	7.7
CaO	56.3	43.2	35.7	7.0	3.7	2.3	0.7
Others*	27.0	20.6	15.3	0.2	0.2	0.1	0.0
<i>Clinker_UM</i>	1000	1100	1200	1300	1350	1400	1450
C ₃ S	-	-	-	3.9	42.8	54.5	60.6
C ₂ S	11.8	26.9	35.4	67.9	31.9	24.8	19.2
C ₃ A	1.5	0.2	1.8	4.9	10.7	9.3	10.0
C ₄ AF	2.3	7.4	10.1	11.0	6.2	5.7	6.3
CaO	57.4	43.0	34.2	11.7	7.6	5.0	3.5
Others*	27.1	22.5	18.5	0.6	0.7	0.7	0.4
<i>Clinker_MO1</i>	1000	1100	1200	1300	1350	1400	1450
C ₃ S	-	-	-	20.2	65.2	71.8	73.8
C ₂ S	13.0	27.7	35.7	58.4	16.0	11.4	10.5
C ₃ A	0.7	0.6	2.5	5.9	9.6	8.4	8.1
C ₄ AF	3.4	8.1	10.9	8.2	6.8	6.8	6.9
CaO	55.9	43.3	36.3	7.3	2.5	1.5	0.7
Others*	27.0	20.3	14.7	0.1	0.0	0.1	0.0
<i>Clinker_MO2</i>	1000	1100	1200	1300	1350	1400	1450
C ₃ S	-	-	-	32.2	59.5	69.3	69.8
C ₂ S	18.4	29.2	34.4	39.7	15.9	11.7	10.1
C ₃ A	1.7	0.3	2.8	5.8	11.9	9.2	9.2
C ₄ AF	3.3	7.3	8.8	11.1	6.7	6.0	8.1
CaO	51.6	44.0	37.0	10.8	5.3	3.1	1.9
Others*	25.0	19.2	17.0	0.4	0.7	0.7	0.9
<i>Clinker_MO3</i>	1000	1100	1200	1300	1350	1400	1450
C ₃ S	-	-	-	26.3	62.6	71.7	73.6
C ₂ S	17.6	31.2	39.3	51.5	17.9	12.0	9.3
C ₃ A	0.7	0.8	2.3	5.2	10.2	8.0	8.4
C ₄ AF	3.4	8.8	10.9	9.4	6.1	6.8	8.0
CaO	52.6	40.2	35.2	7.4	2.9	1.3	0.6
Others*	25.7	19.0	12.3	0.1	0.3	0.3	0.1

Table A1.2 (part I): Phase composition (wt%) of clinkers samples from the eight studied raw meals, at all the temperatures of the burnability test, obtained processing XRPD data by Rietveld refinements. The category “others” refers to C₂AS, C₁₂A₇, S, M and CH. Samples are listed in reverse chronological order from younger to older.

Sample	Temperature [°C]						
	1000	1100	1200	1300	1350	1400	1450
<i>Clinker_MO4</i>	1000	1100	1200	1300	1350	1400	1450
C ₃ S	-	-	-	29.6	66.1	72.0	73.9
C ₂ S	18.0	27.1	34.6	46.4	12.0	8.9	6.8
C ₃ A	0.7	0.4	1.4	5.4	11.9	8.8	9.1
C ₄ AF	3.9	7.0	9.1	9.4	5.7	7.2	7.7
CaO	51.7	44.4	39.4	8.9	3.9	1.7	1.7
Others*	25.7	21.0	15.6	0.3	0.5	1.4	0.8
<i>Clinker_AS</i>	1000	1100	1200	1300	1350	1400	1450
C ₃ S	-	-	-	46.5	66.4	72.5	72.2
C ₂ S	22.0	32.0	39.4	27.4	15.6	10.6	13.1
C ₃ A	1.6	1.0	3.0	8.1	3.5	3.2	3.7
C ₄ AF	5.3	8.8	11.4	10.6	12.2	12.7	10.7
CaO	47.7	40.9	36.3	7.2	2.0	0.9	0.3
Others*	23.4	17.3	9.9	0.2	0.3	0.1	-

Table A1.2 (part II): Phase composition (wt%) of clinkers samples from the eight studied raw meals, at all the temperatures of the burnability test, obtained processing XRPD data by Rietveld refinements. The category “others” refers to C₂AS, C₁₂A₇, S, M and CH. Samples are listed in reverse chronological order from younger to older.

Appendix B1

Clinker_1F

N	SiO ₂	TiO ₂	Al ₂ O ₃	FeO	MgO	CaO	MnO	SrO	Na ₂ O	K ₂ O	SO ₃	F	Cl	O=F+Cl	Total
1	24.10	0.13	1.57	0.59	0.92	70.98	0.09	0.18	0.17	0.03	0.06	0.76	0.00	0.32	99.26
2	22.68	0.24	2.35	1.00	1.17	70.16	0.00	0.00	0.16	0.05	0.03	0.96	0.00	0.40	98.39
3	23.48	0.19	1.80	0.61	0.84	71.19	0.06	0.12	0.12	0.04	0.01	0.69	0.00	0.29	98.85
4	24.42	0.14	1.41	0.48	0.79	71.05	0.07	0.00	0.12	0.05	0.00	0.58	0.03	0.25	98.88
5	23.94	0.14	1.46	0.52	0.81	71.39	0.11	0.14	0.13	0.06	0.02	0.65	0.00	0.27	99.09
6	23.93	0.11	1.61	0.68	0.81	71.18	0.07	0.09	0.13	0.04	0.02	0.51	0.00	0.21	98.98
7	23.85	0.14	1.62	0.68	0.80	71.44	0.00	0.16	0.11	0.06	0.01	0.54	0.00	0.23	99.18
8	24.15	0.10	1.32	0.55	0.80	71.10	0.07	0.12	0.11	0.05	0.02	0.38	0.00	0.16	98.59
9	24.13	0.14	1.36	0.48	0.88	71.45	0.00	0.21	0.07	0.05	0.02	0.66	0.00	0.28	99.17
10	24.02	0.12	1.41	0.57	0.78	71.18	0.01	0.14	0.09	0.04	0.00	0.35	0.00	0.15	98.58
11	24.26	0.14	1.29	0.50	0.84	71.58	0.05	0.00	0.14	0.04	0.03	0.34	0.00	0.14	99.06
12	24.71	0.16	1.33	0.40	0.83	72.55	0.08	0.16	0.16	0.05	0.00	0.61	0.00	0.26	100.79
13	24.51	0.17	1.50	0.50	0.81	72.41	0.03	0.23	0.09	0.04	0.05	0.55	0.02	0.24	100.67
14	24.41	0.12	1.58	0.62	0.79	72.35	0.06	0.13	0.09	0.04	0.04	0.29	0.00	0.12	100.39
15	24.34	0.16	1.33	0.48	0.71	72.38	0.05	0.16	0.11	0.05	0.00	0.25	0.00	0.11	99.93
16	24.36	0.12	1.25	0.44	0.75	72.51	0.06	0.23	0.08	0.06	0.00	0.29	0.00	0.12	100.02
17	31.25	0.29	1.46	0.88	0.31	62.86	0.06	0.41	0.20	0.45	0.58	0.10	0.00	0.04	98.83
18	31.72	0.18	1.24	0.80	0.34	62.90	0.09	0.40	0.19	0.27	0.18	0.00	0.01	0.00	98.33
19	31.15	0.23	1.42	0.86	0.33	62.47	0.06	0.62	0.15	0.33	0.22	0.00	0.00	0.00	97.84
20	31.31	0.26	1.41	0.78	0.24	62.76	0.14	0.19	0.18	0.35	0.34	0.00	0.00	0.00	97.98
21	30.05	0.26	1.73	0.92	0.43	62.73	0.09	0.31	0.30	0.31	0.42	0.01	0.00	0.00	97.55
22	31.56	0.16	1.37	0.80	0.25	63.15	0.07	0.31	0.13	0.28	0.36	0.00	0.00	0.00	98.44
23	30.96	0.15	1.46	0.86	0.34	62.67	0.09	0.31	0.21	0.35	0.35	0.00	0.00	0.00	97.74
24	31.22	0.18	1.42	0.86	0.30	63.17	0.07	0.49	0.20	0.30	0.16	0.00	0.00	0.00	98.37
25	30.63	0.33	1.91	0.97	0.42	62.57	0.13	0.35	0.18	0.37	0.33	0.14	0.00	0.06	98.27
26	31.23	0.18	1.33	1.00	0.31	63.07	0.05	0.50	0.20	0.30	0.28	0.00	0.00	0.00	98.45
27	31.50	0.23	1.40	0.89	0.52	62.92	0.10	0.01	0.24	0.44	0.37	0.00	0.00	0.00	98.62
28	31.60	0.30	1.28	0.81	0.27	64.37	0.02	0.33	0.16	0.29	0.34	0.00	0.01	0.00	99.76
29	31.02	0.30	1.46	0.99	0.35	64.35	0.14	0.28	0.16	0.29	0.26	0.00	0.01	0.00	99.61
30	31.50	0.22	1.44	0.91	0.31	63.45	0.01	0.29	0.17	0.33	0.34	0.00	0.00	0.00	98.96
31	31.41	0.25	1.38	0.84	0.45	64.37	0.00	0.54	0.23	0.38	0.53	0.00	0.00	0.00	100.38
32	31.76	0.22	1.24	0.76	0.26	64.61	0.03	0.46	0.21	0.32	0.36	0.00	0.01	0.00	100.23
33	3.45	1.68	18.84	20.62	2.60	47.59	1.56	0.18	0.04	0.02	0.04	0.00	0.01	0.00	96.62
34	3.60	1.79	18.32	20.58	2.59	47.77	1.63	0.21	0.00	0.05	0.04	0.00	0.00	0.00	96.59
35	3.02	1.33	20.10	19.69	2.50	47.90	1.33	0.25	0.06	0.00	0.00	0.00	0.00	0.00	96.18
36	20.18	0.62	8.21	7.07	0.83	58.06	0.18	0.30	0.07	0.12	0.21	0.00	0.02	0.00	95.86
37	4.47	1.15	20.61	17.12	2.35	49.76	0.85	0.17	0.02	0.03	0.08	0.00	0.00	0.00	96.62
38	3.79	1.42	19.45	19.15	2.46	48.20	1.51	0.32	0.02	0.01	0.04	0.05	0.00	0.02	96.40
39	6.60	1.04	19.50	15.20	2.11	50.58	0.76	0.00	0.05	0.09	0.10	0.03	0.01	0.02	96.05
40	2.99	1.24	20.82	19.57	2.54	47.82	0.98	0.09	0.02	0.03	0.08	0.00	0.01	0.00	96.17

Table B1.1: *Clinker_1F* spot chemical composition (oxides wt%), as determined by electron microprobe analyses. Column *N* refers the number of the punctual chemical analysis marked out in Figure B1.1.

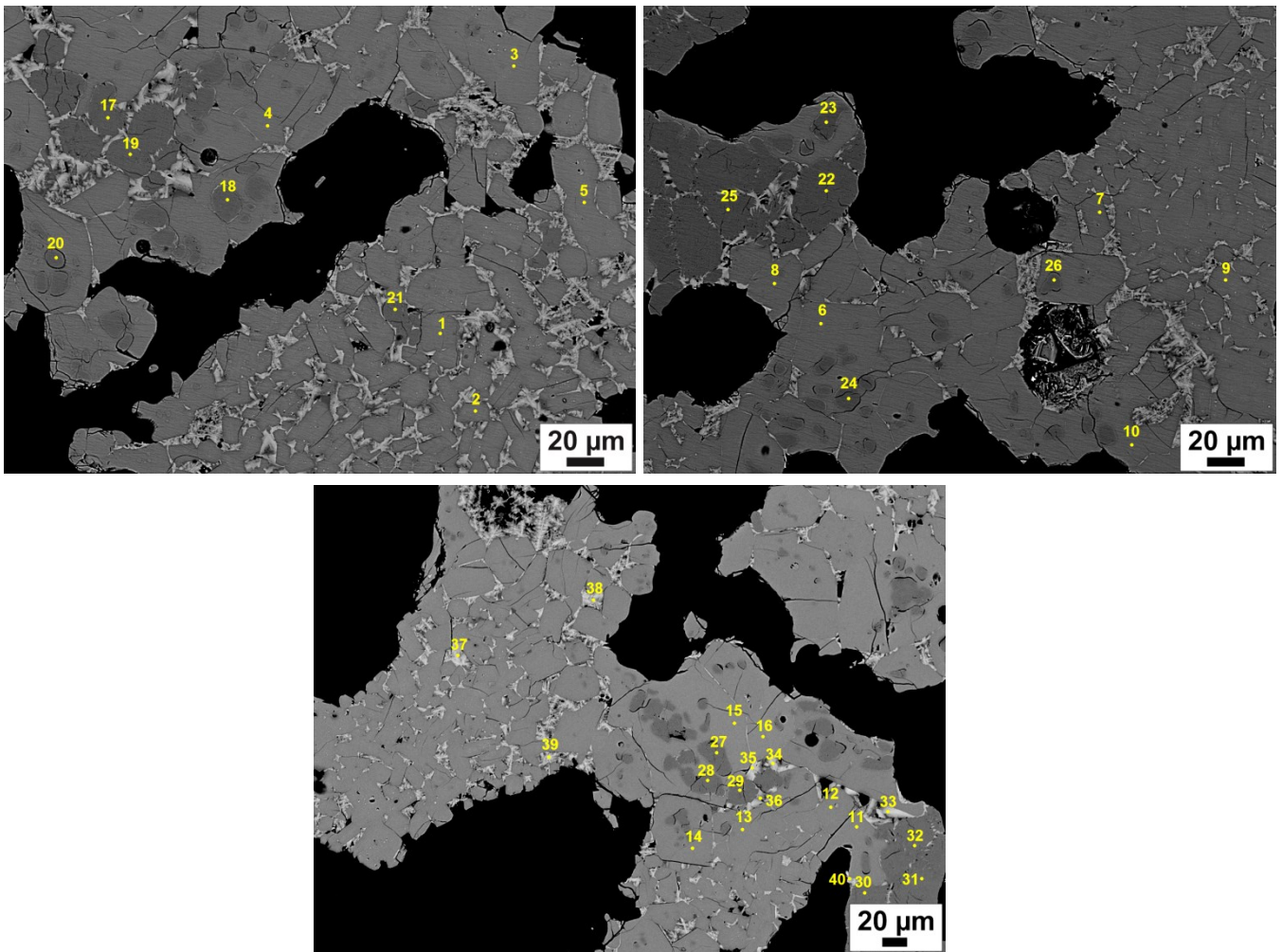


Figure B1.1: *Clinker_1F* SEM images with spots corresponding to punctual chemical analyses reported in Table B1.1.

Clinker_2F

N	SiO ₂	TiO ₂	Al ₂ O ₃	FeO	MgO	CaO	MnO	SrO	Na ₂ O	K ₂ O	SO ₃	F	Cl	O=F+Cl	Total
1	24.85	0.13	1.09	0.46	1.64	70.13	0.05	0.22	0.33	0.04	0.03	0.40	0.02	0.12	99.27
2	24.35	0.08	1.30	0.53	1.59	70.33	0.07	0.13	0.30	0.06	0.00	0.37	0.00	0.11	99.00
3	24.75	0.14	1.05	0.39	1.59	70.20	0.07	0.13	0.36	0.07	0.00	0.37	0.00	0.11	99.00
4	24.95	0.12	1.09	0.43	1.64	69.80	0.14	0.25	0.28	0.06	0.01	0.43	0.02	0.13	99.09
5	24.06	0.19	1.51	0.60	1.74	69.46	0.06	0.34	0.54	0.06	0.00	0.75	0.00	0.22	99.08
6	24.64	0.11	1.03	0.49	1.55	70.42	0.11	0.12	0.32	0.04	0.00	0.33	0.02	0.10	99.07
7	24.44	0.18	1.13	0.60	1.55	70.46	0.03	0.03	0.29	0.05	0.04	0.36	0.01	0.11	99.04
8	24.57	0.17	1.01	0.45	1.55	70.49	0.04	0.01	0.36	0.06	0.01	0.26	0.02	0.08	98.90
9	24.50	0.24	1.32	0.65	1.60	70.40	0.07	0.09	0.32	0.06	0.03	0.50	0.02	0.15	99.65
10	24.54	0.19	1.18	0.60	1.63	70.18	0.01	0.22	0.28	0.03	0.03	0.42	0.00	0.12	99.20
11	25.32	0.16	1.02	0.34	1.63	71.27	0.04	0.01	0.28	0.05	0.00	0.18	0.01	0.05	100.26
12	24.94	0.08	1.00	0.41	1.54	70.98	0.02	0.20	0.32	0.04	0.01	0.34	0.00	0.10	99.79
13	24.87	0.07	1.06	0.39	1.59	71.63	0.04	0.03	0.32	0.06	0.00	0.11	0.00	0.03	100.13
14	25.12	0.08	0.99	0.41	1.47	71.69	0.00	0.39	0.26	0.05	0.00	0.23	0.01	0.07	100.64
15	24.34	0.12	1.46	0.61	1.57	71.50	0.08	0.21	0.28	0.05	0.03	0.52	0.00	0.15	100.64
16	24.39	0.16	1.11	0.49	1.49	71.61	0.00	0.10	0.31	0.06	0.01	0.27	0.01	0.08	99.92
17	31.61	0.19	1.24	0.88	0.45	62.69	0.09	0.31	0.36	0.31	0.37	0.00	0.00	0.00	98.51
18	31.04	0.32	1.19	0.84	0.76	61.89	0.06	0.26	0.68	0.35	0.32	0.00	0.00	0.00	97.72
19	31.99	0.18	1.20	0.87	0.77	62.14	0.08	0.35	0.62	0.36	0.33	0.00	0.01	0.00	98.91
20	31.55	0.23	1.24	0.68	0.61	62.06	0.13	0.28	0.50	0.34	0.24	0.00	0.00	0.00	97.87
21	31.50	0.18	1.22	0.78	0.62	62.37	0.04	0.39	0.50	0.30	0.28	0.00	0.00	0.00	98.17
22	31.10	0.25	1.20	1.00	0.61	62.47	0.02	0.44	0.56	0.33	0.36	0.00	0.01	0.00	98.36
23	31.22	0.19	1.18	1.05	0.69	62.60	0.06	0.28	0.47	0.28	0.38	0.00	0.00	0.00	98.41
24	31.57	0.22	1.17	0.90	0.64	62.26	0.01	0.12	0.48	0.26	0.31	0.01	0.00	0.00	97.95
25	31.55	0.18	1.27	0.84	0.53	62.60	0.07	0.27	0.43	0.27	0.32	0.00	0.00	0.00	98.33
26	31.82	0.27	1.15	0.95	0.70	61.90	0.04	0.22	0.55	0.37	0.39	0.00	0.01	0.00	98.38
27	31.65	0.25	1.15	0.79	0.70	63.27	0.14	0.23	0.71	0.33	0.27	0.00	0.00	0.00	99.48
28	32.21	0.27	1.19	0.76	0.89	61.05	0.13	0.36	0.80	0.34	0.33	0.00	0.00	0.00	98.33
29	32.01	0.17	1.19	0.84	0.62	63.56	0.03	0.48	0.51	0.30	0.29	0.00	0.00	0.00	100.01
30	31.39	0.27	1.23	0.82	0.72	62.90	0.06	0.39	0.70	0.33	0.35	0.00	0.01	0.00	99.16
31	32.13	0.17	1.20	0.82	0.69	63.33	0.02	0.58	0.46	0.30	0.34	0.00	0.00	0.00	100.04
32	31.95	0.20	1.16	0.86	0.54	63.64	0.03	0.34	0.41	0.27	0.33	0.00	0.00	0.00	99.72
33	4.23	1.64	19.44	18.63	2.97	47.62	1.32	0.27	0.27	0.14	0.06	0.11	0.00	0.03	96.67
34	5.80	0.75	22.42	12.88	5.98	47.31	0.47	0.31	0.69	0.25	0.13	1.08	0.01	0.32	97.76
35	4.88	1.17	19.23	16.64	4.25	48.31	0.80	0.10	0.36	0.25	0.28	0.52	0.02	0.15	96.65
36	4.29	1.39	20.35	17.95	2.88	47.93	1.31	0.21	0.30	0.13	0.03	0.51	0.00	0.15	97.13
37	6.29	1.35	18.47	14.66	7.17	47.27	1.09	0.30	0.45	0.25	0.16	0.37	0.00	0.11	97.72
38	6.51	1.07	19.72	13.08	5.63	47.75	0.89	0.21	0.63	0.31	0.18	0.93	0.02	0.28	96.65
39	5.65	0.90	19.54	15.47	4.55	48.10	0.59	0.23	0.52	0.34	0.26	0.57	0.00	0.17	96.55
40	5.49	1.11	19.19	18.75	2.66	48.53	0.90	0.07	0.27	0.27	0.19	0.12	0.01	0.04	97.51

Table B1.2: *Clinker_2F* spot chemical composition (oxides wt%), as determined by electron microprobe analyses. Column *N* refers the number of the punctual chemical analysis marked out in Figure B1.2.

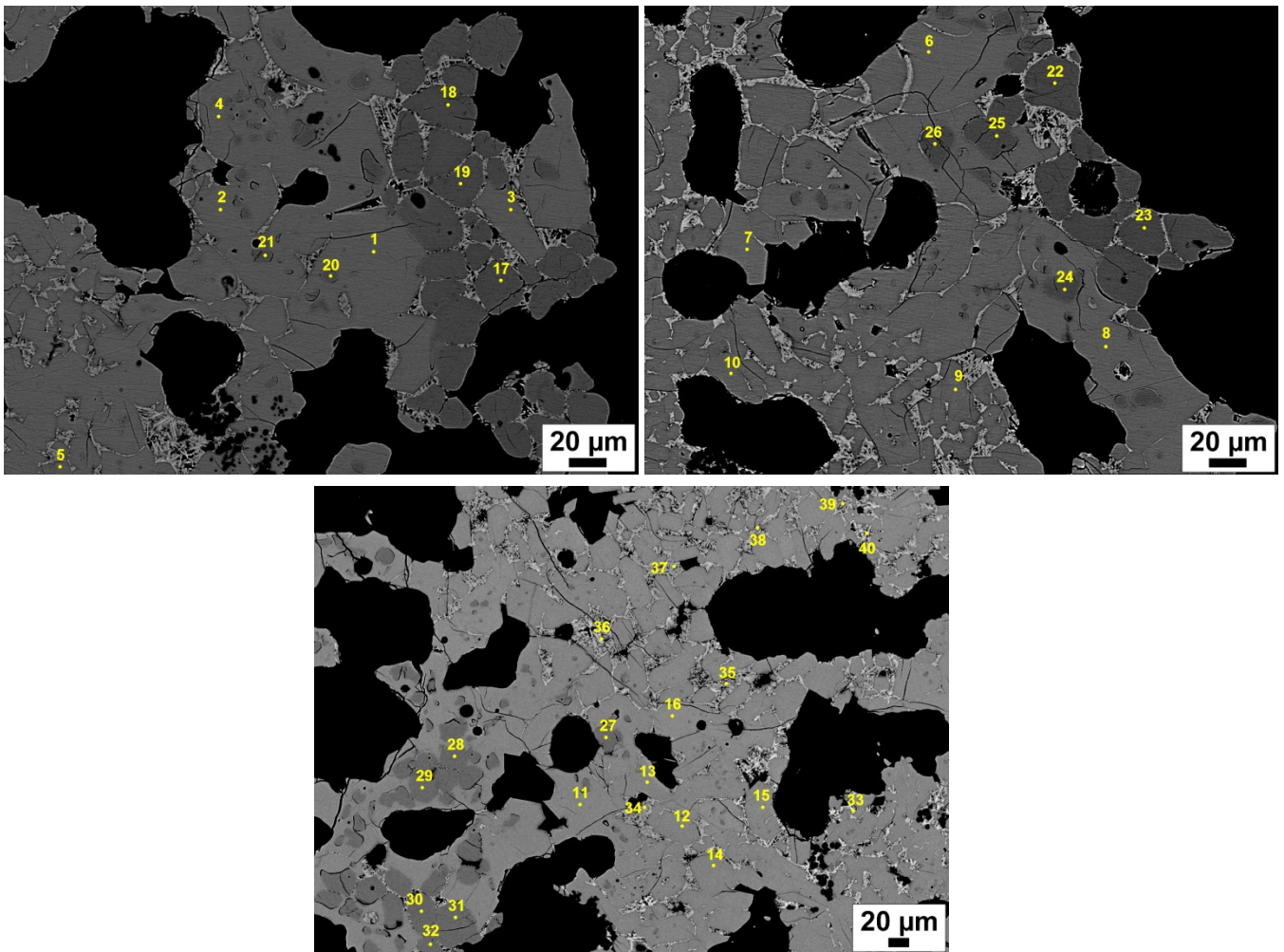


Figure B1.2: *Clinker_2F* SEM images with spots corresponding to punctual chemical analyses reported in Table B1.2.

Clinker_3F

N	SiO ₂	TiO ₂	Al ₂ O ₃	FeO	MgO	CaO	MnO	SrO	Na ₂ O	K ₂ O	SO ₃	F	Cl	O=F+Cl	Total
1	24.30	0.15	1.25	0.53	0.82	71.97	0.01	0.10	0.34	0.03	0.04	0.45	0.01	0.19	99.80
2	24.31	0.11	1.21	0.52	0.80	72.06	0.03	0.06	0.27	0.04	0.03	0.49	0.00	0.21	99.72
3	24.31	0.21	1.29	0.53	0.84	71.66	0.00	0.11	0.22	0.03	0.04	0.64	0.01	0.27	99.62
4	24.69	0.13	1.22	0.41	0.74	72.17	0.05	0.15	0.32	0.02	0.03	0.30	0.01	0.13	100.11
5	24.58	0.19	1.40	0.53	0.84	71.99	0.14	0.23	0.30	0.04	0.04	0.57	0.00	0.24	100.59
6	23.94	0.16	1.54	0.53	0.78	72.19	0.03	0.05	0.27	0.04	0.00	0.55	0.02	0.23	99.85
7	23.89	0.13	1.51	0.58	0.77	71.31	0.06	0.18	0.30	0.05	0.04	0.61	0.01	0.26	99.18
8	24.48	0.14	1.17	0.50	0.78	71.42	0.01	0.16	0.29	0.02	0.07	0.28	0.00	0.12	99.20
9	24.55	0.12	1.46	0.39	0.72	72.13	0.05	0.25	0.23	0.04	0.01	0.44	0.00	0.18	100.21
10	24.17	0.18	1.58	0.63	0.86	71.53	0.11	0.19	0.23	0.03	0.00	0.43	0.01	0.18	99.74
11	24.64	0.14	1.31	0.55	0.83	72.30	0.05	0.12	0.22	0.03	0.02	0.43	0.02	0.18	100.47
12	24.57	0.10	1.22	0.45	0.73	71.99	0.02	0.24	0.18	0.07	0.05	0.48	0.01	0.20	99.90
13	25.03	0.14	1.23	0.47	0.80	72.11	0.05	0.15	0.29	0.02	0.04	0.30	0.00	0.12	100.49
14	25.37	0.10	1.24	0.56	0.74	71.74	0.03	0.34	0.24	0.05	0.08	0.57	0.00	0.24	100.81
15	24.75	0.07	1.17	0.41	0.91	71.48	0.08	0.04	0.34	0.01	0.04	0.48	0.00	0.20	99.59
16	24.84	0.12	1.21	0.45	0.81	71.85	0.05	0.29	0.29	0.03	0.08	0.53	0.01	0.23	100.33
17	31.14	0.26	1.37	0.99	0.26	63.67	0.08	0.53	0.39	0.27	0.83	0.00	0.00	0.00	99.80
18	31.51	0.27	1.55	0.97	0.45	63.60	0.05	0.34	0.54	0.22	0.67	0.01	0.01	0.00	100.17
19	30.68	0.25	2.10	1.68	0.54	63.24	0.05	0.15	0.38	0.28	0.60	0.00	0.01	0.00	99.97
20	31.64	0.25	1.42	0.83	0.22	63.86	0.07	0.15	0.33	0.16	0.58	0.00	0.01	0.00	99.53
21	31.53	0.20	1.48	1.08	0.38	63.83	0.05	0.25	0.41	0.19	0.54	0.00	0.01	0.00	99.93
22	31.28	0.20	1.36	0.91	0.34	63.59	0.01	0.31	0.38	0.22	0.62	0.00	0.00	0.00	99.22
23	31.79	0.12	1.34	0.91	0.26	63.69	0.08	0.40	0.32	0.18	0.43	0.00	0.00	0.00	99.51
24	33.07	0.15	1.31	0.77	0.29	61.14	0.02	0.50	0.41	0.15	0.45	0.00	0.01	0.00	98.25
25	31.43	0.15	1.71	1.26	0.42	62.45	0.06	0.26	0.41	0.17	0.57	0.00	0.00	0.00	98.89
26	31.73	0.20	1.45	1.04	0.65	63.13	0.07	0.21	0.58	0.19	0.69	0.00	0.00	0.00	99.94
27	30.97	0.23	1.43	0.85	0.33	64.02	0.11	0.32	0.45	0.23	0.59	0.00	0.00	0.00	99.54
28	30.86	0.27	1.50	0.94	0.26	63.26	0.12	0.31	0.48	0.20	0.67	0.00	0.01	0.00	98.88
29	31.74	0.19	1.55	1.16	0.44	63.18	0.07	0.33	0.47	0.29	0.78	0.00	0.00	0.00	100.19
30	31.47	0.15	1.32	1.06	0.28	63.57	0.06	0.61	0.36	0.23	0.64	0.00	0.02	0.00	99.77
31	30.58	0.21	1.64	1.05	0.59	63.07	0.06	0.11	0.80	0.41	1.34	0.00	0.00	0.00	99.85
32	31.59	0.16	1.35	1.02	0.33	63.83	0.06	0.45	0.50	0.25	0.79	0.00	0.00	0.00	100.33
33	4.10	1.72	17.12	20.64	2.70	48.13	2.05	0.08	0.08	0.02	0.00	0.15	0.00	0.06	96.73
34	2.17	1.04	22.17	19.78	2.57	47.85	0.36	0.06	0.07	0.02	0.01	0.15	0.00	0.06	96.19
35	3.55	1.44	18.83	20.73	2.70	47.67	1.43	0.10	0.10	0.14	0.05	0.02	0.00	0.01	96.74
36	2.95	1.37	20.04	20.16	3.00	47.75	0.84	0.00	0.09	0.03	0.02	0.20	0.00	0.08	96.36
37	3.61	1.46	20.16	19.60	2.60	48.00	1.27	0.14	0.09	0.06	0.10	0.17	0.00	0.07	97.19
38	4.18	1.80	16.52	21.53	2.46	47.68	2.13	0.31	0.07	0.03	0.09	0.17	0.00	0.07	96.89
39	3.98	1.97	17.38	20.54	2.57	47.68	2.18	0.11	0.07	0.01	0.08	0.00	0.01	0.00	96.58
40	9.59	1.15	15.99	15.04	2.27	53.57	0.92	0.15	0.22	0.01	0.03	0.43	0.01	0.18	99.20

Table B1.3: *Clinker_3F* spot chemical composition (oxides wt%), as determined by electron microprobe analyses. Column *N* refers the number of the punctual chemical analysis marked out in Figure B1.3.

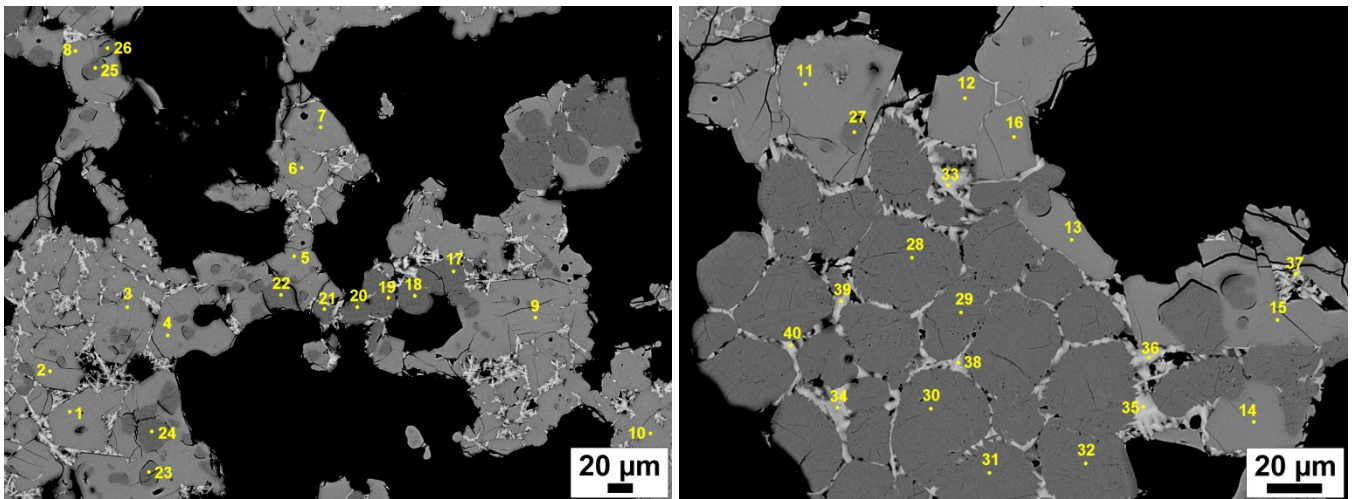


Figure B1.3: *Clinker_3F* SEM images with spots corresponding to punctual chemical analyses reported in Table B1.3.

Clinker_4F

N	SiO ₂	TiO ₂	Al ₂ O ₃	FeO	MgO	CaO	MnO	SrO	Na ₂ O	K ₂ O	SO ₃	F	Cl	O=F+Cl	Total
1	23.62	0.13	1.93	0.82	1.60	71.22	0.06	0.00	0.05	0.05	0.08	0.80	0.00	0.34	100.03
2	23.61	0.16	1.95	0.73	1.74	71.07	0.05	0.13	0.04	0.05	0.06	0.74	0.00	0.31	100.02
3	24.87	0.14	1.26	0.42	1.71	71.58	0.05	0.24	0.12	0.06	0.08	0.40	0.02	0.17	100.76
4	24.39	0.19	1.52	0.58	1.78	70.86	0.12	0.05	0.02	0.05	0.08	0.59	0.00	0.25	99.98
5	23.41	0.19	2.20	1.09	1.87	71.02	0.06	0.34	0.14	0.02	0.02	0.55	0.00	0.23	100.68
6	24.46	0.13	1.35	0.43	1.50	71.60	0.00	0.14	0.12	0.02	0.15	0.67	0.01	0.28	100.28
7	25.00	0.16	1.36	0.56	1.64	70.78	0.02	0.30	0.10	0.03	0.00	0.47	0.00	0.20	100.22
8	24.78	0.09	1.33	0.42	1.61	71.00	0.08	0.20	0.08	0.04	0.01	0.31	0.00	0.13	99.82
9	24.91	0.16	1.21	0.34	1.72	70.82	0.01	0.13	0.11	0.03	0.11	0.39	0.00	0.16	99.77
10	24.93	0.09	1.27	0.43	1.64	71.21	0.03	0.38	0.09	0.05	0.04	0.48	0.01	0.20	100.45
11	24.92	0.13	1.28	0.44	1.62	71.01	0.10	0.20	0.13	0.03	0.10	0.50	0.00	0.21	100.25
12	24.55	0.15	1.53	0.55	1.48	71.53	0.02	0.00	0.10	0.02	0.04	0.51	0.00	0.21	100.27
13	24.31	0.16	1.57	0.57	1.70	71.27	0.02	0.25	0.07	0.03	0.07	0.55	0.00	0.23	100.35
14	23.84	0.12	1.87	0.75	1.83	71.17	0.13	0.06	0.08	0.03	0.00	0.60	0.00	0.25	100.23
15	23.89	0.20	1.71	0.65	1.76	71.09	0.10	0.04	0.07	0.04	0.07	0.32	0.00	0.14	99.81
16	23.77	0.25	2.02	0.72	1.75	70.98	0.10	0.18	0.09	0.07	0.08	0.59	0.01	0.25	100.34
17	31.80	0.24	1.36	0.59	0.64	63.22	0.03	0.29	0.24	0.29	0.68	0.00	0.00	0.00	99.36
18	31.55	0.15	1.43	0.82	0.67	63.69	0.03	0.49	0.16	0.23	0.59	0.00	0.00	0.00	99.80
19	31.24	0.24	1.35	0.82	0.63	63.99	0.00	0.51	0.18	0.26	0.68	0.00	0.01	0.00	99.91
20	31.80	0.21	1.48	0.92	1.20	63.23	0.06	0.59	0.24	0.33	0.66	0.00	0.02	0.00	100.72
21	31.59	0.22	1.26	0.53	0.22	64.52	0.05	0.34	0.11	0.15	0.67	0.00	0.00	0.00	99.66
22	31.52	0.17	1.46	0.74	0.71	63.26	0.13	0.55	0.15	0.21	0.88	0.00	0.00	0.00	99.80
23	32.02	0.24	1.07	0.54	0.40	63.62	0.03	0.54	0.15	0.22	0.54	0.00	0.00	0.00	99.38
24	31.23	0.18	1.56	0.80	0.71	63.67	0.08	0.63	0.17	0.23	0.74	0.00	0.00	0.00	100.01
25	31.94	0.09	1.29	0.70	0.38	64.42	0.04	0.63	0.12	0.19	0.56	0.00	0.01	0.00	100.36
26	32.00	0.18	1.26	0.67	0.73	63.74	0.01	0.36	0.17	0.31	0.88	0.00	0.01	0.00	100.32
27	31.93	0.15	1.33	0.78	0.58	63.58	0.06	0.21	0.16	0.29	0.69	0.00	0.01	0.00	99.77
28	31.38	0.24	1.53	0.84	0.64	63.93	0.10	0.34	0.14	0.17	0.55	0.00	0.00	0.00	99.87
29	31.95	0.18	1.42	0.74	0.56	63.65	0.09	0.44	0.20	0.23	0.89	0.00	0.00	0.00	100.35
30	31.76	0.22	1.34	0.66	0.38	63.94	0.05	0.52	0.17	0.23	0.72	0.00	0.01	0.00	99.99
31	31.69	0.24	1.35	0.67	0.41	63.89	0.04	0.31	0.14	0.27	0.97	0.05	0.00	0.02	100.01
32	32.02	0.16	1.39	0.82	0.97	63.26	0.06	0.50	0.20	0.29	0.70	0.00	0.00	0.00	100.36
33	3.43	1.39	19.51	19.39	3.94	47.86	0.84	0.21	0.03	0.09	0.06	0.20	0.00	0.08	96.87
34	3.97	1.63	17.97	19.02	3.97	48.41	1.24	0.14	0.00	0.02	0.07	0.29	0.01	0.12	96.61
35	3.99	1.90	16.95	19.87	3.80	47.50	1.77	0.21	0.02	0.02	0.13	0.09	0.00	0.04	96.22
36	3.32	1.48	19.97	18.41	3.52	48.44	1.01	0.00	0.00	0.01	0.14	0.52	0.00	0.22	96.60
37	4.23	1.75	17.78	19.59	3.30	48.34	1.62	0.13	0.06	0.03	0.06	0.11	0.00	0.05	96.95
38	2.94	1.40	20.51	20.17	2.80	47.88	0.93	0.13	0.00	0.01	0.07	0.00	0.00	0.00	96.84
39	3.42	1.45	19.51	19.82	3.30	48.09	1.01	0.10	0.08	0.01	0.04	0.05	0.00	0.02	96.87
40	3.40	1.54	19.12	20.39	3.14	47.82	0.99	0.21	0.02	0.04	0.05	0.06	0.01	0.03	96.77

Table B1.4: *Clinker_4F* spot chemical composition (oxides wt%), as determined by electron microprobe analyses. Column *N* refers the number of the punctual chemical analysis marked out in Figure B1.4.

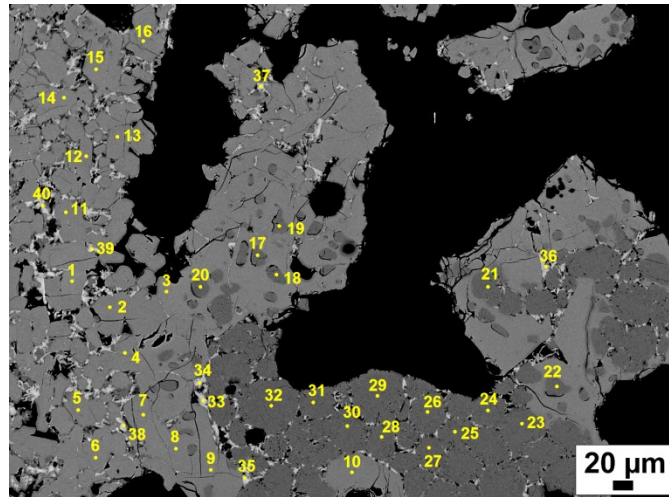


Figure B1.4: *Clinker_4F* SEM images with spots corresponding to punctual chemical analyses reported in Table B1.4.

Clinker_1C

N	SiO ₂	TiO ₂	Al ₂ O ₃	FeO	MgO	CaO	MnO	SrO	Na ₂ O	K ₂ O	SO ₃	F	Cl	O=F+Cl	Total
1	24.13	0.26	1.29	0.63	0.80	71.33	0.06	0.09	0.02	0.00	0.12	0.05	0.00	0.02	98.75
2	24.31	0.13	1.07	0.46	0.81	71.19	0.06	0.05	0.03	0.00	0.16	0.00	0.01	0.00	98.27
3	24.26	0.13	1.13	0.64	0.82	71.07	0.04	0.31	0.01	0.01	0.19	0.04	0.00	0.02	98.63
4	24.60	0.15	1.14	0.60	0.80	71.24	0.09	0.01	0.02	0.01	0.10	0.00	0.00	0.00	98.75
5	24.55	0.13	1.06	0.53	0.78	71.39	0.03	0.10	0.02	0.00	0.12	0.01	0.00	0.01	98.71
6	24.31	0.17	1.14	0.59	0.77	71.10	0.09	0.14	0.02	0.00	0.12	0.01	0.00	0.01	98.45
7	24.73	0.07	0.99	0.58	0.76	71.10	0.00	0.18	0.00	0.01	0.11	0.00	0.02	0.00	98.55
8	24.00	0.13	1.12	0.59	0.84	70.98	0.05	0.04	0.01	0.00	0.09	0.00	0.00	0.00	97.85
9	24.54	0.18	1.03	0.55	0.80	71.15	0.10	0.06	0.01	0.00	0.09	0.09	0.00	0.04	98.56
10	24.00	0.18	1.22	0.65	0.78	71.14	0.03	0.19	0.00	0.00	0.19	0.00	0.02	0.00	98.40
11	24.32	0.18	1.36	0.72	0.87	72.54	0.04	0.13	0.00	0.00	0.21	0.00	0.01	0.00	100.38
12	24.51	0.15	1.05	0.76	0.84	72.19	0.06	0.00	0.00	0.00	0.04	0.00	0.01	0.00	99.61
13	24.55	0.09	0.98	0.72	0.78	71.83	0.10	0.15	0.00	0.00	0.07	0.00	0.00	0.00	99.28
14	24.56	0.14	0.88	0.65	0.85	72.50	0.00	0.18	0.06	0.00	0.09	0.00	0.02	0.00	99.92
15	23.04	0.27	2.50	1.59	0.90	70.96	0.13	0.14	0.03	0.00	0.15	0.00	0.02	0.01	99.72
16	24.75	0.14	0.93	0.60	0.77	72.85	0.04	0.00	0.04	0.00	0.10	0.00	0.00	0.00	100.22
17	29.61	0.32	2.10	1.08	0.17	63.52	0.04	0.37	0.06	0.00	0.77	0.00	0.01	0.00	98.05
18	29.75	0.49	2.10	1.18	0.19	63.34	0.10	0.49	0.04	0.00	0.85	0.00	0.02	0.00	98.54
19	29.98	0.31	1.87	0.88	0.35	63.35	0.09	0.30	0.02	0.00	0.77	0.00	0.01	0.00	97.92
20	29.93	0.30	2.10	0.96	0.40	63.23	0.09	0.30	0.02	0.00	0.72	0.00	0.00	0.00	98.04
21	29.86	0.30	1.97	0.97	0.20	63.69	0.12	0.32	0.02	0.00	0.69	0.05	0.01	0.02	98.19
22	29.16	0.29	2.08	0.98	0.21	63.20	0.07	0.10	0.05	0.00	0.83	0.00	0.00	0.00	96.97
23	29.84	0.22	2.05	1.08	0.68	62.65	0.07	0.34	0.04	0.00	0.74	0.00	0.00	0.00	97.71
24	29.39	0.24	2.20	1.11	0.41	63.01	0.10	0.28	0.03	0.00	0.67	0.00	0.01	0.00	97.46
25	28.59	0.12	2.44	1.10	0.50	62.74	0.11	0.05	0.03	0.00	1.26	0.00	0.02	0.00	96.96
26	29.28	0.22	2.14	0.96	0.37	63.15	0.04	0.23	0.01	0.01	0.73	0.00	0.02	0.00	97.16
27	29.41	0.30	1.99	1.32	0.17	64.60	0.00	0.35	0.03	0.00	0.79	0.00	0.01	0.00	98.96
28	29.71	0.22	1.89	1.23	0.33	64.85	0.09	0.35	0.00	0.00	0.92	0.00	0.00	0.00	99.59
29	29.90	0.18	2.00	1.32	0.93	63.88	0.09	0.40	0.04	0.00	0.87	0.00	0.01	0.00	99.61
30	30.12	0.30	1.87	1.18	0.29	64.88	0.09	0.34	0.00	0.00	0.85	0.00	0.03	0.01	99.93
31	29.57	0.25	1.93	1.29	0.35	64.70	0.07	0.30	0.00	0.00	1.02	0.00	0.01	0.00	99.49
32	30.44	0.14	1.89	1.24	0.30	64.58	0.05	0.26	0.04	0.01	0.74	0.00	0.00	0.00	99.69
33	4.71	0.51	22.30	14.35	2.40	51.70	0.38	0.07	0.04	0.00	0.26	0.00	0.05	0.01	96.76
34	5.17	0.57	22.77	15.51	2.63	50.79	0.35	0.41	0.00	0.00	0.31	0.00	0.07	0.02	98.56
35	6.63	0.98	18.35	15.08	2.75	51.30	0.91	0.12	0.03	0.00	0.54	0.00	0.14	0.03	96.79
36	7.88	0.70	17.33	14.64	2.29	54.19	0.62	0.07	0.00	0.00	0.31	0.00	0.05	0.01	98.07
37	3.75	0.80	20.00	18.14	3.31	47.51	0.64	0.14	0.02	0.02	0.26	0.05	0.04	0.03	94.65

Table B1.5: *Clinker_1C* spot chemical composition (oxides wt%), as determined by electron microprobe analyses. Column *N* refers the number of the punctual chemical analysis marked out in Figure B1.5.

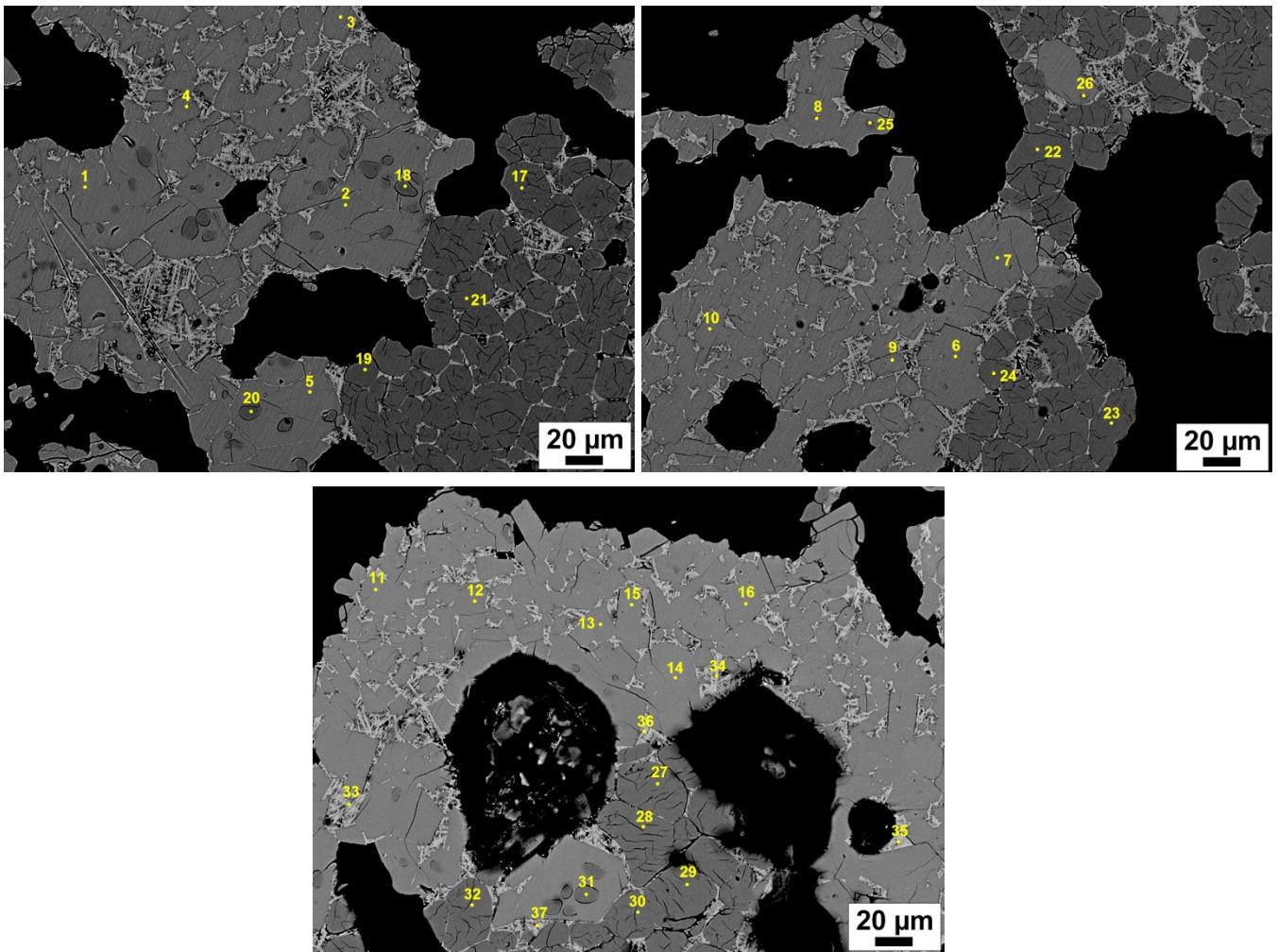


Figure B1.5: *Clinker_1C* SEM images with spots corresponding to punctual chemical analyses reported in Table B1.5.

Clinker_2C

N	SiO₂	TiO₂	Al₂O₃	FeO	MgO	CaO	MnO	SrO	Na₂O	K₂O	SO₃	F	Cl	O=F+Cl	Total
1	24.47	0.14	1.07	0.55	1.50	70.33	0.03	0.21	0.12	0.01	0.16	0.00	0.01	0.00	98.60
2	24.53	0.19	1.00	0.61	1.54	70.42	0.05	0.13	0.14	0.00	0.11	0.00	0.00	0.00	98.73
3	24.71	0.10	0.88	0.50	1.53	70.60	0.00	0.05	0.09	0.01	0.14	0.02	0.00	0.01	98.62
4	24.22	0.14	1.27	0.67	1.61	69.98	0.09	0.14	0.17	0.00	0.10	0.07	0.01	0.03	98.43
5	24.57	0.21	1.15	0.53	1.49	70.12	0.06	0.00	0.12	0.01	0.23	0.00	0.00	0.00	98.49
6	24.75	0.22	1.13	0.56	1.42	70.29	0.00	0.18	0.10	0.00	0.14	0.00	0.01	0.00	98.79
7	24.34	0.14	1.11	0.62	1.55	69.87	0.13	0.01	0.15	0.00	0.14	0.00	0.01	0.00	98.07
8	24.44	0.21	1.13	0.66	1.50	70.27	0.11	0.10	0.16	0.00	0.12	0.01	0.01	0.00	98.71
9	24.67	0.16	0.91	0.52	1.52	70.15	0.08	0.23	0.14	0.01	0.15	0.00	0.02	0.00	98.54
10	30.02	0.27	2.37	1.00	0.78	61.29	0.03	0.44	0.71	0.08	0.83	0.00	0.00	0.00	97.82
11	21.24	0.18	7.70	2.35	2.76	62.35	0.03	0.00	0.50	0.03	0.33	0.00	0.00	0.00	97.47
12	30.79	0.28	1.74	0.86	0.66	61.70	0.10	0.26	0.61	0.08	0.82	0.00	0.00	0.00	97.90
13	29.93	0.30	1.83	0.89	0.66	61.81	0.08	0.40	0.59	0.07	0.90	0.00	0.00	0.00	97.47
14	29.87	0.29	1.78	0.88	0.55	62.66	0.12	0.18	0.68	0.10	0.90	0.00	0.00	0.00	98.00
15	29.71	0.31	1.85	0.84	0.44	62.14	0.08	0.53	0.65	0.06	0.85	0.00	0.01	0.00	97.47
16	29.14	0.31	1.99	0.90	0.44	62.41	0.07	0.28	0.56	0.09	0.96	0.00	0.00	0.00	97.16
17	30.02	0.24	1.86	0.89	0.54	62.26	0.05	0.47	0.65	0.09	0.81	0.00	0.01	0.00	97.88
18	30.01	0.32	1.99	0.94	0.60	61.92	0.07	0.48	0.73	0.08	0.91	0.00	0.00	0.00	98.05

Table B1.6: *Clinker_2C* spot chemical composition (oxides wt%), as determined by electron microprobe analyses. Column *N* refers the number of the punctual chemical analysis marked out in Figure B1.6.

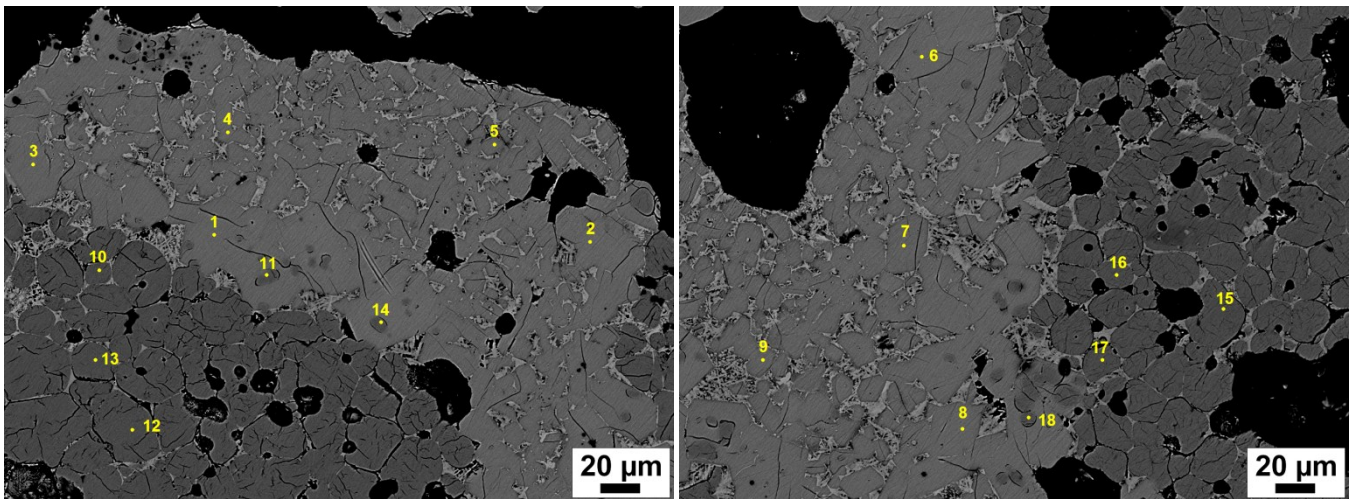


Figure B1.6: *Clinker_2C* SEM images with spots corresponding to punctual chemical analyses reported in Table B1.6.

Clinker_3C

N	SiO ₂	TiO ₂	Al ₂ O ₃	FeO	MgO	CaO	MnO	SrO	Na ₂ O	K ₂ O	SO ₃	F	Cl	O=F+Cl	Total
1	24.85	0.11	0.93	0.58	0.80	72.32	0.00	0.00	0.05	0.01	0.16	0.00	0.01	0.00	99.81
2	24.52	0.19	1.20	0.75	0.93	71.93	0.05	0.03	0.12	0.00	0.23	0.00	0.00	0.00	99.95
3	24.48	0.06	1.03	0.60	0.86	72.54	0.05	0.24	0.07	0.01	0.26	0.00	0.00	0.00	100.20
4	24.76	0.13	1.00	0.58	0.77	72.80	0.01	0.13	0.09	0.00	0.16	0.00	0.00	0.00	100.43
5	25.52	0.20	1.37	0.73	0.75	70.96	0.07	0.24	0.17	0.02	0.21	0.00	0.01	0.00	100.24
6	24.82	0.14	0.94	0.53	0.78	72.78	0.05	0.18	0.15	0.01	0.22	0.00	0.01	0.00	100.60
7	25.00	0.12	0.95	0.58	0.77	72.55	0.09	0.38	0.09	0.01	0.31	0.00	0.00	0.00	100.85
8	24.49	0.09	1.05	0.70	0.74	72.43	0.05	0.06	0.06	0.03	0.21	0.00	0.01	0.00	99.91
9	24.68	0.18	1.05	0.58	0.82	72.56	0.04	0.00	0.10	0.02	0.17	0.00	0.01	0.00	100.19
10	24.55	0.04	1.00	0.63	0.76	72.09	0.11	0.04	0.08	0.01	0.20	0.00	0.00	0.00	99.51
11	24.75	0.14	1.22	0.67	0.78	72.59	0.05	0.30	0.05	0.00	0.22	0.00	0.00	0.00	100.77
12	24.58	0.10	1.13	0.55	0.78	71.78	0.08	0.10	0.17	0.02	0.20	0.00	0.01	0.00	99.50
13	24.56	0.18	1.03	0.50	0.84	72.35	0.09	0.24	0.07	0.00	0.13	0.00	0.01	0.00	99.99
14	24.74	0.15	1.12	0.66	0.90	72.68	0.04	0.12	0.16	0.00	0.21	0.00	0.01	0.00	100.79
15	23.89	0.41	1.46	0.83	0.83	71.40	0.08	0.11	0.05	0.00	0.11	0.00	0.00	0.00	99.18
16	24.74	0.17	1.02	0.55	0.82	72.42	0.12	0.21	0.12	0.00	0.17	0.00	0.01	0.00	100.35
17	29.60	0.18	1.98	1.21	0.44	63.40	0.05	0.44	0.51	0.16	1.58	0.00	0.00	0.00	99.54
18	30.13	0.20	1.84	1.21	0.32	63.98	0.04	0.31	0.40	0.10	1.40	0.00	0.01	0.00	99.94
19	29.99	0.19	2.33	1.23	0.29	60.21	0.05	0.25	0.43	0.09	1.56	0.00	0.00	0.00	96.61
20	29.34	0.28	2.14	1.28	0.28	63.30	0.04	0.48	0.51	0.09	1.63	0.00	0.01	0.00	99.38
21	29.30	0.14	2.15	1.29	0.40	64.11	0.06	0.13	0.56	0.09	1.52	0.00	0.00	0.00	99.74
22	29.49	0.24	2.42	1.24	0.47	60.85	0.05	0.36	0.48	0.10	1.57	0.00	0.00	0.00	97.25
23	29.27	0.26	2.22	1.17	0.45	63.53	0.11	0.22	0.48	0.10	1.62	0.00	0.02	0.00	99.45
24	30.03	0.34	2.30	1.18	0.34	63.08	0.04	0.22	0.45	0.11	1.77	0.00	0.00	0.00	99.86
25	30.21	0.20	1.84	1.25	0.37	63.58	0.02	0.20	0.50	0.10	1.33	0.00	0.01	0.00	99.60
26	29.80	0.22	1.86	1.27	0.75	62.81	0.07	0.27	0.64	0.15	1.27	0.00	0.00	0.00	99.12
27	30.05	0.15	1.83	1.16	0.29	64.86	0.04	0.20	0.32	0.10	0.97	0.00	0.01	0.00	99.97
28	28.85	0.25	2.04	1.14	0.31	63.19	0.09	0.36	0.48	0.10	1.58	0.00	0.01	0.00	98.40
29	28.45	0.26	2.15	1.15	0.32	63.34	0.09	0.46	0.47	0.10	1.49	0.00	0.01	0.00	98.28
30	26.38	0.27	1.71	0.91	0.90	69.07	0.10	0.22	0.32	0.05	0.65	0.00	0.00	0.00	100.59
31	29.26	0.36	2.11	1.14	0.46	63.64	0.04	0.37	0.49	0.11	1.32	0.00	0.01	0.00	99.31
32	29.35	0.26	2.28	1.04	0.36	61.38	0.08	0.36	0.52	0.09	1.47	0.00	0.01	0.00	97.20
33	3.96	1.22	19.04	18.93	3.14	48.54	1.26	0.08	0.16	0.01	0.29	0.00	0.01	0.00	96.65
34	4.11	1.11	19.19	18.81	3.20	48.76	1.33	0.15	0.09	0.01	0.36	0.00	0.01	0.00	97.13
35	4.31	1.33	17.49	19.22	2.97	49.14	1.47	0.18	0.11	0.02	0.54	0.00	0.02	0.00	96.81
36	3.98	1.30	18.10	19.86	3.08	48.59	1.52	0.32	0.09	0.02	0.24	0.00	0.00	0.00	97.09
37	3.54	0.98	21.43	19.33	3.07	49.01	0.75	0.38	0.10	0.00	0.42	0.00	0.00	0.00	99.01
38	3.48	1.12	21.01	18.82	3.14	49.12	0.91	0.25	0.07	0.01	0.19	0.00	0.01	0.00	98.12
39	4.01	0.83	20.64	15.26	2.68	48.82	0.64	0.21	0.44	0.29	1.91	0.00	0.00	0.00	95.72
40	3.73	1.03	19.07	15.77	2.80	47.20	0.89	0.34	0.63	0.17	2.84	0.00	0.00	0.00	94.47

Table B1.7: *Clinker_3C* spot chemical composition (oxides wt%), as determined by electron microprobe analyses. Column *N* refers the number of the punctual chemical analysis marked out in Figure B1.7.

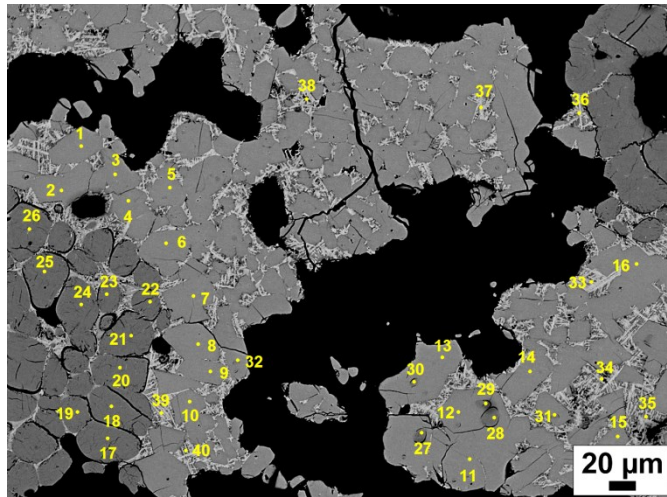


Figure B1.7: *Clinker_3C* SEM images with spots corresponding to punctual chemical analyses reported in Table B1.7.

Clinker_4C

N	SiO ₂	TiO ₂	Al ₂ O ₃	FeO	MgO	CaO	MnO	SrO	Na ₂ O	K ₂ O	SO ₃	F	Cl	O=F+Cl	Total
1	23.48	0.28	1.74	0.90	1.61	71.55	0.08	0.14	0.02	0.01	0.24	0.00	0.01	0.00	100.06
2	24.84	0.13	0.92	0.44	1.60	72.41	0.04	0.00	0.00	0.00	0.13	0.00	0.00	0.00	100.51
3	24.77	0.08	1.00	0.54	1.56	71.18	0.04	0.14	0.00	0.00	0.18	0.00	0.01	0.00	99.50
4	24.59	0.07	1.07	0.53	1.48	71.83	0.04	0.23	0.00	0.00	0.19	0.00	0.01	0.00	100.03
5	24.57	0.13	1.00	0.42	1.51	71.21	0.06	0.10	0.00	0.00	0.18	0.00	0.00	0.00	99.18
6	24.32	0.13	1.09	0.54	1.45	71.40	0.04	0.26	0.03	0.00	0.16	0.00	0.01	0.00	99.42
7	24.00	0.16	1.05	0.53	1.54	71.50	0.00	0.09	0.00	0.00	0.21	0.00	0.01	0.00	99.09
8	24.90	0.07	0.97	0.53	1.60	71.26	0.03	0.55	0.04	0.00	0.23	0.00	0.01	0.00	100.19
9	24.68	0.09	0.93	0.45	1.46	72.47	0.05	0.16	0.02	0.00	0.20	0.00	0.00	0.00	100.52
10	24.64	0.08	1.06	0.64	1.50	72.00	0.06	0.01	0.01	0.00	0.18	0.00	0.01	0.00	100.20
11	24.75	0.11	1.07	0.44	1.49	72.16	0.11	0.00	0.00	0.00	0.17	0.00	0.00	0.00	100.30
12	24.65	0.09	1.15	0.50	1.44	72.16	0.04	0.06	0.03	0.00	0.24	0.00	0.01	0.00	100.37
13	24.80	0.08	1.04	0.48	1.49	72.12	0.05	0.01	0.00	0.00	0.22	0.00	0.00	0.00	100.30
14	24.86	0.13	1.07	0.47	1.49	71.75	0.06	0.00	0.00	0.00	0.21	0.00	0.01	0.00	100.05
15	24.57	0.08	1.03	0.45	1.54	72.13	0.06	0.14	0.00	0.00	0.14	0.00	0.00	0.00	100.13
16	24.86	0.12	0.96	0.44	1.42	72.17	0.01	0.14	0.03	0.00	0.23	0.00	0.00	0.00	100.38
17	29.43	0.23	2.36	1.19	0.64	63.17	0.05	0.40	0.06	0.00	1.71	0.00	0.01	0.00	99.26
18	29.91	0.30	1.96	0.93	0.73	63.93	0.00	0.25	0.00	0.00	1.27	0.00	0.01	0.00	99.29
19	30.15	0.20	2.20	1.08	0.60	62.32	0.07	0.41	0.02	0.01	1.26	0.00	0.01	0.00	98.34
20	29.85	0.27	2.16	0.98	0.19	64.57	0.05	0.28	0.04	0.00	1.21	0.00	0.02	0.00	99.60
21	29.31	0.25	2.02	0.99	0.18	64.77	0.08	0.39	0.03	0.00	1.34	0.00	0.00	0.00	99.37
22	29.20	0.29	2.16	1.16	0.76	63.76	0.11	0.29	0.06	0.00	1.34	0.00	0.01	0.00	99.13
23	29.28	0.31	2.20	1.03	0.37	64.10	0.07	0.19	0.00	0.00	1.46	0.00	0.00	0.00	99.02
24	29.15	0.21	1.96	1.01	0.34	64.53	0.08	0.24	0.05	0.00	1.36	0.00	0.01	0.00	98.93
25	29.52	0.25	2.39	1.06	0.39	62.65	0.08	0.38	0.04	0.00	1.42	0.00	0.02	0.00	98.19
26	29.46	0.26	2.20	0.97	0.93	58.57	0.06	0.41	0.03	0.01	1.25	0.00	0.01	0.00	94.15
27	28.98	0.25	2.21	1.02	0.48	64.38	0.04	0.38	0.05	0.00	1.64	0.00	0.00	0.00	99.42
28	28.57	0.32	2.36	1.07	0.79	64.15	0.08	0.31	0.03	0.01	1.70	0.00	0.00	0.00	99.40
29	29.06	0.21	2.17	1.02	0.62	64.14	0.05	0.26	0.06	0.01	1.51	0.00	0.00	0.00	99.13
30	28.47	0.24	2.42	1.10	0.82	63.48	0.08	0.42	0.03	0.00	1.55	0.00	0.01	0.00	98.61
31	29.46	0.23	2.16	1.04	0.31	63.08	0.07	0.48	0.04	0.00	1.28	0.00	0.01	0.00	98.15
32	29.09	0.28	2.29	0.92	0.99	63.30	0.05	0.30	0.00	0.00	1.41	0.00	0.00	0.00	98.63
33	5.46	1.10	19.32	14.77	4.79	49.91	0.83	0.00	0.00	0.01	1.08	0.00	0.10	0.02	97.34
34	5.28	1.13	17.46	15.33	4.70	49.80	0.98	0.42	0.04	0.00	0.88	0.00	0.08	0.02	96.07
35	5.65	0.68	20.20	12.59	5.04	50.07	0.38	0.11	0.02	0.00	1.15	0.00	0.07	0.02	95.95
36	5.43	1.12	18.40	14.94	4.87	49.91	0.88	0.24	0.04	0.00	0.76	0.00	0.05	0.01	96.64
37	5.23	1.00	19.47	14.13	4.67	49.69	0.85	0.08	0.03	0.01	1.28	0.03	0.14	0.04	96.57
38	5.57	0.64	20.25	13.80	4.54	50.52	0.24	0.22	0.03	0.00	0.99	0.00	0.07	0.02	96.85
39	5.30	0.86	20.73	13.67	4.10	50.38	0.63	0.21	0.02	0.02	1.75	0.00	0.12	0.03	97.76
40	5.39	0.71	21.46	11.87	4.99	49.96	0.49	0.00	0.05	0.00	1.67	0.00	0.23	0.05	96.77

Table B1.8: *Clinker_4C* spot chemical composition (oxides wt%), as determined by electron microprobe analyses. Column *N* refers the number of the punctual chemical analysis marked out in Figure B1.8.

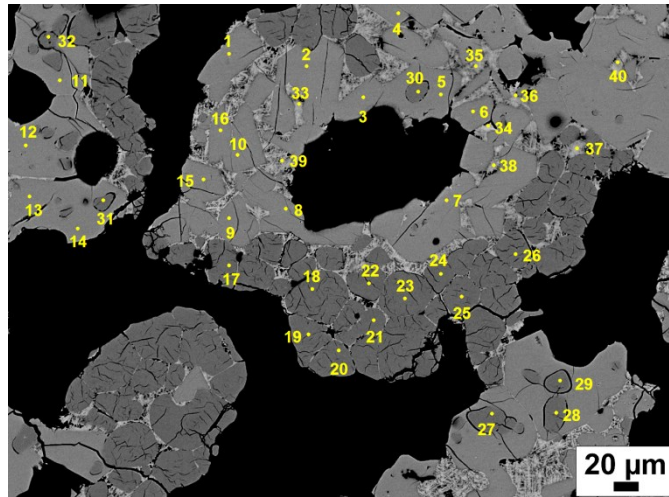


Figure B1.8: *Clinker_4C* SEM images with spots corresponding to punctual chemical analyses reported in Table B1.8.

Appendix B2

Raw meal_1

Raw meal 1_0.0% CaCl ₂	Temperature [°C]								
	900	1000	1100	1200	1250	1300	1350	1400	1450
C ₃ S	0.0	0.0	0.0	0.0	6.8	37.6	57.4	70.6	71.7
C ₂ S	46.4	49.9	53.5	64.2	65.8	45.8	33.0	17.7	16.6
C ₃ A	1.5	0.4	3.0	4.1	3.9	6.3	7.9	0.0	0.0
C ₄ AF	6.0	5.6	6.5	6.6	5.3	2.1	0.0	0.0	0.0
CaO	36.0	35.3	33.5	25.1	18.1	8.1	1.8	0.0	0.0
Other	10.1	8.7	3.4	0.0	0.0	0.0	0.0	0.0	0.0
Liquid	0.0	0.0	0.0	0.0	0.0	0.0	0.0	11.7	11.7
Total	100.0	100.0	100.0	100.0	100.0	100.0	100.0	100.0	100.0
Raw meal 1_0.5% CaCl ₂	Temperature [°C]								
	900	1000	1100	1200	1250	1300	1350	1400	1450
C ₃ S	0.0	0.0	0.0	0.0	0.0	26.9	69.5	96.9	-
C ₂ S	40.8	51.4	61.9	72.5	76.0	49.7	15.0	0.6	-
C ₃ A	0.0	0.0	0.0	0.0	0.0	0.0	0.0	0.0	-
C ₄ AF	0.0	0.0	0.0	0.0	0.0	0.0	0.0	0.0	-
CaO	50.3	42.7	35.1	27.5	24.0	23.4	15.5	2.5	-
Other	8.9	5.9	2.9	0.0	0.0	0.0	0.0	0.0	-
Liquid	0.0	0.0	0.0	0.0	0.0	0.0	0.0	0.0	-
Total	100.0	100.0	100.0	100.0	100.0	100.0	100.0	100.0	-
Raw meal 1_1.0% CaCl ₂	Temperature [°C]								
	900	1000	1100	1200	1250	1300	1350	1400	1450
C ₃ S	0.0	0.0	0.0	0.0	0.0	33.5	75.4	81.5	81.5
C ₂ S	50.8	55.9	60.8	63.8	64.0	38.2	5.8	3.7	3.7
C ₃ A	15.4	13.2	11.0	9.3	8.8	4.9	0.2	0.0	0.0
C ₄ AF	0.0	0.0	1.5	4.7	5.9	3.5	0.1	0.0	0.0
CaO	30.4	28.3	25.0	21.7	21.2	13.5	4.0	0.0	0.0
Other	3.4	2.7	1.7	0.5	0.1	0.0	0.0	0.0	0.0
Liquid	0.0	0.0	0.0	0.0	0.0	6.4	14.5	14.8	14.8
Total	100.0	100.0	100.0	100.0	100.0	100.0	100.0	100.0	100.0
Raw meal 1_1.5% CaCl ₂	Temperature [°C]								
	900	1000	1100	1200	1250	1300	1350	1400	1450
C ₃ S	-	-	10.2	26.0	33.8	50.9	70.3	76.1	-
C ₂ S	-	-	51.2	44.0	40.5	27.0	11.0	6.9	-
C ₃ A	-	-	12.7	10.6	9.6	5.7	1.1	0.0	-
C ₄ AF	-	-	1.0	2.5	3.3	2.1	0.4	0.0	-
CaO	-	-	21.7	14.8	11.4	8.4	5.5	4.0	-
Other	-	-	2.8	1.1	0.2	0.0	0.0	0.0	-
Liquid	-	-	0.4	1.0	1.2	5.9	11.6	13.0	-
Total	-	-	100.0	100.0	100.0	100.0	100.0	100.0	-

Table B2.1: Interpolated quantitative phase analysis results (wt%) during the thermal treatment of chlorine-doped *raw meal_1* series. The dash symbol indicates where interpolated data were not reported because unreliable.

Raw meal_2

Raw meal 2_0.0% CaCl ₂	Temperature [°C]								
	900	1000	1100	1200	1250	1300	1350	1400	1450
C ₃ S	0.0	0.0	0.0	9.8	36.9	62.2	73.8	78.3	80.2
C ₂ S	51.6	55.8	60.1	56.3	35.6	16.2	5.8	2.1	1.6
C ₃ A	4.3	4.8	5.0	4.3	2.0	0.0	0.0	0.0	0.0
C ₄ AF	6.9	7.0	7.4	6.5	3.0	0.0	0.0	0.0	0.0
CaO	35.1	31.1	26.9	21.1	14.6	8.7	7.5	6.7	5.3
Other	2.1	1.3	0.6	0.0	0.0	0.0	0.0	0.0	0.0
Liquid	0.0	0.0	0.0	2.1	7.8	12.9	12.9	12.9	12.9
Total	100.0	100.0	100.0	100.0	100.0	100.0	100.0	100.0	100.0
Raw meal 2_0.5% CaCl ₂	Temperature [°C]								
	900	1000	1100	1200	1250	1300	1350	1400	1450
C ₃ S	0.0	0.0	0.0	0.0	26.7	50.3	66.2	75.0	78.0
C ₂ S	51.3	52.7	56.3	63.2	45.3	28.4	15.7	8.7	5.7
C ₃ A	13.2	15.7	9.8	6.8	2.7	0.0	0.0	0.0	0.0
C ₄ AF	0.0	0.0	0.0	0.0	0.0	0.0	0.0	0.0	0.0
CaO	32.4	29.9	27.0	20.5	11.6	4.9	1.8	0.0	0.0
Other	3.2	1.7	0.3	0.0	0.0	0.0	0.0	0.0	0.0
Liquid	0.0	0.0	6.5	9.5	13.6	16.3	16.3	16.3	16.3
Total	100.0	100.0	100.0	100.0	100.0	100.0	100.0	100.0	100.0
Raw meal 2_1.0% CaCl ₂	Temperature [°C]								
	900	1000	1100	1200	1250	1300	1350	1400	1450
C ₃ S	0.0	0.0	0.0	0.0	38.2	53.4	75.7	81.1	80.7
C ₂ S	52.8	54.5	61.7	64.6	37.2	26.1	6.9	4.0	4.6
C ₃ A	12.7	12.0	11.4	9.3	3.5	1.3	0.0	0.0	0.0
C ₄ AF	0.0	0.0	0.0	5.1	2.2	0.8	0.0	0.0	0.0
CaO	30.8	29.8	26.4	21.0	9.9	5.7	2.6	0.1	0.0
Other	3.7	3.7	0.6	0.0	0.0	0.0	0.0	0.0	0.0
Liquid	0.0	0.0	0.0	0.0	9.0	12.7	14.8	14.8	14.8
Total	100.0	100.0	100.0	100.0	100.0	100.0	100.0	100.0	100.0
Raw meal 2_1.5% CaCl ₂	Temperature [°C]								
	900	1000	1100	1200	1250	1300	1350	1400	1450
C ₃ S	0.0	0.0	-	-	-	-	68.8	75.3	77.5
C ₂ S	52.1	54.5	-	-	-	-	9.4	4.3	3.5
C ₃ A	14.6	14.5	-	-	-	-	0.0	0.0	0.0
C ₄ AF	0.0	0.0	-	-	-	-	0.0	0.0	0.0
CaO	30.1	28.3	-	-	-	-	7.3	5.9	4.6
Other	3.2	2.7	-	-	-	-	0.0	0.0	0.0
Liquid	0.0	0.0	-	-	-	-	14.5	14.5	14.5
Total	100.0	100.0	-	-	-	-	100.0	100.0	100.0

Table B2.2: Interpolated quantitative phase analysis results (wt%) during the thermal treatment of chlorine-doped *raw meal_2* series. The dash symbol indicates where interpolated data were not reported because unreliable.

Raw meal_3

Raw meal 3_0.0% CaCl ₂	Temperature [°C]								
	900	1000	1100	1200	1250	1300	1350	1400	1450
C ₃ S	0.0	0.0	0.0	0.0	15.3	38.5	65.1	75.8	74.6
C ₂ S	59.4	61.5	63.9	70.3	61.3	45.7	25.2	16.3	17.6
C ₃ A	1.1	0.1	0.0	0.0	0.0	0.0	0.0	0.0	0.0
C ₄ AF	1.1	2.0	6.9	7.9	5.4	1.7	0.0	0.0	0.0
CaO	33.9	34.1	28.9	21.8	15.5	7.9	1.9	0.0	0.0
Other	4.5	2.3	0.4	0.0	0.0	0.0	0.0	0.0	0.0
Liquid	0.0	0.0	0.0	0.0	2.4	6.1	7.9	7.9	7.9
Total	100.0	100.0	100.0	100.0	100.0	100.0	100.0	100.0	100.0
Raw meal 3_0.5% CaCl ₂	Temperature [°C]								
	900	1000	1100	1200	1250	1300	1350	1400	1450
C ₃ S	0.0	0.0	0.0	0.0	30.3	60.7	77.6	79.9	80.8
C ₂ S	55.0	56.4	59.5	64.6	41.3	18.0	6.3	5.7	5.5
C ₃ A	12.3	12.8	9.2	6.7	4.0	1.3	0.0	0.0	0.0
C ₄ AF	0.0	0.2	4.2	5.7	3.4	1.1	0.0	0.0	0.0
CaO	29.7	27.8	25.3	21.3	14.5	7.6	2.6	0.8	0.1
Other	3.0	2.7	1.7	0.5	0.3	0.1	0.0	0.0	0.0
Liquid	0.0	0.0	0.0	1.2	6.2	11.2	13.6	13.6	13.6
Total	100.0	100.0	100.0	100.0	100.0	100.0	100.0	100.0	100.0
Raw meal 3_1.0% CaCl ₂	Temperature [°C]								
	900	1000	1100	1200	1250	1300	1350	1400	1450
C ₃ S	0.0	0.0	0.0	0.0	25.0	54.8	68.2	74.2	75.0
C ₂ S	52.7	55.4	62.6	65.0	46.7	25.0	12.6	8.7	8.1
C ₃ A	14.5	14.1	11.4	9.3	4.2	0.0	0.0	0.0	0.0
C ₄ AF	0.0	0.0	0.0	5.3	5.2	0.0	0.0	0.0	0.0
CaO	28.3	26.4	24.6	20.4	13.5	5.5	4.5	2.3	2.1
Other	4.5	4.1	1.4	0.1	0.0	0.0	0.0	0.0	0.0
Liquid	0.0	0.0	0.0	0.0	5.3	14.8	14.8	14.8	14.8
Total	100.0	100.0	100.0	100.0	100.0	100.0	100.0	100.0	100.0
Raw meal 3_1.5% CaCl ₂	Temperature [°C]								
	900	1000	1100	1200	1250	1300	1350	1400	1450
C ₃ S	-	0.0	0.0	0.0	28.3	59.0	69.0	69.7	70.7
C ₂ S	-	53.7	56.4	56.5	32.9	7.3	0.8	1.3	0.0
C ₃ A	-	16.5	13.3	11.5	6.5	1.2	0.0	0.0	0.0
C ₄ AF	-	0.0	0.0	0.0	0.0	0.0	0.0	0.0	0.0
CaO	-	28.9	27.1	27.1	22.4	17.3	13.7	12.5	12.9
Other	-	1.1	0.0	0.0	0.0	0.0	0.0	0.0	0.0
Liquid	-	0.0	3.2	5.0	9.9	15.3	16.5	16.5	16.5
Total	-	100.0	100.0	100.0	100.0	100.0	100.0	100.0	100.0

Table B2.3: Interpolated quantitative phase analysis results (wt%) during the thermal treatment of chlorine-doped *raw meal_3* series. The dash symbol indicates where interpolated data were not reported because unreliable.

Raw meal_4

Raw meal 4_0.0% CaCl ₂	Temperature [°C]								
	900	1000	1100	1200	1250	1300	1350	1400	1450
C ₃ S	0.0	0.0	0.0	0.0	14.2	49.8	68.3	74.3	73.1
C ₂ S	52.4	56.6	61.0	65.5	55.1	25.6	11.6	8.9	8.6
C ₃ A	2.3	4.3	4.4	4.2	3.3	1.0	0.0	0.0	0.0
C ₄ AF	0.0	0.0	2.3	4.8	4.3	1.4	0.0	0.0	0.0
CaO	39.6	34.6	29.7	24.9	21.0	14.9	10.4	7.1	8.6
Other	5.7	4.6	2.6	0.6	0.0	0.0	0.0	0.0	0.0
Liquid	0.0	0.0	0.0	0.0	2.1	7.3	9.7	9.7	9.7
Total	100.0	100.0	100.0	100.0	100.0	100.0	100.0	100.0	100.0
Raw meal 4_0.5% CaCl ₂	Temperature [°C]								
	900	1000	1100	1200	1250	1300	1350	1400	1450
C ₃ S	0.0	0.0	0.0	0.0	13.1	51.8	74.3	77.6	77.7
C ₂ S	59.3	65.2	68.8	68.4	56.9	25.1	7.3	5.1	5.0
C ₃ A	12.3	12.3	10.6	7.9	5.6	1.9	0.0	0.0	0.0
C ₄ AF	0.0	0.5	3.9	8.7	8.6	2.9	0.0	0.0	0.0
CaO	26.4	20.9	16.4	15.0	12.6	5.8	1.0	0.0	0.0
Other	2.0	1.1	0.3	0.0	0.0	0.0	0.0	0.0	0.0
Liquid	0.0	0.0	0.0	0.0	3.2	12.5	17.3	17.3	17.3
Total	100.0	100.0	100.0	100.0	100.0	100.0	100.0	100.0	100.0
Raw meal 4_1.0% CaCl ₂	Temperature [°C]								
	900	1000	1100	1200	1250	1300	1350	1400	1450
C ₃ S	0.0	0.0	0.0	1.5	26.5	56.2	76.3	83.1	82.4
C ₂ S	55.0	60.2	62.1	63.9	41.3	16.4	2.5	1.9	2.6
C ₃ A	12.9	11.8	9.9	11.2	4.1	0.0	0.0	0.0	0.0
C ₄ AF	0.0	0.0	4.6	3.2	1.2	0.0	0.0	0.0	0.0
CaO	28.7	25.8	23.1	19.7	17.3	12.4	6.2	0.0	0.0
Other	3.4	2.2	0.2	0.0	0.0	0.0	0.0	0.0	0.0
Liquid	0.0	0.0	0.0	0.5	9.7	15.0	15.0	15.0	15.0
Total	100.0	100.0	100.0	100.0	100.0	100.0	100.0	100.0	100.0
Raw meal 4_1.5% CaCl ₂	Temperature [°C]								
	900	1000	1100	1200	1250	1300	1350	1400	1450
C ₃ S	0.0	0.0	0.0	4.8	24.8	44.9	69.8	74.8	75.6
C ₂ S	50.0	50.6	57.4	56.5	41.5	26.4	6.8	4.0	3.5
C ₃ A	16.2	16.5	14.0	11.5	8.2	4.8	0.3	0.0	0.0
C ₄ AF	0.0	0.0	0.1	3.5	2.0	0.5	0.0	0.0	0.0
CaO	29.9	29.6	26.6	20.0	14.5	9.0	7.0	5.1	4.7
Other	3.9	3.3	2.0	2.3	1.3	0.3	0.0	0.0	0.0
Liquid	0.0	0.0	0.0	1.5	7.8	14.1	16.1	16.1	16.1
Total	100.0	100.0	100.0	100.0	100.0	100.0	100.0	100.0	100.0

Table B2.4: Interpolated quantitative phase analysis results (wt%) during the thermal treatment of chlorine-doped *raw meal_4* series. The dash symbol indicates where interpolated data were not reported because unreliable.

Appendix B3

Raw meal 1_1.5% CaCl₂

N	SiO ₂	TiO ₂	Al ₂ O ₃	FeO	MgO	CaO	MnO	SrO	Na ₂ O	K ₂ O	SO ₃	Cl	O=Cl	Total
1	33.35	0.08	0.29	0.14	0.03	63.53	0.00	0.36	0.00	0.00	0.18	0.01	0.00	97.97
2	1.69	0.05	38.64	4.48	1.30	45.83	0.01	0.09	0.00	0.00	0.03	4.22	0.95	95.39
3	4.69	1.53	17.21	23.90	1.55	47.61	1.29	0.13	0.00	0.00	0.08	0.41	0.09	98.31
4	8.26	0.05	29.77	3.89	0.13	50.80	0.05	0.25	0.03	0.01	0.27	3.19	0.72	95.97
5	3.21	0.07	36.74	4.51	0.17	46.94	0.01	0.00	0.01	0.00	0.13	3.97	0.90	94.86
6	32.03	0.24	1.24	0.40	0.03	63.25	0.03	0.20	0.00	0.00	0.77	0.01	0.00	98.21
7	11.75	1.36	11.08	21.86	1.21	51.64	1.02	0.15	0.01	0.00	0.27	0.03	0.01	100.37
8	0.00	0.00	0.00	0.00	0.02	0.05	0.06	0.00	0.00	0.00	0.05	0.00	0.00	0.18
9	0.00	0.00	0.00	0.02	0.00	0.04	0.00	0.10	0.03	0.00	0.21	0.00	0.00	0.41
10	3.44	0.10	38.93	4.54	0.69	47.44	0.07	0.16	0.00	0.02	0.04	4.14	0.93	98.63
11	2.84	0.05	36.69	4.79	1.00	47.34	0.01	0.16	0.02	0.01	0.04	3.91	0.88	95.97
12	6.70	0.07	33.79	4.18	0.10	49.70	0.01	0.20	0.01	0.00	0.22	3.52	0.79	97.69
13	24.92	0.21	1.29	1.44	0.72	53.54	0.10	0.18	0.00	0.01	0.31	0.05	0.01	82.75
14	33.77	0.11	0.33	0.14	0.02	64.25	0.00	0.27	0.00	0.00	0.16	0.01	0.00	99.06

Table B3.1: *Raw meal 1_1.5% CaCl₂* spot chemical composition (oxides wt%), as determined by electron microprobe analyses. Column *N* reports the number of the punctual chemical analysis marked out in Figure B3.1.

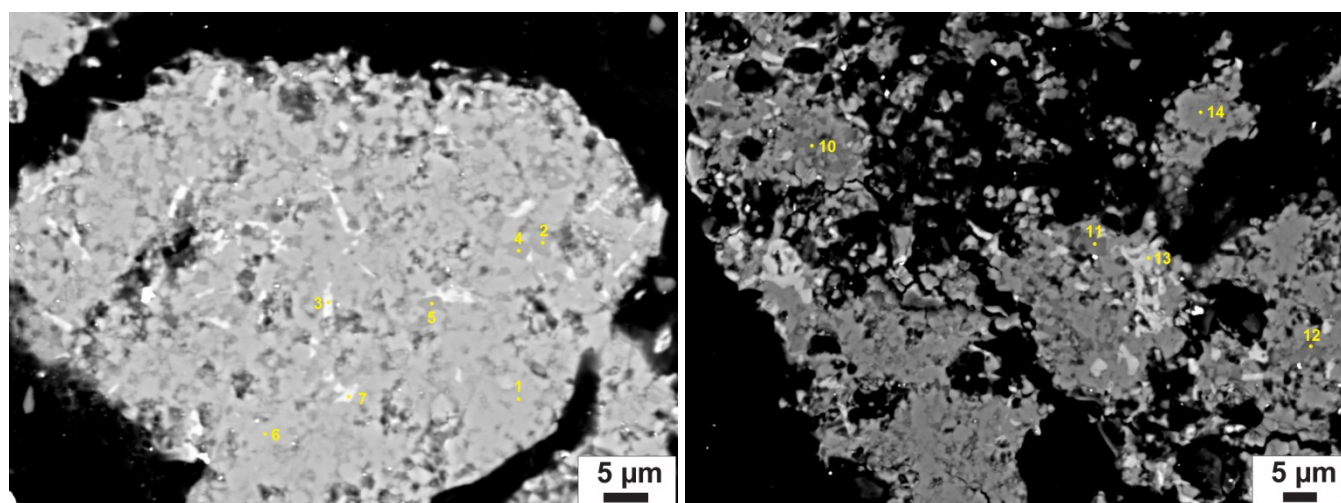


Figure B3.1: *Raw meal 1_1.5% CaCl₂* SEM images with spots corresponding to punctual chemical analyses reported in Table B3.1. Points 8 and 9, collected on the wall of the platinum capillary, are not shown.

Raw meal 2_1.5% CaCl₂

N	SiO ₂	TiO ₂	Al ₂ O ₃	FeO	MgO	CaO	MnO	SrO	Na ₂ O	K ₂ O	SO ₃	Cl	O=Cl	Total
15	29.00	0.33	2.23	1.25	0.31	64.10	0.06	0.36	0.15	0.02	1.47	0.01	0.00	99.29
16	28.16	0.28	2.44	1.33	0.47	62.73	0.02	0.14	0.22	0.01	1.75	0.03	0.01	97.57
17	0.00	0.00	0.00	0.00	0.02	0.03	0.07	0.00	0.00	0.00	0.09	0.00	0.00	0.22
18	0.03	0.00	0.00	0.00	0.00	0.04	0.04	0.00	0.00	0.00	0.19	0.00	0.00	0.30
19	1.48	1.32	22.13	19.52	2.32	47.55	1.44	0.11	0.00	0.00	0.00	0.02	0.00	95.89
20	1.82	1.11	22.97	19.23	1.97	48.73	0.93	0.00	0.01	0.00	0.05	0.00	0.00	96.81
21	28.24	0.30	2.60	1.26	0.38	63.42	0.11	0.26	0.17	0.02	1.57	0.03	0.01	98.35
22	2.10	0.74	23.49	18.30	2.46	48.16	0.81	0.00	0.02	0.01	0.07	0.01	0.00	96.16
23	3.09	0.01	29.67	4.18	0.96	59.62	0.05	0.04	0.13	0.00	0.02	0.02	0.00	97.79
24	26.52	0.19	1.32	0.59	0.82	69.10	0.02	0.27	0.07	0.00	0.34	0.04	0.01	99.28
25	19.93	0.28	5.15	3.43	1.09	67.90	0.27	0.06	0.03	0.00	0.23	0.01	0.00	98.37
26	3.23	0.78	18.63	21.61	2.63	47.73	0.88	0.20	0.04	0.00	0.24	0.03	0.01	95.99
27	2.63	0.01	30.62	3.91	0.54	60.58	0.04	0.15	0.14	0.00	0.03	0.00	0.00	98.66
28	2.65	0.05	30.49	3.58	0.50	60.54	0.00	0.28	0.11	0.01	0.01	0.01	0.00	98.22

Table B3.2: *Raw meal 2_1.5% CaCl₂* spot chemical composition (oxides wt%), as determined by electron microprobe analyses. Column *N* reports the number of the punctual chemical analysis marked out in Figure B3.2.

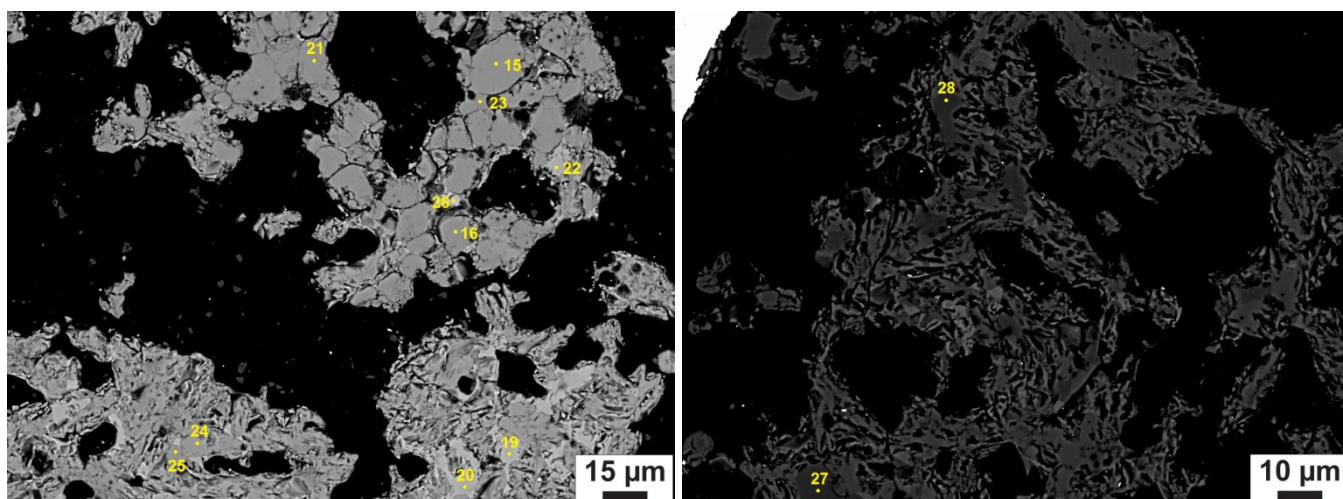


Figure B3.2: *Raw meal 2_1.5% CaCl₂* SEM images with spots corresponding to punctual chemical analyses reported in Table B3.2. Points 17 and 18, collected on the wall of the platinum capillary, are not shown.

Appendix C1

Phase	<i>bc_1</i>	
	1 st series	2 nd series
C ₃ S M1	13.5(4)	17.9(5)
C ₃ S M3	47.9(8)	44.3(9)
C ₂ S β	3.5(3)	2.3(3)
C ₂ S α	6.1(3)	6.3(4)
C ₃ A cubic	4.6(2)	1.2(2)
C ₃ A orthorhombic	9.3(4)	12.3(5)
C ₄ AF	9.8(4)	10.3(3)
CaO	0.1(0)	0.7(1)
Ca(OH) ₂	0.7(2)	0.8(2)
MgO	4.5(2)	3.9(2)
Total	100.0	100.0

Table C1.1: Clinker *bc_1* phase composition (wt%), as determined processing XRPD data by Rietveld refinements.

Phase	<i>C&bc_2</i>	
	1 st series	2 nd series
C ₃ S M1	9.8(5)	13.3(4)
C ₃ S M3	33.4(7)	26.6(6)
C ₂ S β	6.7(5)	10.8(4)
C ₂ S α	18.3(6)	15.5(4)
C ₃ A cubic	6.5(3)	1.5(3)
C ₃ A orthorhombic	9.3(3)	12.2(4)
C ₄ AF	7.0(4)	10.9(4)
CaO	4.6(2)	4.6(2)
Ca(OH) ₂	0.6(2)	1.0(3)
MgO	3.9(2)	3.6(2)
Total	100.0	100.0

Table C1.2: Clinker *C&bc_2* phase composition (wt%), as determined processing XRPD data by Rietveld refinements.

Phase	<i>C&bc_3</i>	
	1 st series	2 nd series
C ₃ S M1	6.7(4)	8.7(5)
C ₃ S M3	26.0(7)	32.7(8)
C ₂ S β	11.2(4)	12.3(4)
C ₂ S α	25.2(5)	14.7(5)
C ₃ A cubic	2.5(3)	1.8(2)
C ₃ A orthorhombic	12.1(4)	12.8(4)
C ₄ AF	9.9(4)	9.8(5)
CaO	1.7(2)	3.3(2)
Ca(OH) ₂	0.8(2)	1.0(3)
MgO	4.1(1)	3.1(1)
Total	100.0	100.0

Table C1.3: Clinker *C&bc_3* phase composition (wt%), as determined processing XRPD data by Rietveld refinements.

Phase	<i>C&bc_4</i>	<i>C&bc_4</i>
	1 st series	2 nd series
C ₃ S M1	11.9(4)	4.6(4)
C ₃ S M3	34.7(7)	44.1(8)
C ₂ S β	12.5(4)	8.5(3)
C ₂ S α	10.1(4)	11.1(4)
C ₃ A cubic	4.8(2)	2.7(2)
C ₃ A orthorhombic	10.2(4)	11.1(3)
C ₄ AF	7.6(3)	10.9(4)
CaO	2.8(2)	3.0(2)
Ca(OH) ₂	1.3(3)	0.4(1)
MgO	4.0(2)	3.6(2)
Total	100.0	100.0

Table C1.4: Clinker *C&bc_4* phase composition (wt%), as determined processing XRPD data by Rietveld refinements.

Phase	<i>C&bc_5</i>	<i>C&bc_5</i>
	1 st series	2 nd series
C ₃ S M1	11.4(4)	8.3(4)
C ₃ S M3	25.8(7)	39.4(9)
C ₂ S β	10.5(5)	6.2(3)
C ₂ S α	25.0(7)	14.5(4)
C ₃ A cubic	6.3(4)	2.1(2)
C ₃ A orthorhombic	9.5(3)	10.1(5)
C ₄ AF	6.4(3)	9.5(3)
CaO	1.3(2)	6.6(3)
Ca(OH) ₂	0.4(1)	0.6(1)
MgO	3.3(2)	2.7(1)
Total	100.0	100.0

Table C1.5: Clinker *C&bc_5* phase composition (wt%), as determined processing XRPD data by Rietveld refinements.

Phase	<i>C&bc_6</i>	<i>C&bc_6</i>
	1 st series	2 nd series
C ₃ S M1	8.6(4)	7.6(4)
C ₃ S M3	14.8(5)	31.4(6)
C ₂ S β	21.8(6)	9.8(3)
C ₂ S α	23.3(7)	17.0(3)
C ₃ A cubic	4.0(2)	3.9(2)
C ₃ A orthorhombic	10.5(3)	7.5(4)
C ₄ AF	11.5(3)	10.5(4)
CaO	1.7(2)	8.3(2)
Ca(OH) ₂	0.3(1)	0.5(1)
MgO	3.6(2)	3.6(2)
Total	100.0	100.0

Table C1.6: Clinker *C&bc_6* phase composition (wt%), as determined processing XRPD data by Rietveld refinements.

Appendix C2

Phase	<i>bc_1F</i>	
	1 st series	2 nd series
C ₃ S M1	13.4(4)	15.3(4)
C ₃ S M3	51.1(9)	47.4(8)
C ₂ S β	1.7(2)	5.7(3)
C ₂ S α	5.9(3)	3.2(2)
C ₃ A cubic	2.8(3)	1.1(2)
C ₃ A orthorhombic	5.9(4)	7.2(3)
C ₄ AF	15.3(5)	15.8(4)
CaO	0.0(0)	0.6(1)
Ca(OH) ₂	0.0(0)	0.3(1)
MgO	4.0(2)	3.4(2)
Total	100.0	100.0

Table C2.1: Clinker *bc_1F* phase composition (wt%), as determined processing XRPD data by Rietveld refinements.

Phase	C&bc_2F	
	1 st series	2 nd series
C ₃ S M1	10.4(4)	11.3(3)
C ₃ S M3	35.9(7)	39.2(6)
C ₂ S β	11.6(3)	16.5(5)
C ₂ S α	9.9(4)	4.5(3)
C ₃ A cubic	5.8(3)	2.6(2)
C ₃ A orthorhombic	6.2(3)	7.6(4)
C ₄ AF	14.1(5)	12.3(4)
CaO	2.3(2)	2.0(1)
Ca(OH) ₂	0.0(0)	0.7(1)
MgO	3.8(2)	3.3(2)
Total	100.0	100.0

Table C2.2: Clinker *C&bc_2F* phase composition (wt%), as determined processing XRPD data by Rietveld refinements.

Phase	C&bc_3F	
	1 st series	2 nd series
C ₃ S M1	6.6(4)	6.2(3)
C ₃ S M3	36.1(7)	44.6(5)
C ₂ S β	18.6(6)	9.6(4)
C ₂ S α	11.9(5)	8.9(4)
C ₃ A cubic	3.8(3)	3.7(3)
C ₃ A orthorhombic	5.4(3)	7.1(4)
C ₄ AF	11.0(4)	11.6(5)
CaO	2.6(2)	4.5(3)
Ca(OH) ₂	0.5(1)	0.4(1)
MgO	3.6(1)	3.6(1)
Total	100.0	100.0

Table C2.3: Clinker *C&bc_3F* phase composition (wt%), as determined processing XRPD data by Rietveld refinements.

Phase	C&bc_4F	
	1 st series	2 nd series
C ₃ S M1	16.2(4)	10.1(4)
C ₃ S M3	39.8(8)	45.8(8)
C ₂ S β	10.0(4)	8.6(4)
C ₂ S α	7.3(3)	5.6(3)
C ₃ A cubic	4.6(3)	3.3(2)
C ₃ A orthorhombic	3.8(3)	7.2(4)
C ₄ AF	12.2(5)	11.4(5)
CaO	2.7(2)	3.8(2)
Ca(OH) ₂	0.4(1)	0.3(1)
MgO	3.2(1)	3.9(2)
Total	100.0	100.0

Table C2.4: Clinker *C&bc_4F* phase composition (wt%), as determined processing XRPD data by Rietveld refinements.

Phase	C&bc_5F	
	1 st series	2 nd series
C ₃ S M1	7.0(4)	15.8(7)
C ₃ S M3	40.4(7)	28.0(9)
C ₂ S β	16.8(5)	15.9(4)
C ₂ S α	3.0(3)	12.8(4)
C ₃ A cubic	5.6(4)	4.3(3)
C ₃ A orthorhombic	3.0(3)	3.9(2)
C ₄ AF	14.1(5)	14.1(4)
CaO	6.3(2)	2.1(1)
Ca(OH) ₂	0.5(1)	0.3(1)
MgO	3.3(2)	2.9(3)
Total	100.0	100.0

Table C2.5: Clinker *C&bc_5F* phase composition (wt%), as determined processing XRPD data by Rietveld refinements.

Phase	C&bc_6F	
	1 st series	2 nd series
C ₃ S M1	7.9(4)	11.2(2)
C ₃ S M3	38.4(9)	37.2(3)
C ₂ S β	13.7(4)	10.9(4)
C ₂ S α	6.1(3)	1.8(2)
C ₃ A cubic	4.4(3)	3.8(2)
C ₃ A orthorhombic	2.1(2)	1.8(2)
C ₄ AF	15.5(4)	12.4(5)
CaO	9.2(2)	17.3(3)
Ca(OH) ₂	0.0(0)	0.7(1)
MgO	2.8(1)	2.9(2)
Total	100.0	100.0

Table C2.6: Clinker *C&bc_6F* phase composition (wt%), as determined processing XRPD data by Rietveld refinements.

Acknowledgements

Thanks to Monica and Nicoletta, my tutor and co-tutor respectively, for both the scientific contribution and the continuous support during my entire PhD course.

Thanks to my PhD colleagues Giorgia and Lucia for having shared with me good and less good times during the last three years, as well as the office.

Thanks to all professors, researchers and technicians of the “Sezione di Mineralogia” of the Department of Earth Sciences. In particular to Fabio, Andrea, Elena, Nicola, Valeria and Franco.

Thanks to Prof. De la Torre, for hosting me at the University of Malaga and for her scientific advice.

Thanks to Dr. Marchi and Dr.ssa Segata for hosting me at Italcementi research centre and making thus this PhD research possible. Special thanks to all the laboratory technicians of the Italcementi research centre, especially to (alphabetically) Alessandro, Bruno, Emanuele, Ennio, Federica, Federico and Nicoletta.

Last but not least, many many many thanks to my family and to Sabrina for their continuous support and patience during this PhD, particularly over the last “tough” few months.